ISBN 978-94-92323-34-7
9 789492 323347

Hybridization of open photonic systems

Kévin G. Cognée

2020

# *Hybridization of open photonic systems*

Kévin G. Cognée

# Hybridization of open photonic resonators

Kévin Georges Guy Cognée

Joint Ph.D. Thesis, University of Amsterdam & University of Bordeaux, January 2020
*Hybridization of open photonic resonators*
Kévin Georges Guy Cognée

ISBN: 978-94-92323-34-7

The work described in this thesis was performed at
AMOLF, Science Park 104, 1098 XG Amsterdam, The Netherlands
and LP2N - Institut d'Optique, Rue François Mitterrand, 33400 Talence, France.

This work is part of the Netherlands Organisation for Scientific Research (NWO) and has benefited from state funding, managed by the French National Research Agency (ANR). The funding is allocated in the framework of the "Investments for the Future" program, with the reference number ANR - n° ANR-10-IDEX-03-02.

A digital version of this thesis can be downloaded from
`https://www.amolf.nl` and `https://tel.archives-ouvertes.fr`.

# Hybridization of open photonic resonators

THÈSE EN COTUTELLE

présentée afin d'obtenir le grade de docteur de l'Université de Bordeaux,
décerné par l'École doctorale des Sciences Physiques et de l'Ingénieur,
(spécialité lasers, matière et nanosciences), et de l'Université d'Amsterdam
et soutenue publiquement à l'Agnietenkapel à Amsterdam (Pays-Bas)
le mardi 28 janvier 2020, à 10:00

par

*Kévin Georges Guy Cognée*

Né à Confolens, France

**Commission d'examen**

*Directeurs de thèse:*

| | |
|---|---|
| Mr. P. Lalanne | Université de Bordeaux / CNRS |
| Mr. A. F. Koenderink | Universiteit van Amsterdam |

*Membres du jury:*

| | | |
|---|---|---|
| Mr. A. Polman | Universiteit van Amsterdam | Président |
| Mme. B. Dagens | Université Paris - Saclay / CNRS | Rapporteur |
| Mr. M. P. van Exter | Universiteit Leiden | Rapporteur |
| Mr. E. Brasselet | Université de Bordeaux | Examinateur |
| Mme. S. M. García Blanco | Universiteit Twente | Examinateur |

École doctorale Sciences Physiques et de l'Ingénieur.

This thesis was prepared within the partnership between the University of Bordeaux and the University of Amsterdam with the purpose of obtaining a joint doctorate degree. The thesis was prepared in the Faculty of Physics and Engineering at the University of Bordeaux and in the Faculty of Science at the University of Amsterdam.

Cette thèse a été préparée dans le cadre d'une collaboration entre l'Université de Bordeaux et l'Université d'Amsterdam afin d'obtenir un diplôme de doctorat conjoint. Cette thèse a été préparée au sein de l'École doctorale Science Physiques et de l'Ingénieur de l'Université de Bordeaux et de la Faculteit der Natuurwetenschappen, Wiskunde en Informatica de l'Universiteit van Amsterdam.

# Hybridization of open photonic resonators

ACADEMISCH PROEFSCHRIFT

ter verkrijging van de graad van doctor aan de Universiteit van
Amsterdam, op gezag van de Rector Magnificus
prof. dr. ir. K.I.J. Maex
ten overstaan van een door het College voor Promoties ingestelde commissie,
in het openbaar te verdedigen in de Agnietenkapel
op dinsdag 28 januari 2020, te 10:00 uur

door

*Kévin Georges Guy Cognée*

geboren te Confolens

*Promotiecommissie*

| | | |
|---|---|---|
| Promotores: | prof. dr. A. F. Koenderink | Universiteit van Amsterdam |
| | prof. dr. P. Lalanne | Université de Bordeaux |
| Overige leden: | prof. dr. M. P. van Exter | Universiteit Leiden |
| | prof. dr. B. Dagens | Université Paris - Saclay |
| | prof. dr. A. Polman | Universiteit van Amsterdam |
| | prof. dr. E. Brasselet | Université de Bordeaux |
| | prof. dr. S. M. García Blanco | Universiteit Twente |

Faculteit der Natuurwetenschappen, Wiskunde en Informatica

Dit proefschrift is tot stand gekomen binnen een samenwerkingsverband tussen de Universiteit van Amsterdam en de Université de Bordeaux met als doel het behalen van een gezamenlijk doctoraat. Het proefschrift is voorbereid in de Faculteit der Natuurwetenschappen, Wiskunde en Informatica van de Universiteit van Amsterdam en de École doctorale Sciences Physiques et de l'Ingénieur van de Université de Bordeaux.

This thesis was prepared within the partnership between the University of Amsterdam and Université de Bordeaux with the purpose of obtaining a joint doctorate degree. The thesis was prepared in the Faculty of Science at the University of Amsterdam and in the École doctorale Sciences Physiques et de l'Ingénieur at the Université de Bordeaux.

*À mes grands-pères*

# Contents

# 1

# Introduction

A common saying in many cultures is that a pot of gold awaits at the end of the rainbow. For a researcher in the field of optics and photonics, the treasure is instead for everyone to see, the rainbow unveiling the majesty of the intangible phenomenon that is light. If we define light as the domain of optics at wavelengths from the ultraviolet to the mid-infrared, then light counts as the most versatile frequency band of the electromagnetic spectrum. First, it is primordial in the emergence of life on earth and is essential to the whole ecosystem of our planet as the primary source of energy received from the sun, driving the process of photosynthesis to convert sunlight to chemical energy. Also, light is a primary carrier of information that reveals to mankind the make up of matter, through virtue of spectroscopic fingerprints - absorption and emission of light specific to the atomic, molecular or solid-state structure of matter, and through the possibility of imaging objects. Thus, the telescope placed us in the universe. Conversely, the optical microscope gave us a deeper understanding of our biology [1–3]. The laser [4] has provided us with the tools to, among many other great achievements, probe the quantum properties of matter [5], settle the Einstein-Podolsky-Rosen paradox surrounding entanglement and nonlocality in quantum mechanics [6], and get a first glimpse of black holes [7]. Together with light-emitting diodes and fibre optics, they also revolutionized telecommunication [8], are instrumental for realizing the ultimate quantum secured network [9], and are among the main tools required for a paradigm shift from digital to analog [10] or quantum computing [11].

The advantage that light has over electromagnetic waves in other frequency bands, and more fundamentally, the reason why this region of the spectrum is so vital for living beings, is to be found in its relatively strong interaction with matter. The matter degree of freedom that is of relevance for any electromagnetic phenomenon, is that of charge separation (coupling to

the electric field), and of charge circulation and spin (entering magnetism). The optical spectrum is of high relevance because electronic transitions of the most common atoms, molecules and materials are located in the visible to ultraviolet range. Thereby, optical frequencies are associated with absorption of light by excitation of electronic states, and conversely also the emission of light by fluorescence of electronic transitions in matter. This imbues optics with the ability to perform spectroscopy, to realize efficient light sources, and to address single quantum systems with single grains of light, also called *photons*. Moreover, light can directly provide the energy for chemical reactions that are intrinsically not possible at room temperature, but that can be activated by the few electron volts of energy carried by a visible photon. When matter is not directly resonantly absorbing photons, it is at least polarizable enough to allow for refraction with refractive indices significantly different from that of vacuum $n \neq 1$). This gives the ability to control light by refractive components such as lenses and prisms, and enables confinement of light in fibres and waveguides. This should be contrasted to the X-ray regime, where all materials are essentially only very mildly different from vacuum in refractive index, or conversely to the MHz to THz regime, where the photon energy is much less then that required to interact with electrons in matter, and is even less than the thermal energy $k_B T$.

While optics is unique for the light-matter interaction with electronic transitions, this strength is nonetheless considered weak for many envisioned applications. The field of *nanophotonics* deals with the miniaturisation of photonic devices to nanoscale dimensions, the scale that is naturally suited for interfacing single quantum systems with light [12]. In a standard optical microscope, one can easily observe a single quantum system driven by light, by monitoring the stream of single photons emitted by a single molecule upon laser excitation. This detection relies on the quality of optical filters to separate fluorescent photons from pump laser light by colour. However, the probability for absorption of a single pump photon is only about $10^{-5}$ for a molecule at room temperature in the diffraction limited focus of a microscope (spot size $\lambda/2$). The low probability of a single photon to interact with a single atom or molecule usually implies that many atoms or molecules are necessary to obtain a sizeable effect on this photon. Conversely, the mission of quantum optics (cavity quantum electrodynamics) to control single photons by single quantum systems and vice versa, requires additional strategies to enhance light-matter interaction. Nanophotonics can provide such strategies by manipulating the light field in its spatial and temporal properties. First, photons can be made to interact repeatedly with the atom or molecule, by ensuring that the same photon has opportunity to pass an atom or molecule not once, but multiple times. To this end, one uses optical cavities of high quality factor Q placed around the matter, so that the residence time of light in the cavity is extended to $Q/\omega$ (with $\omega$ the optical frequency). Record quality factors are of order $10^8$ for optical cavities with a footprint no larger then a few 10s of

microns [13]. Second, light can be focused tightly to remain in an interaction volume much smaller than the diffraction limit through *plasmonic* structures. These are metallic nanostructures in which part of the energy of a photon is transferred to an oscillation of free electrons, which gives rise to very tight confinement of the electric field at a metallic interface. Thus, the energy of a photon can be squeezed into a volume reportedly as small as $\lambda^3/10^6$ (where $\lambda$ is the resonance wavelength) [14], albeit for just a few tens of optical cycles. Over the last few decades, both plasmonic structures and optical cavities have demonstrated their large relevance in the context of the enhanced light-matter interaction. They are considered to be essential building blocks for quantum optics, miniaturized lasers, and optical sensors that can even detect single protein molecules, or that give access to the vibrational Raman fingerprint of single molecules. This thesis is largely devoted to *hybrid* plasmonic-dielectric resonators that combine some of the complementary advantages of optical cavities and plasmonic nanoresonators.

In this introductory chapter, we first introduce the relevant figures of merit for the quantification of the interaction between photons and matter taking the example of the enhancement spontaneous emission of light by a single atom or molecule. Next, we briefly give an overview of currently available optical cavities, plasmonic nanoresonators, and hybrid structures, and present a few milestones they reached. Then, we introduce the quasinormal mode (QNM) formalism, our framework of choice to get a better understanding of the lossy nature of micro- and nanoresonators in electromagnetism. We conclude by detailing the motivation of our work and the outline of this thesis.

## 1.1. Light-matter interaction

One of the most fundamental examples of interaction between light and matter is the resonant absorption and spontaneous emission of a photon by an atom or a molecule [15, 16]. Let us consider such a quantum system initially placed in an eigenstate $|i\rangle$ of a Hamiltonian $\hat{\mathcal{H}}_0$ describing the atom and the light field, transitioning (or decaying), to a set of final states $|f\rangle$. We assume a two-state model for the atom or molecule, with a ground state of energy $E_g$ and an excited state of energy $E_e$. The state $|i\rangle = |e, 0\rangle$ therefore corresponds to the atom in an *excited* state and 0 photon, and has an energy $E_i = E_e$. The states $|f\rangle = |g, 1_{\omega,f}\rangle$ corresponds to the atom in the *ground* state with a single photon of energy $\hbar\omega$ in a photonic mode $f$, and has an energy of $E_f = E_g + \hbar\omega$. The interaction with the light field can be treated as a perturbation $\hat{\mathcal{H}}' = -\hat{\mathbf{p}} \cdot \hat{\mathbf{E}}$ to the Hamiltonian $\hat{\mathcal{H}}_0$. Here $\hat{\mathbf{E}}$ is the electric field operator[1], whereas $\hat{\mathbf{p}}$ is the dipole operator. Fermi's golden rule states that the rate of transition from $|i\rangle$ to the collection of $|f\rangle$, which is always accompanied by the emission of a photon

[1] In the context of stimulated emission, this describes the field of the laser. For spontaneous emission, $\hat{\mathbf{E}}$ describes the vacuum fluctuation of the light field. A proper description is given in the context of second quantization in quantum optics [15]

of energy $\hbar\omega$, is given by [15]

$$\Gamma = \sum_f \frac{2\pi}{\hbar} |\langle f|\hat{\mathbf{p}}|i\rangle|^2 \, \delta(E_i - E_f) \tag{1.1}$$

where the sum runs over all the final states $f$.

By noticing that $\langle f|\hat{\mathbf{p}}|i\rangle = \langle e|\hat{\mathbf{p}}|g\rangle$ and introducing the *local density of optical states* (LDOS) $\rho(\mathbf{r},\omega) \equiv \sum_f \delta(E_i - E_f)$, we recognize that the rate $\Gamma$ can be decomposed as a term $\langle e|\hat{\mathbf{p}}|g\rangle$, which described the electronic part of the system and $\rho(\mathbf{r},\omega)$, that quantifies the number of states available for the photon to be emitted into, given the position $\mathbf{r}$ of the emitter and the transition frequency $\omega$. The electronic wavefunction overlap integral is equivalent to the transition dipole moment, a quantum mechanical matrix element to quantify the strength of transitions. Writing this as a dipole moment $\mathbf{p}$, the transition rate, or equivalently spontaneous emission rate, simplifies to [16]

$$\Gamma = \frac{\pi\omega}{3\hbar\epsilon_0} |\mathbf{p}|^2 \rho(\mathbf{r},\omega) \tag{1.2}$$

While the transition dipole matrix element quantifies quantum mechanical properties of the wave functions of electrons, the LDOS is a purely classical property of the electromagnetic environment surrounding the quantum system. In particular, in a homogeneous medium, such as vacuum, the LDOS is given by Larmor's formula $\rho_0(\omega,\mathbf{r}) = \omega^2 n/(\pi^2 c^3)$ [16] (cf. Fig. 1.1 (c), dashed black line). An inspection of the units [s/m$^3$] teaches that the LDOS can really be read as the number of states that vacuum offers per Hz of spectral bandwidth, and per unit of volume. Instead, if one were able to offer a cavity resonance of resonance frequency $\omega_m$, this would provide a contribution to the LDOS that is a single mode, distributed over the cavity linewidth $\gamma_m$ and a volume that is not 1 m$^3$, but the volume $V_m$ to which the cavity confines a photon. Thus, a cavity leads to a Lorentzian LDOS (cf. Fig. 1.1(a) and (c), red line)

$$\frac{\Gamma}{\Gamma_0} = F_m \frac{\omega_m^2}{\omega^2} \frac{\gamma_m^2/4}{(\omega-\omega_m)^2 + \gamma_m^2/4} \quad \text{with} \quad F_m \equiv \frac{3}{4\pi^2}\left(\frac{\lambda_m}{n}\right)^3 \left(\frac{Q_m}{V_m}\right), \tag{1.3}$$

This equation is due to Purcell who quoted it in a brief abstract in 1946 [17], and the enhancement on resonance $F_m$ has since been called *Purcell factor*. It suggests that an increase in light matter interaction is possible in resonators with high quality factors $Q_m \equiv \frac{\omega_m}{\gamma_m}$, yet strong field confinement through small mode volumes $V_m$. It is worthwhile to note that resonances are not the only way to modify the LDOS. As it was shown by Drexhage in 1960, also a simple metallic mirror can modify the rate of emission of an emitter due to the interaction with the dipole mirror image [18]. More complex structures can lead to even more exotic LDOS, such as photonic bandgaps in photonic crystals, where all modes can be suppressed in a frequency band known as the

photonic band gap [19] (cf. Fig. 1.1 (b) and (c), blue line). The treatment of the modification of a decay rate by a photonic structure also applies to classical current sources in antenna physics, where it is not the decay rate, but the radiated power per unit of current run through the dipole source that is affected by LDOS. This is known as radiative impedance engineering in electrical engineering and acoustics [20].

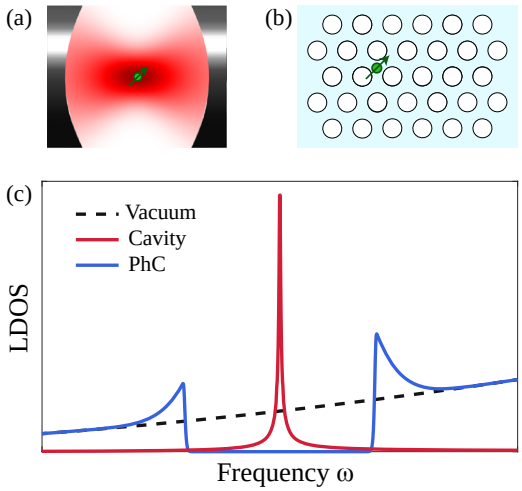


**Figure 1.1:** Quantum emitter places inside a resonant optical cavity (a), or a photonic crystal (b). (c) Local density of state (LDOS). In a homogeneous medium, the LDOS scales as $\omega^2$ (dashed black). For an emitter placed inside a photonic cavity (red) the LDOS will show a Lorentzian lineshape (red). More complex photonic environment, such as photonic crystals (blue) can exhibit peculiar features such as photonic bandgaps where the LDOS is almost null.

The Purcell factor is one of the most famous metrics in optics for the degree to which a resonator enhances light-matter interaction strength. The underlying quantity, i.e., the LDOS is exploited to enhance spontaneous emission for the purpose of producing bright and fast single-photon sources for quantum applications [21], but also for increasing signals from fluorescent markers in biology [22]. Conversely, reciprocity implies that photodetectors or solar cells could also benefit from LDOS control to boost absorption [23]. Surface-enhanced Raman spectroscopy (SERS), i.e., vibrational spectroscopy on basis of scattering of light that undergoes a frequency-shift due to interactions with molecular vibrations, also relies on the increased LDOS at plasmonic hotspots on rough metallic surfaces, sharp metallic tips and plasmonic nanoresonators [24, 25]. Also, there is a lively effort in photonics to develop optical sensors that can detect the presence of even single proteins by virtue of minute frequency shifts in the resonance of a sensing structure. This topic is the remit of perturbation theory for optical cavities [26, 27] which holds that the frequency

shift of a cavity resonance upon perturbation by a tiny object of polarizability $\alpha$ reads

$$\frac{\Delta\omega_m}{\omega_m} = -\frac{\alpha}{2V_m}. \tag{1.4}$$

Therefore, in the context of detection of tiny particles or molecules, the sensitivity $\frac{\Delta\omega_m}{\gamma_m} = -\frac{\alpha Q_m}{2V_m}$ upon perturbation by an analyte is directly proportional to the Purcell factor $F_m$. The Purcell factor and LDOS thus naturally occur in a variety of phenomena that go beyond just spontaneous emission.

## 1.2. Photonic resonators

Any photonic environment that modifies the LDOS modifies light-matter interaction, as demonstrated in systems as diverse as mirrors and dielectric interfaces [18, 28], 1D and 2D waveguides [29–31], photonic crystals [19, 32], and disordered media [33, 34]. While LDOS control does not necessarily imply a resonator, localized resonances are the most common strategy for enhancing the LDOS. According to textbook optics, understanding the relevant properties of resonators only requires knowledge of the two parameters entering the Purcell factor, i.e., the quality factor $Q$ and the mode volume $V$. In this section, we give a brief overview of the available photonic and plasmonic resonators that have been developed over the last decades to control light-matter interaction.

### 1.2.1. Dielectric cavities

Traditional optical cavities make use of mirrors and other photonic structures made out of lossless dielectric materials to confine light with a very high quality factor Q ($10^2 - 10^9$). The most famous example is the Fabry-Perot cavity, in which light bounces back and forth between two highly reflective mirrors. These cavities, originally developed for spectroscopy, accompanied most of the pioneering experiments involving light-matter interaction. In particular, they were a key component of the first lasers [4], enabled the first direct observation of the Purcell effect [35] and strong coupling at optical frequencies [36], and more recently, Bose-Einstein condensation of exciton-polaritons [37]. Progress in nano- and microfabrication has lead to the development of miniaturized versions of Fabry-Perot cavities with mode volumes $V$ reaching the fundamental limit imposed by diffraction [38], i.e. $V \sim (\lambda/2)^3$, where $\lambda$ is the wavelength of light in the high-index medium of the cavity. Micropillars with integrated Bragg reflectors fabricated from epitaxially grown III-V semiconductors have provided us with very efficient single photons sources [39, 40], and the first single-emitter strong coupling in solid-state [41]. In the same material platform, 2D membrane photonic crystals (PhC) cavities have been realized as a natural evolution from Fabry-Perot cavities into integrated devices [42, 43] that interface well with on-chip waveguides. Light confine-

ment in this type of cavities relies on defects in a carefully designed periodic arrangement of dielectric materials (photonic crystal), which leads to the existence of a photonic bandgap, i.e. conditions under which light cannot propagate [44, 45]. The small mode volume of PhC cavities ($\approx (\lambda/n)^3$) combined with very high Q-factors (up to $10^7$, achieved in silicon, [13]), has not only enabled a refinement of previous achievements in light-matter interactions [46–49], but also opened up the road to new exciting physics, in particular in cavity optomechanics, where experiments such as cooling of a mechanical resonance into its quantum ground state (cf. Fig. 1.2 (a)) have been carried out using photonic crystal nanobeams [50, 51]. Finally, despite modes volumes limited to a few tens of cubic wavelength, whispering-gallery-mode (WGM) cavities present the interest of reaching extremely high-Q, with much higher fabrication tolerance than photonic crystals and Fabry-Perot cavities [52–54]. In WGM cavities, realized in microdisks, microspheres and microtoroids, light is trapped at the rim of a rotationally invariant resonator by total internal reflection. Performance in Q is fundamentally solely limited by the resonator curvature, while loss from scattering by roughness can be extremely small due to the ability to smoothen glass microtoroids and microspheres by heating. Due to their versatility, WGM cavities are commonly used for single-particle biosensing [55] or detection of chemical traces [56, 57], and low-threshold lasers [58]. The existence of a discrete set of modes separated by a fixed free spectral range has lead to the development of integrated frequency combs [59, 60], which are in high demand for metrology purposes [61–63]. WGM cavities have historically also been studied for cavity QED experiments [64, 65], while it has recently been realized that the intrinsic existence of degenerate pairs of resonant modes also provides opportunities to study exotic, yet classical, physics such as exceptional points [66–69], and non-reciprocity [70–72].

### 1.2.2. Plasmonic nanoresonators

Light can interact with free electron excitations of metals. In particular, the strong interaction between light and the electron gas at an interface between a metal and a dielectric gives rise to a hybridization of charge oscillations and photons, also called *surface plasmon-polaritons* (SPP). These SPP are evanescent both into the metal and into the dielectric above it, and have an in-plane wavelength which can be much smaller than the wavelength of the free photon in the dielectric. A resonant response of free electrons in metals also gives rise to strong scattering resonances of nanoparticles, an effect known as *localized surface plasmon resonances*. The quality factor of these resonances is limited to approximately $Q = 40$ due to the intrinsic Ohmic damping rate of noble metals, and is usually lower since scatterers also present radiative loss. At the same time, the resonances are associated with very strongly confined fields. While the attribution of mode volumes to such resonances is contentious, claimed values reach as low as $\lambda^3/10^6$ [21, 74, 75]. Simple shape plasmonic

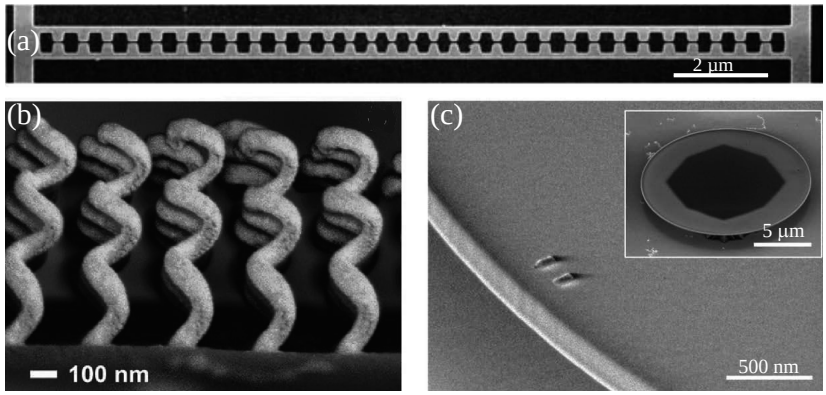


**Figure 1.2:** A few examples illustrating the diversity of micro- and nanoresonators. (a) Scanning electron micrograph of a silicon sliced nanobeam. Reproduced with permission from [51]. (b) Chiral core-shell (glass-gold) nanohelices. Reproduced with permission from [73]. (c) Hybrid resonators composed of $Si_3N_4$ microdisk cavity dressed by two aluminium antenna, cf. Chapter 4.

antennas have been demonstrated to enable enhancement of the emission rate of single molecules up to a factor of 9 for gold nanorods [76]. The most successful structures to enhance light-matter interaction actually make use of a dielectric nanogap in between two metals. In particular, antenna dimers have been reported to provide a >700-fold LDOS enhancement [77, 78], while nanopatch antennas, composed of a silver cubes on a gold mirror, easily reach a factor of $\sim 1000$ [79]. This is to compare to the record enhancement of 75 enabled by photonic crystal cavities [48]. Outside the domain of fluorescence control, also so-called *picocavities* with even smaller mode volumes have been claimed [14] in the context of nonlinear single molecule Raman spectroscopy. Such nano/pico-gap structures push electromagnetic field confinement to the length scale of atomic lattice spacings in solids, and to the length scales associated with electron tunneling, and electron wave function spill-out in solids. Thereby they push nano-optics beyond the classical Maxwell equations with a local dielectric constant, and a proper description requires non-local material descriptions with quantum mechanical corrections [80, 81].

Plasmonic structures also offer interesting tools to tailor the spatial directionality of emission and scattering, for instance by transposing the concept of phased array antennas [82–85]. In this concept, one uses an array of plasmonic scatterers around a fluorophore, with their scattering response tailored in amplitude and phase such that, collectively, they scatter emitted photons in preferred directions. The existence of multiple resonant modes in such oligomers of plasmon antennas, and the interference between them in the far field and near field, is being actively investigated as a mean to provide sensitive detectors exploiting sharp Fano-like spectral features [86,

87]. Finally, recent developments in fabrication techniques, such as multi-step electron lithography and 3D growth of materials, have enabled the possibility to fabricate 3D structures presenting chiral behaviour [73, 88], with applications in enantiomer detection and manipulation on the single-molecule level [89], and circular dichroism of metasurfaces [90].

### 1.2.3. Antenna - cavity hybrids

Both dielectric cavities and plasmonic nanoresonators have been the cornerstone to many great achievements in the context of light-matter interaction, with both allowing to reach high values of $Q/V$. However, since microcavities are optimized for $Q$, while plasmon antennas instead sacrifice $Q$ for confinement, they have very complementary merits for applications. Indeed, in the case of dielectric cavities, the diffraction limit imposes a lower bound to achievable mode volumes, meaning that high quality factors are needed for high Purcell factors. This leads to narrow bandwidths, and slow temporal responses. Hence microcavities are generally associated with narrowband emitters at cryogenic temperatures, and with picosecond to nanosecond dynamics, not femtosecond temporal control. On the other hand, the field confinement in plasmonic resonators is in practice only limited by quantum effects, and the large bandwidth allows for fast responses (fs time scale). A large part of this large bandwidth is, however, due to Ohmic losses, intrinsic to even the best metals. These losses are detrimental for applications requiring, e.g., high-fidelity single-photon sources [91]. Also, plasmonic resonators are naturally subwavelength scatterers, meaning that they do not naturally interface to integrated optics waveguides. A solution was suggested in between these two worlds [92, 93] and consist of a dielectric cavity dressed by one or many plasmonic nanoresonators. In the limit of weak antenna-cavity coupling, the system exhibits an antenna-like and a cavity-like mode [94]. This second mode is the one of choice for light-matter interaction, as it can reach similar values for Q as its bare cavity component, while it does benefit from nanoscale confinement at its plasmonic component. With a proper design [95], this means that a hybrid resonator can exceed the performance of its bare constituents in term of Purcell factor [94], and can present quality factors in the range of $Q \sim 10^3 - 10^4$ at mode volumes of order $\lambda^3/10^2$. Hybrid resonators have been reported in several contexts, such as particle detection in biosensing [96–100], Raman spectroscopy [92, 101–103], and trapping [99, 104–106]. As for light emission, even though theoretical works recognize the pertinence of such resonators as a way towards efficient single photon sources [94, 107–109], few experimental works have been carried out so far [93, 110]. Doeleman recently realized hybrids composed of microdisks and single aluminium plasmon antennas coupled to single quantum dots, with estimated LDOS enhancement of 39 (cf. Chapter 7 of the PhD thesis [111]).

1

## 1.3. Resonances and modes

### 1.3.1. Hermitian (closed) systems

This thesis deals with the physics of hybridized resonators. The most basic framework in physics to deal with hybridized resonators, is to understand resonators in terms of *normal modes*. The most illustrative example for the concept of normal modes comes from acoustics. Indeed, each musical note produced by any musical instrument is related to the modes of the structures, which can be the vibration of a string for guitars, a membrane for drums, or the vibration of air constrained by the size of an acoustic cavity for a flute. Essentially, these objects support so-called *eigenmodes* that correspond to a specific spatial pattern, and that are each associated with a natural frequency at which the field varies harmonically in time. The response of a system to an arbitrary excitation can be decomposed as a superposition of its normal modes, making the knowledge of this basis of modes a valuable tool. Normal modes, by definition, do not exchange energy, and are therefore said to be *orthogonal*. The textbook explanation of quantum mechanics [112] follows exactly this route. Here one considers the Schrödinger equation

$$\hat{\mathcal{H}}|\psi(t)\rangle = i\hbar\frac{\partial}{\partial t}|\psi(t)\rangle, \tag{1.5}$$

and for a time-independent potential energy term, first seeks eigenstates $|\psi_m\rangle$ of energy $E_m$ of the Hamiltonian $\hat{\mathcal{H}}$ as

$$\hat{\mathcal{H}}|\psi_m\rangle = E_m|\psi_m\rangle. \tag{1.6}$$

In the case where the quantum system is closed, there exists an inner product, defined on the space of wave functions, which guarantees states orthogonality and is expressed as

$$\langle\psi_m|\psi_n\rangle \equiv \int_\Omega \psi_m^*(\xi)\psi_n(\xi)d\xi = \delta_{m,n} \tag{1.7}$$

where $\Omega$ is a space spanned by the parameter $\xi$ (for instance the position $\xi = \mathbf{r}$ in the 3-dimensional space $\Omega = \mathbb{R}^3$). The Hamiltonian $\hat{\mathcal{H}}$ is then said to be *Hermitian* and it is guaranteed to be diagonalizable in a basis of eigenstates (normal modes) with real eigenvalues (energy/resonance frequency). General solutions of the time-dependent Schrodinger equation with any initial condition can then be constructed by linear superposition of eigenstates, where one needs to solve for the superposition coefficients.

The mathematical framework outlined above in fact applies also to many realms of classical physics, such as acoustics and electromagnetism [43]. Indeed, mathematically it only rests on the requirements that the underlying equation of motion (differential operator) is Hermitian (relative

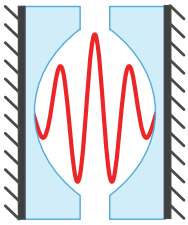

**Figure 1.3:** When on resonance with a cavity mode, light is localized inside the cavity (blue mirrors). In the Hermitian hypothesis, the system is bound by lossless boundaries (perfect mirrors).

to an appropriately defined inner product, and given imposed boundary conditions). In electromagnetics, the frequency domain wave-equation derived from Maxwell equations without sources can be seen as an eigenvalue problem similar to Eq.(1.6), for $\mathbf{H}$, the magnetic field[2]

$$\nabla \times [\epsilon^{-1}(\mathbf{r}) \nabla \times \mathbf{H}(\mathbf{r})] = \left(\frac{\omega}{c}\right)^2 \mathbf{H}(\mathbf{r}). \tag{1.8}$$

If one considers nondispersive lossless materials and a finite volume of space at the boundary of which solutions vanish (block of space enclosed by perfectly conducting walls as sketched in Fig. 1.3), the linear operator acting on $\mathbf{H}$ on the left hand side of this equation is Hermitian. Indeed, an inner product between two vectors $|\psi\rangle = [\mathbf{H}; \mathbf{E}]$ and $|\psi'\rangle = [\mathbf{H}'; \mathbf{E}']$ can be defined

$$\langle \psi | \psi' \rangle \equiv \frac{1}{2} \iiint_V \epsilon \mathbf{E}^* \cdot \mathbf{E}' + \mu_0 \mathbf{H}^* \cdot \mathbf{H}' d\mathbf{r}. \tag{1.9}$$

Note that this inner product corresponds to electromagnetic energy when calculating the norm of a field. The Hermitian nature of the wave equation operator under these assumptions implies the existence of normal modes $|\psi_m\rangle = [\mathbf{H}_m; \mathbf{E}_m]$ is guaranteed with real positive eigenvalues $\left(\frac{\omega_m}{c}\right)^2$ (corresponding to infinite lifetime). The modes are orthogonal

$$\langle \psi_m | \psi_n \rangle = \delta_{m,n} \tag{1.10}$$

and can be normalized through the condition

$$\langle \psi_m | \psi_m \rangle = \frac{1}{2} \iiint_V \epsilon |\mathbf{E}_m|^2 + \mu_0 |\mathbf{H}_m|^2 d\mathbf{r} = 1 \tag{1.11}$$

The total electromagnetic field $[\mathbf{H}, \mathbf{E}]$, upon excitation of the system by an arbitrary incident field $[\mathbf{H}_{inc}; \mathbf{E}_{inc}]$, can then be expanded over the normal

[2] $\mathbf{H}$ can be directly deduced from $\mathbf{E}$ via Maxwell-Faraday equation

modes as

$$\begin{bmatrix}\mathbf{H}\\ \mathbf{E}\end{bmatrix} = \begin{bmatrix}\mathbf{H}_{inc}\\ \mathbf{E}_{inc}\end{bmatrix} + \sum_m \beta_m \begin{bmatrix}\mathbf{H}_m\\ \mathbf{E}_m\end{bmatrix}, \tag{1.12}$$

where the excitation coefficients $\beta_m(\omega)$, or amplitudes, of normal modes $m$ are resonant for $\omega = \omega_m$. Note that with the normalization defined by Eq.(1.11), the unit of the normalized electric and magnetic fields are not $\mathrm{V{\cdot}m^{-1}}$ and $\mathrm{A{\cdot}m^{-1}}$ anymore, but $\mathrm{V{\cdot}m^{-1}{\cdot}J^{-1/2}}$ and $\mathrm{A{\cdot}m^{-1}{\cdot}J^{-1/2}}$, while the electromagnetic energy of a normal mode is $U_m = 1$. Therefore, in the normal mode expansion (Eq.(1.12)), the intensity $|\beta_m(\omega)|^2$ quantifies the amount of energy stored in the normal mode $m$ at the frequency $\omega_m$.

The mode volume as it appears in the famous Purcell factor formula first stated by Purcell in 1946 [17] (cf. Eq 1.3) is defined as the ratio between the total energy in the normal mode ($U_m \equiv 1$) and the maximum value of the density of electric energy $\max(\epsilon|\mathbf{E}_m|^2/2)$

$$V_m = \frac{\iiint_V \epsilon|\mathbf{E}_m|^2 + \mu_0|\mathbf{H}_m|^2 d\mathbf{r}}{\max_{\mathbf{r}}\{\epsilon(\mathbf{r})|\mathbf{E}_m|^2(\mathbf{r})\}} = \frac{2U_m}{\max_{\mathbf{r}}\{\epsilon(\mathbf{r})|\mathbf{E}_m|^2(\mathbf{r})\}}. \tag{1.13}$$

In this thesis, we also use a practically convenient definition of an *effective* mode volume

$$V_{m,\mathrm{eff}}(\mathbf{r}) \equiv \frac{2U_m}{\epsilon(\mathbf{r})|\mathbf{E}_m|^2(\mathbf{r})} \geq V_m. \tag{1.14}$$

This effective mode volume accounts for the spatial dependence of the density of energy, and is relevant in the common case where the emitter is not placed at the maximum of the cavity field.

### **1.3.2.** Non-Hermitian systems and quasinormal modes (QNM)

Although the normal mode formalism is a cornerstone of the classical and quantum theory of light, real electromagnetic system systems are all dissipative and dispersive. Indeed, a refractive index $n \neq 1$ always involves dispersion and absorption by Kramers-Kronig relations [113]. Also, for 3D localized resonances, radiation is unavoidable. While weak absorption and radiation loss is often treated perturbatively with the Hermitian formalism [114, 115], the fundamental tenets underlying normal mode theory evidently fail. In some specifically symmetric geometries, the symmetry of the system itself suggests an orthogonal set of basis functions on which to expand solutions (e.g., plane waves in free space, vector spherical harmonics for Mie spheres [116]). For arbitrary geometries, however, a generalization of the normal mode concept to describe dissipative resonances is highly desirable. To this end, several groups are presently developing the formalism of so-called *quasinormal modes* (QNMs) [117–123]. Here we provide a brief introduction to the QNM formulation pioneered by Sauvan and coworkers [124], following the review in Ref. [125].

Similar to normal modes in the Hermitian formulation, quasinormal modes are solutions of Maxwell equations in the absence of sources, but now accounting for material dispersion and an outgoing wave condition (such as Sommerfeld radiation condition, or perfectly matched (absorbing) layers (PMLs))

$$\begin{bmatrix} 0 & i\mu_0^{-1}\nabla\times \\ -i\epsilon^{-1}(\tilde{\omega}_m)\nabla\times & 0 \end{bmatrix}\begin{bmatrix} \tilde{\mathbf{H}}_m \\ \tilde{\mathbf{E}}_m \end{bmatrix} = \tilde{\omega}_m \begin{bmatrix} \tilde{\mathbf{H}}_m \\ \tilde{\mathbf{E}}_m \end{bmatrix}. \tag{1.15}$$

This eigenproblem yields a complete basis of QNMs at least when the resonator is immersed in a uniform background and when we consider the field inside the resonator [126–128], with complex eigenfrequencies $\tilde{\omega}_m = \omega_m + i\gamma_m/2$, where $\omega_m$ is the resonance frequency as defined in the Hermitian formalism (Eq.(1.8)), and $\gamma_m$ is the decay-rate of the resonance. The complete basis, or more practically, a truncation of it, can then be used to describe the response of complex environment to any excitation.

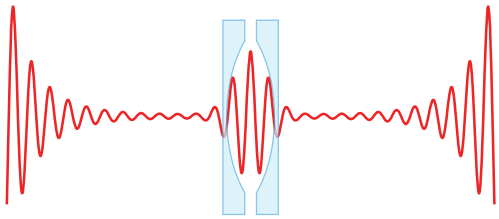

**Figure 1.4:** Quasinormal modes of real electromagnetic systems satisfy the outgoing-wave boundary condition, and therefore always have at least radiation losses and a complex resonance frequency $\tilde{\omega}_m \equiv \omega_m + i\gamma_m/2$. An important feature of this leaky QNM is the exponential divergence of the field distribution for $|r| \to \infty$ (roughly as $e^{+\frac{\gamma_m}{2c}|r|}$).

A key feature of QNM is the fact that the electromagnetic field diverges away from the resonators as $|\mathbf{r}| \to \infty$ (Fig.1.4) and therefore completness is not guaranteed everywhere. Mathematically, this comes from the fact that the wave-vector $k_m = n\tilde{\omega}_m/c$ is also complex in the far-field. If the propagation term $e^{i(\tilde{\omega}_m t - k_m|\mathbf{r}|)}$ converges in time for a decaying resonance, then it must diverge in space. [124, 129, 130] This property intrinsically ensures that the total power of the outgoing wave-front is conserved during propagation in a lossless medium instead of decaying in time with a rate $\gamma_m$. Paradoxically, it also implies that the density of electromagnetic energy diverges in space, and that it is therefore nonsensical to normalize a QNM with Eq.(1.11). Instead, a new normalization relationship based on reciprocity arguments has been introduced by Sauvan et al. [124] that reads

$$\iiint_\Omega \left.\frac{\partial \omega\epsilon(\omega)}{\partial\omega}\right|_{\tilde{\omega}_m} \tilde{\mathbf{E}}_m \cdot \tilde{\mathbf{E}}_m - \mu_0 \tilde{\mathbf{H}}_m \cdot \tilde{\mathbf{H}}_m d\mathbf{r} \equiv 1. \tag{1.16}$$

The derivative now accounts for dispersion and, importantly, *unconjugated* products $\tilde{\mathbf{E}}_m \cdot \tilde{\mathbf{E}}_m$ and $\tilde{\mathbf{H}}_m \cdot \tilde{\mathbf{H}}_m$ appear. It can be demonstrated that this normalization leads to finite values when integrating over the whole space, while for true normal modes of closed systems, the new normalization is equivalent to Eq.(1.11) (modulo an inconsequential factor[3] 1/2). Another consequence of the diverging electromagnetic energy density is the need to redefine the mode volume since Eq.(1.14), and more generally the concept of energy stored in a QNM, is not valid anymore [130, 131]. Sauvan et al. [124] therefore introduced a complex-valued mode volume

$$\tilde{V}_m(\mathbf{r}) \equiv \frac{\iiint_\Omega \left.\frac{\partial \omega \epsilon(\omega)}{\partial \omega}\right|_{\tilde{\omega}_m} \tilde{\mathbf{E}}_m^2 - \mu_0 \tilde{\mathbf{H}}_m^2 d\mathbf{r}}{2\epsilon(\mathbf{r})\tilde{\mathbf{E}}_m^2(\mathbf{r})}. \tag{1.17}$$

It can be shown that the spontaneous emission factor in a cavity, i.e. the Purcell factor, reads as in this formalism

$$F_m \equiv \frac{3}{4\pi^2}\left(\frac{\lambda_m}{n}\right)^3 \mathrm{Re}\left(\frac{Q_m}{\tilde{V}_m}\right). \tag{1.18}$$

Beyond the mere replacement of $V_m^{-1}$ by $\mathrm{Re}\tilde{V}_m^{-1}$ in $F_m$, the complex nature of the mode volume has also a more fundamental implication on the frequency dependence of the emission rate enhancement

$$\frac{\Gamma}{\Gamma_0} = F_m \frac{\omega_m^2}{\omega^2} \frac{\gamma_m^2/4}{(\omega-\omega_m)^2 + \gamma_m^2/4}\left[1 + 2Q_m \frac{\omega-\omega_m}{\omega_m}\frac{\mathrm{Im}\,\tilde{V}_m}{\mathrm{Re}\,\tilde{V}_m}\right]. \tag{1.19}$$

The response is no longer Lorentzian in the general case, and can even be negative. However, in the case where the contribution of one QNM is indeed negative, it simply means that at least one other QNM has a positive LDOS that balances the negative one. Surprisingly for those trained by the Hermitian theory of subsection 1.3.1, the enhancement is generally not maximum at the resonance frequency, i.e. when the emitter and the resonance are matched in frequency (see Eq.(1.19)).

The benefit of expressing properties in just a few dominant QNM contributions is not only conceptual, but also computational. QNMs can be computed with frequency-domain full wave solvers quickly, and can then be used to construct any observable over a wide spectral range (set by the spectrum of the object). This should be constrasted to usual full-wave solving, in which each incidence condition and frequency requires a new simulation. Importantly, this benefit extends to dispersive permittivities. The QNM eigenproblem formulated in Eq.(1.15) is not only non-Hermitian, but also non-linear in case of

[3] Note that if we assume a closed, lossless system, the electric field is real, while the magnetic field is imaginary. This leads to a negative $\tilde{\mathbf{H}}_m \cdot \tilde{\mathbf{H}}_m$.

frequency dependence of the permitivity $\epsilon(\omega)$. For arbitrary dispersion, this means that solving for QNM either requires cumbersome iterative algorithm [132], or a local linearization of $\epsilon(\omega)$ to make use of efficient linear solvers, at the expense of the exactness of the solution. Over the last few years, efforts have been made to tackle this issue in different numerical frameworks (FEM, FDFD, RCWA,...) [133], and an elegant solution has been found in the important case of materials which can be described by a $N$-pole Lorentz-Drude model $\epsilon(\omega) = \epsilon_\infty - \epsilon_\infty \sum_{i=1}^{N} \omega_{p,i}^2/(\omega^2 - \omega_{0,i}^2 - i\omega\gamma_i)$, with plasma frequencies $\omega_{p,i}$, damping coefficients $\gamma_i$, resonant frequencies $\omega_{0,i}$ and offset $\epsilon_\infty$. It was proposed [125] that the addition of *auxiliary fields* $\mathbf{P}_i = -\epsilon_\infty \omega_{p,i}^2/(\omega^2 - \omega_{0,i}^2 - i\omega\gamma_i)\mathbf{E}$ and $\mathbf{J}_i = i\omega\mathbf{P}_i$, allows one to derive a linear eigenproblem from Eq.(1.15). This expanded formulation then yields higher dimensional fields $|\psi\rangle = [\mathbf{H};\mathbf{E};\mathbf{P};\mathbf{J}]$, and on this new space, and an inner product can be defined.

$$\langle\psi|\hat{\mathbf{D}}|\psi'\rangle \equiv \frac{1}{2}\iiint_V \epsilon_\infty \mathbf{E}\cdot\mathbf{E}' - \mu_0\mathbf{H}\cdot\mathbf{H}' + \omega_0^2/(\epsilon_\infty\omega_p^2)\mathbf{P}\cdot\mathbf{P}' - 1/(\epsilon_\infty\omega_p^2)\mathbf{J}\cdot\mathbf{J}' d\mathbf{r}, \quad (1.20)$$

with $\hat{\mathbf{D}} = \mathrm{diag}\{-\mu_0, \epsilon_\infty, \omega_0^2/(\epsilon_\infty\omega_p^2), -1/(\epsilon_\infty\omega_p^2)\}$. This leads to the existence of the orthogonality relationship between eigenvectors [134]

$$\langle\tilde{\psi}_m^*|\hat{\mathbf{D}}|\tilde{\psi}_n\rangle = \delta_{m,n}, \quad (1.21)$$

where $|\tilde{\psi}_i\rangle = [\tilde{\mathbf{H}}_i;\tilde{\mathbf{E}}_i;\tilde{\mathbf{P}}_i;\tilde{\mathbf{J}}_i]$ with $i = m, n$ are the eigenvectors, still formally associated to the same complex eigenfrequencies $\tilde{\omega}_i$ solved for in Eq.(1.15). It can then easily be shown that one obtains the same normalization condition as in Eq.(1.16) for the eigenvectors. Furthermore, the inner product applied between a source and QNMs leads to semi-analytical expressions for the excitation coefficients $\beta_m$ used in the field decomposition presented in Eq.(1.12)

$$\beta_m(\omega, \mathbf{E}_D) = \iiint_{\mathrm{res}} \tilde{\mathbf{E}}_m(\mathbf{r}) \cdot \left( \frac{-\tilde{\omega}_m}{\omega - \tilde{\omega}_m} [\epsilon(\tilde{\omega}_m) - \epsilon_b] + [\epsilon_b - \epsilon_\infty] \right) \mathbf{E}_D(\omega, \mathbf{r})\, d\mathbf{r}, \quad (1.22)$$

where the overlap integral between the QNM electric field $\tilde{\mathbf{E}}_m$ and the driving field $\mathbf{E}_D$ runs over the volume of the resonator. The analyticity of the decomposition can be exploited outside of the frequency domain, and can be used to predict the (linear) temporal response of resonators excited by short pulses [135].

A very common treatment of Maxwell equations involves the use of *Green functions* [16]. A Green function is defined for a system as a bi-linear mapping of space with coordinate $\mathbf{r}$ and $\mathbf{r}'$, $\mathbf{G}(\mathbf{r}, \mathbf{r}', \omega)$ such that the electric field $\mathbf{E}(\mathbf{r}, \omega)$ emitted by a dipole $\mathbf{p}(\mathbf{r}')$ placed at a position $\mathbf{r}'$ writes

$$\mathbf{E}(\mathbf{r}, \omega) = \mu_0\omega^2\mathbf{G}(\mathbf{r}, \mathbf{r}', \omega)\mathbf{p}. \quad (1.23)$$

The Green function of a system basically contains all the information required to understand the response to any excitation, at any frequency and for any

point in space. However, if there exists analytical expressions for simple systems, for instance homogeneous media [16], more complicated geometries such as cavities can, on some conditions, rely on QNM expansions [117, 136]. In Chapters 2, 4 and 5, in the case of a cavity in a homogeneous background, we use the following expansion for the Green function [137]

$$\mathbf{G}(\mathbf{r},\mathbf{r}',\omega) = \mathbf{G}_0(\mathbf{r},\mathbf{r}',\omega) + \sum_m \frac{-\tilde{\omega}_m}{\omega - \tilde{\omega}_m} \tilde{\mathbf{E}}_m(\mathbf{r}) \otimes \tilde{\mathbf{E}}_m(\mathbf{r}'), \tag{1.24}$$

where $\mathbf{G}_0(\mathbf{r},\mathbf{r}',\omega)$ the Green function of an homogeneous background (vacuum). For practical applications, we truncate the QNM basis to one or two QNMs of interest to restore some analyticity, however at the expanse of exactness.

The quasinormal mode formalism has been shown to be a powerful formalism for quantitatively predicting the scattering properties and LDOS enhancement characteristics of both plasmonic and dielectric photonic resonators. A select body of work has considered the coupling of several photonic objects, from on one hand, the viewpoint of hybridization of resonances viewed as a problem of coupled QNMs [138], and on the other hand, the viewpoint of perturbation of a QNM by a small scattering object [139, 140]. When a resonator is perturbed by a small object, one expects a shift in its resonance frequency and a change in its linewidth. The theory of perturbation of an optical resonator has a long standing history, with original contributions due to Bethe and Schwinger in optics [27] and Waldron in the radio-frequency domain [26, 141]. The perturbation theory for optical resonators has also been demonstrated to benefit immensely from a proper QNM treatment of losses [139, 140, 142]. With a QNM treatment, Eq.(1.4) becomes

$$\frac{\Delta\tilde{\omega}_m}{\tilde{\omega}_m} = -\frac{\alpha}{2\tilde{V}_m}, \tag{1.25}$$

and now predicts complex-valued frequency shifts, i.e. resonance frequency shifts, but also the change in decay rate, in particular the one due to changes in radiation losses. Indeed, the complex mode volume $\tilde{V}_m(\mathbf{r})$ contains phase information needed to describe the interference between the field radiated by the QNM, and the one scattered by a perturbation placed at $\mathbf{r}$.

## 1.4. Motivation and outline

This thesis studies the hybridization of eigenmodes of nano- and micro-resonators, and in particular the properties of hybrid resonators composed of a dielectric cavity and plasmonic nanoantennas. The motivation of this work can be summarized as three main questions: Can we control the scattering of a hybrid resonator into far-field and/or guided modes using not only one, but an array of plasmonic antennas phased through their

electromagnetic interaction with a photonic resonator? Do we then still benefit from the superior Purcell factor allowed by photonic-plasmonic hybridization as reported for single antenna-cavity systems? Can we define versatile theoretical and numerical tools pertinent to the design of assemblies of micro- and nanoresonators, with tailored properties? This thesis addresses these questions through theoretical studies within the quasinormal mode formalism, as well as experimental studies of hybrid resonators composed of $Si_3N_4$ microdisk cavities and aluminium antennas.

**Chapter 2**, discusses the relevance of the quasinormal modes (QNM) formalism, originally introduced for lossy plasmonic resonators, in the context of the perturbation of high quality factor cavities by small objects. We show that the complex mode volume of a photonic cavity can be directly revealed by measurements of the changes in the quality factor Q of the cavity perturbed by a tiny probing object. We present an extension of the QNM formulation of perturbation theory and discuss its range of validity.

In **Chapter 3**, we present a semi-analytical formalism, based on a generalized linear eigenproblem, to construct the QNMs of ensembles of 3-dimensional resonators from the knowledge of the QNMs of the individual constituents of the ensemble. In essence, this is a proposition for the quasinormal mode equivalent of *hybridization theory* or *coupled QNM theory*, a commonly used language to describe the coupling of normal modes. Our proposition enables one to estimate resonance frequencies and decay rates, but also to quantify observables such as extinction and scattering cross-sections, and near-field field distribution.

In **Chapter 4**, we study a hybrid structure composed of a microdisk cavity supporting a pair of degenerate whispering gallery modes, dressed by two plasmonic antennas placed at the circumference of the microdisk. We first theoretically predict interesting directionality and enhanced LDOS properties. Next, we relate the directionality to the spectral properties of the two perturbed cavity modes, and explain the importance of the relative position of the two antennas. We then present spectroscopic evidence for the predicted mode structure collected on an experimental realization of the system in a platform composed of silicon nitride disks and aluminium antennas. The measurements demonstrate the tunability of the spectral properties of the modes as a function of the relative distance between the antennas.

In **Chapter 5**, we demonstrate the interest of hybrid platforms composed of a microdisk cavity dressed by an azimuthally distributed array of antennas in the context of generation beams carrying *orbital angular momentum* (OAM). In particular, after carefully studying the scattering and resonant properties of such structures, we propose a design which enables the emission of pure OAM associated with a single state of polarization. An experimental realization validates our concept.

Finally, **Chapter 6** investigates theoretically the relevance of hybrid resonators composed of a single antenna and a single cavity in the context of

*molecular optomechanics*. We show that hybrid resonators respect the commonly accepted factorization of the enhancement of Raman scattering as a pump and an LDOS effect. This factorization consequently ensures a spectral selectivity of the collected Raman signal in the output channels of the cavity, and provides simple design rules for molecular optomechanics.

# 2

# Mapping Complex Mode Volumes with Cavity Perturbation Theory

## 2.1. Introduction

Predicting how the presence of a tiny foreign object near a resonant optical cavity perturbs the optical response is a classical problem in electromagnetics, with important implications spanning from the radio-frequency domain to present-day nano-optics. The perturbation results in a modification $\Delta\tilde{\omega}$ of the initial complex resonance frequency $\tilde{\omega} \equiv \omega_0 + i\gamma_0/2$ of the unperturbed cavity mode, $\mathrm{Re}\,\Delta\tilde{\omega}$ and $\mathrm{Im}\,\Delta\tilde{\omega}$ respectively representing the frequency shift and linewidth change. For a tiny perturbation quantified by a dipolar polarizability $\alpha$ (assumed small and isotropic) and placed at $\mathbf{r}_0$, $\Delta\tilde{\omega}$ usually reads as

$$\frac{\Delta\tilde{\omega}}{\tilde{\omega}} \approx \frac{-\alpha\epsilon(\mathbf{r}_0)|\tilde{\mathbf{E}}(\mathbf{r}_0)|^2}{\iiint \epsilon|\tilde{\mathbf{E}}|^2 + \mu_0|\tilde{\mathbf{H}}|^2 d^3\mathbf{r}} \equiv \frac{-\alpha}{2V(\mathbf{r}_0)}, \tag{2.1}$$

where $\epsilon$ is the permittivity of the unperturbed cavity, $\epsilon_0$ and $\mu_0$ are vacuum permittivity and permeability, and $\tilde{\mathbf{E}}$ and $\tilde{\mathbf{H}}$ are the unperturbed-cavity-mode electric and magnetic fields. The seminal Eq.(2.1) has been initially proposed by Bethe and Schwinger in optics [27], and Waldron in the radio frequency domain [26, 141], and has been used in similar variants until recently [143–146]. For convenience, we have introduced the mode volume $V$. The concept of cavity $V$ was initially proposed by Purcell [17] and then promoted as a real-valued positive quantity in the field of cavity quantum electrodynamics. This energy-based expression, which suggests positioning the quantum object

at the field-intensity maximum, can be theoretically derived for Hermitian systems [43]. It can be useful for monomode photonic crystal cavities, but becomes unfounded for systems involving coupled-modes (even high Qs) and for the important case of low-Q plasmonic cavities. The mode volume $V$ is usually defined for an assumed dipole placed exactly at the field-intensity maximum, where the coupling is also maximum. For convenience, we rather consider a spatially-dependent mode volume to directly take into account the dependence of $\Delta\tilde{\omega}$ on the perturber position.

Equation (2.1) has the merit of being intuitive and easy to evaluate, since $\Delta\tilde{\omega}$ solely depends on the unperturbed mode. It has been widely used for determining the dielectric and magnetic parameters of materials or testing the functionalities of microwave circuit components [141], and in the optical domain, to detect [55, 147] or trap [146] nanoparticles, tune the resonance of photonic-crystal (PhC) cavities [143, 148–153], analyse the impact of fabrication imperfections on these cavities [144], or study magnetic-like light-matter interactions [145, 154]. Remarkably, Equation (2.1) cannot accurately predict perturbation-induced changes of the quality factor, $Q = -\frac{\mathrm{Re}\,\tilde{\omega}}{2\mathrm{Im}\,\tilde{\omega}}$. In particular, it predicts that changes in cavity loss rate follow the exact same spatial dependence as changes in the real frequency, with the sign of the polarizability setting the sign of the change in loss rate. This issue is known since the very beginning of perturbation theory and is sometimes accounted for by appending an additional flux-like term to Eq.(2.1) [141], even in recent works [153]. This term unfortunately requires solving the perturbed problem.

With the recent advent of theoretical results on the normalization of leaky resonator modes [124, 155, 156], it becomes evident that cavity perturbation theory cannot rely on modes with a normalization based on energy. Instead quasinormal-mode (QNM) formalism may account for the non-Hermitian character of the problem. Thus it has been proposed recently that Eq.(2.1) is conveniently replaced by

$$\frac{\Delta\tilde{\omega}}{\tilde{\omega}} \approx \frac{-\alpha\epsilon(\mathbf{r}_0)\tilde{\mathbf{E}}^2}{\iiint \epsilon\tilde{\mathbf{E}}^2 - \mu_0\tilde{\mathbf{H}}^2 d^3\mathbf{r}} \equiv \frac{-\alpha}{2\tilde{V}(\mathbf{r}_0)}. \tag{2.2}$$

The sole difference between Eqs.(2.1) and 2.2) is the replacement of the *real* modal volume $V$ by a *complex* one, $\tilde{V}$ which is calculated from the QNM field distribution ($\tilde{\mathbf{E}}$, $\tilde{\mathbf{H}}$). So far, only purely computational studies have been used to test the predictive force of Eq.(2.2) and the studies targeted highly-non-Hermitian systems, e.g., low-Q plasmonic nanoantennas [139] and metallic gratings [122, 125, 157].

Important open questions surround the proposed alternative perturbation formula, Eq.(2.2). For instance, even if it is evident that strongly non-Hermitian systems like low-Q plasmonics require a revised perturbation theory, one may wonder which genuine benefits, if any, can be expected from Eq.(2.2) for high-$Q$ microcavities since these operate in a manner closely analogous to Hermitian systems with infinitesimal absorption or leakage [158].

More fundamentally, the question arises in QNM theory whether the concept of complex mode volume introduced in [124] is just an abstract mathematical construct, or carries true physical significance. In particular, the question of the physics captured by $\mathrm{Im}\tilde{V}$ in Eq.(2.2) arises, for which simple intuitive arguments have not yet been presented in earlier works [125, 139]. Finally, we note that no experiment has validated Eq.(2.2) so far. Even beyond the question whether this equation correctly captures real perturbation experiments, such an experiment could for the first time test if QNMs, which are widely regarded as difficult mathematical objects with complex frequencies and divergent fields, are in fact directly measurable physical quantities that can be mapped through unique signatures in experiments. This chapter aims to answer these questions. We show that quasinormal mode formalism is relevant, if not even stricly necessary, to describes high-Q resonators. In particular in the context of cavity perturbation, QNM formalism predicts changes in quality factors arising from modification in radiative losses induced by a perturbation, inaccessible to conventional Hermitian theories, and we confirm this fact thanks to confrontation to experimental results obtained with photonic crystal cavities. Then, as a direct consequence of the relation between $\Delta\tilde{\omega}$ and $\tilde{V}$ in Eq.(2.2), we show that perturbation measurements of $\Delta\tilde{\omega}$ allow for a direct mapping of the spatial distribution of $\tilde{V}$. This is an important result since $\tilde{V}$ determines the local density of electromagnetic states (LDOS) of resonators and thus is deeply involved in important light-matter interaction phenomena in non-Hermitian open systems [124, 125]. We also conclusively clarify the physics captured by $\mathrm{Im}\tilde{V}$. Finally, we provide the first analysis of the validity domain of Eq.(2.2), pinpointing the physics that causes the breakdown even of revised perturbation theory[1].

## 2.2. QNM Perturbation theory

We provide in subsection 2.2.1 a derivation of Eq.(2.2) by using QNM expansion with the scattering-field formulation. Equation (2.2) was derived in the same exact form in [139] using straightforward mathematics essentially based on the divergence theorem. Interestingly, we note that the divergence theorem leads to an exact expression for $\Delta\tilde{\omega}$ (see Eq.(4) in [139]) which is valid for any reciprocal system and naturally leads to the important local field corrections for the QNM field $\tilde{E}$ at the position of the perturber. Equation (2.2) can also be quite straightforwardly derived from early works [159] on the exact perturbation theory of open systems using QNM expansions. Here we use the word *exact* to emphasize that if many (up to an infinity) QNMs of the unperturbed system are known, the QNMs of the perturbed systems can be exactly computed as the eigen vector of a generalized eigenvalue problem (see Eq.(2.14) in [159]), as long as we assume that the QNMs form a complete basis.

[1] This Chapter is an expanded version of [140], and based on the work [139].

We also refer to the more recent work in the group of Muljarov [117, 136], which essentially conveys the same approach in the so-called resonant state expansion. Similar to the approach they took, we adopt a QNM expansion, but instead of assuming that the Green tensor (a singular quantity) of the cavity can be expanded in the QNM basis, we assume that the regular scattered Green tensor $\Delta\mathbf{G}$ (see below for a definition) is expandable. This approach, used for instance for a theoretical study of superradiance assisted by a resonance [137], converges much faster and does not require more complicated mathematics. We simply need to use a scattered field formulation [124, 125]. In subsection 2.2.2, we numerically test the validity of Eq.(2.2) with a L3 photonic crystal cavity perturbed by a tiny air sphere placed in median symmetry plane of the photonic crystal slab.

### 2.2.1. Derivation of QNM perturbation theory

We start our derivation by considering a scattering problem with an external source that is illuminating a complex medium in which a tiny scatterer is placed at $\mathbf{r}_0$ [137, 160]. Here the isotropic but non-homogeneous permittivity $\epsilon(\mathbf{r},\omega)$ will describe the unperturbed cavity, while the scatterer represented by $\Delta\epsilon(\mathbf{r},\omega)$ represents the perturbation. The total field $[\mathbf{E},\mathbf{H}]$ satisfies

$$\begin{cases} \nabla\times\mathbf{E} &= -i\omega\mu_0\mathbf{H} \\ \nabla\times\mathbf{H} &= i\omega\epsilon\mathbf{E} + i\omega\Delta\epsilon\mathbf{E} + \mathbf{J}_b, \end{cases} \tag{2.3}$$

where $\mathbf{J}_b(\mathbf{r},\omega)$ is the driving current distribution. The total field for the unperturbed system in absence of the scatterer satisfies

$$\begin{cases} \nabla\times\mathbf{E}_b &= -i\omega\mu_0\mathbf{H}_b \\ \nabla\times\mathbf{H}_b &= i\omega\epsilon\mathbf{E}_b + \mathbf{J}_b, \end{cases} \tag{2.4}$$

while the field scattered by the scatterer $[\mathbf{E}_S,\mathbf{H}_S] = [\mathbf{E},\mathbf{H}] - [\mathbf{E}_b,\mathbf{H}_b]$ obeys

$$\begin{cases} \nabla\times\mathbf{E}_S &= -i\omega\mu_0\mathbf{H}_S \\ \nabla\times\mathbf{H}_S &= i\omega\epsilon\mathbf{E}_S + i\omega\Delta\epsilon\mathbf{E}. \end{cases} \tag{2.5}$$

We focus on perturbations small enough such that the point dipole approximation applies, in which case we can identify the perturber as a Dirac distribution $i\omega\Delta\epsilon(\mathbf{r},\omega)\mathbf{E}(\mathbf{r}) \equiv i\omega\mathbf{p}\delta(\mathbf{r}-\mathbf{r}_0)$, with $\mathbf{p}$ the induced dipole moment of the perturbation. It immediately follows that $\mathbf{E}_S(\mathbf{r}) = \mu_0\omega^2\mathbf{G}(\mathbf{r}_0,\mathbf{r},\omega)\mathbf{p}$, with $\mathbf{G}(\mathbf{r}',\mathbf{r},\omega)$ the Green tensor of the bare cavity [16].

Without loss of generality, we separate the Green function into a background Green tensor $\mathbf{G}_0(\mathbf{r}_0,\mathbf{r},\omega)$ appropriate to a uniform medium of permittivity $\epsilon(\mathbf{r}_0,\omega)$, taken as the medium at the location of the perturbation, plus a scattered Green tensor $\Delta\mathbf{G}\equiv\mathbf{G}-\mathbf{G}_0$ that is regular. Thus, if the system is driven,

the dipole causes a scattered field $\mu_0\omega^2\Delta\mathbf{G}(\mathbf{r}_0,\mathbf{r},\omega)\mathbf{p}$. With this definition, the total incident field driving the dipole is the sum of the driving field $\mathbf{E}_b(\mathbf{r},\omega)$ and the field scattered by the resonator $\mu_0\omega^2\Delta\mathbf{G}(\mathbf{r}_0,\mathbf{r}_0,\omega)\mathbf{p}$,

$$\mathbf{p} = \boldsymbol{\alpha}\epsilon\left\{\mathbf{E}_b + \mu_0\omega^2\Delta\mathbf{G}\mathbf{p}\right\}, \tag{2.6}$$

where our definitions imply that $\boldsymbol{\alpha}$ is the polarizability of the perturbation.

We now expand the regular Green tensor over the (assumed) complete basis of quasinormal modes. We are interested in the perturbation of a single cavity mode, labelled $N$. Therefore we further isolate the contribution of the cavity mode $N$ in $\Delta\mathbf{G}$

$$\boldsymbol{\Delta G}(\mathbf{r},\mathbf{r}',\omega) = \boldsymbol{\Delta G}_N(\mathbf{r},\mathbf{r}',\omega) + \delta\mathbf{G}(\mathbf{r},\mathbf{r}',\omega), \tag{2.7}$$

where all modes except the cavity mode are gathered in the term $\delta\mathbf{G}(\mathbf{r},\mathbf{r}',\omega)$ while the Green function contribution due to the cavity mode reads [117, 125, 136]

$$\mu_0\omega^2\boldsymbol{\Delta G}_N(\mathbf{r},\mathbf{r}',\omega) = \frac{-\tilde{\omega}_N}{\omega-\tilde{\omega}_N}\tilde{\mathbf{E}}_N(\mathbf{r})\otimes\tilde{\mathbf{E}}_N(\mathbf{r}'). \tag{2.8}$$

We now have all ingredients at hand for the perturbation problem. As we aim to find the (perturbed) eigenmode, we require a solution of Eq.(2.5) in absence of driving ($\mathbf{E}_b = 0$), and for a frequency $\tilde{\omega}$ close to $\tilde{\omega}_N$, i.e, close to the unperturbed quasinormal mode itself. By exploiting Eqs.(2.6 and 2.7), in absence of driving, Eq.(2.5) becomes a non-linear eigen-problem

$$\mathbf{p} = \boldsymbol{\alpha}\epsilon\left[\frac{-\tilde{\omega}_N}{\tilde{\omega}-\tilde{\omega}_N}\tilde{\mathbf{E}}_N\otimes\tilde{\mathbf{E}}_N + \mu_0\omega^2\delta\mathbf{G}\right]\mathbf{p}. \tag{2.9}$$

For the typical case of a microcavity (GHz linewidth), we can safely neglect variations of $\boldsymbol{\alpha}$ on the scale of the frequency shift $\Delta\tilde{\omega} \equiv \tilde{\omega} - \tilde{\omega}_N$. Multiplying Eq.(2.8) by $\Delta\tilde{\omega}$, and performing a $1^{st}$ order expansion leads to a generalized linear eigen-problem

$$\frac{\Delta\tilde{\omega}}{\tilde{\omega}_N}[\mathbf{1} - \boldsymbol{\alpha}\epsilon\mu_0\omega^2\delta\mathbf{G}(\tilde{\omega}_N)]\mathbf{p} \approx -\left[\boldsymbol{\alpha}\epsilon\tilde{\mathbf{E}}_N\otimes\tilde{\mathbf{E}}_N\right]\mathbf{p}. \tag{2.10}$$

This system can be reduced to a scalar linear equation

$$\frac{\Delta\tilde{\omega}}{\tilde{\omega}_N} \approx -\tilde{\mathbf{E}}_N\left[\mathbf{1} - \mu_0\omega^2\boldsymbol{\alpha}\epsilon\delta\mathbf{G}\right]^{-1}\boldsymbol{\alpha}\epsilon\tilde{\mathbf{E}}_N. \tag{2.11}$$

Evidently, for weak perturbations $\left|\mu_0\epsilon\omega^2\boldsymbol{\alpha}\delta\mathbf{G}\right| \ll 1$ and Eq.(2.11) simplifies to

$$\frac{\Delta\tilde{\omega}}{\tilde{\omega}_N} \approx -\tilde{\mathbf{E}}_N\cdot\boldsymbol{\alpha}\epsilon\tilde{\mathbf{E}}_N, \tag{2.12}$$

which leads to the the result of [139] and Eq.(2.2) for isotropic perturbation $\boldsymbol{\alpha} = \alpha\mathbf{1}$.

### 2.2.2. Predicting changes in quality factor Q

We study the pertinence of Eq.(2.2) for high-Q cavities using as a well known example, the L3 photonic crystal cavity [42, 161] shown in Fig. 2.1(a). In this initial theoretical study, the perturber is assumed to be a small air sphere placed right in the symmetry plane where the mode strength is maximum. We simulate a finite crystal immersed in air, with 8 rows of holes surrounding the cavity, and compute the resonance mode of the unperturbed and perturbed cavity with the QNM-solver QNMEig [134] implemented in COMSOL Multiphysics. QNMEig provides normalized QNMs $\left[\tilde{\mathbf{E}}, \tilde{\mathbf{H}}\right]$, with $\iiint (\epsilon \tilde{\mathbf{E}}^2 - \mu_0 \tilde{\mathbf{H}}^2) d^3\mathbf{r} = 1$, and $\tilde{V}(\mathbf{r}_0)$ is simply given by $\left(2\epsilon(\mathbf{r}_0)\tilde{\mathbf{E}}^2(\mathbf{r}_0)\right)^{-1}$. We compare the complex resonance shift $\Delta\tilde{\omega}$ of the fundamental mode predicted with Eq.(2.2) with the exact shift $\Delta\tilde{\omega}$ computed as the difference of the complex resonance frequencies of the perturbed and the unperturbed QNMs.

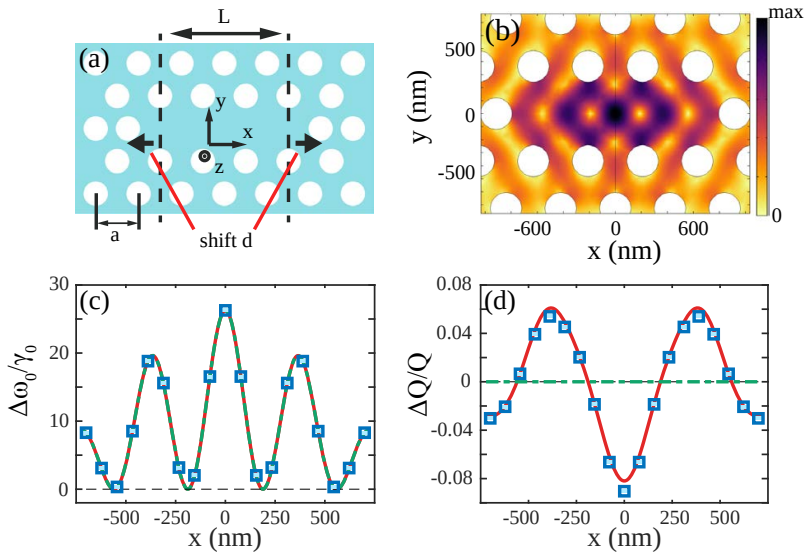


**Figure 2.1:** Numerical test of Eq.(2.2) showing its substantial superiority for predicting Q-change. (a) Simulated L3 photonic crystal cavity, formed by a 2D triangular lattice of air holes in silicon slab ($n = 3.42$). Lattice constant $a = 0.42$ µm, slab thickness 0.6a and holes radii $0.29a$. Following [42, 161], we displace the 2 holes of a distance $d = 0.18a$. (b) Mode profile $\|\tilde{\mathbf{E}}\|$ for the fundamental TE mode, $Q = 9.2 \times 10^4$ and $\lambda = 1.575$ µm. (c),(d) Frequency shift and linewidth change of the resonance as a function of the position of a 20 nm-diameter air sphere perturbation in the median plane of the PhC slab, along the cavity long axis $x$. Blue squares are FEM calculations made with COMSOL Multiphysics, green dot-dashed line is obtained with Eq.(2.1), and red solid line with Eq.(2.2).

Figures. 2.1(c) and (d), show the frequency shift and change in quality factor as the perturbation (diameter 2R = 10 nm) position is varied along the main cavity centerline. The frequency shift $\Delta\omega_0$ is normalized by the

unperturbed resonance linewidth $\gamma_0$. To quantify the change in linewidth $\Delta\gamma_0$ we plot the (relative) change in quality factor $\Delta Q/Q_0$, where $Q_0 \equiv \omega_0/\gamma_0$. To compare full simulations and perturbation formalism, we take the polarizability of the perturbation equal to the Rayleigh's quasi-static expression $\boldsymbol{\alpha}_{static} = 4\pi R^3 \frac{1-\epsilon_{Si}/\epsilon_0}{1+2\epsilon_{Si}\epsilon_0}\mathbf{1}_3$, an approximation that is likely to be relatively accurate since the scatterer is deeply subwavelength. Figure. 2.1(c) shows an excellent agreement between the perturbation formula and the exact frequency shift. This result does not come as a surprise, as it is well established that Eq.(2.1), which is based on energy density arguments and therefore its refined version that is Eq.(2.2), accurately predicts resonance shifts - $\mathrm{Re}\,\tilde{\mathbf{E}}\cdot\tilde{\mathbf{E}}$ almost equals $\|\tilde{\mathbf{E}}\|^2$ for high-Q resonators. The change in linewidth follows a very different variation as a function of the position of the perturber than the frequency shift (itself proportional to the mode energy density). Importantly, this dependence is well captured by Eq.(2.2), showing that the cavity Q can both decrease and increase due to modifications of the scattering losses. These Q-changes are encoded in $\mathrm{Im}\,\tilde{\mathbf{E}}\cdot\tilde{\mathbf{E}}$, and are inaccessible to Hermitian formalisms.

The success of Eq.(2.2) to predict $Q$-changes resides in the replacement of a real mode volume by a complex one, and more precisely, of $|\tilde{\mathbf{E}}(\mathbf{r}_0)|^2$ by $\tilde{\mathbf{E}}^2(\mathbf{r}_0)$ in the denominator of $\tilde{V}$. This replacement preserves the phase information $\phi(\mathbf{r}_0)$ of the mode at the perturber location. For an intuitive picture that explains why the phase is essential, consider a driving field impinging onto a perturbed cavity. The field does not see the tiny perturber and in first instance excites the cavity as if it were unperturbed. The cavity then directly scatters in free space and also excites the perturber, which in turn re-excites the cavity mode with a round-trip dephasing delay of $2\phi(\mathbf{r}_0)$. The total radiated field by the cavity results from the interference of the direct initial radiation and the delayed one. Depending on whether these interferences are constructive or destructive, the total cavity radiation can be higher or lower than the intrinsic cavity radiation, possibly allowing for either an increase or a decrease of $Q$. This *a posteriori* explains why Eq.(2.1), that relies on an $\tilde{\mathbf{E}}\cdot\tilde{\mathbf{E}}^*$ product and hence loses the phase information, fails to predict $Q$-changes.

In order to clarify the impact of the replacement for high-$Q$ microcavities, we consider perturbations formed by deep-subwavelength isotropic dielectric perturbers (volume $V_p$, permittivity $\Delta\epsilon + \epsilon_b$) that are introduced into a background material of permittivity $\epsilon_b$. In the static limit, the perturbers act as point isotropic electric dipoles, with a polarizability proportional to their perturber volume $\alpha = \alpha' V_p \mathbf{1}$, $\alpha'$ being a dimensionless coefficient. For spherical perturbers at optical frequencies, $\alpha' = \frac{3\Delta\epsilon}{\Delta\epsilon+3\epsilon_b}$ with -1.5 < $\alpha'$<3 for perturbers with a positive permeability. Replacing $\alpha$ in Eq.(2.2), and assuming

that $\alpha'$ is a real number, we get

$$\frac{\mathrm{Re}\,\Delta\tilde{\omega}}{\mathrm{Re}\,\tilde{\omega}} \approx -\frac{\alpha'}{2}\left[\mathrm{Re}\,\frac{V_p}{\tilde{V}} - \frac{1}{2Q}\mathrm{Im}\,\frac{V_p}{\tilde{V}}\right] \tag{2.13a}$$

$$\frac{\mathrm{Im}\,\Delta\tilde{\omega}}{\mathrm{Im}\,\tilde{\omega}} \approx -\frac{\alpha'}{2}\left[\mathrm{Re}\,\frac{V_p}{\tilde{V}} + 2Q\,\mathrm{Im}\,\frac{V_p}{\tilde{V}}\right]. \tag{2.13b}$$

For high-$Q$ photonic cavities, $\mathrm{Im}\,\tilde{\mathbf{E}} \ll \mathrm{Re}\,\tilde{\mathbf{E}}$ and $\mathrm{Re}\,\frac{V_p}{\tilde{V}} \approx \frac{V_p}{V} \gg \frac{1}{2Q}\mathrm{Im}\,\frac{V_p}{\tilde{V}}$ (remember that $V$ is the approximate (real) mode volume defined in Eq.(2.1)), so that Eq.(2.13a) reduces to

$$\mathrm{Re}\,\Delta\tilde{\omega} \approx -\omega_0\alpha'\frac{V_p}{V}, \tag{2.14}$$

which is exactly the shift predicted by Eq.(2.1). Note that this conclusion does not hold for low-$Q$ plasmonic resonators. Quite the contrary, the imaginary part $\mathrm{Im}\,\frac{V_p}{\tilde{V}}$ cannot be neglected in general in Eq.(2.13b). Even for our micro-cavity, Fig. 2.3(a) evidences that the imaginary part dominates over the real part $\frac{1}{2Q}\mathrm{Re}\,\frac{V_p}{\tilde{V}}$ , i.e.,

$$\mathrm{Im}\,\frac{V_p}{\tilde{V}} \gg \frac{1}{2Q}\mathrm{Re}\,\frac{V_p}{\tilde{V}} \tag{2.15a}$$

$$\mathrm{Im}\,\Delta\tilde{\omega} \approx -\frac{\alpha'}{2}\mathrm{Re}\,\tilde{\omega}\,\mathrm{Im}\,\frac{V_p}{\tilde{V}}. \tag{2.15b}$$

This mathematically justifies why Eq.(2.1) fails at predicting $\mathrm{Im}\,\Delta\tilde{\omega}$.

## 2.3. Near-field perturbation experiments

We had the opportunity to confirm our theory with cavity perturbation experimental data gathered by the group of Massimo Gurioli, at LENS (Florence, Italy) for a PhC cavity formed by four missing holes organized in an hexagonal array of holes to test our formalism. In subsection 2.3.1 we present the primary results obtained in the experiment, in particular the observation of decrease but also increase in quality factor of the cavity when perturbed by a near-field probe. Next, in subsection 2.3.2 we study the sample used in the experiment with finite element method (FEM) simulations and confront Eq.(2.2) to the numerical results, and in subsection 2.3.3, we analyse the domain of validity of Eq.(2.2). Finally, in subsection 2.3.5, we apply the QNM perturbation theory of Eq.(2.2) to interpret the experimental results presented in subsection 2.3.1 as the first experimental mapping of a complex cavity mode volume.

### 2.3.1. Experimental observation of complex frequency shift

The primary experimental results obtained at LENS are summarized in Fig. 2.2. Electron beam lithography followed by reactive ion etching

was used to fabricate the perforated air-membrane [151]. InAs quantum dots emitting at 1300 nm and excited at 780 nm are embedded in the GaAs membrane. The measurments were carried out using a commercial Scanning Near-field Optical Microscope (NSOM) from TwinNSOM-Omicron in illumination/collection configuration. The fibre tip, a chemically etched, uncoated near-field fibre probe [151], plays the role of the perturber and the probe. It is raster scanned at a constant height above the membrane surface, and for each position, the fluorescence spectrum is recorded, see Appendix (Section 2.5) for details. By fitting the recorded lineshape with a Lorentzian profile, the resonance wavelength and the $Q$ can be inferred. Three spectra recorded for three tip positions, labeled A, B and C in Fig. 2.2(a), are plotted in Fig. 2.2(c). The perturbation is dominantly localized at the tip apex, while the fluorescence intensity is collected at the apex and along the tip sides (the intensity only decreases by a factor 2 between $z = 0$ and $z = 300$ nm). Then the perturbation position can be finely tuned, while maintaining nearly constant the signal-to-noise ratio of the fluorescence measurements.

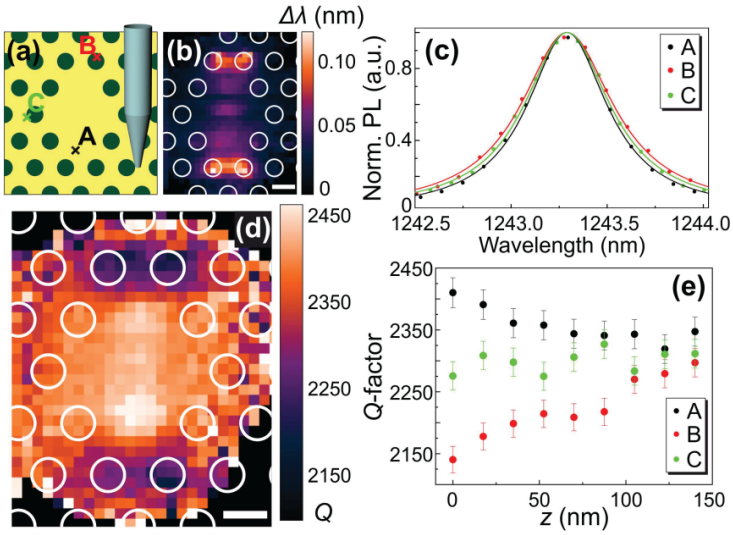


**Figure 2.2:** Experimental results obtained at LENS. (a) Sketch of the PhC cavity. (b) Wavelength-shift map as the tip is scanned over the cavity, with superimposed holes. (c) Photoluminescence recorded for 3 tip positions, A, B and C shown in (a). Curves are Lorentzian fits of the data small points. The black and red points are blue-shifted by 0.05 and 0.08 nm to ease the visual comparison for cavity $Q$'s. (d) Perturbation-induced $Q$ map. (e) $Q$ as a function of the offseted distance $z - d_{\min}$ between the tip and the PhC membrane. Conclusively, the same tip may either enhance or decrease the intrinsic $Q = 2300 \pm 40$, depending on its position. The PhC parameters are: lattice period $a = 331$ nm, hole diameter $\approx 206$ nm, and GaAs-membrane thickness 320 nm.

The results, shown with the resonance-shift map in Fig. 2.2(b), are in quan-

titative agreement with previous reports [143, 150, 151, 162] showing resonance red-shifts with tiny dielectric perturbers. The spatial resolution, which defines the dimension of the tip perturbation, is estimated to be $\approx 70$ nm. More importantly in the present context are the tip-induced variations of $Q$, whose map in Fig. 2.2(d) shows both $Q$-increases and $Q$-decreases for the first time[2]. In order to link all these observations to the intrinsic cavity $Q$ (without perturber), the NSOM scans are additionally repeated for different tip distances $d$ with respect to the membrane interface. Note that the minimum separation distance, $d_{\min} \approx 30$ nm, depends on the tip-interface interaction and cannot be accurately measured. The data recorded for the three tip positions are given in Fig. 2.2(e). The three series of data all tend to $Q = 2300 \pm 40$, which is also the intrinsic $Q$ value measured when the tip is 1 µm away from the sample. An important and simple outcome of Figs. 2.2(c-e) is that the *same* perturber may either increase $Q$ (point A), leave $Q$ unchanged (point C) or decrease $Q$ (point B). Therefore the present hyperspectral mapping of the of the QNM near field refutes the general validity of Eq.(2.1). Further analysis of the experimental $\Delta\tilde{\omega}$ map will be provided afterwards.

### 2.3.2. Numerical predictions for the studied sample

In this section, we confront Eq.(2.2) to the experimental results of subsection 2.3.1. We consider the same geometry and material as in the experiment (the membrane refractive index is assumed to be 3.46), and replace the tip by a point dipole with a polarizability equivalent to that estimated for the tip in the experiment.

This presents the advantage to remove errors coming from the 3-dimensional nature of our perturbation when comparing to our theory which explicitly assumes perfect 0-dimensional electric dipole. This allows us, in subsection 2.3.3, to discuss the limits of our formulation due to the properties of the photonic environment rather than the perturbation itself. We compute again the resonant mode of the unperturbed cavity with the QNM-solver QNMEig [134]. However, COMSOL does not explicitly allow for point perturbation. Therefore, on the same mesh as used with QNMEig, we drive the system by a dipole source $\mathbf{p}$ placed at the position of the perturber $\mathbf{r}_p$, and compute with COMSOL the field scattered back onto the dipole . This allows us to retrieve the exact Green function $\Delta\mathbf{G}(\mathbf{r_p}, \mathbf{r_p}, \omega)$, which we then use to iteratively look for the complex frequency $\omega$ (exact) solution to the scattering problem of Eq.(2.6), leading to the exact value for the shift of the cavity induced by a point perturbation.

The computed eigenfrequency is $\tilde{\lambda} = 2\pi c/\tilde{\omega} = 1364 + i0.13$ nm, imply-

[2] $Q$-increases by modifying cavity geometry have been previously reported using slabs [152] and scatterer gratings [153] in near fields, but not with a localized perturbation, nor with scanning through the mode to determine the relation between $Q$-changes and mode distributions. Perturbations by extended structures like slabs, have rather been understood as radiation pattern engineering to control $Q$.

ing that the computed $Q$ is twice larger than the experimental one, probably because of losses induced by layer absorption, surface roughness or other extrinsic effects. A spatial map of $|\tilde{\mathbf{E}}|^2$ in a plane 30-nm above the cavity surface is shown in Fig. 2.3(a).



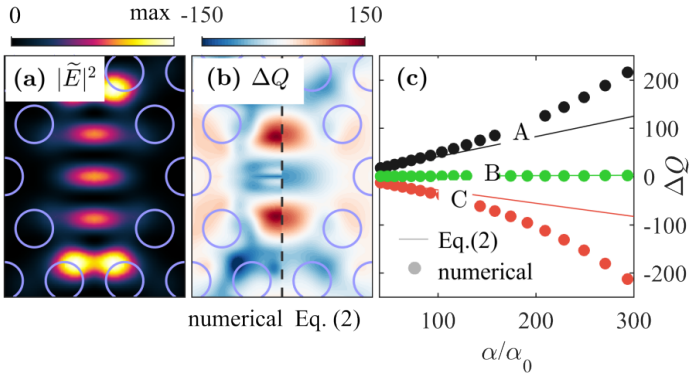


**Figure 2.3:** Numerical test of Eq.(2.2) for the cavity used in the experiment. (a) Maps of $|\tilde{\mathbf{E}}|^2$. (b) Comparison between the $\Delta Q$ maps predicted with Eq.(2.2) (left) and exact values (right) for $\alpha = 166\alpha_0$. (c) Validity of Eq.(2.2) for increasing values of the polarizability and for the three tip positions, A, B and C, used in the experiment. $\alpha_0$ denotes the static polarizability of a 10-nm-radius silica sphere in air, so that the full horizontal scale covers silica spheres with radii from 10 to 70 nm. Note that Eq.(2.1) predicts $\Delta Q = 0$ for all positions and all $\alpha$. In (b) and (c), the point dipole perturber is assumed to be located in a plane 30 nm above the semiconductor PhC membrane, and the exact values are computed by iteratively searching the complex-frequency pole of Eq.(2.6) for $\mathbf{E}_b = 0$ with the regularized scattering tensor $\Delta\mathbf{G}(\mathbf{r},\mathbf{r}',\omega)$ computed with COMSOL Multiphysics.

Figure 2.3(b) compares the $\Delta Q$'s predicted with Eq.(2.2) with exact values computed by solving the perturbed cavity. The data are obtained for a dipole polarizability $\alpha = 4\pi R^3 \frac{\epsilon_{SiO_2}/\epsilon_0 - 1}{\epsilon_{SiO_2}/\epsilon_0 + 2}$ corresponding to the static polarizability of a silica ($\epsilon_{SiO_2} = 2.25\epsilon_0$) nanosphere in air of radius $R = 55$ nm. Since we use exactly the same mesh for the two computations, numerical dispersion is negligible and the comparison strictly quantifies the error due to the single mode approximation. Figure 2.3(c) compares the $\Delta Q$ predictions of Eq.(2.2) with exact numerical values for increasing values of the perturber polarizability $\alpha$. Three perturber locations, corresponding to the three tip positions used in the experiment, are considered. Remarkably, our key experimental observation that the same perturber may either decrease or increase $Q$ as its position is varied, independently of the wavelength-shift sign, is well captured by Eq.(2.2). This confirms that QNM formalism indeed accounts for the non-Hermitian nature of photonic resonators, even in the context of high quality factors Q.

### 2.3.3. Validity domain of Eq.(2.2)

As expected, Fig. 2.3(c) evidences that for vanishing $\alpha$'s, Eq.(2.2) is virtually exact. However, some differences, not observed in previous studies for low-$Q$ plasmonic structures [125, 139], are observed for $\alpha > 150\alpha_0$. Since we enforced 0-dimensional point dipole perturbation in our simulation, this begs the question what the conditions are under which Eq.(2.2) may be used with confidence and what parameters are impacting its domain of validity. In this subsection, we therefore quantify under which condition Eq.(2.2) may be approximately valid and used with confidence to predict both resonance shifts and $\Delta Q$-changes. We analyse the impact of omitting $\delta\mathbf{G}$. Since both terms in the right-hand side of Eq.(2.7) depend on the perturber position differently, we have to make several approximations.

In Eq.(2.11), the second term inside the bracket, $\alpha\epsilon\mu_0\omega^2\delta\mathbf{G}$ gathers the contribution of all other modes that contribute to the mode density at the cavity, except for the cavity mode that is singled out by $\tilde{\mathbf{E}}_N$. In the limit where this contribution is negligible, Eq.(2.11) simply reduces to Eq.(2.2). Accordingly, the validity of Eq.(2.2) requires that

$$\|\alpha\epsilon\mu_0\tilde{\omega}^2\delta\mathbf{G}\|_\infty \ll 1, \tag{2.16}$$

where the operation $\|\cdots\|_\infty$ represents the infinite norm of a matrix.

Though Eq.(2.16) formally quantifies the domain of validity of Eq.(2.2), it is difficult to extract more information, since $\delta\mathbf{G}$ is a $3\times3$ symmetric matrix containing 6 different components. To bypass this difficulty, we make the approximation $\delta\mathbf{G} \approx \delta G,\mathbf{I}$, with $\delta G \equiv \mathrm{Tr}\,\delta\mathbf{G}/3$, i.e. neglecting the vectorial character of $\delta G$, where $\mathbf{I}$ represents the identity matrix, and further assume $\alpha$ is real, i.e., neglecting radiation loss and material absorption of the perturber. Under these approximations, we compare $\Delta\tilde{\omega}$ predicted from Eqs.(2.14 and 2.15) and Eq.(2.2), and derive that the dominant conditions for Eq.(2.2) to accurately predict $\mathrm{Re}\,\Delta\tilde{\omega}$ and $\mathrm{Im}\,\Delta\tilde{\omega}$ are respectively

$$|\alpha| \ll \alpha_r \text{ and } |\alpha| \ll \alpha_i, \tag{2.17}$$

where $\alpha_r$ and $\alpha_i$ are given by

$$\alpha_r = \min\left\{\left|\frac{1}{\mu_0\epsilon\mathrm{Re}(\omega^2\delta G)}\right|, \left|\frac{1}{\mu_0\mathrm{Im}\epsilon(\omega^2\delta G)}\right|\left|\frac{\mathrm{Re}\,\tilde{V}^{-1}}{\mathrm{Im}\,\tilde{V}^{-1}}\right|\right\}, \tag{2.18a}$$

$$\alpha_i = \min\left\{\left|\frac{1}{\mu_0\epsilon\mathrm{Re}(\omega^2\delta G)}\right|, \left|\frac{1}{\mu_0\epsilon\mathrm{Im}(\omega^2\delta G)}\right|\left|\frac{\mathrm{Im}\,\tilde{V}^{-1}}{\mathrm{Re}\,\tilde{V}^{-1}}\right|\right\}. \tag{2.18b}$$

Note that, to derive Eqs.(2.17 and 2.18), we have used the relations, $\mathrm{Re}\,\tilde{V}^{-1} \gg \frac{1}{2Q}\mathrm{Im}\,\tilde{V}^{-1}$ and $\mathrm{Im}\,\tilde{V}^{-1} \gg \frac{1}{2Q}\mathrm{Re}\,\tilde{V}^{-1}$ which are valid for high-$Q$ cavities.

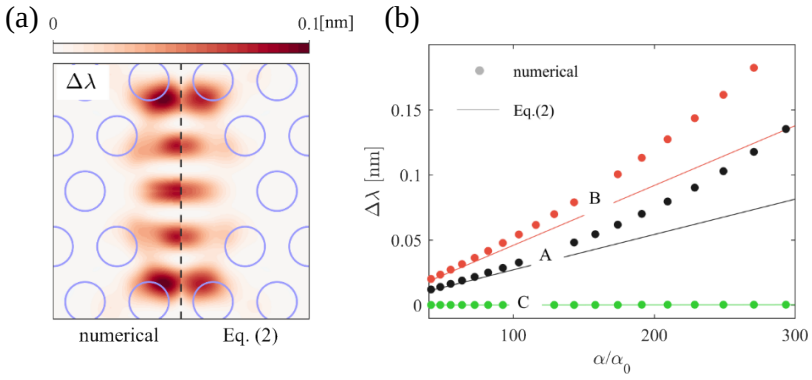


**Figure 2.4:** Validation of Eq.(2.2) for the resonance wavelength shift $\Delta\lambda$ by comparison with exact numerical data obtained by solving the perturbed cavity. (a) Comparison between the $\Delta\lambda$ maps predicted with Eq.(2.2) (left) and exact values (right) for the same configuration and $\alpha = 166\alpha_0$ as in the Fig. 2.3. (b) Validity of Eq.(2.2) in predicting $\Delta\lambda$ for increasing values of the polarizability. The perturber polarizability $\alpha$ is normalized by $\alpha_0$, the static polarizability of a silica sphere with 10-nm radius in air. Three perturber positions, 30 nm above the semiconductor membrane, are considered; they are labelled as "A", "B", "C", corresponding to the positions in the experiment, see in Fig. 2.2(e)

The expressions of $\alpha_r$ and $\alpha_i$ can be further simplified by first noting that $\left|\frac{\mathrm{Re}\,\tilde{V}^{-1}}{\mathrm{Im}\,\tilde{V}^{-1}}\right| \gg 1$ for high-Q cavity, and we generally have $|\mathrm{Re}(\omega^2\delta G)| \gg |\mathrm{Im}(\omega^2\delta G)|$ (as confirmed by numerical simulations[3]) for perturbers placed in the near-field of the cavity. We finally obtain simplified expressions for $\alpha_r$ and $\alpha_i$

$$\alpha_r = \left|\frac{1}{\mu_0\epsilon\mathrm{Re}(\omega^2\delta G)}\right|, \tag{2.19a}$$

$$\alpha_i = \min\left\{\alpha_r, \left|\frac{1}{\mu_0\epsilon\mathrm{Im}(\omega^2\delta G)}\right|\left|\frac{\mathrm{Im}\,\tilde{V}^{-1}}{\mathrm{Re}\,\tilde{V}^{-1}}\right|\right\}, \tag{2.19b}$$

which imply that $\mathrm{Im}\,\Delta\tilde{\omega}$, i.e. $\Delta Q$, can be predicted, at best, with the same accuracy as $\Delta\lambda$, but not better. Moreover, as $Q$ increases, $\left|\frac{\mathrm{Im}\,\tilde{V}^{-1}}{\mathrm{Re}\,\tilde{V}^{-1}}\right|$ decreases towards zero, and so does $\alpha_i$. Therefore, it is more difficult to predict $\Delta Q$ accurately for a high-$Q$ cavity than for a low-$Q$ one. This explains why no visible deviation between the predictions of Eq.(2.2) and exact numerical data have been detected in earlier works on plasmonic nanoresonators, even for large shell perturbers [122, 139].

[3] $\delta\mathbf{G}$, and then $\delta G$, have been computed with COMSOL Multiphysics. A reasonable estimate for the typical magnitude of $\delta G$ is that it is essentially the non-resonant contribution to the full system Green function [scattered part strictly] on top of which the resonant cavity mode adds. The non-resonant background is of the same order as the Green function of free space for a perturber placed outside the cavity.

Finally, for the sake of completeness, we study in Fig. 2.4 the accuracy in predicting $\Delta\lambda$ with the same parameters as used in Fig. 2.3. We numerically find that $\alpha_r = \alpha_i = 665\alpha_0$ at position A, and $\alpha_r = 702\alpha_0$ at position B and $\alpha_i = 541\alpha_0$ at position C. For all cases, $\alpha_r$ and $\alpha_i$ have similar values, and this a posteriori explains why Eq.(2.2) is as accurate in predicting wavelength shifts $\Delta\lambda$ in Fig. 2.4(b), as it is at predicting $Q$-changes in Fig. 2.3(c).



### 2.3.4. Influence of the environment on the perturbation

The previous subsection 2.3.3 gives mathematical conditions (Eq.(2.17)) for the validity of Eq.(2.2). In this subsection, we intend to give a more physical interpretation of these conditions. To do so, we take the example photonic crystal cavity studied in subsection 2.2.2, and we fix the position of the air perturbation in the cavity at $x = 360$ nm, where the destructive interference effect is the strongest in Fig. 2.5(d). We increase the polarizability of the perturbation by increasing its diameter. However, since the perturbation is now a physical object and not a perfect point dipole as in subsections 2.3.2 and 2.3.3, we restrict our study to diameters up to a quarter of the wavelength in silicon $\lambda_{Si}/4$ to mitigate the influence of higher order multipoles of our spherical perturbation. Figure 2.5 shows that Eq.(2.2) applies only for perturbations smaller than $\lambda_{Si}/10$. For bigger perturbations, Eq.(2.2) only predicts an unbounded increase in quality factor Q, whereas exact calculations indicate that Q reaches a maximum almost 20% higher than the original cavity Q, and then drops dramatically. Indeed, for a perturbation strong enough, which corresponds to a sphere bigger than $\lambda_{Si}/10$ in Fig. 2.5, one of the conditions in Eq.(2.17) is not respected anymore. An interpretation is that the polarizability that enters in Eq.(2.2) is not actually the static polarizability, but a polarizability that is *dressed* by its environment through $\alpha_d^{-1} = \alpha^{-1} - \mu_0\epsilon\omega^2\delta G$ as explicit in Eq.(2.11).

The concept of a *dressed* polarizability is commonly used in the theory of multiple scattering [163]. For instance, it is well known that the electrostatic polarizability of a small sphere ($\alpha_0 = 4\pi a^3(\epsilon/\epsilon_0 - 1)/(\epsilon/\epsilon_0 + 2)$ for a sphere of radius $a$ and dielectric constant $\epsilon$ in free space) in itself can not be used to build an energy conserving scattering theory. It leads to a violation of the optical theorem. Instead, one can construct a dynamic polarizability, also known as $t$-matrix for a dipolar scatterer, from the static polarizability, by evaluating $\boldsymbol{\alpha}^{-1} = \boldsymbol{\alpha}_0^{-1} - \mu_0\epsilon\omega^2 i\mathrm{Im}\,\mathbf{G}_0(\mathbf{r},\mathbf{r})$. Here the added term quantifies the impact of the environment on the polarizable object, which is to cause radiation loss. This radiation loss in vacuum is quantified by the LDOS of free space, or equivalently $\mathrm{Im}\,\mathbf{G}_0(\mathbf{r},\mathbf{r})$. It is important to note that the impact of this term is negligible for very small scatterers, and becomes increasingly important with increasing $\alpha_0$. Various works have noted that if one replaces the background medium of the scatterer by a complex environment, then if one chooses to account for that complex environment by incorporating it in a

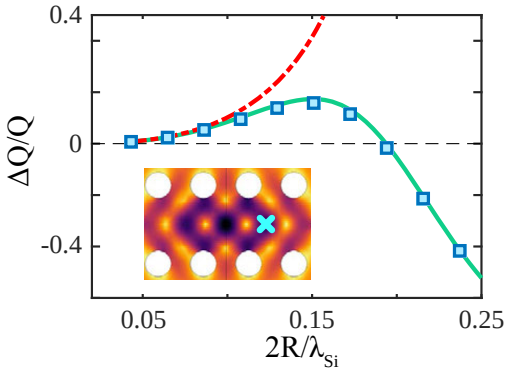


**Figure 2.5:** Broadening and narrowing of the resonance as a function of the size of a air sphere perturbation in the median plane of the PhC slab, at a fixed position $x = 360$ nm (indicated by a blue cross in the caption of the mode profile). Blue squares are calculations from COMSOL, red dashed line is Eq.(2.2) with the static polarizability $\alpha$, and green solid line is with the dressed polarizability $\alpha_d$.

Green function, its scattering part enters as a further dressing of polarizability through $\boldsymbol{\alpha}_d^{-1} = \boldsymbol{\alpha}^{-1} - \mu_0\epsilon\omega^2\mathbf{G}_s(\mathbf{r},\mathbf{r})$. The scattering part of the Green function in this expression accounts for all the multiple scattering interactions between the point dipole and the environment.

Returning to the perturbation problem at hand, we note that in Eqs.(2.1 and 2.2) it is not *a priori* clearly specified which polarizability is pertinent in perturbation theory. Our result Eq.(2.11) indicates that it is in fact the perturber polarizability dressed by the environment, where the environment is defined as the photonic system *excluding* the cavity mode that is singled out for the perturbation theory. We verify this by comparing the exact result in Fig. 2.5 with the perturbation result Eq.(2.2) evaluated with an estimated dressed polarizability. We note that since the static polarizability $\alpha$ is a real number, the imaginary part of $\mu_0\epsilon\mathrm{Im}(\omega^2\delta G)$ directly gives the imaginary part of the dressed polarizability $\alpha_d$. The real part of $\mu_0\epsilon\omega^2\delta G$ can to first order be neglected since the first condition of Eq.(2.17), $|\alpha| \ll |\mu_0\epsilon\mathrm{Re}(\omega^2\delta G)|^{-1}$ is relatively easy to respect. We show in Fig. 2.5 that dressing the static polarizability by only $\mu_0\epsilon\mathrm{Im}(\omega^2\delta G)$ is indeed enough to restore the accuracy of our perturbation theory. The correction term $\mu_0\epsilon\mathrm{Im}(\omega^2\delta G)$ that we use, however, is not trivial to obtain since it should quantify the local density of optical states (LDOS) at the location of the scatterer that is due to all the modes *except* the cavity QNM at $\tilde{\omega}$. We calculate the correction by first using COMSOL to obtain the *total* LDOS across a real frequency interval spanning the cavity resonance $\mathrm{Re}\,\tilde{\omega}$, and then a posteriori subtracting the Lorentzian contribution of the unperturbed cavity QNM. Owing to the 2D photonic band gap, the LDOS is suppressed by a factor 10 compared to that in free space, but not identically zero [164]. For sufficiently large perturbations, these radiative loss

channels nonetheless limit the polarizability, and hence for larger perturbation volumes the radiation loss spoils the increase in Q arising from the destructive interference between the perturbation and the cavity mode. For non-resonant perturbations as considered in this work, the real part $\mu_0\epsilon\mathrm{Re}(\omega^2\delta G)$ is irrelevant. For resonant perturbations, however, it would be important as it corresponds to a frequency (Lamb) shift of the perturber. From the practical viewpoint of perturbation theory, the unfortunate conclusion is that calculating the correction $\delta G$ to the polarizability is computationally difficult. An alternative viewpoint to dressing the polarizability is that perturbation theory is not complete with just one QNM. Indeed, all other QNMs of the system enter through $\delta G$. A positive outcome of our analysis is that perturbation of a cavity by an object *could* give access to measuring the ratio of cavity Purcell factor and background LDOS. This ratio is instrumental for quantifying the performance of cavities for single photon sources and lasers, as it establishes the so-called $\beta$-factor [165, 166]. Our claim is that this quantity is *in principle* accessible by purely classical near-field measurements.

### 2.3.5. Mapping complex mode volumes $\tilde{V}$

The concept of complex $\tilde{V}$'s is recent [124, 131] and it seems to be connected with highly relevant phenomena of light-matter interactions in non-Hermitian open systems [125]. For instance, the ratio $\mathrm{Im}\,\tilde{V}^{-1}/\mathrm{Re}\,\tilde{V}^{-1}$ quantifies the spectral asymmetry of the mode contribution (or LDOS) to the modification of the spontaneous emission rate of an emitter weakly coupled to a cavity [124]. For strong coupling, it modifies the usual expression of the Rabi frequency [155] by blurring and moving the boundary between the weak and strong coupling regimes [125, 167]. Despite these strong roots, complex $\tilde{V}$'s are often seen as a mathematical abstraction. In fact, Eq.(2.2) and the experiment of subsection 2.3.1 show that complex $\tilde{V}$'s are not just a mathematical tool, but in fact are directly measurable.

Figure 2.6 shows the maps of $\mathrm{Re}\,\tilde{V}^{-1}$ and $\mathrm{Im}\,\tilde{V}^{-1}$, which have been directly inferred from the $\Delta\tilde{\omega}$ measurements by injecting a tip polarizability $\alpha_{\mathrm{tip}} = 166\alpha_0$ (tip curvature radius of $R = 55$ nm) in Eq.(2.2). For comparison, we also plot the theoretical maps computed with the QNM-solver. Note that to allow for a better comparison, we have multiplied the experimental values of $\mathrm{Re}\,\tilde{V}^{-1}$ and $\mathrm{Im}\,\tilde{V}^{-1}$ by a $\times 1/4$ rescaling factor. The latter corresponds to a tip radius only 30% larger ($R = 73$ nm), and can be understood by considering that a static sphere dipolar polarizability is a simplistic model for the tip used in our experiment. There are differences between the experimental maps and the computed ones. Nevertheless, the experimental and theoretical maps qualitatively share the same dominant features, notably a successful agreement on the *locations* and *amplitudes* of the minimum and maximum values, and an overall 10-fold difference between $\mathrm{Re}\,\tilde{V}^{-1}$ and $\mathrm{Im}\,\tilde{V}^{-1}$.

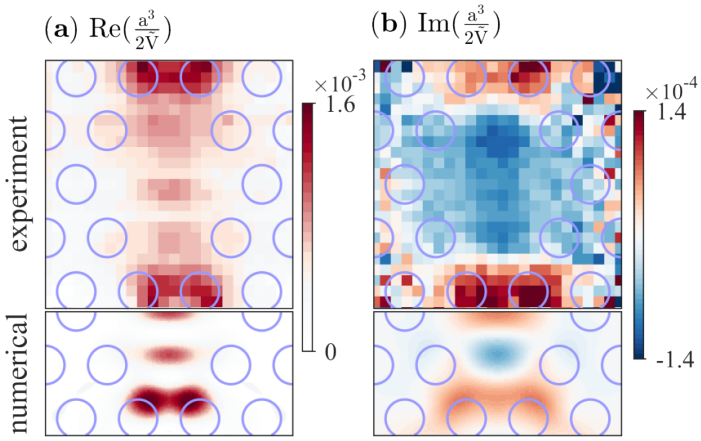


**Figure 2.6:** Maps of (a) $\mathrm{Re}\,\tilde{V}^{-1}$ and (b) $\mathrm{Im}\,\tilde{V}^{-1}$ computed with the QNM-solver 30 nm above the semiconductor membrane (bottom) and directly inferred from the $\Delta\tilde{\omega}$ measurements using Eq.(2.2) with a tip polarizability $\alpha_{\mathrm{tip}} = 166\alpha_0$ (top). Note that the experimental values are all rescaled by a factor $1/4$.

## 2.4. Conclusion and outlook

We have shown that, for high-Q systems, QNM theory allows for a quantitative prediction of both $\mathrm{Re}\,\Delta\tilde{\omega}$ and $\mathrm{Im}\,\Delta\tilde{\omega}$ as a function of the perturber position, whereas classical theory based on Hermitian physics only gives access to $\mathrm{Re}\,\Delta\tilde{\omega}$. Furthermore, we have demonstrated, thanks to hyperspectral-imaging near-field experiments, that the perturbation theory of high-$Q$ microcavities should rely on complex modal volumes to fully account for the role of the perturber at the nanoscale, even in the context of high-Q resonators. This demonstration extends earlier results on the low-Q plasmonic systems [139] and is the first and direct evidence of the importance of complex mode volumes, arising from the intrinsic property of all photonic resonators of being open (i.e. non-Hermitian) systems. Equation (2.2) combines great simplicity and predictive power, its limitations mostly arising due to multiple scattering events between the perturbed resonant mode and its photonic background (other modes and continuum) mediated by strong perturbations. It may find applications in various problems related to sensing or trapping, as the additional information provided by dual maps may help lifting the degeneracy of single $\Delta\lambda$-maps, for instance allowing not only the detection of binding event in sensing but also the binding location [147]. Other perspectives concern the analysis of the impact of fabrication imperfections on $Q$'s, post-fabrication $Q$-control [148], optimization of cavities with large $Q$'s, or inverse design of cavities with tailored $\Delta\lambda$ and $\Delta Q$-maps. Equation (2.2) also offers the possibility to perform direct measurement of the complex mode volume of microcavities, giving greater visibility and operational capacity to an important physical

quantity of resonant light-matter interactions.

## 2.5. Appendix



### 2.5.1. Reliability of the $\Delta Q$-measurements

This appendix reports supplementary information about the experiment. The contribution of the author of this thesis to the work reported in this chapter concerns solely the theory and simulations, and not the experiment. The supplementary information is only provided for completeness, and should be credited to F. La China, D. Balestri, F. Intonti and M. Gurioli. In the ex-

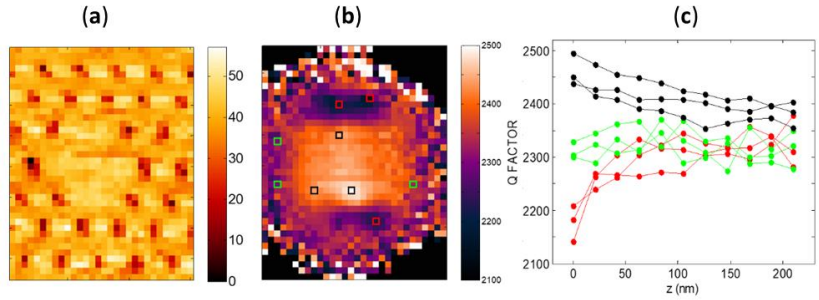


**Figure 2.7:** (a) Topography map. (b) Corresponding $Q$-variation map. The coloured squares represent several tip locations. (c) $Q$-variation as a function of the offseted distance $z - d_{\min}$ between the tip and the photonic-crystal membrane. The black, green and red curves are obtained for tip locations shown in (c) with the squares of the same colors.

periment, the near-field tip is used to excite the embedded InAs QD with a c.w. laser at 780 nm and, for every tip position, the QD photoluminescence spectrum is measured. At room temperature, the spectrum covers more than 100 nm. It exhibits a Lorentzian peak for each cavity resonance. Due to the interaction with the tip, $\mathrm{Re}\,\tilde{\omega}$ and $\mathrm{Im}\,\tilde{\omega}$ are both modified. By fitting the spectra for every tip position, one obtains the $\Delta\lambda$ and $Q$ maps reported in Fig. 2.2. The feedback mechanism of the NSOM is able to maintain the tip on the sample surface at constant height, whenever the sample is flat. In photonic crystal cavities, it forces the tip to follow the topography and then, when the tip is on an air pore, the tip height is reduced by few tens of nm. The measure of the tip-height map, see Fig. 2.7(a), allows one to reconstruct, a posteriori, the perturbation map with a spatial alignment of a few tens of nanometers, which is needed for a comparison with theoretical prediction. The $z$-scan is then performed by moving the sample vertically with steps of 20 nm. During the vertical scan, the tip is maintained at a constant height. Then, after each $z$-scan, the sample is repositioned thank to the feedback mechanism to keep the spatial alignment, and then is moved in the $(x, y)$ plane. In order to detect

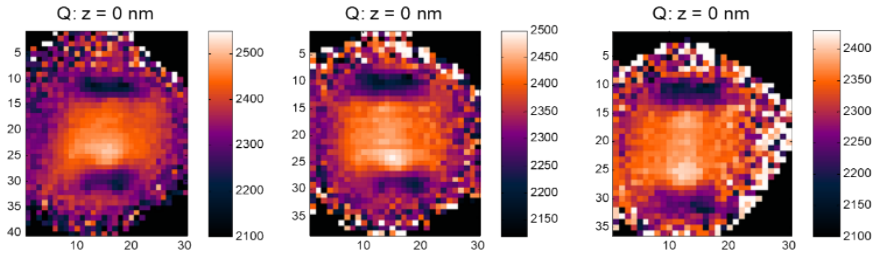


**Figure 2.8:** Three different maps of the $Q$-variation induced by the NSOM tip measured for three different days without changing the tip.

possible systematic errors in the $z$-scan (such as sample/tip drift), the $z$-scan is repeated several times for different $(x, y)$ locations. An example is shown in Figs. 2.7(b-c). Figure 2.7(b) reports the $Q$ map at $z = 0$ for three A points (red squares), three B points (black squares) and three C points (green squares), all located at quite different positions. Figure 2.7(c) reports the $Q$-variation for every point. All the data converge to a common value with similar trends, denoting the reliability of the presented data. Finally, the problem of repeatability of the NSOM measurements to detect possible artefacts is addressed in Figure 2.8, which shows three different maps of the $Q$-factor obtained with the same tip on three different days. The data comparison conclusively evidences a quantitative agreement between the three sets of data.

# 3

# COUPLED QNM THEORY

## 3.1. Introduction

In the last two decades, the nanophotonics community has been very prolific in proposing new designs for a large panel of applications, encouraged notably by the development of nanoscale lithography techniques and shape-controlled colloidal synthesis of nanoparticles. A particular class of designs involves the hybridization of two or more resonators. One of the very first examples would be colloidal clusters of plasmonic nanoparticles, where the field is enhanced at plasmonic hotspots due to cooperative effects. These structures enabled the first single-molecule surface enhanced Raman measurements in the end of the 1990s [168, 169]. For assemblies of nanoparticles with deterministic arrangements, in particular dimers with narrow gaps such as bowtie antennas in Fig. 3.1(a-c), the strong field confinement allows to reach LDOS enhancements > 700 [77, 78]. Radiative properties can also be engineered to exhibit directionality of the light scattered in the far-field [82, 84], or to exploit Fano resonances, in particular for detection [86, 87, 170]. Indeed, composite structures usually exhibit multiple resonant modes which can interfere in the near-field as well as the far-field and lead to sharp spectral features, even for purely plasmonics resonators (cf. Fig. 3.1(d-e)).

Although the previous illustrative examples were all taken from the field of plasmonic, hybridization of resonances is by no means a topic limited to plasmonics. In the domain of photonic microcavities, coupled resonances play an important role in several applications. For instance, *photonic molecules* are studied in the context of slow light propagation [172] and parity-time (PT) symmetric systems [66], and are of large interest in cavity optomechanics as a mean to achieve quadratic coupling [173, 174]. Dielectric and plasmonic resonators may be hybridized as well [94–96], an emblematic example being shown in Fig. 3.1(g). Chapters 4 to 6 deal with this kind of hybridization for

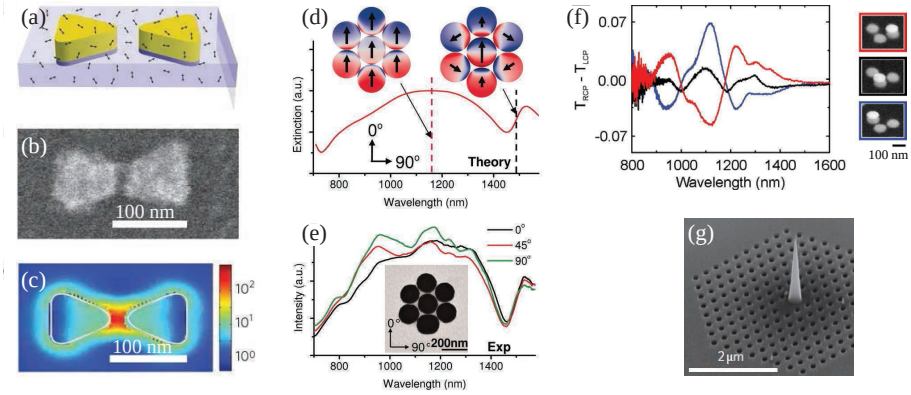


**Figure 3.1:** (a) Schematic of bowtie nanoantenna (gold) coated with molecules (black arrows) in PMMA (light blue) on a transparent substrate. (b) Scanning electron microscopy (SEM) image of a gold bowtie nanoantenna. (c) FDTD calculation of the field enhancement. (a-c) reproduced from [77]. (d) Calculated extinction spectrum exhibiting a Fano feature and charge density plots for a heptamer excited at normal incidence with a 0° linear polarization orientation. The inset and corresponding vertical dashed line indicate the resonance of bright (left, dashed pink line) and dark modes (right, dashed black line) (e) Transmission electron microsope (TEM) image, and extinction spectra of a heptamer measured at three different incident electric-field orientation angles, all exhibiting a Fano feature predicted in (d). (d-e) reproduced from [170]. (f) Experimental $\Delta_{LCP-RCP}$ spectra calculated as the difference in the transmittance of right (red) and left-handed (blue) circularly polarized light for a metasurface composed of 3-dimensional chiral plasmonic molecules. The transmittance properties are opposite for opposite handedness. The achiral structure (black) shows small differences in the transmittance which can be assigned to fabrication errors. Reproduced from [90]. (g) Scanning electron microscope (SEM) image of a photonic-plasmonic hybrid resonator composed of a $Si_3N_4$ photonic crystal and a silver tip for near-field optical microscopy application. Reproduced from [171].

which it may be anticipated that we can combine the best of the two contrasted properties of plasmonics (low Vs and low Qs) and photonics (high Qs and large Vs).

Contemporary resonator constructs are complex; they mix different physics and materials and rely on many degrees of freedom, even in 3-dimensions [90, 175, 176] (cf. Fig. 3.1(f)). It thus becomes essential to have access to adequate tools to design their structural ingredients and study their optical properties. Temporal coupled-mode theory (CMT) of resonators [177] appears to offer an ideal platform to study resonators composed of several coupled resonances. However, it relies on phenomenological coupling coefficients, which are fitted from experimental or numerical data. Therefore, it does not provide a viable path for designing these structures. Some works proposed formalisms to describe hybridization of resonances, but they often rely on strong assumptions. First of all, most of these formalisms are restricted

to analytically treatable geometries such as spheres [178–180]. Second, the majority of works study highly symmetric assemblies to make use of the irreducible representation predicted by group theory [181], as we do in Chapter 5. More frequently, a quasi-static approximation is made to simplify the description of the interaction between resonators. In plasmonics this is known as *plasmon hybridization theory*, proposed by Prodan et al. [182]. However, only the resonance frequencies (or *energies*) can be predicted, not the decay rates which are intrinsically related to dynamical radiation effect.



In recent years, works studying the interaction of light with open electromagnetic systems using a description in terms of quasinormal modes (QNM) have grown in visibility [135, 139, 140, 183]. This trend was seeded by the gain in physical insight and computational time that QNMs provide while still relying on semi-analytical treatments [132, 134, 184]. In the QNM framework, a resonator is described by a set of quasinormal modes [117, 123, 124], which are strictly the source-free solutions of Maxwell equations, with a normalized electromagnetic field $\tilde{\mathbf{E}}_N, \tilde{\mathbf{H}}_N$ and a complex resonance frequency $\tilde{\omega}_N$ (real part is the resonance frequency, while the imaginary part is the decay rate) (cf. review paper [125] and Introduction/Chapter 1). To our surprise, despite the fact that such theories are casually used to describe ensemble of many plasmonic nanoresonators [134, 185] and even antenna-cavity hybrids [109, 186], there exists, to our knowledge, only one formulation of a QNM theory allowing to study the hybridization of resonators. In ref. [138], Vial et al. express the QNMs of the coupled system as a linear combination of the QNMs of the bare components to obtain a generalized eigenvalue problem. Their formulation is however restricted to non-dispersive materials and, therefore, cannot apply for plasmonic resonators. Also, the theory of Vial et al. relies on cumbersome integrals over the whole universe (or simulation domain in practice). Furthermore, even though the formalism should apply for 3-dimensional systems and should be generalizable to $N$ coupled resonators, the validity of the work was only demonstrated for dimers, in 2-dimensional systems.

In this chapter, we present a general semi-analytical formalism, based on a generalized linear eigenproblem, to calculate the QNMs of an ensemble of 3-dimensional resonators solely based on the knowledge of the QNMs of the individual components, even in the context of dispersive materials. Our proposition not only enables one to estimate resonance frequencies and decay rates, but also to quantify observables such as extinction and scattering cross sections, and near-field field distribution. This chapter is structured as follows. Section 3.2 presents a derivation of a coupled QNM theory as a generalized linear eigenproblem using multiple scattering formulation as a starting point, tackles the issue of the normalization of the modes and the coupling coefficient to an external driving field. Next, after having simplified the model to treat the case of two coupled plasmonic resonators, each described by a single QNM, we discuss the analogy with the didactic case

of the hybridization of two resonant point dipoles. Then, in subsection 3.3.2, we demonstrate the strength of our formulation to characterize the extinction properties for different arrangement of a homo- or heterodimer composed of two gold nanorods. In subsection 3.3.3, we apply the theory to study the case of an oligomer composed of four resonators as in [87] and demonstrate the relevance of our formalism in the context of Fano-like resonances. Finally, in Section 3.4 we explore briefly the potential of our work to converge toward an exact solution for the QNMs of the coupled system when we increase the number of QNMs taken to described each resonator of the ensemble.



## 3.2. Formalism

In this section, we derive a coupled QNM formalism. Using as a starting point the problem describing multiple scattering between an assembly of resonators, we obtain a generalized eigenproblem, whose resolution allows us to compute the new coupled QNMs of the assembly from the QNMs of its bare components. We start by considering the particularly didactic example of the hybridization of two resonant point dipoles coupled via a Green function into bonding and anti-bonding states [187]. Throughout this chapter, notations involving a tilde $\tilde{}$ represent a quantity intrinsic to a certain QNM $n$ (eigenfrequency $\tilde{\omega}_n$, normalized eigenfield $\tilde{\mathbf{E}}_n$).

### 3.2.1. Coupling two resonant point dipoles

Let us consider two dipoles, which are either aligned (head to tail), or parallel (side by side). This hypothesis allows us to use scalar notation for the dipole moments $p_{A/B}$ of dipoles $A$ and $B$ and their polarizability $\alpha_{A/B}$, as well as the electric field driving $A$ and $B$, $E_{dr,A/B}$ and the field scattered by $A$ on $B$, $E_{B\to A}$ (and conversely $E_{B\to A}$). This scalar notation does not remove any generality of our treatment. The total field driving each dipole is the sum of the incident driving field and the field scattered by the other dipole

$$\begin{cases} p_A = \alpha_A \left[E_{dr,A} + E_{B\to A}\right] \\ p_B = \alpha_B \left[E_{dr,B} + E_{A\to B}\right], \end{cases} \tag{3.1}$$

where $E_{i\to j}(\omega) = \frac{\omega^2}{\epsilon_0 c^2} G_0(\mathbf{r}_i, \mathbf{r}_j, \omega) p_i$ (with $i, j = A$ or $B$), and $G_0$ is the Green function which can be obtained analytically for a homogeneous background such as vacuum [16]. We assume resonant dipoles, and the polarizabilities for a dipole $i$ are assumed to have a Lorentzian form

$$\alpha_i(\omega) = -\frac{\beta_i}{2\omega} \frac{1}{\omega - \tilde{\omega}_i}, \tag{3.2}$$

with $\beta_i$ the oscillator strength of dipole $i$, and $\tilde{\omega}_i \equiv \omega_i + i\gamma_i/2$ the complex resonance frequency, composed of the resonance $\omega_i$, and the total decay rate

$\gamma_i$. If we introduce the notation

$$K_i(\omega) \equiv \beta_i \frac{\omega}{2\epsilon_0 c^2} G_0(\mathbf{r}_i, \mathbf{r}_j, \omega), \tag{3.3}$$

we can rewrite Eq.(3.1 in a matrix form

$$\begin{bmatrix} \omega - \tilde{\omega}_A & K_A \\ K_B & \omega - \tilde{\omega}_B \end{bmatrix} \begin{pmatrix} p_A \\ p_B \end{pmatrix} = \begin{pmatrix} -\frac{\beta_A}{2\omega} E_{dr,A} \\ -\frac{\beta_B}{2\omega} E_{dr,B} \end{pmatrix}. \tag{3.4}$$



Since we are interested in the resonant modes of the system, we look for eigen-solutions of Eq.(3.4), i.e. for complex resonance frequencies (or eigenfrequencies) $\tilde{\omega}$ such that there exists a source-free solution $(\tilde{p}_A; \tilde{p}_B)_n$ when $E_{dr,A} = E_{dr,B} = 0$

$$\begin{bmatrix} \tilde{\omega}_A & -K_A \\ -K_B & \tilde{\omega}_B \end{bmatrix} \begin{pmatrix} \tilde{p}_A \\ \tilde{p}_B \end{pmatrix} = \tilde{\omega} \begin{pmatrix} \tilde{p}_A \\ \tilde{p}_B \end{pmatrix}. \tag{3.5}$$

Note that because $G_0$ contains a complex exponential to account for retardation, $K_{A/B}$ contains it as well, and the system is therefore non-linear. However, the exponential origin of the non-linearity of Eq.(3.4) implies that there are an infinite but discrete amount of complex frequencies solutions to this equation. All these modes can be ascribed a physical meaning as Fabry-Perot-like modes connecting the two dipoles. A simplification is often used to predict the cooperative effects of large collections of classical or quantum oscillators, such as Dicke superradiance [188]. It consists in performing a Taylor expansion of the equation at the original dipole resonances. For small dipole separations, only the two modes with complex resonance frequencies $\tilde{\omega}_+$ and $\tilde{\omega}_-$ closest to the original uncoupled dipoles $\tilde{\omega}_A$ and $\tilde{\omega}_B$ are relevant. Therefore, if we assume that the two dipoles have the same oscillator strength $\beta_A = \beta_B$, and that we can neglect the frequency dependence of $K \equiv K_A = K_B$, the eigenfrequencies of the system are given by

$$\begin{cases} \tilde{\omega}_+ = \frac{1}{2}(\tilde{\omega}_A + \tilde{\omega}_B) + \frac{1}{2}\sqrt{(\tilde{\omega}_A - \tilde{\omega}_B)^2 + 4K^2} \\ \tilde{\omega}_- = \frac{1}{2}(\tilde{\omega}_A + \tilde{\omega}_B) - \frac{1}{2}\sqrt{(\tilde{\omega}_A - \tilde{\omega}_B)^2 + 4K^2}. \end{cases} \tag{3.6}$$

In the general case, $\tilde{\omega}_A - \tilde{\omega}_B$ but also $K$, are complex numbers. Equation (3.6) therefore contains a lot of interesting physics about the hybridization of two resonant dipoles depending on the phase of these two complex numbers. We note that the eigenvectors are also complex, and in the general case, not orthogonal. We give a flavour of the richness contained in this simple two coupled dipoles model by making a few simplifying hypothesis. We always assume that the two dipoles have the same decay-rate $\gamma$ and oscillator strength $\beta$. This leads to $\tilde{\omega}_A - \tilde{\omega}_B$ being a real quantity. Furthermore, we use the convention $\omega_A > \omega_B$ such that we have $\tilde{\omega}_A - \tilde{\omega}_B = |\tilde{\omega}_A - \tilde{\omega}_B| > 0$. We also note that according to Ref. [16], in the case when $d < \lambda/2$, $K$ is mostly a positive

real number, with a small negative imaginary part for **aligned dipoles** (head to tail), and is mostly a negative real number, with a small negative imaginary part for **parallel dipoles** (side by side).

**Homodimer:** $\tilde{\omega}_A = \tilde{\omega}_B$
We first consider the case of a homodimer composed of two identical dipoles, i.e. $\tilde{\omega}_A = \tilde{\omega}_B \equiv \tilde{\omega}_0$, Eq.(3.6) simplifes to

$$\begin{cases} \tilde{\omega}_+ = \tilde{\omega}_0 + K \\ \tilde{\omega}_- = \tilde{\omega}_0 - K. \end{cases} \tag{3.7}$$

The eigenvectors are then trivially obtained as

$$\begin{cases} (\tilde{p}_A\,;\tilde{p}_B)_+ = \frac{1}{\sqrt{2}}(1\,;-1) \\ (\tilde{p}_A\,;\tilde{p}_B)_- = \frac{1}{\sqrt{2}}(1\,;+1). \end{cases} \tag{3.8}$$

We understand that for an aligned or parallel arrangement of the dipoles, the properties of the modes of the coupled system are different. This is summarized in Fig. 3.2. For aligned dipoles (head to tail, 0°), mode "+" is blue-shifted ($\mathrm{Re}\,K > 0$) and has a lower loss rate ($\mathrm{Im}\,\mathrm{K}<0$) than the uncoupled dipole. Indeed, the two components of the corresponding vector have opposite sign (anti-bonding mode), which means that the radiation of the two dipoles interferes destructively, and therefore the mode radiates less than the uncoupled dipoles: it is *subradiant* or *dark*. Conversely, mode "−" is red-shifted and has a higher loss rate: it is *superradiant* or *bright*. For parallel dipoles (side by side, 180°), mode "+" is now red-shifted ($\mathrm{Re}\,K < 0$) but still has a lower loss rate ($\mathrm{Im}\,\mathrm{K}<0$) than the uncoupled dipole. Conversely, mode "−" is now blue-shifted but still superradiant. **For orthogonal dipoles** (90°), the assembly is in an intermediate regime, and both hybridized modes can radiate light. For a homodimer, mode + and − have orthogonal net dipole moments and therefore radiate light with orthogonal linear polarizations.

**Heterodimer in the weak coupling regime:** $|\tilde{\omega}_A - \tilde{\omega}_B| \gg |K|$
For weak coupling $K \to 0$ with a heterodimer composed of two different dipoles, we can perform a Taylor expansion of the eigenfrequencies expressed in Eq.(3.6) to obtain

$$\begin{cases} \tilde{\omega}_+ \approx \tilde{\omega}_A + \frac{K^2}{|\tilde{\omega}_A - \tilde{\omega}_B|} \\ \tilde{\omega}_- \approx \tilde{\omega}_B - \frac{K^2}{|\tilde{\omega}_A - \tilde{\omega}_B|}. \end{cases} \tag{3.9}$$

In this approximation, it is straightforward to show that the associated eigenvectors are approximately

$$\begin{cases} (\tilde{p}_A\,;\tilde{p}_B)_+ \approx \left(1\,;\frac{-K}{|\tilde{\omega}_A - \tilde{\omega}_B|}\right) \\ (\tilde{p}_A\,;\tilde{p}_B)_- \approx \left(\frac{+K}{|\tilde{\omega}_A - \tilde{\omega}_B|}\,;1\right). \end{cases} \tag{3.10}$$

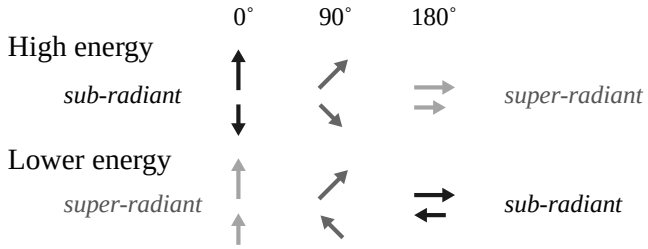


**Figure 3.2:** Radiative properties of dipole dimers when changing the angle between dipole moments. We obtain a super-radiant mode when the dipole moments of both dipoles are pointing in the same direction because the field radiated by the equivalent dipoles interfere constructively (collectively) in the far-field. Conversely, we obtain sub-radiant modes when dipole moments are pointing in opposite direction.



We observe that the mode "+" has an eigenfrequency $\tilde{\omega}_+$ close to $\tilde{\omega}_A$ , while its eigenvectors consist of the mode of $A$ plus a small contribution of $B$. This can be summarized as mode "+" being $A$ perturbed by $B$. Conversely, mode "−" is $B$ perturbed by $A$. A second peculiar observation is the fact that the shift of the eigenfrequencies of the coupled system now scales as $K^2$ instead of $K$ for the homodimer.

We present in Fig. 3.3 calculations for aligned and parallel dipoles, with $\tilde{\omega}_A = (2.1 + 0.12i) \times 10^{15}$ rad/s and $\tilde{\omega}_B = (2.4 + 0.12i) \times 10^{15}$ rad/s and oscillator strength $\beta = 0.12$ C/kg. Since we solve exactly Eq.(3.4) by iteratively looking for the poles of the non-linear eigenproblem, we observe additional features not captured by the hybridization rules. First, for short distances $d \ll \lambda$, the frequency shifts and changes in decay rates are increased because of strong near-field dipole-dipole interactions entering in the coupling $K$ (but we are still in the weak coupling regime). Then, for $d > \lambda/2$, we observe that the hybridization rule does not hold anymore as the resonance frequency and decay rates of "+" and "−" start oscillating around the values for $A$ and $B$. This comes from the fact that the phase of $K$ contains retardation effects due to the propagation of light between $A$ and $B$. As $d$ increases even further, the asymptotic behaviour of the change in linewidth is slower than the frequency shift. This is due to the fact that the frequency (energy) shift is mostly due to near-field, "static" interactions, whereas the change in linewidth is related to "dynamic" radiation loss. This radiation loss is directly linked to the interference between the fields radiated by $A$ and $B$ in all direction in space. As the distance $d$ increases, this interference averaged out over all direction in space eventually drops to 0. Therefore the total radiated power converges towards the incoherent sum of the radiation of $A$ and $B$, causing the decay rate to converge to the rate of a single dipole. The extent of this mid/far field effect is on the order of $\approx \lambda/2$, larger than the range of near-field interaction. The asymptotic behaviour in decay rates also differs between aligned and parallel dipoles. Indeed, longitudinal electric fields cannot propagate in free

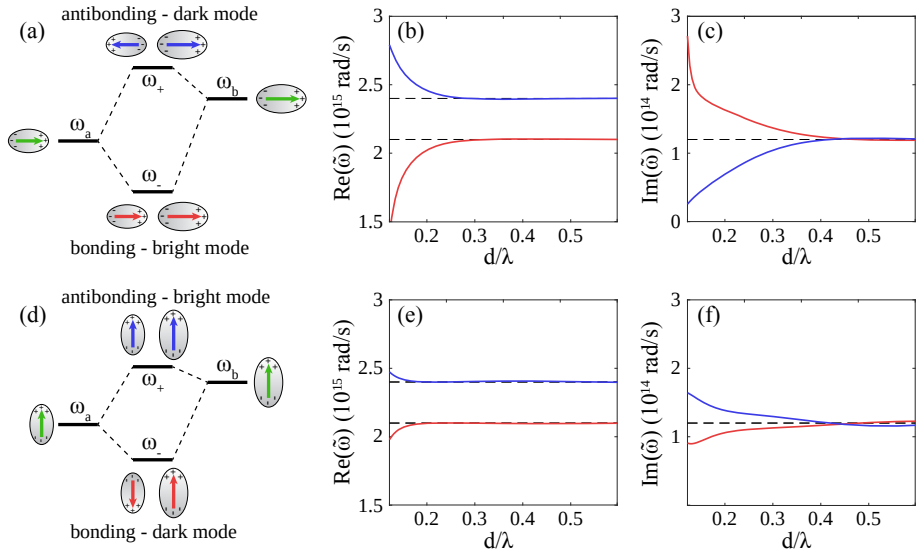


**Figure 3.3:** Coupling of two point dipoles. (a,d) Hybridization diagram. (b,e) Resonance frequencies (or energies) and (c,f) decay rates of the bonding (red) and anti-bonding (blue) modes as a function of the distance between the dipole. Top panels are for aligned dipoles, bottom ones for parallel dipoles. The numerical data is obtained by solving the non-linear eigenproblem of Eq.(3.4), for initial energies equal to $\tilde{\omega}_A = (2.1 + 0.12i) \times 10^{15}$ rad/s, $\tilde{\omega}_B = (2.4 + 0.12i) \times 10^{15}$ rad/s, i.e. resonant at $\approx 890$ and $\approx 780$ nm, and an oscillator strength $\beta = 0.12$ C/kg. We define $\lambda \equiv \pi c/\omega_A + \pi c/\omega_B$.

space. However, for symmetry reasons, two align dipoles can only interact via longitudinal fields, and parallel via transverse fields. Therefore, there cannot be any long range (far-field) interaction for aligned dipoles, whereas these interactions are maximum for parallel dipoles.

### 3.2.2. Coupled QNM theory

In the previous subsection, we recalled the classical formalism for studying the hybridization of two electric-dipole oscillators. We here employ a similar approach to derive a coupled quasinormal modes (QNM) theory to find the hybridized modes of an assembly of arbitrary resonators immersed in the same background material of homogeneous and isotropic permittivity $\epsilon_b$.

Figure 3.4 sketches the mathematical formulation of the scattering by two coupled resonators. The resonators are excited by an arbitrary driving field $\mathbf{E}_{dr,A/B}$. Additionally to this external driving field, the QNM $i$ of resonator $A$ is driven by the field scattered by the normalized field $\tilde{\mathbf{E}}_j^B$ of the QNM $j$ of resonator $B$ with a certain (complex) weight $\beta_j^B$. The total fields driving a

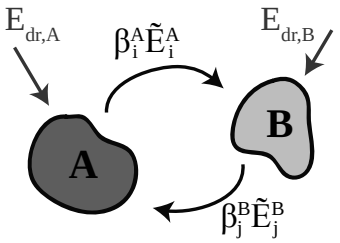


**Figure 3.4:** Sketch of the bidirectional interaction between two resonators described QNM. The resonators are driven by an external source and they scatter onto each other a field proportional to a superposition normalized QNMs (here we only indicate QNM $i$ for $A$ and $j$ for $B$).



QNM $i$ of $A$, is therefore

$$\mathbf{E}'_D = \sum_{j\in B} \beta_j^B \tilde{\mathbf{E}}_j^B + \mathbf{E}_D. \tag{3.11}$$

Similarly, the field driving each mode $j$ of $B$ will be a sum of the contributions by the QNM $i$ of $A$ and the external driving field.

Most materials can be described by a multi-pole Lorentz-Drude permittivity [189, 190]. Assuming a single pole, the permittivity can be written

$$\epsilon^X(\omega) = \epsilon_\infty^X - \epsilon_\infty^X \frac{\omega_p^2}{(\omega^2 - \omega_0^2 - i\omega\gamma_0)} \equiv \epsilon_\infty^X + \epsilon_L^X(\omega), \tag{3.12}$$

with $\omega_p$ the plasma frequency, $\omega_0$ the resonance frequency and $\gamma_0$ the damping rate of the material. Following Ref. [134] where the QNM eigenproblem is linearized by considering auxiliary fields[1], the excitation coefficient of a QNM $i$ of a resonator $X$, with normalized field $\tilde{\mathbf{E}}_i$ and complex resonance frequency $\tilde{\omega}_i$, driven by a field $\mathbf{E}_D$, is given by

$$\beta_i^X(\omega, \mathbf{E}_D) = \iiint_X \tilde{\mathbf{E}}_i^X(\mathbf{r}) \cdot \left( \frac{-\tilde{\omega}_i}{\omega - \tilde{\omega}_i} \left[ \epsilon^X(\tilde{\omega}_i) - \epsilon_b \right] + \left[ \epsilon_b - \epsilon_\infty \right] \right) \mathbf{E}_D(\omega, \mathbf{r})\, d\mathbf{r}, \tag{3.13}$$

where the integral runs over the volume of resonator $X$. The present formula implicitly assumes homogeneous resonators made of single material, but can straightforwardly be extended to more general structures (like core-shell resonators).

Equations (3.13 and 3.11) applied to every QNM of each resonators give us

[1] The linearization has important consequences on the orthogonality and completness of the QNM basis.

the system of equations

$$\begin{cases} \beta_i^A & = \iiint_A \tilde{\mathbf{E}}_i^A \cdot \left( \dfrac{-\tilde{\omega}_i^A}{\omega - \tilde{\omega}_i^A} \left[ \epsilon^A(\tilde{\omega}_i^A) - \epsilon_b \right] + \left[ \epsilon_b - \epsilon_\infty^A \right] \right) \left( \sum_{i \in A} \beta_j^B \tilde{\mathbf{E}}_j^B + \mathbf{E}_D \right) d\mathbf{r} \\ & \vdots \\ \beta_j^B & = \iiint_B \tilde{\mathbf{E}}_j^B \cdot \left( \dfrac{-\tilde{\omega}_j^B}{\omega - \tilde{\omega}_j^B} \left[ \epsilon^B(\tilde{\omega}_j^B) - \epsilon_b \right] + \left[ \epsilon_b - \epsilon_\infty^B \right] \right) \left( \sum_{j \in B} \beta_i^A \tilde{\mathbf{E}}_i^A + \mathbf{E}_D \right) d\mathbf{r} \\ & \vdots \end{cases} . \tag{3.14}$$

For a more compact notation, we isolate the offset term and the dispersive part $\epsilon^X(\omega) = \epsilon_\infty^X + \epsilon_L^X(\omega)$ in the Lorentz-Drude model, and use the definitions

$$\begin{cases} \Delta\epsilon_\infty^X & \equiv \epsilon_\infty^X - \epsilon_b \\ \Delta\epsilon_L^X(\omega) & \equiv \epsilon_L^X(\omega) - \epsilon_b, \end{cases} \tag{3.15}$$

and equation 3.14 becomes

$$\begin{cases} (\omega - \tilde{\omega}_i^A)\beta_i^A & = \iiint_A \tilde{\mathbf{E}}_i^A \cdot \left( -\tilde{\omega}_i^A \Delta\epsilon_L^A(\tilde{\omega}_i^A) - \omega\Delta\epsilon_\infty^A \right) \left( \sum_{j \in B} \beta_j^B \tilde{\mathbf{E}}_j^B + \mathbf{E}_D \right) d\mathbf{r} \\ & \vdots \\ (\omega - \tilde{\omega}_j^B)\beta_j^B & = \iiint_B \tilde{\mathbf{E}}_j^B \cdot \left( -\tilde{\omega}_j^B \Delta\epsilon_L^B(\tilde{\omega}_j^B) - \omega\Delta\epsilon_\infty^B \right) \left( \sum_{i \in A} \beta_i^A \tilde{\mathbf{E}}_i^A + \mathbf{E}_D \right) d\mathbf{r} \\ & \vdots \end{cases} . \tag{3.16}$$

This system is equivalent to Eq.(3.4) in the case of points dipoles.

We are interested in finding the hybridized QNMs of the coupled system, therefore we look for eigen-solutions, without driving field, of equation 3.16. We recognize a generalized linear eigenvalue problem for the eigenfrequency $\tilde{\omega}_n$ and eigenvectors $\left(\tilde{\boldsymbol{\beta}}^A; \tilde{\boldsymbol{\beta}}^B\right)_n$ of a hybridized QNM $n$

$$\begin{bmatrix} \boldsymbol{\Omega}^A & -\boldsymbol{\Omega}^A \boldsymbol{\Delta\epsilon}_L^A \langle \mathbf{A}|\mathbf{B}\rangle \\ -\boldsymbol{\Omega}^B \boldsymbol{\Delta\epsilon}_L^B \langle \mathbf{B}|\mathbf{A}\rangle & \boldsymbol{\Omega}^B \end{bmatrix} \begin{pmatrix} \tilde{\boldsymbol{\beta}}^A \\ \tilde{\boldsymbol{\beta}}^B \end{pmatrix}_n = \tilde{\omega}_n \begin{bmatrix} \mathbf{1} & \Delta\epsilon_\infty^A \langle \mathbf{A}|\mathbf{B}\rangle \\ \Delta\epsilon_\infty^B \langle \mathbf{B}|\mathbf{A}\rangle & \mathbf{1} \end{bmatrix} \begin{pmatrix} \tilde{\boldsymbol{\beta}}^A \\ \tilde{\boldsymbol{\beta}}^B \end{pmatrix}_n . \tag{3.17}$$

where we assumed isotropic materials to factorize the overlap integrals, and

introduced the matrix notations

$$\begin{cases} (\tilde{\boldsymbol{\beta}}^X)_n & \equiv \begin{pmatrix} \tilde{\beta}_i^X \\ \vdots \end{pmatrix}_n \\ \boldsymbol{\Omega}^X & \equiv \mathrm{diag}\left\{\tilde{\omega}_i^X\right\}_{i\in X} \\ \boldsymbol{\Delta\epsilon}_L^X & = \mathrm{diag}\left\{\Delta\epsilon_L^X(\tilde{\omega}_i^X)\right\}_{i\in X} \\ \langle \mathbf{X}|\mathbf{Y}\rangle_{i,j} & \equiv \iiint_X \tilde{\mathbf{E}}_i^X \cdot \tilde{\mathbf{E}}_j^Y \, d\mathbf{r}. \end{cases}$$

This equation is similar Eq.(3.5), with an additional matrix on the right hand side of the system. As it was the case for point dipoles, the coefficients of the matrix of the system are complex, accounting for losses, and retardation effects in open electromagnetic systems. We however also observe that since in the general case $\langle \mathbf{X}|\mathbf{Y}\rangle_{i,j} \neq \langle \mathbf{Y}|\mathbf{X}\rangle_{j,i}$, the system has no particular symmetry properties.

With such a formulation, we implicitly make the hypothesis that the electromagnetic field of a new hybridized QNM $n$ at all points in space, outside of $A$ and $B$, is a linear combination of the different original QNM $i$ of $A$ and $j$ of $B$, weighted by the coefficients $\beta_{i\to n}^A$ and $\beta_{j\to n}^B$ specific for this hybridized QNM $n$

$$\begin{bmatrix} \tilde{\mathbf{E}}_n \\ \tilde{\mathbf{H}}_n \end{bmatrix} = \sum_{i\in A} \tilde{\beta}_{i\to n}^A \begin{bmatrix} \tilde{\mathbf{E}}_i^A \\ \tilde{\mathbf{H}}_i^A \end{bmatrix} + \sum_{j\in B} \tilde{\beta}_{j\to n}^B \begin{bmatrix} \tilde{\mathbf{E}}_j^B \\ \tilde{\mathbf{H}}_j^B \end{bmatrix}. \tag{3.18}$$

We further assume that the field inside $A$ and $B$ is solely described by respectively the QNMs of $A$ and $B$ since the QNM basis is complete inside the resonators [126–128, 191]. This hypothesis is relevant in subsection 3.2.5.

The problem we derive here is similar to the formulation of Ref. [138]. In their work, Vial et al. indeed derive directly from Maxwell equations, with an outgoing wave condition, a generalized eigenproblem by solely assuming that the hybrid QNMs are linear combinations of uncoupled QNMs. We use the same assumption in Eq.(3.18), however, in addition, we make an assumption on the expression of the coupling coefficients between QNMs which enter Eq.(3.17). Both the work of this chapter and the work of Vial et al. require to perform overlap integrals between the QNM fields of $A$ and $B$. However, our formulation conveniently only requires the perform these integrals over the volumes of the resonators, whereas in [138] they run over the whole space. In a practical numerical implementation, this means that the formulation of Vial et al. requires integration over the full simulation domain including numerical perfectly matched layers (PMLs), and relies completely on the fact that the modes of the two resonators are calculated on the exact same mesh. In this chapter, we also use the same mesh for the two resonators, but only as a convenience to take advantage of the very efficient numerical integration methods programmed in the finite element method software COMSOL.

Additionally, the formulation of Vial et al. requires the material to be non-dispersive to define an inner product to project the hybridized QNMs onto to the original QNMs. Our formulation does not have this restriction, but requires an assumption presented in the following subsection.

### 3.2.3. Normalization of the hybrid states

To fully exploit the effectiveness of our approach, one should not only find the hybridized QNMs of the coupled system, but also normalize these QNMs in order to predict the response of the hybridized system to a driving field. Indeed, the QNM field expressed in Eq.(3.18) is not normalized if the coefficients $\tilde{\beta}^A_{i\to n}$ and $\tilde{\beta}^B_{j\to n}$ are not normalized. We therefore attempt to define a normalization condition based on algebraic properties of the eigenproblem that we solve in Eq.(3.17). Generalized eigenproblems can, in practical situations, always be diagonalized. However, an orthogonality relationship does not always exist. Instead, a bi-orthogonality relationship can be defined using left and right eigenvectors for each hybridized QNM $n$. The right (column) eigenvectors $\begin{pmatrix}\tilde{\beta}^A\\ \tilde{\beta}^B\end{pmatrix}_n$ are directly obtained by solving Eq.(3.17) :

$$\mathbf{M}\begin{pmatrix}\tilde{\beta}^A\\ \tilde{\beta}^B\end{pmatrix}_n = \tilde{\omega}_n \mathbf{C}\begin{pmatrix}\tilde{\beta}^A\\ \tilde{\beta}^B\end{pmatrix}_n, \tag{3.19}$$

where we introduce matrices $\mathbf{M}$ and $\mathbf{C}$ for compact notations. The left (line) eigenvectors $(\tilde{\xi}^A \quad \tilde{\xi}^B)_n$ are however solution of the transposed problem

$$(\tilde{\xi}^A \quad \tilde{\xi}^B)_n \mathbf{M} = \tilde{\omega}_n (\tilde{\xi}^A \quad \tilde{\xi}^B)_n \mathbf{C}. \tag{3.20}$$

The bi-orthogonality relationship between hybridized modes $n$ and $m$ can then be expressed as

$$(\tilde{\xi}^A \quad \tilde{\xi}^B)_m \mathbf{C}\begin{pmatrix}\tilde{\beta}^A\\ \tilde{\beta}^B\end{pmatrix}_n = \delta_{m,n}, \tag{3.21}$$

and serve as a normalization condition for $m = n$. This normalization does not explicitly map onto the normalization introduced by Sauvan [124]. For discretized formulations of Maxwell equations used in any numerical solvers (FEM, FDFD, RCWA,...), we believe that it can be shown that when one uses the complete basis of all QNMs of both resonators, the normalization of Eq.(3.21) converges towards Sauvan's normalization.

### 3.2.4. Truncation of the basis: one QNM for $A$ and $B$

Using the complete basis of QNM to describe each resonator is not only cumbersome, but in practice impossible as it requires to calculate as many QNMs as there are degrees of freedom in the numerical model [134]. Additionally, the

main purpose of developing a coupled QNM theory is that one expects to gain physical insight in a coupled system on basis of just the main resonances of the constituent building blocks. While in this work we were able to perform computations with the order of a few hundred QNMs (400 in this chapter), it is of particular use to consider the simplest case of just two objects, each described with just one QNM. This simple case has an elegant mapping back onto the case of two resonant coupled dipoles (cf. subsection 3.2.1). In the case of one QNM per resonator, we obtain a $2 \times 2$ generalized linear eigenproblem

$$\begin{bmatrix} \tilde{\omega}^A & -\tilde{\omega}^A \Delta\epsilon_L^A(\tilde{\omega}^A)\langle A|B\rangle \\ -\tilde{\omega}^B \Delta\epsilon_L^B(\tilde{\omega}^B)\langle B|A\rangle & \tilde{\omega}^B \end{bmatrix} \begin{pmatrix} \beta^A \\ \beta^B \end{pmatrix} = \omega \begin{bmatrix} 1 & \Delta\epsilon_\infty^A \langle A|B\rangle \\ \Delta\epsilon_\infty^B \langle B|A\rangle & 1 \end{bmatrix} \begin{pmatrix} \beta^A \\ \beta^B \end{pmatrix}. \quad (3.22)$$

This equation differs from Eq.(3.5) by the matrix on the left side of the equation. Note however that the anti-diagonal terms of the right matrix in Eq.(3.22) are usually negligible. Indeed, for frequencies $\omega$ far below the plasma frequency $\omega_p$ (metallic behaviour), a simple analysis of the Lorentz-Drude model shows that $|\Delta\epsilon_\infty^X \langle X|Y\rangle| \ll |\Delta\epsilon_L^X(\omega)\langle X|Y\rangle| \ll 1$.

To draw the comparison with the case of a two coupled identical dipoles studied in subsection 3.2.1, we simplify Eq.(3.22) by assuming a symmetric homodimer. We therefore assume $\tilde{\omega}^A = \tilde{\omega}^B \equiv \tilde{\omega}_0$, $\epsilon^A = \epsilon^B \equiv \epsilon$ and the overlap integrals in Eq.(3.22) are identical $\langle A|B\rangle = \langle B|A\rangle \equiv K$, which straight-forwardly exactly leads to the eigenfrequencies

$$\begin{cases} \tilde{\omega}^+ = \tilde{\omega}_0 \dfrac{1 + \Delta\epsilon_L(\tilde{\omega}_0)K}{1 - \Delta\epsilon_\infty K} \\ \tilde{\omega}^- = \tilde{\omega}_0 \dfrac{1 - \Delta\epsilon_L K(\tilde{\omega}_0)}{1 + \Delta\epsilon_\infty K}, \end{cases} \quad (3.23)$$

and the associated normalized eigenvectors

$$\begin{cases} (\tilde{\beta}_A\,;\tilde{\beta}_B)_+ = \frac{1}{\sqrt{2}}(1\,;-1) \\ (\tilde{\beta}_A\,;\tilde{\beta}_B)_- = \frac{1}{\sqrt{2}}(1\,;+1). \end{cases} \quad (3.24)$$

We find very similar expressions as in the case of two identical point dipoles in Eqs.(3.7 and 3.8). Here again, the sign of the real and imaginary part of $\Delta\epsilon_L(\tilde{\omega}_0)K$ prescribes the hybridization rule between the two resonators. We note that the presence of a denominator in the hybridized eigenfrequencies $\tilde{\omega}_\pm$ in Eq.(3.23) suggests that the new resonance frequencies and decay rates are not completely symmetric with respect to the uncoupled QNM. However, the effect of this denominator is negligible in virtue of the discussion on the left matrix in Eq.(3.22). Furthermore, in Eq.(3.7), taking into account the frequency dependence of the Green function $G_0$ would also lead to an asymmetric shift

in the complex eigenfrequencies of the hybridized modes, related to a change in the retardation phase between dipoles as the resonance wavelength shifts.

### 3.2.5. Excitation coefficients

Once the hybridized QNMs of the coupled systems are known and normalized, they can be used to calculate observables, such as extinction cross sections and Purcell factors. This endeavour requires to calculate excitation coefficients of the hybridized QNM. We assume that these coefficients can still be calculated using Eq.(3.13), with the overlap integral between driving field and normalized QNM running over both resonators $A$ and $B$

$$b_n(\omega,\mathbf{E}_D) = \iiint_{A\cup B} \tilde{\mathbf{E}}_n(\mathbf{r})\cdot\left(\frac{-\tilde{\omega}_n}{\omega-\tilde{\omega}_n}\left[\epsilon^{A\cup B}(\tilde{\omega}_n)-\epsilon_b\right]+\left[\epsilon_b-\epsilon_\infty^{A\cup B}\right]\right)\mathbf{E}_D(\omega,\mathbf{r})\,d\mathbf{r}. \tag{3.25}$$

To calculate the coupling coefficients, we use the fact that the field for the coupled QNM $n$ in resonator $A$ (resp. $B$) is given by the field in resonator $A$ (resp. $B$) only. Then we obtain

$$b_n(\omega,\mathbf{E}_D) = \sum_{i\in A}\tilde{\beta}^A_{i\to n}\, b^A_{i\to n}(\omega,\mathbf{E}_D) + \sum_{j\in B}\tilde{\beta}^B_{j\to n}\, b^B_{j\to n}(\omega,\mathbf{E}_D), \tag{3.26}$$

with

$$\begin{cases} b^A_{i\to n}(\omega,\mathbf{E}_D) & \equiv \iiint_A \tilde{\mathbf{E}}^A_i(\mathbf{r})\cdot\left(\frac{-\tilde{\omega}_n}{\omega-\tilde{\omega}_n}\left[\epsilon^A(\tilde{\omega}_n)-\epsilon_b\right]+\left[\epsilon_b-\epsilon^A_\infty\right]\right)\mathbf{E}_D(\omega,\mathbf{r})\,d\mathbf{r} \\ b^B_{j\to n}(\omega,\mathbf{E}_D) & \equiv \iiint_B \tilde{\mathbf{E}}^B_j(\mathbf{r})\cdot\left(\frac{-\tilde{\omega}_n}{\omega-\tilde{\omega}_n}\left[\epsilon^B(\tilde{\omega}_n)-\epsilon_b\right]+\left[\epsilon_b-\epsilon^B_\infty\right]\right)\mathbf{E}_D(\omega,\mathbf{r})\,d\mathbf{r}. \end{cases} \tag{3.27}$$

Note that the coefficients $\tilde{\beta}^X_{i\to n}$ are describing the eigenmodes of the hybridized QNM $n$ and therefore do not depend on the frequency $\omega$ or the driving field $\mathbf{E}_D$. The coefficients $b^X_{i\to n}$, on the other hand, quantify the coupling of each uncoupled QNMs of $A$ and $B$ with the driving field at a certain frequency. They are however defined for each hybridized QNM $n$ as they contain a resonant term at $\tilde{\omega}_n$ and the permittivity is also evaluated at $\tilde{\omega}_n$ [134].

## 3.3. Numerical implementation

In this section, we first test the predictive force of the coupled QNM theory to predict complex eigenfrequencies, i.e. energies and decay rates, of hybridized QNMs in the case of a symmetric homodimer composed of two identical aligned gold nanorods. We confront the predictions to the intuition on the hybridization of dipoles gathered from subsection 3.2.1. Then we

demonstrate the capacity of our formalism to predict the usual observables upon excitation of coupled resonators. We take the example of gold nanorod hetero- or homodimers in different arrangements, and compare the model predictions for the extinction of plane-waves with exact calculations. Finally, we show that the coupled QNM theory is relevant in the context of oligomers, i.e. assemblies composed of more than two resonators, in the particular case of a four-nanorods assembly studied in Ref. [87].

### 3.3.1. Symmetric homodimer



To test the validity of our formalism, we start by considering a homodimer composed of two identical gold cylindrical nanorods with spherical apex (90 nm long, 30 nm diameter), aligned along their long axis as sketched in Fig. 3.5(a). The background medium is water ($\epsilon_b = 1.33^2$) and we take a Drude model $\epsilon(\omega) = \epsilon_\infty - \epsilon_\infty \omega_p^2/\omega(\omega - i\gamma_d)$ for gold with parameters, with $\epsilon_\infty = 1$, $\omega_p = 1.26 \times 10^{16}$ rad/s, $\gamma_d = 1.41 \times 10^{14}$ rad/s. Such a system is described by the simplified formalism presented in subsection 3.2.4.

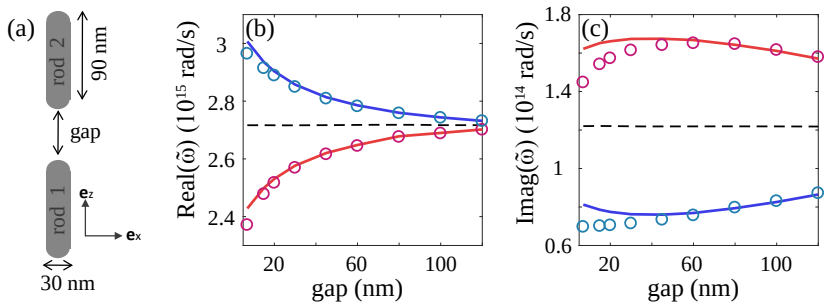


**Figure 3.5:** Test of the coupled QNM theory (Eq.(3.23)) for symmetric gold nanorod dimer. (a) We couple two identical gold nanorods (90 nm long, 30 nm diameter), separated by a small gap measured between nanorods' apices. (b) Real part of the complex resonance frequency $\tilde{\omega}_-$ and $\tilde{\omega}_+$ of resp. the bonding (red) and anti-bonding (blue) modes of the homodimer. Circles are exact values from simulation, solid lines are predictions by Eq.(3.23). (c) Imaginary part of the complex resonance frequencies (i.e. decay-rate). We observe for both real and imaginary part of the complex frequencies a good agreement between prediction and exact values. For smaller gaps however the agreement is degraded.

We vary the gap separation and for each separation, we study the hybridization of the dipolar modes of the two nanorods by calculating the exact complex resonance frequency of two hybridized modes. In this section, all QNMs are calculated and normalized using the finite element method (FEM) software COMSOL, according to the method described in Ref [132]. We then compare with the predictions of Eq.(3.23), as shown in Fig. 3.5(b,c). To mitigate numerical errors when performing overlap integrals, we compute the QNMs of the two uncoupled nanorods, as well as the two hybridized QNMs on the

exact same numerical mesh, thereby recalculating all four QNMs for every gap value. As expected, the dipole modes of nanorods hybridize the same way as aligned point dipoles, i.e. with a lower energy, superradiant bonding mode and a higher energy, subradiant anti-bonding mode. Already for the case of simple point dipoles in Fig. 3.3 we saw that, as the distance between dipoles is increased, the asymptotic behaviour of the resonance frequency of the hybridized mode converges faster towards the values for uncoupled dipoles than the decay rates. We assign this to the fact that the shift in energy of the modes is related to near-field interactions, whereas the change in loss rates is related to interference effects with longer range interaction. This observation is even more stringent in the case of two nanorods as can

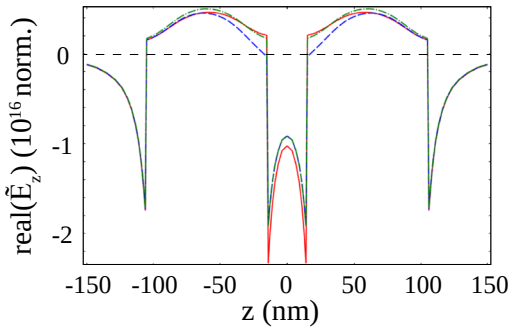


**Figure 3.6:** Normalized electric field (z-component) for the bonding bright QNM formed when coupling two nanorods (same parameters as Fig. 3.5) with a gap of 30 nm. Solid red line is the exact normalized field (Sauvan normalization [124]), dashed lines are normalized with Eq.(3.21). Green assumes the field is a linear superposition everywhere in space (Eq.(3.18)), where blue assumes that the field inside each resonator is only described by the uncoupled QNM.

be seen by comparing Figs. 3.5(b) and (c). Indeed, in the case of a point dipole, the near-field interaction always scales as the inverse of the separation to the cube. In the case of a plasmonic resonators on the other hand, this interaction, mediated by surface plasmons, decreases exponentially with the distance to the interface metal/glass for small distances. Finally, we observe a very good agreement between Eq.(3.23) and the exact result for gap separation larger than 20 nm. Interestingly, as the gap is reduced to values smaller than 40 nm, the decay rate of the bright mode starts decreasing, and conversely the decay rate of the dark mode increases. This observation is assumed to be related to retardation effects averaged over the non-negligible length of the nanorods (90 nm $\approx \lambda/8$), and was not observed in the point dipole model (cf. subsection 3.2.1). Even-though Eq.(3.23) is not quantitative for such small gaps, it does predict qualitatively this inflection of the variation of decay-rates for small gaps. This means that the QNM formalism captures all the physics of the hybridization of realistic resonators, in particular the prediction of decay

rates, which is inaccessible to quasi-static theories [182]. Note that, in virtue of the discussion on the denominators in Eq.(3.23), since $\Delta\epsilon_L(\tilde{\omega}_0) = -23.2 + 0.81i$ and $\Delta\epsilon_\infty = 0.77$, we do not predict a significant asymmetry between $\tilde{\omega}_+$ and $\tilde{\omega}_-$.

Figure 3.6 compares the exact normalized electric field ($z$-component) of the bonding bright mode for a gap of 30 nm. The normalized mode is well reproduced except in the nanogap, and inside the resonators, in the proximity of the nanogap. The fact that the predictions are better for larger gaps and worsen for smaller gaps relates to the fact that we only use two QNMs in the expansion. Indeed, it is well known from, e.g. generalized Mie calculations [178] for dimers of spheres, that large field gradients that occur in small gaps involve higher order multipolar terms. We expect by analogy that strong field gradients in dimers require inclusion of higher order QNMs. In Section 3.4 we will return to this issue, as we consider the convergence of the field in the gap of a dimer as a function of the number of QNMs.



### 3.3.2. Response of hybridized QNMs to a driving field

In this subsection, we show that the normalized coupled-QNMs estimated with the coupled QNM theory can also be used to predict extinction properties of the system upon plane wave illumination.

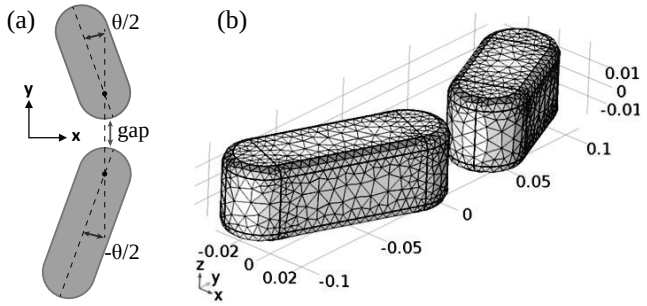


**Figure 3.7:** Geometry of the gold nanorods dimer used for numerical tests. (a) Parametrization of the dimers. Nanorods are 40 nm thick and wide. Their length is chosen to be 90 or 120 nm. We use a Drude model for gold (same parameters as in subsection 3.2.4), the background is homogeneous water ($\epsilon_b = 1.33^2$). The geometry is parametrized by a gap which is defined as the minimal distance between the two nanorods, and an angle $\theta$ between the long axis of the rods. (b) Typical mesh used, denser at edges, to improve stability and also accuracy of FEM simulations using COMSOL.

We test the formalism on homodimers and heterodimers composed of rectangular gold nanorods with cylindrical apex. We use the same Drude model as in subsection 3.2.4, and the nanorods are immersed in water of permittivity $\epsilon_b = 1.33^2$. The geometry is sketched in Fig. 3.7; the width and height of the gold nanorods is fixed to 40 nm, and we use two 90 nm long nanorods for

homodimers, and a 90 and 120 nm long nanorods for heterodimers. To move away from the aligned configuration studied in Section 3.2 with point dipoles and nanorods, we change the geometry by allowing for angle $\theta$ of 0, 90 or 180° between nanorods, and a gap of 20 or 60 nm.

We study the extinction of a plane wave at normal incidence ($z$-direction) with right handed circular polarization. We proceed by first computing the dipolar QNM of both nanorods as in subsection 3.2.4 as input to solve Eq.(3.22) for eigenvalue and eigenvectors. Then we normalize the two hybridized QNMs using the condition Eq.(3.21), and calculate the excitation coefficients $b_\pm$ of the two new QNMs by the plane wave $\mathbf{E}_D$ with Eq.(3.26), and finally calculate the extinction cross section $\sigma_{ext}$ via formulas established in [132]

$$\sigma_{ext}(\omega) = -\frac{\omega}{2S_0}\iiint_{A\cup B} \mathrm{Im}\left\{\Delta\epsilon^{A\cup B}(\omega)\,(\mathbf{E}_D+\mathbf{E}_S)\cdot\mathbf{E}_D^*\right\} d\mathbf{r}, \tag{3.28}$$

where $S_0$ is the intensity of the incident plane wave. The scattered field $\mathbf{E}_S$ decomposed over the two hybridized QNMs obtained from Eq.(3.18)

$$\mathbf{E}_S(\omega,\mathbf{r}) = b_+(\omega)\cdot\tilde{\mathbf{E}}_+(\mathbf{r}) + b_-(\omega)\cdot\tilde{\mathbf{E}}_-(\mathbf{r}). \tag{3.29}$$

**Case of a heterodimer**

We first consider the case of a heterodimer. We choose the sizes of the two nanorods such that the frequency detuning allows us to be in the weak coupling regime (cf. subsection 3.9). Figure 3.8 summarizes COMSOL simulations and the predictions of the coupled QNM theory for different configurations.

Let us first discuss the general trends. A first point is that since we are in the weakly coupled regime, the hybridized modes can be thought of as perturbation of the uncoupled QNMs. This explains why a gap changed from 20 to 60 nm does not seem to have a strong influence on the spectral position and intensity of the peaks. A second observation, related to radiative properties of the hybridized modes, is that for 0°, the red mode has a much stronger extinction cross section than the blue mode. This is due to the superradiant and subradiant properties of, respectively, the red and blue modes. From a purely mathematical point of view, this difference in extinction properties comes from the fact that the overlap integral between a homogeneous field, the plane wave, and the hybridized subradiant mode, with normalized field in resonators $A$ and $B$ pointing in opposite directions, is smaller than the overlap with superradiant modes for which the fields inside resonators $A$ and $B$ point in the same direction.

**Case of a homodimer**

We now move on to the case of a homodimer composed of two nanorods of 90 nm length. Figure 3.9 summarizes the simulation results obtained for the

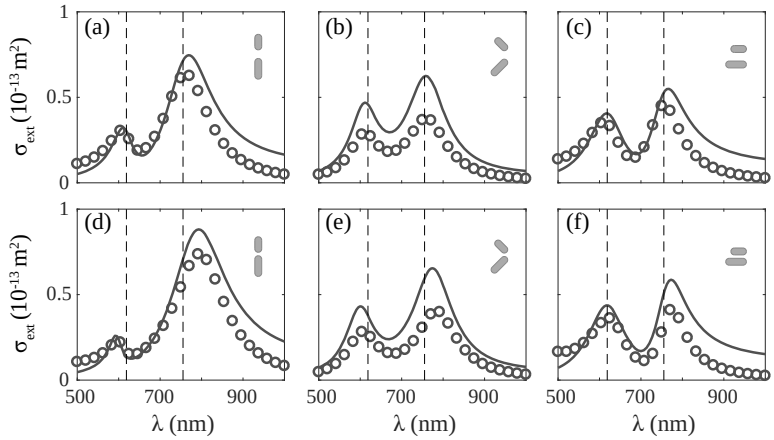


**Figure 3.8:** Extinction cross section of different heterodimers, illuminated by a plane wave with right handed circular polarization at normal incidence ($z$ direction). (a-c) Gap is fixed to 60 nm and the angle $\theta$ is respectively 0, 90 and 180°. (d-f) Gap is fixed to 20 nm. In all plots, circles are exact data, and solid lines are predictions with the coupled QNM theory. Vertical dashed lines indicate the original resonance frequencies of the uncoupled nanorods. We observe a qualitative agreement between prediction and exact calculation.

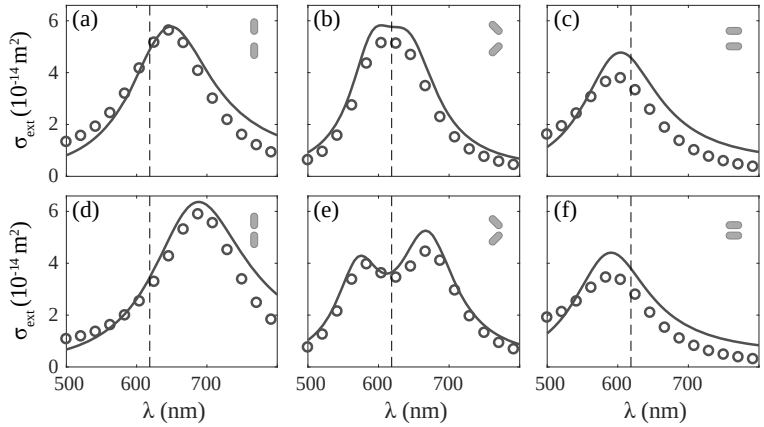


**Figure 3.9:** Same as in the caption of Fig. 3.8, here for the homodimer case.

same configuration and illumination as in subsection 3.3.2. A first observation is that the resonance frequency of the hybridized modes depends much more strongly on the gap size than in the case of the heterodimer presented in Fig. 3.8. This is directly related to an observation we made in subsection 3.2.1, where the shifts of hybridized modes scale as $K$ for homodimer (or a heterodimer in the strong coupling regime), but as $K^2$ for heterodimer in the

weak coupling regime. A second important observation is the fact that for angles 0 and 180°, we obtain a single extinction peak. Indeed, because of incompatible symmetry properties between the QNM field and the excitation, a plane wave at normal incidence cannot couple to the anti-bonding mode. For angle 90°, the red and blue modes can both radiate as they possess a net dipole, respectively along the $y$ and $x$ axis as can be observed in Fig. 3.2. Therefore, a circularly polarized plane wave can couple to both modes, and we obtain two extinction peaks. The theoretical predictions are more accurate than those obtained for the heterodimer. We assign this to the fact that, in the case of the heterodimer, the dipolar modes couple less to each other than for the homodimer. The coupling of the dipolar QNM to higher order QNMs is however of the same strength as in the heterodimer case, therefore reducing the relative importance of these higher order modes in the hybridization for the homodimer, and thereby the error made by neglecting them.



**Predictions for different excitations**

One of the strengths of quasinormal mode formalism is that the knowledge of the QNMs of a resonator enables us to analytically recalculate the response of the system to any excitation without having to rerun any computationally heavy simulation. We demonstrate this property by changing the angle of the polarization of the incident plane wave. The treatment is indeed straightforward once the hybridized QNMs of the system have been found and normalized. We show in Figure 3.10, for a fixed geometry of the homodimer (gap of 20 nm, angle of 135°), that the coupled QNM theory accurately reproduces the response of the assembly as we vary the angle of the linear polarization of the normally incident plane wave. As explained earlier (Fig. 3.2), for angles $\theta$

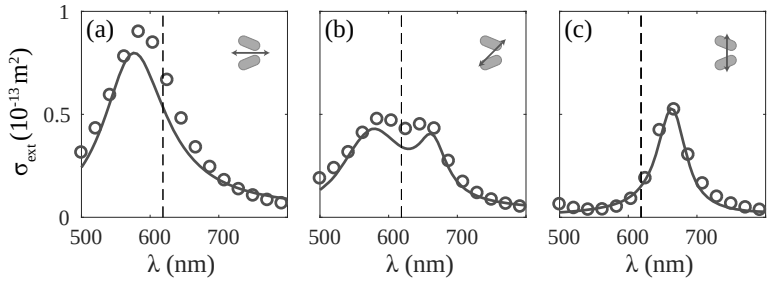


**Figure 3.10:** Extinction cross section of a homodimer for an incident plane wave polarized along the $z$-direction. The gap is 20 nm, and the angle is 135°. (a-c) The angle of the polarization is respectively 0, 45 and 90° with the $x$-axis. In all plots, circles are exact calculations, and solid lines are predictions by the coupled QNM theory. Vertical dashed line indicate the original resonance of uncoupled nanorods. We observe a qualitative agreement between prediction and exact calculation.

that are different than 0 and 180°, the bonding mode has a net dipole moment aligned with the $x$-axis, and the anti-bonding mode has a net dipole moment

aligned with the $y$-axis. Therefore, for a plane wave illumination linearly polarized along the $x$-axis, we only observe a single peak for the red mode, and for $y$-polarized illumination, we only observe the blue mode. We also note that, since the blue anti-bonding mode is subradiant, the related extinction peak under optimum polarization ($x$ direction) has a smaller magnitude, but is also narrower than the superradiant red mode (which is optimum for $y$-polarized light). A 45° polarized plane wave excites both blue and red modes. The coupled QNM theory predicts all these observations.



### 3.3.3. Application to oligomers

Apart from a notable gain in computation time, an operational coupled QNM theory could be a powerful tool for the design of complex ensembles of nanoresonators also known as *oligomers*. The formulation of coupled QNM theory in Eq.(3.17) can easily be extended to account for several resonators by adding a new diagonal block $\mathbf{\Omega}^X$ for each additional resonator $X$, and off-diagonal blocks $\Delta\epsilon_\infty^X \langle \mathbf{X}|\mathbf{Y}\rangle$ and $-\mathbf{\Omega}^X \mathbf{\Delta\epsilon}_L^X \langle \mathbf{X}|\mathbf{Y}\rangle$ containing the cross-terms (coupling) between all the QNMs of all the resonators of the assembly.

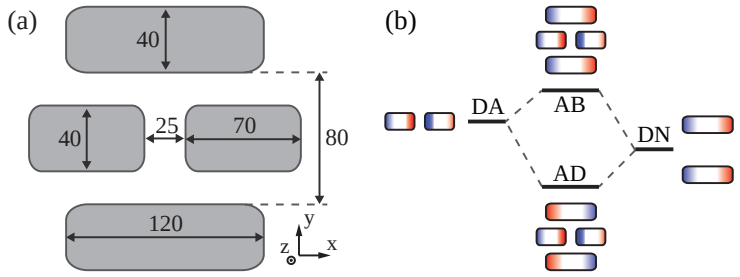


**Figure 3.11:** (a) The oligomer is composed of two pairs of identical nanoresonators [87]. The first pair is composed of two aligned gold nanoantennas. The second pair is composed of two parallel gold nanorods. Dimensions are indicated in nm, thickness is 40 nm for nanorods and antennas. We use a Drude model for gold (same parameters as subsection 3.2.4 and subsection 3.3.2). (b) Hybridization of superradiant modes (DA) and (DN) into the subradiant bonding (AD) and superradiant anti-bonding (AB) modes of the oligomer.

We test our formulation by analysing the oligomer structure studied by Lovera and his coworkers in Ref. [87]. This oligomer is composed of four gold nanorods immersed in water ($\epsilon_b = 1.33^2$) as sketched in 3.11(a). For convenience, the authors of [87] called the shorter nanorods, *nanoantennas*, while keeping the name *nanorods* for the longer ones. In this subsection we use the same designation. The main conclusion in [87] was that the proposed structure exhibits a strong Fano-like resonance in extinction when illuminated under normal incidence. This property is assigned to the interference between the field scattered by two dipole-like modes, one superradiant AB (for "adiabatic bright") and the other subradiant (for "adiabatic dark"). These modes

originate from the hybridization of a superradiant bonding mode DA that would be formed by the two nanoantennas taken as a dimer (DA for "diabatic antenna"), and a superradiant anti-bonding mode DN that would be formed by the two nanorods taken as a dimer (DN for "diabatic nanoantenna"). Figure. 3.11(b) summarizes this hybridization scheme. The approach taken by Lovera et al. to describe the system is however limited to symmetric structures and with normal incidence illumination. This ensures that the equivalent dipoles of DA, DN, AB and AD can be assumed to be located at the same position in space, and it guarantees a real valued coupling parameter $g$ in Lovera's model (no retardation effect). We note that in Ref. [87], the parameters of said model, in particular the oscillator strength of DA and DN, and the coupling parameter $g$ need to be extracted by a phenomenological oscillator-model fit to full wave simulations.



In the simulation, we illuminate the assembly with a $x$-polarized plane wave at normal incidence ($z$ direction). Figures 3.12 (b) and (c), respectively show the exact extinction and absorption cross sections with solid circles. First, a simple QNM decomposition [124], i.e. without applying coupled QNM theory (dashed black line in Fig. 3.12), shows an excellent agreement of the prediction with exact calculations. This confirms the interpretation of Lovera et al. [87] that a Fano-dip occurs in the extinction spectrum and originates from the interference of two resonances (or QNMs).

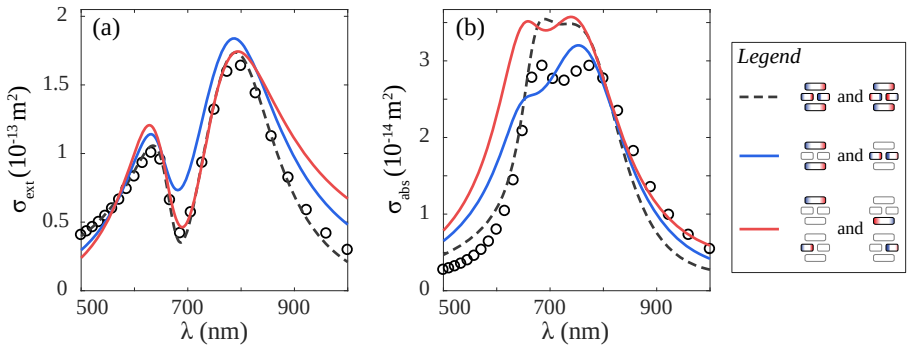


**Figure 3.12:** Extinction and absorption of a plane wave under normal incidence and $y$ linear polarization by an oligomer composed of a pair of nanoantennas and a pair of nanorods. (a) Extinction cross section. (b) Absorption cross section. For (a),(b), black circles are exact values obtained with COMSOL fullwave simulation, solid blue lines are obtained using coupled QNM theory on the DA and DN modes, solid red lines are obtained using the long axis dipole modes of each of the four nanoantennas/nanorods, and black dashed lines are the exact QNM predictions using the exact AD and AB QNM of the oligomer.

Since the system is composed of four resonators, we can study the hybridization of modes from different perspectives. We choose to apply the coupled QNM theory to predict the AD and AB modes with two different

formulations. On the one hand, we built a $2 \times 2$ coupled QNM eigenproblem from the DA and DN modes, and predict the two hybridized QNMs AD and AB as in Ref. [87]. On the other hand, we built a $4 \times 4$ coupled QNM eigenproblem from the dipolar modes of each of the two nanoantennas and nanorods. In this situation, we predict four QNMs; AB and AD, but also two dark modes which do not couple to the plane wave used in the calculation and are therefore irrelevant. We observe that the coupled QNM theory gives a good qualitative agreement with exact calculations for extinction. In particular the relative heights and spectral positions of the Fano peaks are accurately predicted. For the absorption cross section, the accuracy is even comparable to the exact 2-QNMs decomposition (black dashed line), which is the most accurate two mode approximation that can be made for this system. Surprisingly, the Fano dip is better reproduced when using the coupled QNM theory on a more "primitive" level, i.e. using the $4 \times 4$ formulation instead of using DA and DN, and almost as good as the exact 2-QNM decomposition. This is encouraging for the study of broken symmetry Lovera-like structures, which would exhibit multiple Fano-resonance in extinction due to the interference with the additional two modes predicted by the $4 \times 4$ model.



## **3.4.** Going towards a complete description of each resonators

The accuracy of the coupled QNM theory is limited by the number of QNMs used to described each resonator. Recent developments in QNM solvers, in particular QNMeig developped by Yan et al. [134], have made it possible to calculate reliably all these QNMs in discretized numerical implementations. However, since it is unrealistic to calculate and store all these modes (at least a few hundreds of thousand for a typical numerical mesh), one needs to truncate the basis and use only a much smaller subset of modes. Therefore, in this section, we discuss qualitative improvement of the predictions by adding more QNMs to the coupled QNM model, however limiting the treatment to 200 QNMs per resonator.

To test this extension of the theory, we use a gold homodimer. We keep the $xy$ planar symmetry of the system, and break all the others in a configuration described in Fig. 3.13 to guaranty that more than simply the long axis dipolar QNM per rod is needed to reproduce the field of the dimer. Typically, we expect the short axis dipolar QNM to play a significant role. For the same reason, the dimensions of the nanorod, 60 nm diameter and 80 nm length, are chosen such that the long and short axis dipolar resonances are not degenerate, but have a frequency detuning smaller than their linewidths. To decouple the gap size from other degrees of freedom of the geometry, we parametrize the dimer with an angle $\theta$, a gap size (surface-surface) $g$, and a parameter $p$ to describe the position of the point where the gap between rods is minimal

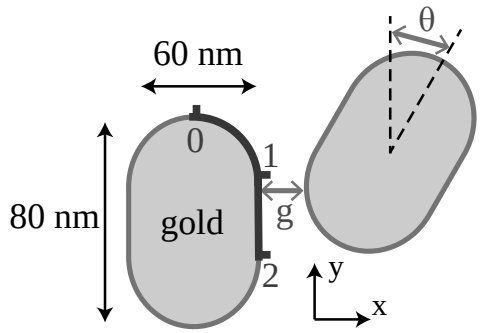


**Figure 3.13:** The broken symmetry dimer is composed a two identical cylindrical nanorods with spherical apex, in water. Each nanorod is 60 nm wide and 80 nm long. The dimer is parametrized by the gap width $g$ defined as the minimal distance between the two nanorods, by the angle $\theta$ of rod 1 with the $y$ axis, and a parameter $p$ describing the position of the point of rod 2 closest to rod 1. $p$ varies linearly from 0 to 1 on rod 2 apex, and 1 to 2 on the side of rod 2. The dimer studied in the section is obtained for $\theta = 45°$, $g = 20$ nm and $p = 0.5$.

(cf. Fig. 3.13). We break the symmetry of the dimer with $p = 0.5$, $\theta = 45°$ for a gap $g = 20$ nm to make sure that at least the long and short axis dipolar modes are coupling to each other.

We apply the coupled mode theory to predict the electric field magnitude $|\tilde{\mathbf{E}}|$ in the median plane $xy$, for 2 QNMs taken in the decomposition (long axis dipolar mode of both nanorods), for 6 QNMs (3 most important QNMs for both nanorods, cf Fig3.15(a-b)) and the set of 400 modes that we calculated (QNMs + numerical). The results are summarized in Fig. 3.14(a-c), where we compare the reconstructions of the model (Eq.(3.18)) with the exact field of the dimer shown in (d). We see that the enhancement of the field in the nanogap of the dimer bright mode requires a few higher order modes to be reproduced by the coupled QNM theory. Indeed, the higher is the order of a plasmonic QNM, the more confined its field is at the interface of a nanorod. Therefore, when the gap between two nanorods is reduced, the dipolar QNM of one rod can couple to an increasing number of higher order QNMs of the other rod.

We show in Fig. 3.15(a) and (b) the complex frequencies of all the 200 modes we solved for with QNMeig [134], which are formally identical for both nanorods. We indicate with insets the dipolar QNMs, with a complex frequencies of $(3.93 + 0.44i) \times 10^{15}$ rad/s for the long axis dipole and $(4.82 + 0.69i) \times 10^{15}$ rad/s for the short axis one. We also display two higher order *multipolar*[2] QNMs, here two quadrupoles with differents symmetries. Higher or-

[2]Higher order QNM are in practice standing wave plasmon with a number of nodes of the normal electric field (or *order*) higher than two (two node corresponds to a dipolar mode for a nanorod). For a sphere, these higher order QNMs strictly correspond to multipolar radiation modes described in Mie theory [116]. Here, we extend this denomination to the nanorods.

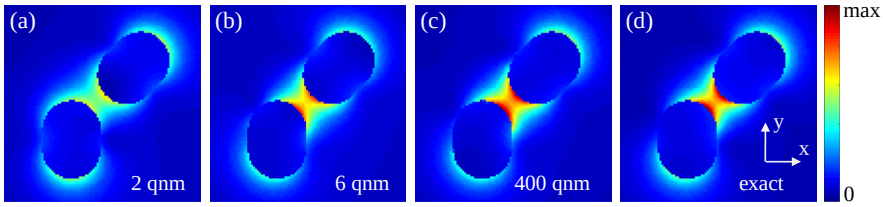


**Figure 3.14:** Convergence of electric-field. (a-c) show the magnitude $|\tilde{\mathbf{E}}|$ of the normalized QNM electric field in the median plane $xy$ predicted by coupled QNM theory for a reconstruction with two (only long axis dipole of both nanorods), 6 or 400 QNMs. We compare it with the exact normalized $|\tilde{\mathbf{E}}|$. We use same colour axis for all figures to ease up comparison. We observe that the enhancement of the electric field in the nanogap formed between the nanorods is due to the excitation of higher order QNMs.



der plasmonic QNMs accumulate towards the real frequency $\omega_p/\sqrt{1+1.33^2}$, with a low imaginary part. Close to this frequency, dispersion for the surface plasmons polariton (SPP) at a gold/water interface is flat, therefore the wavelength of the SPP converges towards zero, and the number of nodes of the plasmon field that can be squeezed in the circumference of the nanorods (i.e. mode order) diverges. Additionally, the imaginary part of the complex eigenfrequencies of these QNMs converges towards $\gamma_d/2$. Indeed, higher order QNMs do not radiate, and their loss rates are fundamentally limited by the absorption of gold. Finally, all the modes with an imaginary part stronger than that of the dipolar modes are numerical modes, also known as *perfectly matched layers modes* or *PML modes* [125, 134]. They are strictly eigensolutions of the discretized Maxwell equations in a numerical implementation. They are required to guaranty a complete basis in a numerical framework [134], but their electromagnetic fields are mostly confined inside the PMLs, and not at the nanorods as it is the case for true QNMs.

We colourcode each QNMs of the two nanorods according to its relative weight in the reconstruction of the bonding superradiant dimer mode. The weight $|\beta_{1,dipole}|$ of the dipolar mode of rod 1 accounts for 30 % of the norm $|\boldsymbol{\beta}|$ of the normalized eigenvectors containing the weights for all the QNMs of rods 1 and 2 predicted by the coupled QNM theory, while $|\beta_{2,dipole}|$ represents 50 %. Therefore, as expected, for both nanorods, the most important QNMs for the hybridization leading to the superradiant dimer mode are the long axis dipolar modes. Since the symmetries of the system are broken (apart from $xy$ plane, not relevant in this discussion), there is no fundamental reason why a mode $m$ of rod 1 should be as important as the same mode $m$ of rod 2 in the decomposition. This is indeed observed for the long axis dipolar modes, and we see in (a) and (b) that the short axis dipole is the $2^{nd}$ most important mode from rod 1 in the decomposition with a 10% contribution, but it is only the $3^{rd}$ most important for rod 2 with a 8.8 % contribution. Even more, for both nanorods, we find one quadrupolar QNM amongst the first three most

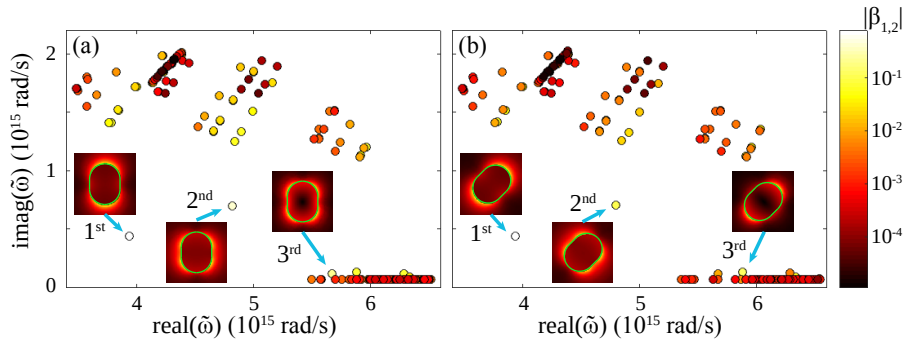


**Figure 3.15:** Relative contribution of the QNMs of nanorods 1 and 2 in the reconstruction of the dimer bright mode. (a) and (b) show the position in the complex frequency plane of the 200 QNMs used to described nanorod 1 and nanorod 2 in the coupled QNM theory. The two nanorods should theoretically have exactly the same QNM, and we indeed observe that the first 200 QNMs of rod 1 and rod 2 have the same complex resonance frequencies. Each point is colour coded (in logarithmic scale) with respect to the magnitude of the coefficient $\beta_{i,m}$ describing the contribution of mode $m$ of nanorod $i$ in the reconstruction of the bright mode of the dimer. The insets show the mode profiles of the first three most important modes in the reconstruction. The most important mode of rod 1 and 2 is, as expected, the long axis dipolar mode.

important modes, but it is not the same quadrupolar mode for rod 1 and for rod 2. Finally, we cannot justify with a physics argument why PML modes seem to play a non-negligible role in the reconstruction.

## 3.5. Conclusion and outlook

In this work, we have introduced a theory to describe the hybridization of quasinormal modes (QNMs) of a set of resonators. Our formulation does not rely on any assumption on the symmetries of the assembly, and accounts for the non-Hermitian nature of electromagnetic resonators. Through a series of realistic examples, we demonstrated the predictive force of the coupled QNM theory to not only estimate the resonance frequency and decay-rate of the hybridized modes, but also to calculate observables such as extinction cross section of the assembly under various illumination conditions. We foresee that the approach could become a powerful tool to guide the design of complex assemblies. Not only does it allow one to gather physical insight about the structure under investigation thanks to an elegant modal decomposition, but also could enable a sizeable gain in computation time. For example, with the geometries studied in subsection 3.3.2, the exact computation using FEM of an extinction spectrum of 100 wavelength points, for 3 different angles $\theta$, and 3 differents gap values (9 geometries), illuminated by 3 different plane wave polarizations, would require 45 hours of computation (assuming 1 min per point for each geometry and illumination). The coupled QNM theory only

requires slightly more than 2 mins compute the QNMs, and the computation time of the overlap integrals takes approximately 30 sec per geometry with a non-optimized algorithm. The computation time with the coupled QNM theory, therefore, amounts to a total of less than 5 mins. These performances could even be immensely improved by using an appropriate method to compute the overlap integrals, which should represent a negligible CPU time. One could then envision to store a complete library of resonator QNMs as building blocks for complex designs.

The present framework, however, still possesses a few unresolved limitations that will require further investigations. In particular, the normalization condition in subsection 3.2.2 has not formally been confirmed. Furthermore, if one wished to use the present theory to design hybrid metallic-dielectric resonators [95], they would be confronted to to the difficulty of considering a rapidly-divergent field (the plasmon field) over an extended volume (the dielectric cavity), implying a large interaction at complex frequency although the remote interaction is weak at real frequency. There is no theoretical inconsistency since the QNM and PML-mode basis is complete [134], but this simply implies that many PML-modes will be needed in the expansion, making the practical implementation inefficient. The coupled-QNM theory is thus effective only for near-field couplings which require taking into account the non-Hermitian character of the leaky field. Finally, we mention that more tests remain to be performed to fully quantify the convergence rate of the approach, in continuation of the work done in Section 3.4 . Further extensions of this approach may consider non-local effects [80, 192, 193] of particular interest for ultra-narrow gap resonators [81, 194–196].

# 4

# COOPERATIVE INTERACTIONS BETWEEN NANOANTENNAS IN A HIGH Q CAVITY FOR UNIDIRECTIONAL LIGHT SOURCES

## 4.1. Introduction

Tailoring optical resonators to have any desired quality factor $Q$ and mode volume $V$ is a major endeavor in nano- and micro-optics, as the basic stepping stone to controlling light-matter interaction in diverse scenarios that range from cavity QED, to nonlinear optics, to vibrational spectroscopy, to building lasers and solid-state lighting devices [75, 197]. Notably, it is desirable to *independently* control the field strength per photon (gauged by $V$), the resonator linewidth $Q$ [198], and the channel to which the resonator favourably couples with far-field radiation. For instance, when controlling the rate of spontaneous emission experienced by a quantum emitter placed in a resonator, it is desirable to control the Purcell factor $F = (3\lambda^3/4\pi^2)Q/V$, while at the same time tune the cavity to the emitter frequency, make sure that the cavity linewidth is matched to the emitter spectrum [21, 94], and ensure that light extraction occurs through one highly efficient channel. Similar arguments

hold for strong coupling between light and matter [198–200], SERS and cavity/molecular optomechanics [201], and generally, processes that at the same time need high field enhancement, yet also matching of linewidths to other experimental constraints. In the last decade great progress has been made in realizing extremely confined resonators of $V \sim \lambda^3/10^4$ and low $Q \sim 20$ through plasmonics on one hand [21, 200, 202–204], and high-Q microcavity resonators with $V > (\lambda/2)^3$ on the other hand [166]. Reaching very large $F$ at intermediate $50 < Q < 10^4$ factors, however, has remained elusive, despite the large possible relevance for matching the linewidths of room temperature emitters.

Recently several groups have explored if so-called *hybrid plasmonic-photonic resonators* could access the regime of deep subwavelength confinement, owing to their plasmonic consituents [93, 94, 108, 186, 186, 205], while at the same time inheriting larger quality factors from their dielectric microcavity character. Efforts in this direction include hybridizing single plasmonic nano-antennas with photonic resonances like whispering gallery modes (WGM) supported by Mie spheres, microtoroids or microdisks, or localized modes in photonic crystal cavities [93, 100, 153, 206, 207]. Recent computational predictions indicate that hybrid modes offer Purcell factors exceeding those of the individual constituents, with $Q$-factors on the same order as those of the microcavity mode, and therefore with mode volumes $V$ profiting from the hybridization [94, 108, 186, 208].

In this chapter, we consider the hybridization of microcavities with not one, but multiple metal nanoparticles. This problem is interesting from three different perspectives. First, it is an implementation of cooperative scattering engineered by dipole-dipole coupling in a resonator, mirroring the physics of sub-radiant and super-radiant collective states in which many dipoles coupled to one cavity hybridize, thereby providing a classical precursor to the important quantum optics problem of cooperative emission [137, 209]. Second, from an antenna viewpoint, it introduces the notion of phased array antennas into hybrid systems, associated with the control not only over Purcell enhancement, but also over the distribution of light into far-field radiation channels [21, 85, 210]. The seminal example in free space is the so-called Yagi-Uda antenna, in which a single quantum emitter drives a single antenna element surrounded by a set of "director" scatterers to ensure unidirectional emission [82, 83, 211]. In this chapter we present a minimal phased-array on whispering gallery mode platform (Figure 4.1), and show that this can similarly result in unidirectional emission. A third perspective instead focuses on the physics of the cavity modes in hybrids, rather than the antenna physics. Indeed, this work is the first step of a plasmonic implementation of a proposition by Wiersig [212], who proposed that dielectric scatterers on WGM cavities support chiral eigenmodes, associated with exceptional point physics [69]. This chapter combines all these three perspectives and explores the capabilities of plasmonic dimers to both enhance the hybrid emission and allow for

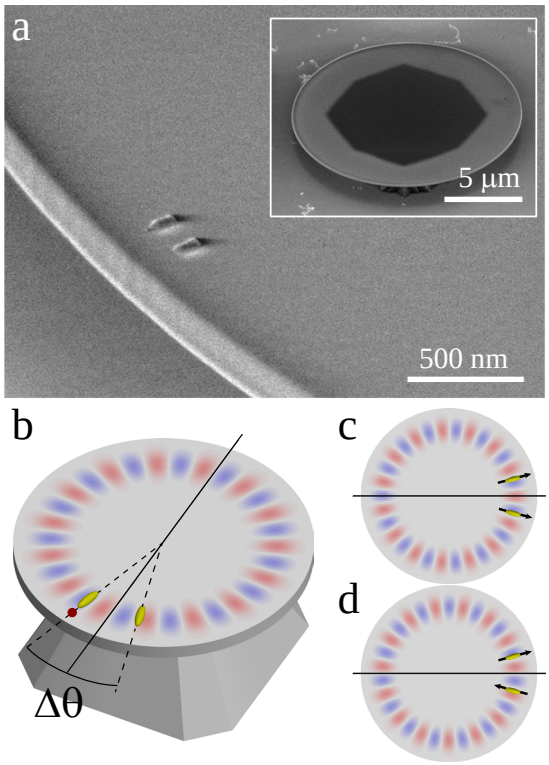


**Figure 4.1:** (a) Scanning electron micrograph (SEM, angled view) showing the geometry, consisting of two radially oriented aluminium nanorods on the perimeter of a silicon nitride microdisk. Inset: zoomed-out SEM of a full microdisk cavity. The dark angular pattern marks the contact with the silicon support pedestal. (b) Sketch of the geometry, where the antennas are separated by a subtended angle $\Delta\theta$. One antenna is driven by a spontaneous emitter (red dot). (c,d) Sketch of the symmetric and antisymmetric hybrid modes (mirror plane indicated as black line). Samples are fabricated by H. M. Doeleman, following a technique he developed.

directivity, here meaning the direction of circulation of light emitted into the cavity. Our theoretical analysis examines the distinct fingerprints in the mode lineshift and linewidth that may occur depending on the positioning of antennas in the whispering gallery mode profile. At the same time, in vein of the proposition of Wiersig that eigenmodes can become chiral [212], we assess if selective unidirectional emission is possible in the case where a single antenna out of a pair is driven by an emitter, and study its directionality contrast and Purcell factor. This proposition can be seen as realizing a two-elements directive phased array antenna design. We complement theory based on dipole-dipole interactions mediated by degenerate quasinormal modes (QNMs) with experiments, studying silicon nitride microdisk resonators coupled to dimers

of aluminium nanorod antennas. We quantified the dependence of the perturbed mode frequencies and quality factors on antenna separation, finding direct evidence for cooperative antenna effects on the linewidth and lineshift that extend over large antenna separations.

This chapter is structured as follows. First we sketch an analytical model for describing $M$ antennas coupled to a set of cavity modes. Next, we focus on the particular case of a WGM disk coupled to a plasmon dimer, examining the local density of states as well as the distribution of emission over clockwise and anticlockwise circulation in the cavity, and in the far-field. We then explain the spectral structure and the apparent unidirectional power distribution of emission by finding the quasinormal modes (complex frequency modes) of the coupled QNM equations. In the second half of this chapter we report experiments, focusing on narrowband mode spectroscopy of WGM-antenna dimer hybrids.



## 4.2. Model

The starting point of our work is to consider $M$ antennas as $M$ polarizable objects with dipole moments $\mathbf{p}_i$ ($i = 1 \dots M$) and to model their mutual interaction through the master microring cavity with a quasinormal-mode formalism. Previous related works on one hand include coupled-mode theory and Green's function theory for polarizable objects coupled to resonators [94, 181] and on the other hand QNMs for a semi-analytical model of the optical properties of a plasmonic resonator interacting with a single quantum object [185] and ensembles of classical dipolar oscillators [137, 167]. The present model features two extensions. First it deals with the important case of degeneracy of the underlying bare resonator modes, and second it considers changes of the resonator properties induced by the polarizable objects. This aspect relates to perturbation theory of resonators [139, 140, 153] Both features are essential for the properties reported hereafter. The induced dipole moments are given by [137, 213]

$$\mathbf{p}_i = \epsilon_0 \boldsymbol{\alpha}_i \Big[ \mathbf{E}_{\mathrm{dr,i}} + \mathbf{E}_{\mathrm{bs,i}} + \mathbf{E}_{\mathrm{dp,i}} \Big], \tag{4.1}$$

where $\boldsymbol{\alpha}_i(\omega)$ is the dipole polarizability tensor (normalized by vacuum permittivity $\epsilon_0$), $\mathbf{E}_{\mathrm{dr,i}}(\mathbf{r}_i, \omega)$ represents an externally applied driving field, $\mathbf{E}_{\mathrm{bs,i}}(\mathbf{r}_i, \omega)$ is the field radiated by the dipole $i$ and scattered back onto $i$ by the environment and the term $\mathbf{E}_{\mathrm{dp,i}}(\mathbf{r}_i, \omega)$ quantifies the field exerted on dipole $i$ due to fields scattered by all dipoles labelled by $j \neq i$. In the hypothesis where all polarizable objects are immerged in the same isotropic medium of refractive index $n$, one can decompose the system's dyadic Green's function $\mathbf{G}(\mathbf{r}, \mathbf{r}', \omega)$ such that $\mathbf{G} = \mathbf{G}_0 + \Delta\mathbf{G}$, where $\mathbf{G}_0(\mathbf{r}, \mathbf{r}', \omega)$ represents the homogeneous Green's function of a medium of index $n$, and $\Delta\mathbf{G}(\mathbf{r}, \mathbf{r}', \omega)$ is referred to as the Green's function of the scattered field. With these definitions,

we can formally express

$$\mathbf{E}_{\mathrm{dp,i}} = \sum_{j\neq i} \mu_0 \omega^2 \mathbf{G}(\mathbf{r}_i, \mathbf{r}_j, \omega)\mathbf{p}_j,$$

and

$$\mathbf{E}_{\mathrm{bs,i}} = \mu_0 \omega^2 \Delta\mathbf{G}(\mathbf{r}_i, \mathbf{r}_i, \omega)\mathbf{p}_i,$$

where $\mu_0$ is the vacuum permeability. We then use a partial quasinormal mode (QNM) expansion of the Green's function [125, 137]

$$\Delta\mathbf{G} = \frac{1}{\mu_0\omega^2} \sum_{k=1}^{N} \frac{-\tilde{\omega}_k}{\omega - \tilde{\omega}_k} \tilde{\mathbf{E}}_k(\mathbf{r}) \otimes \tilde{\mathbf{E}}_k(\mathbf{r}') + \delta\mathbf{G}_N \tag{4.2}$$

where $\tilde{\mathbf{E}}_k(\mathbf{r})$ is the normalized electric field of the QNM indexed by $k$ and $\tilde{\omega}_k = \omega_k + i\frac{\gamma_k}{2}$ its complex frequency ($\omega_k$ and $\gamma_k$ being respectively the resonance frequency and linewidth) and $\delta\mathbf{G}_N(\mathbf{r}, \mathbf{r}', \omega)$ is the residue of the decomposition, accounting for all other modes of the system besides the ones explicit in the sum, and non-resonant terms. This starting point is similar to previous work [140], where we examined perturbation theory for the interaction between a single polarizable object and a cavity mode, and adapted it to deal with multiple perturbers and cavity modes. Here, we will furthermore assume that two, initially degenerate, cavity modes are dominant ($N = 2$) as appropriate for a whispering gallery mode cavity, and that all other QNMs and non-resonant interactions, grouped in $\delta\mathbf{G}_N$ can simply be neglected. These non-resonant interactions would be tedious to calculate accurately in a real geometry [134], however one would expect them to be dominated by an electrostatic/near-field $1/r^3$ term interaction that is captured in $\mathbf{G}_0$.

We focus on the specific case of antennas interacting with a single degenerate pair of whispering gallery modes, as would be the case in a microdisk, microtoroid or microsphere cavity (as in Figure 4.1). This implies the specific choice $N = 2$ and a pair of symmetric (s) and antisymmetric (as) mode functions of the form (in cylindrical coordinates $(r, \theta, z)$)

$$\tilde{\mathbf{E}}_s \cdot \mathbf{e}_r = \cos(m\theta)\tilde{E}_r(r, z), \tag{4.3a}$$

$$\tilde{\mathbf{E}}_{as} \cdot \mathbf{e}_r = \sin(m\theta)\tilde{E}_r(r, z). \tag{4.3b}$$

Note that from these normalized QNMs, clockwise and counterclockwise combinations can be formed through $\tilde{\mathbf{E}}_{cw/ccw} = \frac{1}{\sqrt{2}}(\tilde{\mathbf{E}}_s \pm i\tilde{\mathbf{E}}_{as})$. The following considers antennas that are only polarizable along their long axis by TE whispering gallery modes (relevant for nanorods near resonance, aligned along the radial direction of a microdisk), and that are offset in the azimuthal direction (angle $\theta$), but with a fixed radial position $r$ on the edge of the microring cavity (see Fig. 4.1). Under these assumptions, the only relevant functional dependence on the antenna position is through $\theta_i$ (angle parametrizing the nanorod

location), or equivalently, the antennas angular separation $\Delta\theta = \theta_2 - \theta_1$. The QNM strength at the antenna position $(r_i, z_i)$ (resp. distance of antenna to origin, height of the antennas relative to the disk plane) is set by $\tilde{E}_r(r_i, z_i)$, which is directly related to the on-resonance local density of states (LDOS) enhancement at the location of the antenna.

We now consider the emission enhancement of a dipole emitter placed in the vicinity of one of the nanoantennas. Therefore we calculate the LDOS enhancement, which is defined as the total work required to maintain a drive dipole moment $\mathbf{p}_{\mathrm{dr}}$ located at $\mathbf{r}_{\mathrm{dr}}$

$$P = \frac{\omega}{2}\,\mathrm{Im}(\mathbf{p}^*_{\mathrm{dr}} \cdot \mathbf{E}_{\mathrm{tot}}(\mathbf{r}_{\mathrm{dr}}, \omega)), \tag{4.4}$$

4

normalized to the power required to drive the same dipole in free space as given by Larmor's formula $P_0 = \frac{\omega^4 \|\mathbf{p}_{\mathrm{dr}}\|^2}{12\pi\epsilon_b\epsilon_0 c^3}$, where $\omega$ is the driving frequency, $\mathbf{E}_{\mathrm{tot}}$ is the the total field radiated by the dipole evaluated in the presence of the cavity, and $\epsilon_b$ is the permittivity of the homogeneous isotropic, non-absorptive background medium. To obtain the relevant quantities, we substitute as the drive field $\mathbf{E}_{\mathrm{dr,i}}$ in Eq.(4.1) the field imposed by a drive dipole

$$\mathbf{E}_{\mathrm{dr,i}} = \mu_0\omega^2\mathbf{G}(\mathbf{r}_i, \mathbf{r}_{\mathrm{dr}}, \omega)\mathbf{p}_{\mathrm{dr}},$$

and solve for the induced (antenna) dipoles $\mathbf{p}_i$, and we calculate the total field returning to the drive dipole as

$$\mathbf{E}_{\mathrm{tot}} = \mu_0\omega^2\left[\mathbf{G}(\mathbf{r}_{\mathrm{dr}}, \mathbf{r}_{\mathrm{dr}}, \omega)\mathbf{p}_{\mathrm{dr}} + \sum_{i=1}^{M}\mathbf{G}(\mathbf{r}_{\mathrm{dr}}, \mathbf{r}_i, \omega)\mathbf{p}_i\right]. \tag{4.5}$$

Finally, we also reconstruct the directionality of emission into the cavity, i.e., how emission into the cavity modes is distributed over the clockwise and anticlockwise directions. To this end, we exploit the fact that the excitation of the symmetric and asymmetric degenerate modes ($\tilde{\omega}_1 = \tilde{\omega}_2 \equiv \tilde{\omega}$) is given in the QNM formalism as [124]

$$a_{s,as} = \frac{-\tilde{\omega}}{\omega - \tilde{\omega}}\left[\tilde{\mathbf{E}}_{s,as}(\mathbf{r}_{\mathrm{dr}}) \cdot \mathbf{p}_{\mathrm{dr}} + \sum_{i=1}^{M}\tilde{\mathbf{E}}_{s,as}(\mathbf{r}_i) \cdot \mathbf{p}_i\right]. \tag{4.6}$$

Since the (counter)clockwise mode amplitudes are then proportional to $a_{cw/ccw}(\omega) = \frac{1}{\sqrt{2}}(a_s(\omega) \mp i a_{as}(\omega))$, we can introduce the directivity parameter $\sigma = \frac{|a_{cw}|^2 - |a_{ccw}|^2}{|a_{cw}|^2 + |a_{ccw}|^2} = \frac{|a_s - i a_{as}|^2 - |a_s + i a_{as}|^2}{|a_s - i a_{as}|^2 + |a_s + i a_{as}|^2}$ which is $(-)1$ if all light in the cavity is circulating in the (counter-)clockwise cavity mode, or 0 if light is distributed equally over both circulation directions.

## 4.3. Theory results

### 4.3.1. LDOS and directionality

We focus on plasmon dimers ($M = 2$), placed on top of a microdisk cavity with parameters identical to those in Section 2 of Ref. [94]. They show a quality factor $Q = 10^4$ and deliver a Purcell enhancement of 75 in the plane of the antennas above the microdisk (the effective mode volume is real valued and around $10\lambda^3$), further taking as azimuthal mode number $m = 22$, as typical for silicon nitride microdisks in the near infrared of $\sim$4 $\mu$m diameter. We take $\omega_c/(2\pi) = 360$ THz as cavity resonance frequency, implying operation near 800 nm, near the wavelength of the experiments also reported in this chapter. For the antenna polarizability we take a Lorentzian polarizability with resonance frequency $\omega_0/(2\pi) = 460$ THz and Ohmic damping rate $\gamma_i/(2\pi) = 19.9$ THz corresponding to gold, which is equivalent to taking the polarizability of a sphere and assuming a Drude model. We take a scatterer volume of $(80\text{ nm})^3$ and incorporate radiation damping exactly as in Ref. [94]. This is equivalent to an on-resonance extinction cross section of 0.18 $\mu m^2$ and scattering albedo of 85 %, as typically achieved by large plasmonic dipolar antennas, and matches the polarizability retrieved from full-wave simulations (Ref. [94]). We place the source at 60 nm distance from one of the two antennas and assume that the dipole is polarized along the disk axis, see Fig. 4.1. In the absence of the microdisk, the Purcell factor provided by the uncoupled nanorod is $\approx 200$ at antenna resonance.

Figure 4.2 shows the local density of states normalized to that in vacuum as function of frequency around the bare cavity resonance and the angular separation between the antennas, calculated using the simple formalism that we presented. For reference, if just a single antenna is present, the hybrid antenna-cavity system presents a Fano lineshape in LDOS, with a peak LDOS enhancement of almost 700, as was also verified independently of the approximations of the model by full wave simulations [94]. This value is almost an order of magnitude larger than the one provided by just the bare cavity, and more than three times higher than the *maximum* LDOS enhancement of 200 provided by just a bare antenna at its resonance. Figure 4.2(a) reveals that in the dimer case, the LDOS enhancement reaches similar large values, but with two resonant features that present a distinct oscillatory behaviour as function of the angular separation between the antennas. In the presence of two antennas, the hybrid modes can still be classified by symmetry, as there is mirror symmetry through the line from the cavity center to the midpoint between antennas (cf. Figure 4.1). Thus, one of the QNMs is symmetric and displays a node in the radial field between the antennas (Eq.(4.3a)), and polarizes both antennas in the same radial direction. The other QNM is antisymmetric, with a null between the antennas (Eq.(4.3b)), and polarizes both antennas in opposite directions. When the antennas are shifted by a multiple of 1/2 of the cavity spatial period, one QNM is not perturbed by the antennas,

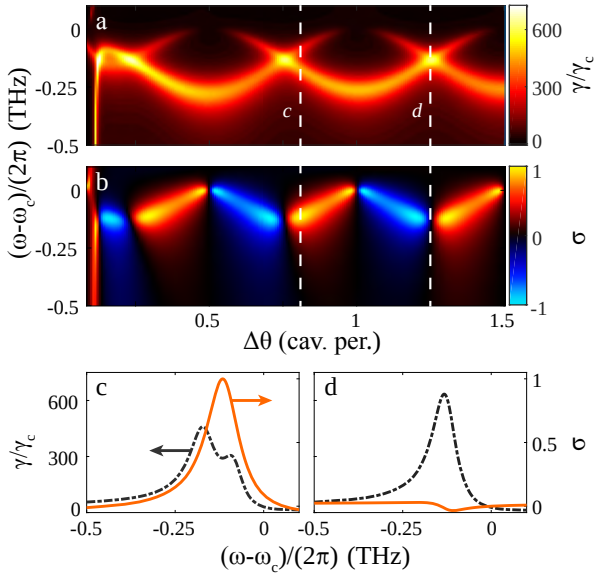


**Figure 4.2:** (a) Local density of states enhancement for a source at antenna 1, as function of the antenna separation expressed in cavity mode profile azimuthal period, and as function of frequency. The bare cavity resonance $\omega_c/(2\pi)$ is at 360 THz. (b) Directionality of the emission into the cavity. (c,d) LDOS enhancement (black dashed) and directionality (orange solid curves) versus frequency for two antenna-separations, as indicated by vertical dashed lines in panels (a,b), just off degeneracy (c) at unit directionality, and exactly on degeneracy (d), with no directionality.

while the other is perturbed by *both*, giving a large broadening and frequency-shift. Midway between these conditions, both modes have identical overlap with the antennas, meaning they are shifted equally in real frequency and in Q, maintaining degeneracy. In the first scenario, an emitter placed at one of the antennas couples just to the symmetric mode, that is maximally perturbed. In the second scenario, both modes contribute to the LDOS, explaining why the degeneracy point also corresponds to highest LDOS. This LDOS is approximately the same in value as in the single-antenna hybrid: while *two* hybrid modes contribute to the LDOS instead of one, each of them contributes only half as much, owing to the fact that the antennas are more weakly coupled to the pertinent cavity modes than in the single antenna case, by virtue of not being at the mode maxima of either the S or AS mode.

The picture sketched above essentially repeats itself with increasing antenna separation, with a repetition period equal to $\theta = \pi/m$, reflecting the fact that the antenna interaction is dominated by the $\cos m\theta$ resp. $\sin m\theta$ dependence of the cavity modes. At very short distances however, the behaviour is qualitatively different, with very strong perturbation (frequency shift and broadening) of the cavity modes. The physical picture is that at close distances

(below, say $\lambda/2\pi$), the two antennas hybridize forming a symmetric, bright, strongly polarizable bonding combination that is blue-shifted, and an anti-symmetric, dark, weakly polarizable anti-bonding mode that is red-shifted from the bare antenna resonance. This behavior is approximately captured in our model through $\mathbf{G}_0$ in the Green's function $\mathbf{G} = \mathbf{G}_0 + \Delta\mathbf{G}$, which contains near field $1/r^3$ and mid-field interactions. However, an exact quantitative treatment of this regime would require to account for the residue $\delta\mathbf{G}_N$ of our QNM expansion which may play a role in near and mid-field regimes. The hybridization physics with the cavity modes is rich since when the two antennas hybridize, for a certain antenna-antenna distance, the red-shifting dark dimer mode tunes through resonance with the cavity, which had its bare resonance chosen to the red of the single antennas. At this distance, the dark mode very strongly perturbs the cavity. On the other hand, the coupling strength of the blue-shifting bonding mode gets weaker with reduced particle separation, as blueshifting tunes it out of cavity resonance.



For the case of an emitter driving a single nano-antenna, in the absence of a second antenna, symmetry dictates that emission will be injected only into the symmetric mode, i.e. with equal contributions of the clockwise and anticlockwise directions. The presence of the second antenna, however, implies that both the symmetric and antisymmetric QNM can contribute to LDOS. Hence, it is interesting to resolve into which direction the light is emitted into the cavity. We find that the second antenna can make the emission largely unidirectional. Figure 4.2b represents the splitting ratio $\sigma$. Essentially unidirectional emission is achievable, at combinations of frequency and geometry that are close to, but not at, the mode degeneracy points $\Delta\theta = (n + \frac{1}{2})\pi/m$ and that bring simultaneously large LDOS enhancement. Figure 4.2(c,d) highlights the behaviour for two distinct antenna separations, namely $\Delta\theta = 0.81$ cavity periods (i.e., just beyond the degeneracy at 0.75) and right at degeneracy, $\Delta\theta = 1.25$ cavity periods. Unidirectional emission $\sigma = 1$ can coincide with large LDOS enhancement, exceeding 300 times. This occurs at angular separations close to, but not at a point of maximum LDOS. Conversely, near-equal power splitting, at near maximum LDOS enhancement (enhancement > 600) occurs at points of degeneracy. It should be noted that while we report total LDOS in this chapter (including also nonradiative enhancement), Ref. [94] shows that up to 95% of radiated power can be extractable through the cavity loss channels for single antennas. The implication is that for the geometry in Figure 4.2(c), if the microdisk would be addressed by a tapered waveguide as main input/output channel, the fluorescence could be efficiently captured into just one waveguide direction. Conversely, by reciprocity one would expect the emitter to be addressable from just one waveguide direction. The basic requirements for this behavior in emission and excitation are (I) the correct separation between the antennas, and (II) placement of the emitter such that it dominantly couples to just one of the antennas, instead of coupling to both antennas equally (emitter in-between the two antennas), dominantly coupling

to just the (spoiled) cavity (emitter on the disk perimeter, but more than 50 nm away from the surface of any antenna), or dominantly coupling to free space (emitter well away from antennas and the whispering gallery mode profile). This means that our predictions hold as long as the emitter is placed within the near-field hot spot of the intended feed antenna, i.e., within 20 nm or so of the distal end for a nanorod antenna realization. On basis of Ref. [95], we expect the predictions to also hold if the feed-antenna to which the emitting dipole couples is replaced by a dimer gap antenna of similar dipole polarizability, where placement of the emitter in the gap could significantly enhance the LDOS. Finally, we note that while already $M = 2$ antennas are very successful in creating unidirectionality, our model is easily extended to more than 2 antennas. For creating unidirectional emission we note that similar performance is possible for $M = 3$ antennas, while generally at larger M there is no further improvement in unidirectionality but a large penalty in LDOS. This is a consequence of the reduction of Q with the addition of antennas.



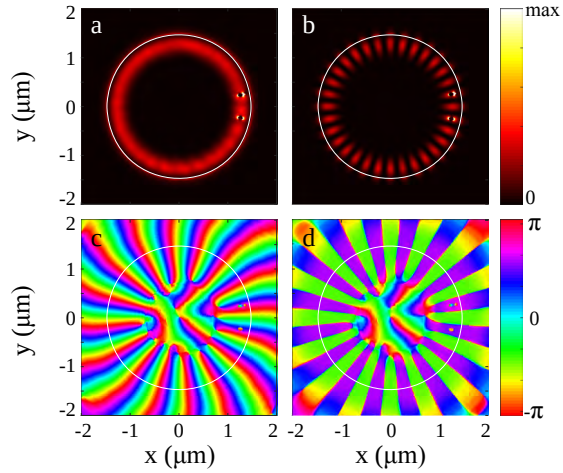


**Figure 4.3:** (a,b) Simulated intensity and (c,d) phase of the radial component $E_r$ of the electric field on the top interface of microdisk cavity dressed by two aluminium antennas. The antenna separation is 0.94 cavity period for panels (a,c) and 1 cavity period for panels (b,d), and the simulation is driven by a radial dipole placed 10 nm radially outward from the top antenna. In panels (a) and (c) the intensity is almost perfectly homogenous in the azimuthal direction with the phase indicating clockwise propagation. On the contrary, panels (b) and (d) exhibit a standing wave pattern as antennas and dipole only couple the symmetric cavity mode.

To verify that the semi-analytical predictions from our model are not an artefact of the approximations, we have performed real-space FEM simulations using COMSOL to verify the occurrence of unidirectional emission (see Ref.[94] for LDOS benchmarking). We analysed a $Si_3N_4$ microdisk (thickness 200 nm, diameter 2.95 μm) decorated with two aluminium nanorod antennas

(100 nm long, 50 nm high, 40 nm wide). We first evaluated the bare cavity mode profile ($m = 16$ mode at 396.675 THz, $Q = 4000$) and its frequency shift upon perturbation by a single antenna (at 396.3 THz, $Q = 800$). From these, we predicted the operation points (frequency and antenna spacing) for unidirectional and completely symmetric emission to occur at antenna separations of 0.94 resp. 1 cavity period, both at a frequency of 396.650 THz. Next, we performed driven simulations for these operation conditions, with a single drive dipole next to one antenna. Figure 4.3 shows the cycle-averaged field intensity $|E|^2$ and the phase for both cases. In the first case we find the signature of constant field intensity and circulating phase corresponding to excitation of a travelling wave, while in the second case we find the constant-phase field intensity nodes and antinodes characteristic of a standing wave. The slight residual fringe contrast for the unidirectional case indicates that over 96% of the energy travels in a single direction. Thus the simulation confirms the predicted phased-array action, as well as the operation points at which the distinct scenarios occur.



### 4.3.2. Complex-frequency analysis

The spectral structure, i.e., the Fano lineshapes, and the unidirectionality evident from Figs. 4.2 and 4.3 clearly involve the interference of several modes. This structure can be further understood from a complex-frequency eigenmode analysis of the coupled antenna-cavity equations. In the absence of driving terms, taking Eq.(4.1) through Eq.(4.6) together leads to

$$\mathbf{p}_i = \epsilon_0 \boldsymbol{\alpha}(\omega)\Bigg[\mu_0\omega^2 \sum_{j\neq i}^{M} \mathbf{G}_0(\mathbf{r}_i,\mathbf{r}_j,\omega)\mathbf{p}_j + \mu_0\omega^2\mathbf{G}_0(\mathbf{r}_i,\mathbf{r}_i,\omega)\mathbf{p}_i + \sum_{k=s,as} a_k\tilde{\mathbf{E}}_k(\mathbf{r}_i)\Bigg], \quad (4.7)$$

keeping in mind that we neglect the residue $\delta\mathbf{G}_N$ of the QNM expansion. Eq.(4.7) defines a linear system $\mathbf{Ax} = \mathbf{0}$, for $\mathbf{x} = [\mathbf{p}_i, a_k]$, from which the complex dressed eigenfrequencies $\omega'$ can be determined through the condition $\det\mathbf{A}(\tilde{\omega}') = 0$. These represent the complex eigenfrequencies of the hybrid system QNMs. Figure 4.4(a,b) represents the real and imaginary part of the eigenfrequencies. This analysis confirms the oscillatory behaviour of both the real and imaginary part of frequency with the angular antenna separation. Notably, at points where the antenna separation fits the distance between cavity mode antinodes, one of the two cavity modes is neither shifted in Q nor in frequency from the bare mode. In this configuration, the other mode is maximally shifted in both Q and frequency. At points of degeneracy in the real part of the frequency, the QNMs also have identical Q, with both experiencing approximately half the shift that is seen at points of maximum mode separation.

Considering the symmetry of our system and the fact that we expect two perturbed solutions of Eq.(4.7) close to the unperturbed cavity (complex) frequency $\tilde{\omega}_c$, the frequency shift of the two QNMs with respect to $\tilde{\omega}_c$ can be effectively parametrized through [140]

$$\frac{\tilde{\omega}'_{s,as} - \tilde{\omega}_c}{\tilde{\omega}_c} = \frac{-\epsilon_0 \alpha(\tilde{\omega}_c)\tilde{E}_r^2(r_i, z_i)[1 \pm \cos(m\Delta\theta)]}{1 \pm \mu_0 \tilde{\omega}_c^2 \alpha(\tilde{\omega}_c) g_0(\tilde{\omega}_c)}, \tag{4.8}$$

where $i$ designates equivalently 1 or 2, $g_0(\tilde{\omega}_c) = \mathbf{u}_{r_i} \cdot \mathbf{G}_0(\mathbf{r}_i, \mathbf{r}_j, \tilde{\omega}_c)\mathbf{u}_{r_j}, i \neq j$ is the Green's function element between the two dipoles, and the $\pm\cos(m\Delta\theta)$ accounts for the coherent addition of the two perturbers, while the denominator accounts for the hybridization effect on polarizability, that is especially apparent in the mid-field and near-field (short distances).

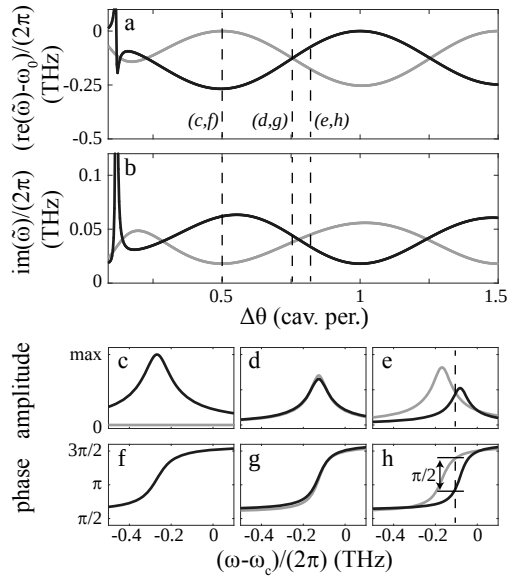


**Figure 4.4:** Real (a) and imaginary (b) part of the eigenfrequency of the symmetric (black) and antisymmetric (gray) hybrid QNMs versus the angular separation between antennas. The amplitude (panels c,d,e) and phase (panels f,g,h) show the physics underlying directional emission at three salient antenna separations (Dashed verticals in (a,b)). Since the amplitude of the symmetric mode is null in (c), its phase is not defined, and therefore not plotted in (f). Dashed line in (e,h) is a guide for the eye. Where one mode is maximally perturbed and the other is not (c,f), the source only excites one of the two hybrid WGMs (symmetric, black curves). Where symmetric and antisymmetric mode are perturbed equally (d, g), both modes are excited equally and in phase, leading to no directionality. Just away from degeneracy (e,h), one can achieve equal amplitude and $\pi/2$ phase difference, leading to unidirectionality.

For a sufficiently large antenna separation the denominator of Eq.(4.8) is essentially equal to one, and the complex detuning between the modes S and

AS traces

$$\frac{\Delta\tilde{\omega}}{\tilde{\omega}_c} = \frac{\tilde{\omega}'_{as} - \tilde{\omega}'_s}{\tilde{\omega}_c} = \frac{\alpha}{\tilde{V}}\cos(m\Delta\theta). \tag{4.9}$$

where $\tilde{V}(r_i, z_i)$ is the effective complex mode volume [124] of each WGM of the unperturbed cavity at the position of the antenna without the sinusoidal dependence present Eq.(4.3) (therefore identical for the S and AS mode). Aside from the expected inverse dependence of shift on mode volume, this result also brings out the role of the phase of the polarizability. Since the complex mode volume is almost real in our example, the phase of the polarizability directly sets the balance between the real and imaginary part of the frequency shift. If the antennas are red (blue) detuned compared to the cavity the frequency splitting between the symmetric and antisymmetric mode is (anti-)correlated with the difference in linewidth. If the antennas are on resonance with the cavity, there is no frequency splitting, but instead the amplitude difference in linewidth is maximal. In other words, in that limit the cavity is near degeneracy but the two modes have very different Q's. The example considered in Figs. 4.2, 4.4 corresponds to blue detuning (mainly a frequency shift).

Unidirectionality and LDOS enhancement can now be understood from the amplitude and phase with which the two QNMs are driven by a point emitter and can be calculated from the overlap (inner product) between the eigenvectors of **A** defined from Eq.(4.7) and the driving from a single dipole source. Directionality of emission occurs as a consequence of interference of the symmetric and asymmetric modes, with strict unidirectionality requiring destructive interference in one direction. Thus, the first requirement for perfect unidirectional emission to occur is that the localized excitation at one of the antennas must have the same projection on the hybrid basis. The second condition is that the relative phase is appropriate for destructive interference in the clockwise (counterclockwise) direction (with simultaneous constructive interference in the other channel guaranteed by symmetry). Figure 4.4(c,d,e) and (f,g,h) report the amplitude and phase of excitation of the two modes for three distinct antenna separations for the example system considered in Fig. 4.2. In the first (for antenna distance of $\Delta\theta = 0.5$, Fig. 4.2(c,f)), the antenna separation fits the distance between mode antinodes, meaning that the distance is half-integer in units of the cavity period. The dipole emitter only couples to the strongly perturbed symmetric normal mode of the system, so there is no directionality. Next, we consider an antenna-separation chosen right at degeneracy (example chosen $\Delta\theta = 0.75$, Fig. 4.2(d,g)). Again, the emission is equally distributed over both directions. The mechanism is, however, different from that at work at half-integer antenna distances. Now both modes of the system are excited instead of just a single one, but since there is no constructive/destructive interference, the excitation has equal phase for both. For a separation just away from degeneracy (example chosen: antenna distance of $\Delta\theta = 0.81$ cavity periods, Fig. 4.2(e,h)) the emitter can still couple

to both modes of the system, but with a phase difference. Indeed, by appropriate choice of frequency one can obtain a $\pi/2$ phase shift, at equal excitation amplitude for the two modes, leading to perfect unidirectionality. The sign of the unidirectionality is controlled by choosing $\Delta\theta$ on opposing sides of the degeneracy point.

We finally note that this mechanism for unidirectional emission is distinct from the interesting exceptional-point studies reported by Peng et al. in Ref. [69], obtained by perturbing a WGM with two near field probes as scatterers. In a true exceptional point scenario, unidirectionality is intrinsic to the eigenmodes, and not due to phase relations in the linear superposition of modes, as upon coalescence of the eigenfrequencies the remaining eigenmode is chiral. In contrast, here we exploit the asymmetric location of the emitter at just one antenna for unidirectionality, while our eigenmode set still retain even and odd parities. The mechanism relies on tuning the operation point near, but not on, mode degeneracy. An exceptional point instead requires the geometry to break parity symmetry by either using different radial positions, or considering two geometrically different antennas, or adding a third antenna [214]. While outside the scope of this chapter, our QNM based model for M antennas at arbitrary cavity locations (Methods sections) does provide a comprehensive framework for analysing and designing exceptional-point optical-cavity systems. The model quantitatively accounts for multiple scattering and antenna-antenna interactions and exceptional-point physics is revealed from an optical mode analysis instead of requiring to be postulated by a non-Hermitian Hamiltonian parametrization, as common in literature [69].

## 4.4. Spectroscopy of hybrid microdisk devices

We report experiments that interrogate the cavity mode perturbation physics, i.e., the predicted shift in frequency and change in linewidth of the modes in Eq.(4.9), which depends on the complex polarizability, the mode volume, and the azimuthal mode number. To this end, we apply tapered-fibre mode spectroscopy to samples based on $Si_3N_4$ disks hybridized with aluminium antennas (see Methods section). The experiments are performed on microdisks that are 15 $\mu$m in diameter and 200 nm in thickness. On top of them, we place two ~130 nm long ~50 nm wide and ~40 nm thick, radially oriented aluminium antennas, 300 nm from the disk edge (Figure 4.1(a)). The disks stand on a ridge which is 150 $\mu$m in width and height, so that they are accessible for optical fibre taper coupling. A tapered optical fibre setup (Fig. 4.5) provides excitation by an external-cavity diode laser that is widely tunable, yet narrowband (New Focus Velocity) around 780 nm. The observables that we can simultaneously collect are fibre taper transmission, fibre taper reflection as well as out-of-plane scattering collected with a microscopy set up. The microscope allows real space and Fourier space imaging of scattered light.

### 4.4.1. Sample fabrication

We use two-step lithography to realize $Si_3N_4$ disks, hybridized with aluminium antennas. First, we fabricate $Si_3N_4$ disks on pyramidal silicon pedestals by electron beam lithography and reactive ion etching of silicon wafers with a 200 nm LPCVD layer of $Si_3N_4$ (Lionix BV). After base piranha cleaning, we perform e-beam lithography in 450 nm of CSAR 62 resist (All Resist GmbH) at 50 keV (Raith Voyager), using a 0.4 nA current and 160 $\mu C/cm^2$ dose. Following development in pentyl-acetate followed by an o-xylene dip, the samples are post-baked at 130 °C for one minute to harden the resist which will act as a plasma etch mask. After plasma-etching through the nitride (RIE-ICP, $SF_6/CHF_3$ chemistry), we remove the resist using acetone and a base piranha clean, immediately followed by a Si underetch (KOH) to create free-standing disk edges. To realize the antennas, we then spincoat a MMA/PMMA bilayer resist stack (120 / 60 nm as measured at the edge of the cavity) to perform a second e-beam step, aligned to the first. After e-beam writing (500 $\mu C/cm^2$ dose) and development in a 1:3 methyl isobutyl ketone and isopropanol mixture , we perform aluminium evaporation (thermal evaporator at 0.05 nm/s evaporation rate, targeting 40 nm thickness) and lift-off in acetone at 40 °C. Finally, we make sure that the samples are accessible to optical fibre taper coupling by using a diamond saw to remove a 150 $\mu$m thick layer from the entire sample, except for a 150 $\mu$m wide ridge on which the structures stand. During this process the sample is covered by a protective polymer resist that is stripped after sawing (Microposit S1800). Two samples were made with a slightly different electronic dose for the second lithographic step. This resulted in a length difference of the antennas between the two samples sufficient to ensure that for one sample the antennas were almost on resonance with the cavity, that is, near 780 nm, while for the other sample they were designed to be resonant at 630 nm.

### 4.4.2. Optical set up, analysis framework

We interrogate the structures using a tapered optical fibre setup, sketched in Fig. 4.5(b). The fibre is a Corning HI 780C fibre that is single mode at our operation wavelength around 780 nm and is pulled to an adiabatic taper using an automated motorized hydrogen flame setup. The fibre is precisely positioned to evanescently couple to the cavities using a piezo-stage setup, and excitation light is coupled in from an external-cavity diode laser that is widely tunable, yet narrowband (New Focus Velocity). The frequency axis of our cavity transmission scans is calibrated against a Fabry-Perot reference cavity (finesse > 150, free spectral range 10 GHz). We simultaneously collect reflected and transmitted signals on photodiodes, as well as collecting scattered light (Fig. 4.5(b)). The scattered light is collected from the air side using a microscope objective and directed to a Basler CMOS camera, where we have access to both real-space, and $k$-space (angle-resolved) images. We can only

interrogate modes of 1st and 2nd radial order because the fundamental mode is too strongly perturbed and therefore broadened by the antennas to be probed by tapered-fibre coupling and narrowband laser frequency scanning. The radial order mainly affects the cavity mode volume, as QNMs of increasing radial order have lower field amplitudes at the antenna locations.

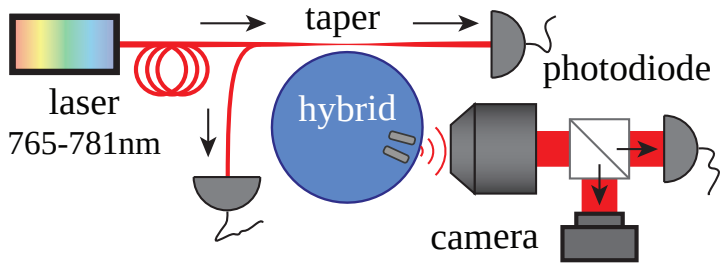


**Figure 4.5:** Setup schematic, indicating tapered-fibre excitation of microdisks with a narrowband tunable diode laser, while recording simultaneously taper reflection, taper transmission and out-of-plane scattering collected with an objective onto a camera or photodiode.



### 4.4.3. Experimental results

We studied 70 cavities consisting of a duplicated set of 35 different hybrid configurations where the separation angle between antennas varies, by design, from 0.8 to 13.5° (0.1 to 1.8 $\mu$m), corresponding to ~0.2 to 3.45 cavity azimuthal periods of the mode profile for our QNMs of interest (azimuthal mode numbers $80 < m < 86$ fall within our scan range).

Figure 4.6 shows a typical raw data set measured on a single device (antenna separation $\Delta\theta = 11.2°$ (1.46 µm) for $m = 80$, 2nd radial order). The transmission spectrum through the tapered fibre clearly shows power transfer to the cavity, with the lineshapes of two Lorentzian minima consistent with a broad and narrow QNMs. Depending on geometry these are not always clearly separable, particularly since the coupling strength to tapered fibre channels depends strongly on the modes linewidth, or when modes are very close to degeneracy. The reflection signal generally shows significant reflection features coincident with the transmission signature, however with asymmetric lineshapes that suggest interference with parasitic contributions (e.g. parasitic reflections at fibre connections). The scattering signal, finally, shows very clear Fano features, indicative of the coherent addition of the radiation patterns of the symmetric and antisymmetric QNMs. Qualitatively, these radiation patterns can be understood both for the symmetric and for the antisymmetric QNMs as the sum of interfering dipole contributions (sketch in Fig. 4.6(a, bright QNM only), predictions in Fig. 4.6(b,c)). These predictions are formed as the coherent sum of the symmetric resp. antisymmetric dipole

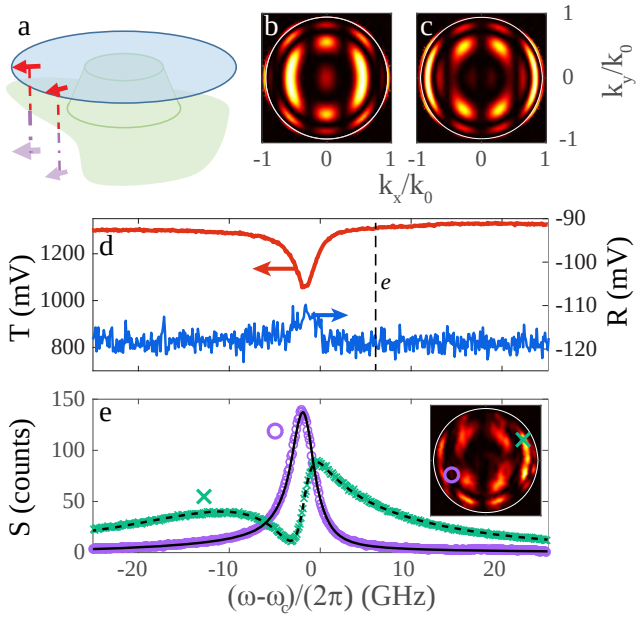


**Figure 4.6:** (a) Sketch of image dipole analysis explaining the far-field radiation pattern of the symmetric (S) QNM. (b,c) Predicted approximate angular radiation patterns into the air side for S and AS QNMs, plotting intensity per solid angle as function of in-plane momentum in units of $\omega/c$. (d) Taper transmission (red) and reflection (blue) diode signals for an antenna dimer (separation $\Delta\theta = 11.2°$ (1.46 µm)) on a microdisk, versus frequency relative to $\omega_c/(2\pi) = 385.37$ THz. (e) Inset: collected radiation pattern at frequency labelled (e) in panel (d). Purple and green curve marked ∘,× - collected scattered intensity at chosen $(k_x, k_y)$ indicated in inset, versus driving frequency.

combinations (dipoles located at the antenna centers, radially oriented). This leads to interference fringes in the far-field radiation pattern of both S and AS modes. Notably, for small $\Delta\theta$, the dipoles are almost parallel and the field radiated by the anti-symmetric AS mode exhibits a dark fringe centered around $k_x = 0$. For each dipole, one furthermore needs to account for the reflective air-silicon interface above which it is located as highlighted in the sketch (Fig. 4.6(a)). The interface-effect gives rise to an additional circular fringing concentric with $k_x = k_y = 0$ (vertical emission). An example measurement of a radiation pattern is shown in Fig. 4.6(e, inset), which excellently agrees with the prediction for the asymmetric QNM. Scattering spectra at a select set of wave vectors chosen at salient features in the radiation pattern directly reveal the coherent superposition of QNMs through Fano lineshapes, as shown by the representative curves in Fig. 4.6(e) for the wave vectors marked in the inset. The advantage of these scattering spectra is that they are essentially background free, as the cavity excitation is through the taper, not through free space.

To extract QNM frequencies and Qs from the raw data, we simultaneously fit reflection, transmission (data as plotted in Fig. 4.6(d)), and scattering spectra taken from the radiation pattern. To this end we perform a simultaneous fit to the Fano-like reflection, transmission, and scattering data with a sum of two complex Lorentzians:

$$T(\omega) = \left| 1 - \frac{\beta_{T;s}}{\omega - \tilde{\omega}_s} - \frac{\beta_{T;as}}{\omega - \tilde{\omega}_{as}} \right|^2, \tag{4.10}$$

$$R(\omega) = \left| \frac{\beta_{R;s}}{\omega - \tilde{\omega}_s} + \frac{\beta_{R;as}}{\omega - \tilde{\omega}_{as}} \right|^2, \tag{4.11}$$

$$S(\mathbf{k}, \omega) = \left| \frac{\beta_{S;s}(\mathbf{k})}{\omega - \tilde{\omega}_s} + \frac{\beta_{S;as}(\mathbf{k})}{\omega - \tilde{\omega}_{as}} \right|^2, \tag{4.12}$$

where the complex frequencies $\tilde{\omega}_{s,as}$ are common to all three fit functions, while the coefficients $\beta$ are observable-dependent. For scattering, we found that for a good fit it is not necessary to determine the full wave-vector dependent, yet frequency independent, amplitude functions $\beta_{S;s,as}(\mathbf{k})$ for each QNM). Instead, for just obtaining the complex frequencies taking just two wave vectors in the radiation pattern with a distinct Fano spectrum suffices (data as plotted in Fig. 4.6(e)).

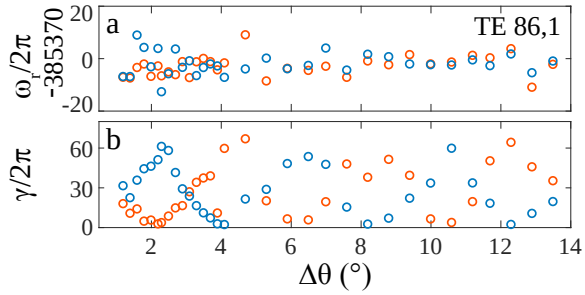


**Figure 4.7:** (a) Resonance frequencies and (b) linewidths (in GHz) of the symmetric (blue) and antisymmetric (red) modes as function of antenna separation for antennas hybridized with the 1st radial mode at azimuthal mode number $m = 86$ (TE 86-1). The largest variation is in the linewidth (panel b). The resonance frequencies show a spread due to disk fabrication variations. These subtract out when considering differences in frequency.

Figure 4.7 presents the dependence of frequency and quality factor that results from fitting data on many hybrid devices for various antenna-antenna spacing. The cavity mode is assumed to be TE for $m = 86$, and 1st radial order antenna (estimated from finite element simulations for a 15 µm diameter $Si_3N_4$ micro-disk) and the antenna size is the same as in Fig. 4.6(d-e). The oscillatory behaviour of the perturbed frequencies of the symmetric

and anti-symmetric QNMs with antenna separation is especially clear in the linewidth, where the symmetric and antisymmetric QNMs show anti-correlated behaviours. The real frequencies show much smaller variations, which are furthermore masked by frequency variations between devices, that arise from small fabrication inaccuracies. Indeed, spectroscopy on devices without antennas show that the bare cavity frequencies themselves vary by about 100 GHz, or equivalently about 0.2 nm in wavelength, equating to a spread in disk diameters around 3.5 nm. While the absolute real frequencies of the two perturbed QNMs are not useful as information due to the disk size disorder, their difference is, since the random variations due to disk diameter disorder cancel out. Fig. 4.8(a-b) reports on the systematic mode separation (blue) and the difference in linewidth (in red) for the symmetric and asymmetric QNM, for hybridization of antenna dimers with two different cavity modes. The mode $m = 86$ of first radial order (case of Figs. 4.6 and 4.7), and a mode with a substantially different azimuthal quantum number $m = 80$ and mode volume ($2^{\text{nd}}$ radial order) are shown. The period of the oscillation in $\Delta\theta$ fitted from experimental data is consistent with the anti-node spacing of the QNMs set by $m$, while the magnitude of the perturbation is markedly smaller for QNMs of radial order 2, resulting from the larger mode volumes. We traced similar results for all the whispering gallery modes within the bandwidth of our laser, which amounts to four combinations of azimuthal and radial quantum numbers in total. Panel 4.8(e) summarizes the match between the azimuthal quantum number extracted from bare cavity spectroscopy (horizontal-axis) and the value extracted from fitting Eq.(4.9) to the measured traces of linewidth versus antenna spacing.

Of the striking features predicted by our analysis, the experiments in Figs. 4.7 and 4.8(a-b) confirm that (I) the magnitude of the mode splittings varies inversely with cavity mode volume and (II) the periodicity of the splitting with antenna separation varies with the azimuthal mode number as $\cos m\Delta\theta$. As this experiment was conducted with a fixed antenna size (varying the separation $d$, as well as $m$ and $\tilde{V}$ in Eq.(4.9), but not $\alpha$), it did not give access to two other salient predictions, namely that (III) the tradeoff between real and imaginary contributions to the mode splitting depends on the phase of the polarizability $\alpha$ and (IV) that at very small separations, near-field hybridization should change the detuning behaviour. Regarding the phase of the polarizability, for Figs. 4.7 and 4.8(a-b), the antenna size was such that the antennas were close in resonance to the cavities. Since within less than a linewidth from the plasmon resonance the antenna polarizability is almost fully imaginary, the cavity perturbation should almost entirely appear through the cavity damping and not through a real frequency shift. Indeed, Fig. 4.8(a-b) directly show that for these structures the splitting in frequency (real part) is much smaller than the maximum difference in linewidth. In a second experiment (Fig. 4.8 panel (c) for the real and imaginary part of the difference frequency between symmetric and asymmetric QNMs, panel

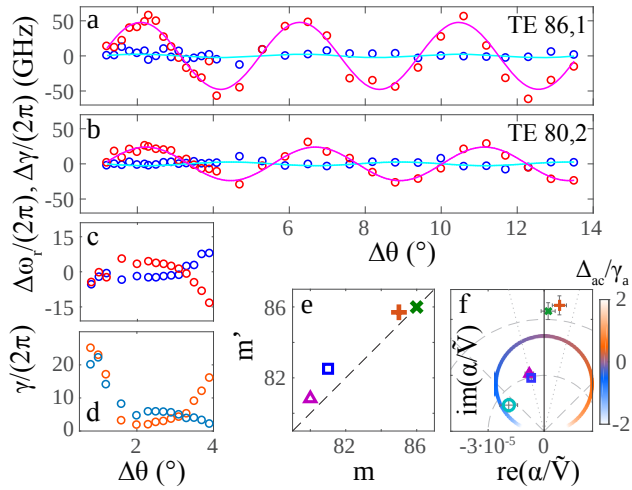


**Figure 4.8:** (a,b) The difference in resonance frequency (blue, weakly varying) and linewidth (red, strongly varying) between symmetric and antisymmetric mode as function of antenna separation for antennas hybridized with (a) the 1st radial mode at azimuthal mode number $m = 86$ (TE 86-1), and (b) a mode of larger mode volume and different azimuthal mode number (2nd order radial mode $m = 80$, TE 80-2). Panels (c,d) similar study with strongly blue-detuned antennas, where (c) shows the difference in resonance frequency (blue), and linewidth (red), while (d) reports the individual linewidths of symmetric (blue) and antisymmetric (red) modes. (e) Azimuthal mode numbers $m'$ extracted from fitting the oscillation in perturbed frequency to Eq.(4.9), versus simulated mode number $m$ for all WGM modes in the laser bandwidth. (f) Polar representation of the measured complex-valued $\alpha/\tilde{V}$ obtained by fitting the amplitude and phase of oscillation in frequency and linewidth to Eq.(4.9) (△: TE 80-2, □: TE 81-2, +: TE 85-1, ×: TE 86-1 for on-resonant antenna, and ∘ for strongly blue-detuned antenna). For reference, the circular curve shows the expected frequency dependence of $\alpha/\tilde{V}$ for a Lorentzian polarizability (Choosing $\tilde{V} \approx 300\lambda^3$, and an on resonance extinction cross section of 0.12 μm$^2$). With frequency detuning $\Delta_{ac}$ from antenna resonance (colour coding of the curve, in units of antenna linewidth) the factor $\alpha/\tilde{V}$ goes from purely imaginary to partly real (dashed and dotted lines: $\Delta_{ac}$ set to $1/2$ resp. $1/8^{th}$ of the antenna linewidth).

(d) showing mode linewidths) we have also studied a family of devices with deliberately smaller, i.e., blue-detuned antennas, focusing on a range of small antenna separations. The results on these samples highlight the role of the phase of the polarizability. For the chosen detuning $\Delta_{ac} = \omega_c - \omega_a$ of approximately half the antenna linewidth $\gamma_a = \gamma_i + \gamma_{\text{rad}}$, the polarizability had about $\pi/4$ phase, as opposed to $\pi/2$ on resonance. Consistent with the regime $\text{Re}(\alpha) \approx \text{Im}(\alpha)$, the mode splitting in the real and imaginary part of the frequency (representing respectively resonance frequency and half damping rate) are now approximately equal in size. Overall, the splittings are smaller however, owing to the fact that the polarizability of the antennas

are off-resonance at the cavity frequency. In fact, we argue that one can *use* the ratio of the real and imaginary mode splitting to estimate the ratio of $\mathrm{Re}(\alpha)$ to $\mathrm{Im}(\alpha)$, through Eq.(4.9), while one can estimate the *magnitude* of $\alpha$ by comparing the overall size of the complex frequency shift with the cavity mode volume. Figure 4.8(f) illustrates this idea. For all data sets, we have extracted the complex prefactor $\alpha/\tilde{V}$ in Eq.(4.9). The magnitude is taken from the amplitude of the cosine behaviour for the absolute value of the complex frequency shift, while the phase of $\alpha/\tilde{V}$ is taken from the complex argument of $\Delta\tilde{\omega} = \Delta\omega + i\frac{\Delta\gamma}{2}$, where we have averaged over all datapoints with $\Delta\theta > 2.5°$ to avoid the regime of near-field hybridization discussed below. The data sets with the antennas resonant near the interrogation frequency, i.e. near 780 nm, result in $\alpha/\tilde{V}$ on the imaginary frequency axis. This is consistent with the notion that the QNM mode volume $\tilde{V}$ is essentially real for high-Q cavities, while the on-resonance polarizability of a plasmon antenna is imaginary. The data further clearly shows the effect of mode volume ($n_r = 2$ radial order mode appears at significantly smaller $\alpha/\tilde{V}$ for the same antenna size, i.e. fixed $\alpha$). If one would be able to tune through the resonance of an antenna, one would expect $\alpha/\tilde{V}$ to sweep out a circle in the complex plane. The data sets with smaller antennas (Figure 4.8(f), lower left datapoints) indeed are distinctly shifted in phase by about $\pm\pi/4$, equivalent to a detuning by about half the antenna linewidth (Antenna resonance near 630 nm).

Finally, our theoretical analysis projected that at very small antenna separations deviations from the simple oscillatory dependence of mode splitting on scatterer separation would set in. While only few devices in our sample set access this regime, Figure 4.8(c,d) indeed reveal that for the smallest antenna separations, the cavity perturbation does not follow the simple oscillatory dependence of mode splitting with antenna separation. Instead, at the smallest separations, the system response is dominated by a very strong broadening of the antisymmetric cavity mode. This observation is a manifestation of near-field hybridization of the two antennas.

## **4.5.** Conclusion and outlook

We have reported a simple model for the emission enhancement properties of multimode, multi-antenna hybrid plasmon-photonic resonators, in particular focusing on whispering gallery mode cavities coupled to plasmon antenna dimers. The model projects that such hybrids sustain similarly high hybrid Purcell factors as hybrids with just a single plasmon antenna, but with the added benefit that one can tailor where emission goes, with freedom to arrange for branching ratios anywhere between symmetric and unidirectional circulation. As an example, if one would make a side-coupled waveguide the dominant loss channel for the cavity, this means that one could selectively extract light from emitters located at one of the antennas from just one waveguide port. Conversely, balancing the phase and amplitude of the two waveg-

uide input ports would enable the selective excitation of emitters placed at just one of the antennas. Our analysis shows that the perturbative effects of the antennas is tailorable through the phase relation set by antenna placement, which in turn controls the interferences required for unidirectionality and linewidth/lineshift control. The essential physics of this hybridization is confirmed by experiments in an experimental platform based on silicon nitride microdisks and aluminium nano-antennas. While most systematic cavity perturbation experiments to date had to resort to scanning probe microscopy or scanning in order to avoid having to compare different devices with their inevitable spread in fabricated dimensions, our experimental platform is sufficiently reproducible to systematically *compare* plasmon-antenna induced perturbations between devices, even for such narrowband cavities having GHz linewidths. The observations confirm our model for the hybridization physics, suggesting that indeed high-Q plasmonic hybrid modes offer advantageous LDOS and unidirectional light-matter coupling. A next step will be to actually evidence such unidirectional light-matter coupling. This would require a strictly localized placement of emitters, such as quantum dots or fluorophores, at one of the antennas. This highly challenging placement may be possible by extending the multi-step lithography approach to emitter placement, Curto et al. [82] provided that a functionalization recipe to attach quantum dots to aluminium is available, or alternatively could be possible with scanning probe microsopy using a fluorescent tip. A main challenge will lie in the fact that the unidirectionality occurs over a bandwidth equal to the linewidth of the hybrid modes ($< 0.1$ nm, up to 1 nm possible with antenna-disk hybrids) while room temperature emitters have a far larger linewidth (20 nm for typical quantum dots) [95]. We furthermore note that multimode antenna-cavity hybrids can also be of interest for controlling ensembles of emitters (distributed or localized), e.g. in the context of directional lasing, as has been already discussed for WGM cavities in the context of PT-symmetry and exceptional points [67]. To this end, it would be necessary to enrich the system with a broken symmetry, by introducing a third antenna, or unequal placement in the radial mode profile [69, 214].

# 5

# GENERATION OF PURE OAM BEAMS WITH A SINGLE STATE OF POLARIZATION

## 5.1. Introduction

It is common knowledge that photons carry energy as well as momentum. The quantized nature of energy in light has been demonstrated in the seminal demonstration of the photoelectric effect. The momentum of light, instead, is responsible for the radiation pressure phenomenon and expresses itself in the fact that absorption, scattering, or emission of a photon by an object imparts momentum to the object. This transfer of momentum is the key to optical trapping, optical tweezers and optomechanics. Less generally known is that a light beam can also carry *angular momentum* [215]. First, circular polarization, i.e., the rotation of the electric field along the direction of propagation, corresponds to *spin angular momentum* of $\pm 1$ (rigorously $\pm\hbar$). Second, light beams can also carry *orbital angular momentum* (OAM). As first proposed by Allen et al. [216], the paraxial wave equation allows uniformly polarized Laguerre-Gauss beams as a solution that have helical wave-fronts, meaning that constant phasefronts are not perpendicular to the axis of propagation, but instead form a corkscrew, as sketched in Figure 5.1(a). This directly implies that such beams carry a phase singularity right on the beam axis, around which the phase takes the form $e^{i\ell\phi}$ ($\phi$ being the azimuthal coordinate in the transverse plane). In other words, OAM beams carry an optical vortex, of integer topological charge $\ell$ equal to the OAM[1] (cf. Fig. 5.1(b)), and the ampli-

[1] Rigorously, the orbital angular momentum is OAM $= \hbar\ell$. However, in this thesis we omit the factor $\hbar$ to lighten notations.

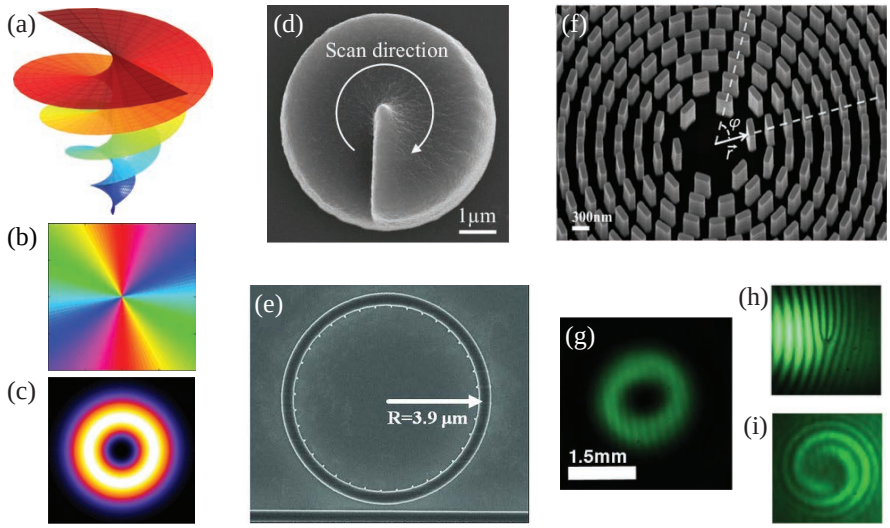


**Figure 5.1:** Orbital angular momentum (OAM) of light: concept and generation. (a) Helical wavefront carrying an OAM of +2. (b-c) Resp. transverse phase and intensity profiles of a Laguerre-Gaussian beam carrying an OAM of +2. (d) Scanning electron microscopy (SEM) image of a 5 µm diameter spiral phase plate. Reprinted from [217]. (e) SEM image of a microring resonator with angular grating patterned along the inner wall. Reprinted from [218]. (f) SEM image of a Q-plate metasurface. Reprinted from [219]. (g-i) Typical measurements of OAM beams (here carying an OAM −2), showing an intensity profile transverse to the beam with a null in its center (g), and interferograms obtained with a tilted plane wave reference beam (pitchfork dislocation, (h) and a spherical phasefront reference (spirals (i)) [219].

5

tude of the electromagnetic field vanishes at the phase singularity as depicted in Fig. 5.1(c). The discrete topological charge is of particular interest in the context of classical and quantum communication as it enables multiplexing by superposition of many orthogonal beams with different OAM [220–223]. In analogy to the momentum of light, also angular momentum can be transferred from light to matter, for instance leading to optical torque [216]. This has been studied in depth for its opportunities in optical micro-manipulation, in particular for particle sorting, and longitudinal trapping [224–227]. So called *spin-orbit* coupling for light, where the polarization degree of freedom, or *spin* of a paraxial beam is made to interact with the orbital angular momentum [228, 229], can also be exploited for probing at the nanoscale [230, 231]. Importantly, in near-field optics, outside the paraxial approximation where field and wave vector are transverse to each other, the angular momentum of a electromagnetic field cannot always be unambiguously defined. Indeed, there is a large current debate about how to separate spin and orbital contributions to angular momentum in the near field, particularly in the context of chiral light-matter interactions, and the phenomenon of spin-momentum

locking [229, 232–234].

The most intuitive way to generate OAM beams is to have a light beam propagate through (or reflect off) a structure exhibiting an azimuthal phase gradient. Conceptually simple implementations are spiral phase plates [217, 235, 236] (example shown in Fig. 5.1(d)), where the thickness of a transparent material is varied azimuthally. The emergence of liquid crystal based spatial light modulators in the early 2000s has opened the possibility to replace static phase plates with a versatile reconfigurable device to imprint amplitude and phase patterns on beams [237–241]. In the recent years, OAM generation has also become a topic of interest in the field of *nano*-photonics, pushed by a growing interest in chiral plasmonic structures [232, 242–246], and compact and broadband dielectric [219, 247, 248] and metallic metasurfaces [249, 250]. Recently, there has been a number of reports regarding OAM generation by microresonators [251, 252], and particularly microring laser cavities dressed by azimuthally periodic scattering corrugation [68, 218, 253]. These structures could allow for integrated, waveguide-accessible devices [254, 255]. Converse to the generation of OAM, the readout of orbital angular momentum is also a research topic in itself. Sorting and (de-)multiplexing techniques based on the orthogonality of modes supporting different OAM can be implemented, by properly designed holographic filters [256, 257]. However, the most common method for qualitative assessment of OAM content remains interferometry. For instance, off-axis mixing with a plane wavefront, or a spherical wavefront results in interferograms that exhibit, respectively, characteristic pitchfork (Fig. 5.1(h)) or spiral fringe patterns (Fig. 5.1(i)). For pure OAM beams, the number of branches, or arms corresponds directly to the OAM. Quantitative decomposition of a beam into its OAM content is possible with traditional [258–260] or digital off-axis holography [243, 261], which enable a full characterization of the electric field phase, amplitude and polarization which can then be projected onto OAM mode basis functions.

In this chapter, we report on the physics of rings of $N$ evenly spaced antennas placed along the perimeter of a microdisk cavity operated at azimuthal mode number $m$, generating radiation patterns that carry OAM values set by $|N - m| \pm 1$ upon evanescent incoupling using a waveguide. While this work falls in the class of literature reports on corrugated microcavity and microring systems that generate OAM, the new aspect is that we consider resonant antenna designs that allow control over the polarization content of the outcoupled light. The underlying physics is that, similarly to diffraction orders of a 1D grating, the OAM orders, which can in principle be generated by an antenna-cavity system, are directly related to the number $N$ of repeating scattering units placed along the azimuthal direction and the azimuthal quantum number $m$ (Figure 5.2) of the cavity whispering gallery modes to which the antenna array couples [218] with the caveat that, due to spin-orbit effects, the selection rules depend not only on geometry but also on polarization helicity. As in a grating, even if selection rules are fixed by $m$ and $N$, the

amplitude distribution and polarization that goes into the various allowed OAM channels is not fixed by $m$ and $N$, but by the unit cell design. We propose a design allowing for the suppression of either the right or left circular polarized OAM output, based on replacing $N$ simple linear antennas by dimers of differently oriented antennas, where the spacing and angle of the two constituent antennas causes a polarization selectivity into the unit cell. We experimentally validate the concept with interferometric measurements on fabricated devices. This is a first step towards the creation of beams for applications where the purity of the OAM beams is an important parameter, as for instance the generation of vector vortex beam lying at arbitrary position on higher-order Poincaré spheres [262].

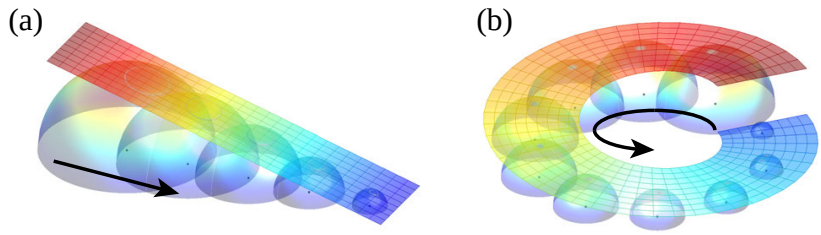


**Figure 5.2:** Scattering of a wave propagating along arrays of point scatterer according to the Huygens principle. (a) Case of a linear array: each point scatters spherical wavefronts, which are delayed in time relative to each other due the finite propagation speed of the incident wave. This scattering is equivalent to diffraction by a grating as the coherent sum of individual wavefronts in the far-field approximates to a tilted plane wave. (b) Case of an azimuthal array: the description is similar to the linear case except that the coherent sum is now a helical wave.

This chapter is structured as follows. First, in Section 5.2 we introduce the scenario of a WGM cavity decorated with a discrete set of antennas, and analyse the perturbed cavity mode structure. Next, in Section 5.3 we explain the mechanisms for generating OAM in the far field by inducing localized phased currents, laying the foundations for understanding OAM selection rules in relation to polarization. In Section 5.4 we present calculations, highlighting the OAM distribution expected for different unit cells of antennas placed in a ring. Finally, we report in Section 5.5 on the design of a structure enabling the generation of beam carrying pure OAM in a single polarization channel, leading in Section 5.6 to an experimental realization verifying our predictions.

## 5.2. Mode structure of a microdisk perturbed by a ring of $N$ antennas

In this section we discuss the hybridization of $N$ antennas with the whispering gallery modes of a disk of azimuthal quantum number $m$, particularly examining the frequency spectrum. To this end, it is useful to first examine

the physics of a ring of radially oriented dipoles concentric with the $z$-axis of an arbitrary cylindrically symmetric system (be it free space, or a micro disk). For highly symmetric ensembles in plasmonics, group theory has been shown to be a powerful tool for identifying irreducible representations [263, 264]. In a regular ring array of antennas, the analysis is even simpler as the modes complex eigenfrequencies and eigenstates can be obtained analytically [244, 246, 265].

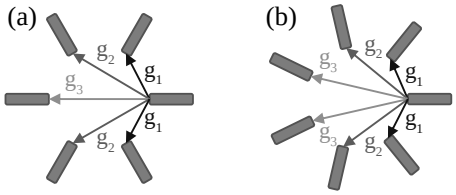


**Figure 5.3:** Sketch of the coupling between regularly spaced antennas arranged on a ring, with an even (a) or odd (b) number of elements.



### **5.2.1.** Symmetry constraints on ring modes

We consider the geometry of the system described in Figure 5.3, and assume that dipole $i$ in the chain is solely driven by the interaction with all the other particles in the chain neighbors $p_i = \epsilon_0 \alpha(\omega) \sum_{j \neq i} E_{j \to i}$. Here $\alpha(\omega)$ is the polarizability of the (identical) antennas (normalized by $\epsilon_0$) and the fields $E_{j \to i} = \frac{\omega^2}{c^2} G(\mathbf{r}_j, \mathbf{r}_i, \omega) p_j$ are specified by some Green function. The set of dipole moments is specified by a linear system

$$\mathbf{M}(\omega)\mathbf{p} = \mathbf{0}, \tag{5.1}$$

with $\mathbf{p} = [p_1, p_2, \cdots]^T$ and the interaction matrix of the form:

$$\mathbf{M}(\omega) = \begin{bmatrix} \alpha^{-1} & g_1 & g_2 & \cdots & g_2 & g_1 \\ g_1 & \alpha^{-1} & g_1 & g_2 & \cdots & g_2 \\ \vdots & \ddots & \ddots & \ddots & \ddots & \vdots \\ g_2 & \ddots & g_2 & g_1 & \alpha^{-1} & g_1 \\ g_1 & g_2 & \cdots & g_2 & g_1 & \alpha^{-1} \end{bmatrix} \tag{5.2}$$

where we defined $g_n(\omega) = -\frac{\omega^2}{c^2} G(\mathbf{r}_i, \mathbf{r}_{i+n}, \omega)$. The fact that the right hand side of Eq.(5.1) is set to zero signifies the fact that we consider the ring in absence of any external driving field. The matrix $\mathbf{M}(\omega)$ is circulant, and therefore can be diagonalized for all (complex) $\omega$

$$\mathbf{M}(\omega)\mathbf{v}_k = \lambda_k(\omega)\mathbf{v}_k, \tag{5.3}$$

with $k$ an integer constrained to the interval $k \in [\![-\lfloor \frac{N}{2} \rfloor; \lfloor \frac{N}{2} \rfloor]\!]$. Here we have introduced the eigenvectors:

$$\mathbf{v}_k = \frac{1}{\sqrt{N}} \begin{pmatrix} 1 \\ e^{i\frac{2\pi}{N}k} \\ e^{i2\frac{2\pi}{N}k} \\ \vdots \\ e^{i(N-1)\frac{2\pi}{N}k} \end{pmatrix},$$

and also the corresponding eigenvalues

$$\lambda_k(\omega) = \alpha^{-1}(\omega) + g_1(\omega)e^{i\frac{2\pi}{N}|k|} + g_2(\omega)e^{i2\frac{2\pi}{N}|k|} + \ldots + g_1(\omega)e^{i(N-1)\frac{2\pi}{N}|k|}.$$

The eigenvectors are independent of the specific form of the Green function, the diagonalization is valid at any frequency, and thus eigenvectors are not generally to be interpreted as modes (in the sense of quasinormal modes or states that we considered in previous chapters). Note that the eigenvalues are identical (degenerate) for $-k$ and $+k$. Solving for resonances of the ring Eq.(5.1) is equivalent to looking for the frequencies where null eigenvalues occur, which according to Eq (5.4), corresponds to

$$\lambda_k(\omega) = 0. \tag{5.4}$$

Each value of complex $\omega$ respecting this condition is a resonance frequency with corresponding antenna eigenstate $\mathbf{v}_k$.

Since the eigenvalues $\lambda_k(\omega)$ come in pairs only depending on the absolute value $|k|$, also the resonance frequencies come in pairs, except for the unpaired $k$-value $k = 0$, and if $N$ is even, $k = \frac{N}{2}$. For even $N$, we obtain $\frac{N}{2} - 1$ pairs of twice-degenerate modes and two non-degenerate modes. The two non-degenerate modes correspond to the extremal k-values $k = 0$ and $\frac{N}{2}$. The complex resonance frequencies follow from solving the non-linear but scalar equation

$$\lambda_k(\omega) = \alpha^{-1}(\omega) + (-1)^k g_{\frac{N}{2}}(\omega) + 2\sum_{n=1}^{\frac{N}{2}-1} g_n(\omega)\cos\left(k\frac{2\pi}{N}n\right) = 0, \tag{5.5}$$

obtained by pairwise grouping of terms. For odd $N$, we instead find $\lfloor \frac{N}{2} \rfloor$ twice-degenerate modes and a single non-degenerate mode. The resonance frequencies are given by

$$\lambda_k(\omega) = \alpha^{-1}(\omega) + 2\sum_{n=1}^{\lfloor \frac{N}{2} \rfloor} g_n(\omega)\cos\left(k\frac{2\pi}{N}n\right) = 0. \tag{5.6}$$

### 5.2.2. Whispering gallery mode system

We now focus on the specific case where the ring of antennas is coupled to a whispering gallery mode cavity, and analyse the system close to a resonance of a (degenerate) mode of azimuthal order $m$. As the system is still cylindrically symmetric, the eigenvector and eigenvalue analysis of Eqs.(5.5,5.6) still directly applies. However, near a whispering gallery mode resonance of order $m$, the Green function can be expanded over a set of QNMs [125]. If we consider a single pair of WGMs of azimuthal mode number $m$, we have

$$\begin{aligned} G(\mathbf{r}_i,\mathbf{r}_j,\omega) &= \frac{-1}{\mu_0\omega^2}\frac{\tilde{\omega}_m}{\omega-\tilde{\omega}_m}\Big[\tilde{E}_{S,m}(\mathbf{r}_i)\tilde{E}_{S,m}(\mathbf{r}_j)+\tilde{E}_{A,m}(\mathbf{r}_i)\tilde{E}_{A,m}(\mathbf{r}_j)\Big] \\ &= \frac{-1}{\mu_0\omega^2}\frac{\tilde{\omega}_m\tilde{E}_m^2}{\omega-\tilde{\omega}_m}\Big[\cos(m\phi_i)\cos(m\phi_j)+\sin(m\phi_i)\sin(m\phi_j)\Big] \\ &= \frac{-1}{\mu_0\omega^2}\frac{\tilde{\omega}_m\tilde{E}_m^2}{\omega-\tilde{\omega}_m}\cos(m(\phi_i-\phi_j)), \end{aligned} \tag{5.7}$$

where $\tilde{E}_{S,m}(\mathbf{r}) = \tilde{E}_{S,m}(r,\phi,z)$, and $\tilde{E}_{A,m}(\mathbf{r})$ are the normalized electric field of, respectively, the symmetric and anti-symmetric WGM of interest with azimuthal number $m$ (projected onto the direction of antenna dipole moment for simplicity). Here we introduced $\tilde{E}_m(r,z)$ to correspond to the transverse mode profile such that $\tilde{E}_{S,m}(r,\phi,z) = \tilde{E}_m(r,z)\cos(m\phi)$ and $\tilde{E}_{A,m}(r,\phi,z) = \tilde{E}_m(r,z)\sin(m\phi)$. With this assumption we obtain an expression for the coupling terms entering Eq.(5.1),

$$g_n(\omega) = -\frac{\omega^2}{c^2}G^{(m)}(\omega)\cos(m\Delta\phi_n), \tag{5.8}$$

where $\Delta\phi_n = 2\pi\frac{n}{N}$ represents the angular separation between an antenna and its $n^{th}$ neighbor. For compactness, we have introduced

$$G^{(m)}(\omega) = \frac{-1}{\mu_0\omega^2}\frac{\tilde{\omega}_m\tilde{E}_m^2}{\omega-\tilde{\omega}_m}$$

as an $m$-dependent amplitude function that describes the frequency spectrum of mode $m$. More generally, one would need to describe the cavity not by a single (degenerate) mode, but by a sum over many quasi-normal modes.

Taking the particular form of terms $g_n$ for azimuthal mode number $m$ and inserting it in Eqs.(5.5,5.6) we obtain for even $N$,

$$\begin{aligned} \lambda_k(\omega) = \alpha(\omega)^{-1} - \frac{\omega^2}{c^2}G^{(m)}(\omega)\Big[1+(-1)^{m+k} \\ +\sum_{n=1}^{\frac{N}{2}-1}\cos\left(2\pi\frac{m+k}{N}n\right)+\cos\left(2\pi\frac{m-k}{N}n\right)\Big], \end{aligned} \tag{5.9}$$

and for odd $N$,

$$\lambda_k(\omega) = \alpha(\omega)^{-1} - \frac{\omega^2}{c^2} G^{(m)}(\omega) \left[1 + \sum_{n=1}^{\left\lfloor \frac{N}{2} \right\rfloor} \cos\left(2\pi \frac{m+k}{N} n\right) + \cos\left(2\pi \frac{m-k}{N} n\right)\right]. \quad (5.10)$$

By analysing these equations, we identify three scenarios:

a). Generically, neither $m+k$ nor $m-k$ are divisible by $N$, leading to

$$\lambda_k(\omega) = \alpha(\omega)^{-1}.$$

b). $m+k$ and $m-k$ can be simultaneously divisible by $N$ in which case

$$\lambda_k(\omega) = \alpha^{-1}(\omega) - N \frac{\omega^2}{c^2} G^{(m)}(\omega).$$

c). When only $m+k$ or $m-k$ is divisible by $N$, but not both, we have

$$\lambda_k(\omega) = \alpha^{-1}(\omega) - \frac{N}{2} \frac{\omega^2}{c^2} G^{(m)}(\omega). \quad (5.11)$$

Since $k$ must lie in the irreducible range $[\![-\lfloor \frac{N}{2} \rfloor; \lfloor \frac{N}{2} \rfloor]\!]$, only a single $k$ can respect either b) or c) for a chosen cavity mode number $m$ and a set $N$. These cases can be understood as follows.

- For the collective antenna modes of case a), the effective polarizability of the antennas is not perturbed at all by the cavity, which implies that these collective antenna modes are decoupled from the cavity. In this work we will only consider scenarios that address the antennas *through* the cavity. Hence, the uncoupled collective antenna modes are irrelevant for this work.

- Case b), occurs particularly when the number of antennas $N$ exactly equals the azimuthal mode order of the cavity modes. In this case the degeneracy of the two cavity modes is lifted in the standing wave basis. The $\cos m\phi$ standing mode is maximally perturbed because all antennas are located at the maximum of the mode profile, and each mode profile maximum has an antenna in it. The dipole moment either points in the same direction as the cavity field (always radial at $k = 0$), or alternates from dipole to dipole for $k = \frac{N}{2}$. The $\sin m\phi$ mode is not perturbed by the antennas, since they are located at the nodes of the mode field.

- In case c), both cavity modes are perturbed by the antennas, but both are shifted in equal amounts so that the degeneracy remains. Assuming (without loss of generality) that $m > 0$ $k > 0$, if $m - k$ is divisible by $N$, then the cavity mode of mode number $m$ couples to antenna mode $k$, and conversely cavity mode $-m$ coupled to antenna mode $-k$. This is the basis for literature reports on OAM generation by microring systems. For instance, Cai et al. report in [218] on the simplest case where $m - k = N$, and they show that their devices emit an OAM of $\ell = k$ ($\pm 1$ for right/left circular polarization, cf. Section 5.3.3). If instead $m + k$ is divisible by $N$, the cavity mode $m$ will couple to antenna mode $-k$ (and $-m$ to $k$).

To conclude this classification, our analysis shows that even though, in principle a ring of $N$ antennas has $N$ eigenmodes, most of these are decoupled from WGM of order $m$, with the exception of either one or two modes. The scenario for the coupled modes depends on the arithmetic relationship between $m$ and $N$. The first scenario occurs exactly when $N$ and $m$ are equal or satisfy a commensurate relationship, the antennas lift the WGM mode degeneracy, leaving one unperturbed standing wave mode and one strongly shifted standing wave mode. The induced distribution of dipole moments carries no azimuthal phase gradient. The second experimentally relevant scenario occurs when $m$ and $N$ are not quite equal. Both WGMs are equally shifted and remain degenerate while coupling to eigenmodes with angular momentum $\pm k$ set by the difference between $m$ and $N$.



### 5.2.3. Perturbation formula

In this work we consider generating OAM by operating in the scenario of coupling WGM modes of mode number $m$ close to but not equal to the number of antennas $N$. We analyse the cavity frequency shift induced by the antennas on both the cavity modes. In other words, we analyse the eigenvalue problem for coupling WGM modes of mode number $m$ to $N$ antennas, with $N$ not commensurate with $m$. Eq.(5.11) then reads

$$\lambda_k(\omega) = \alpha(\omega)^{-1} - \frac{N}{2}\frac{\tilde{\omega}_m \epsilon_0 \tilde{E}_m^2}{\omega - \tilde{\omega}_m}. \tag{5.12}$$

We can solve Eq.(5.4) for the eigenfrequency $\tilde{\omega}'_m$ in the perturbative regime by a Taylor expansion of $(\omega - \tilde{\omega}_m)\lambda_k(\omega)$ close the complex resonance frequency of the cavity mode of interest $\tilde{\omega}_m$

$$\tilde{\omega}'_m = \tilde{\omega}_m - \tilde{\omega}_m \frac{N}{2}\alpha(\tilde{\omega}_m)\epsilon_0 \tilde{E}_m^2 = \tilde{\omega}_m - \tilde{\omega}_m \frac{N}{2}\frac{\alpha(\tilde{\omega}_m)}{2\tilde{V}_m}, \tag{5.13}$$

where we introduce the effective mode volume at the position $\mathbf{r}$, $\tilde{V}_m(\mathbf{r}) \equiv \frac{1}{2\epsilon\epsilon_0(\tilde{E}_m(\mathbf{r}))^2}$ [124]. The complex frequency shift of the cavity mode is proportional to the perturbation caused by a single antenna $\frac{\Delta\tilde{\omega}}{\omega} = -\frac{\alpha}{2\tilde{V}_m}$ as it is

given in [139, 140], multiplied by half of the number of antennas (degenerate modes share equally the perturbation of N antennas). For a cavity dressed by near-resonant antennas the quality factor $Q'_m$ of the perturbed (high-Q) cavity mode(s) $m$ can be approximated by

$$Q'_m \approx Q_m \left(1 - Q_m N \frac{\alpha_i(\tilde{\omega}_m)}{2\tilde{V}_m}\right)^{-1} \tag{5.14}$$

where $Q_m$ is the unperturbed quality factor, $\alpha_i$ is the imaginary part of the polarizability of each antenna, and we approximated $\tilde{V}_m$ as real. For strong perturbations the intrinsic quality factor becomes irrelevant and the quality factor is determined solely by the number of antennas, their polarizabilities and the cavity mode volume

$$Q'_m \approx -\frac{2\tilde{V}_m}{N\alpha_i(\tilde{\omega}_m)}. \tag{5.15}$$

5

As an estimate, if we consider the $Si_3N_4$ microdisk cavities from Chapter 4, the original unpertubed Q is $10^5$, and two antennas reduce it to $10^4$. To produce modest values of OAM with these WGM ($m = 80 - 86$), one would need in the order of $\sim 10^2$ antennas. At the coupling strength used in Chapter 4, with antennas directly on the disk, $10^2$ antennas would lower the Q to values below $Q \sim 100$, so low that the linewidth starts to exceed the free spectral range. Therefore, if the lowest Q one accepts is $10^3$ to avoid spectral overlap between different WGM, one would need to reduce the coupling strength of the antennas to the cavity by a factor 10 compared to the design of Chapter 4, for instance by spacing antennas further away from the disk surface.

## 5.3. How currents on a ring generate OAM radiation

In the previous section we have established that if one addresses a discretized ring of $N$ antennas by a whispering gallery mode of mode number $m$ close to but not equal to $N$, this induces a dipole moment distribution with azimuthal phase dependence $e^{i\ell\phi}$, where $|\ell| = |m - N|$. This section aims to guide the reader through the mechanisms by which the radiation pattern of a circular chain of antennas with a phase pattern varying as $e^{i\ell\phi}$ contains orbital angular momentum. To this end, we first consider the scalar wave equation and focus on the far-field radiation pattern from a continuous current distribution on a ring. Next we discuss the impact of discretization of the current distribution into $N$ segments. Finally, we add polarization to the continuous current distribution and discuss how it governs the far-field orbital angular selection rules.

### 5.3.1. Continuous scalar current distribution

Let us consider a ring $S$ of radius $R$ on which a current distribution is imposed that is constant in strength over the ring, but carries a phase $e^{i\ell\phi}$ that varies with position on the ring (azimuth $\phi$, radius $R$ and $z = 0$ in spherical coordinates) [266]

$$p(\mathbf{r}) \propto e^{i\ell\phi}\delta(z = 0, r = R). \tag{5.16}$$

At this stage we ignore polarization effects and assume that each of the points on the ring radiates a scalar spherical wave into the far-field. This assumption means that the field radiated in the direction of wave-vector $\mathbf{k}$ by a point on the ring at position $\mathbf{r}_p$ (azimuth $\phi_p$, radius $R$ and $z = 0$ in spherical coordinates) reads [16]

$$F(\mathbf{r}_p, \mathbf{k}) = \frac{e^{ikd_{\text{obs}}}}{4\pi\epsilon_0 d_{\text{obs}}} e^{-i\mathbf{k}\cdot\mathbf{r}_p} e^{i\ell\phi_p}, \tag{5.17}$$

where we evaluate the field at an observation point a distance $d_{\text{obs}}$ away from the origin, in a viewing direction specified by the orientation of the wave vector $\mathbf{k}$ that has length equal to the wave number $k = n\omega/c$ of light in the medium of index $n$ surrounding the ring. Since, in the following, the overall spherical wave $\frac{e^{ikd_{\text{obs}}}}{4\pi\epsilon_0 d_{\text{obs}}}$ is a common prefactor to all radiation patterns, we omit it. The field radiated by the full ring of phased current elements is therefore obtained by superposition

$$\begin{aligned} F_S(\mathbf{k}) &\propto \int_S e^{i\mathbf{k}\cdot\mathbf{r}_p} e^{i\ell\phi_p} d\mathbf{r}_p \propto \int_0^{2\pi} e^{i\ell\phi_p - ikR\sin(\theta)\cos(\psi-\phi_p)} d\phi_p \\ &\propto (-i)^\ell e^{i\ell\psi} J_\ell(kR\sin(\theta)), \end{aligned} \tag{5.18}$$

where $k = \|\mathbf{k}\|$, $\theta$ is the angle of $\mathbf{k}$ with normal direction and $\psi$ is the azimuth far-field coordinate. Mathematically this procedure just states that the radiation pattern of a sum of currents reflects the Fourier transform of the current distribution. We note that the ensemble radiates light in the far-field according to a Bessel function of the first kind, with a phase distribution that varies as $e^{i\ell\psi}$, i.e., as the imposed phase on the current distribution. For any integer $\ell$, this means a pure orbital angular momentum of $\ell$ specifying the azimuthal distribution of radiation.

### 5.3.2. Discrete versus continuous current distributions

While in the previous discussion we considered a continuous current distribution, in this chapter we are actually focusing on a scenario where a discrete set of $N$ scatterers are evenly spaced on a ring are driven by a circulating whispering gallery mode, and where we assume we can consider each scatterer as a driven point source. The purpose of this section is to explain how discretized current distributions differ from a continuous current distribution.

Remaining in a scalar picture, recall that the continuous current distribution of a pure OAM state:

$$p(\mathbf{r}) \propto e^{i\ell\phi}\delta(z=0, r=R) \tag{5.19}$$

gives as far field output a Bessel beam with a single OAM contribution

$$F_S(\mathbf{k}) \propto (-i)^{\ell} e^{i\ell\psi} J_m(kR\sin(\theta)). \tag{5.20}$$

A discrete current distribution of $N$ dipoles

$$p_N(\mathbf{r}) \propto \sum_{n=1}^{N} e^{i\ell\phi}\delta\left(z=0, r=R, \phi=\frac{2\pi}{N}n\right) \tag{5.21}$$

is simply the product of a continous current distribution and a sum of delta-functions. Evidently, the discretized distribution has higher order Fourier components $\tilde{p}_{N,q}$ not present in the original:

$$p_N(\mathbf{r}) = \sum_{q=-\infty}^{\infty} \tilde{p}_{N,q} e^{iqN\phi} \propto \sum_{q=-\infty}^{\infty} e^{i(\ell+qN)\phi}. \tag{5.22}$$

These Fourier components occur at all integers equal to $\ell$ modulo $N$. This can be viewed as similar to 'aliasing' in discrete Fourier transforms: if one discretely samples a harmonic signal of order $\ell$ on $N$ points, its sampling is indistinguishable from that of any harmonic signal with $\ell' \equiv \ell \mathrm{mod} N$. Constructing the radiation pattern by superimposing the radiation from all Fourier components of the current, we conclude that the scattering of $N$ antennas driven by a field with azimuthal dependence $e^{i\ell\phi}$ (angular momentum $\ell$) will contain a sum of terms $J_{\ell'}(kR\sin\theta)e^{i\ell'\phi}$ with contributions of all orbital angular momentum of orders $\ell' = \ell + qN$, with $q \in \mathbb{Z}$. In the following, we call fundamental OAM (or simply *OAM*) $\ell_0$ the smallest (relative) integer to respect the OAM selection rule, and the sideband separated by integer times $N$ from $\ell_0$ are referred to as harmonic orbital angular momentum.

### 5.3.3. Polarization imposed on the driven current distribution

Since electromagnetic waves are not scalar but vectorial in nature, one generally has to consider that the source dipole moments have a polarization direction, while the far-field radiation pattern can be studied in various far-field polarization channels. To highlight the implications we return to the case of a continuous current distribution, and first consider the case where each element of the ring is identically polarized, with for instance, all elements being a linear dipole moment along $x$ as sketched in Figure 5.4(a). We denote by $|\mathbf{X}\rangle$ the radiation pattern of an $x$ oriented dipole at the origin, which for wave vectors close to the $k_z$-axis (paraxial regime, viewing the ring head on) is $x$-polarized. The radiation pattern of an $x$-dipole displaced to $\mathbf{r}_p$ from the

origin simply follows the logic of Eq.(5.17), but multiplied with $|\mathbf{X}\rangle$. Therefore the radiated vector far-field of the entire ring, i.e. of a dipole distribution $\mathbf{p}_x(\phi) \propto e^{i\ell\phi}\mathbf{e}_x$, can be expressed as

$$\mathbf{F}_{S,x}(\mathbf{k}) \propto (-i)^\ell e^{i\ell\psi} J_\ell(kR\sin(\theta))|\mathbf{X}\rangle. \tag{5.23}$$

Similarly, a ring of dipoles oriented in $y$ direction (Fig. 5.4(b)), i.e. a dipole distribution $\mathbf{p}_y(\phi) \propto e^{i\ell\phi}\mathbf{e}_y$ would give

$$\mathbf{F}_{S,y}(\mathbf{k}) \propto (-i)^\ell e^{i\ell\psi} J_\ell(kR\sin(\theta))|\mathbf{Y}\rangle. \tag{5.24}$$

In other words, if the current elements on the ring are linearly and *identically* polarized, and driven with an azimuthally dependent phase increment $e^{i\ell\phi_p}$, then the radiated far field simply inherits the orbital angular momentum of $\ell$, and the Bessel-beam type polar distribution from the scalar case, but now in the polarization channel along the imposed dipole moments.

For currents on a ring, rotational symmetry considerations make it more intuitive to consider radial and azimuthal linear orientations of the current elements along the ring

$$\mathbf{p}_r = p_r\mathbf{e}_r \text{ and } \mathbf{p}_\phi = p_\phi\mathbf{e}_\phi,$$

as opposed to Cartesian linear orientation $\mathbf{p}_x = p_x\mathbf{e}_x$ and $\mathbf{p}_y = p_y\mathbf{e}_y$. We now show how the OAM generated by such current distributions with phased driving can be understood, using a circular polarization basis as an intermediate step. We first consider circular polarization in the Cartesian lab frame, i.e., with identical circular polarization for all current elements in the $xy$ lab frame. By linear superposition of two rings polarized along $x$ and $y$ one can generate circular left and right handed current distributions $\mathbf{p}_{L/R} = \frac{1}{\sqrt{2}}\left(\mathbf{p}_x(\phi) \pm i\mathbf{p}_y(\phi)\right)$ that (in the paraxial approximation) radiate circular left and right-handed polarized light $|\mathbf{L/R}\rangle = \frac{1}{\sqrt{2}}(|\mathbf{X}\rangle \pm i|\mathbf{Y}\rangle)$ (Figure 5.4(c))

$$\mathbf{F}_{S,R/L}(\mathbf{k}) \propto (-i)^\ell e^{i\ell\psi} J_\ell(kR\sin(\theta))|\mathbf{R/L}\rangle. \tag{5.25}$$

Thus labframe circular left/right handed current distributions with a phase $e^{i\ell\phi}$ will scatter a lab-frame circular left/right handed polarized beam carrying an OAM of $\ell$, at least at moderate scattering angles (ignoring that in a high NA microscope dipole radiation patterns do have crossed polarized contributions).

A subtle point is that the circularly polarized source distribution in the *lab frame* at orbital angular momentum $\ell$ can be interchangeably written as a circularly polarized source distribution expressed in the *cylindrical coordinate frame*, but at a shifted orbital angular momentum $\ell \pm 1$. To see this, consider

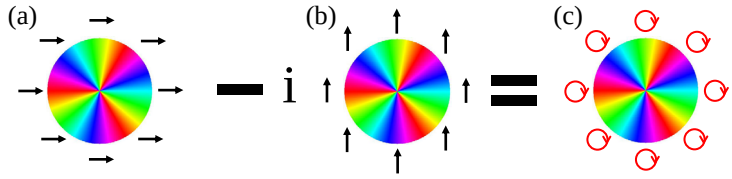


**Figure 5.4:** Schematic representation of polarized beams carrying OAM ($\ell = +3$ here). (a-b) Show respectively, a $x$ and a $y$-polarized beams carrying the same OAM of $\ell$ (generated by a $x$ and a $y$-polarized array of antennas). (c) A linear superposition of a $x$ and a $y$-polarized array of antenna in phase quadrature ((c) = (a) – $i$(b)), i.e. a circularly polarized array of antenna, radiates a circularly polarized beam, here circular right.



the cylindrical linear vectors that are radially outwards resp. azimuthal, i.e. $\mathbf{p}_r$ and $\mathbf{p}_\phi$. They can be expressed in the Cartesian basis vectors $\mathbf{p}_x$ and $\mathbf{p}_y$ as $\mathbf{p}_r = \cos\phi\,\mathbf{p}_x + \sin\phi\,\mathbf{p}_y$ resp. $\mathbf{p}_\phi = -\sin\phi\,\mathbf{p}_x + \cos\phi\,\mathbf{p}_y$. Evidently circular source polarization in the cylindrical basis ($\mathbf{p}^{Cy}_{L/R} = \frac{1}{\sqrt{2}}(\mathbf{p}_\theta \pm i\mathbf{p}_\phi)$ is equivalent to circular polarization in the Cartesian basis, but with an additional phase factor due to the redefinition of the basis vectors, that carries a *single* unit of OAM. This simply reflects the fact that going around the circle, the cylindrical basis vector pair rotates by exactly $2\pi$ relative to the lab frame basis. This simple geometry analysis can be directly used to understand the appearance of helicity in selection rules for OAM generation. For instance, consider a ring of radially oriented antennas, i.e., a radially oriented source distribution carrying a phase distribution $e^{i\ell\phi}$. The radial distribution can be decomposed as the coherent sum of a right and a left-handed circularly polarized source distribution in the cylindrical basis that each carry the same phase profile $e^{i\ell\phi}$. However, reexpressing this source distribution in lab-frame circular polarization, the radially oriented source distribution is equivalent to a coherent sum of a right and a left-handed circularly polarized source distribution at a *different* OAM number (i.e., $\ell \pm 1$ for the two helicities). Since lab-frame source polarization translates to lab-frame radiation pattern polarization, the implication is that a radially oriented source distribution of phase profile $e^{i\ell\phi}$ generates a pure OAM of $\ell + 1$ in the left-handed circularly polarized component of the radiation pattern, and $\ell - 1$ in the right-handed circularly polarized component. Figure 5.5 graphically illustrates this construction, starting with a radially polarized source distribution of OAM +2, which decomposes in left resp. right handed polarization carrying an OAM +2 in the *cylindrical coordinate frame*, but an OAM +1 resp. +3 in the *lab frame*. While the argument is purely geometrical, some authors view this as conservation of total angular momentum whereby the sum of OAM and spin (+1 for LHCP, −1 for RHCP) must be the same for both polarization channels [229] for a source distribution with no intrinsical spin.

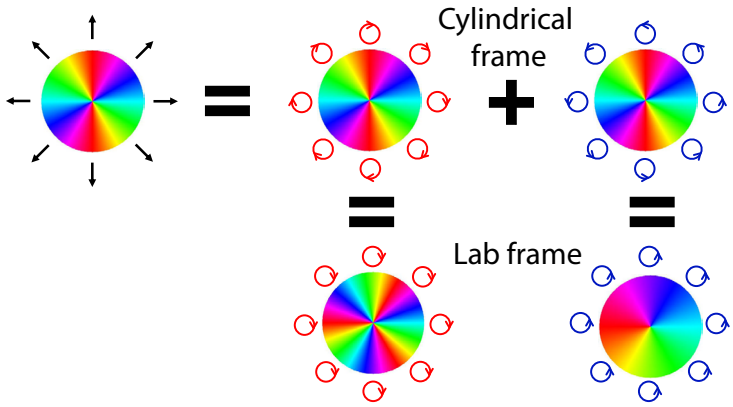


**Figure 5.5:** Equivalence between polarization decompositions. A latitudinal vector beam carrying an OAM $\ell = +2$ can intuitively be decomposed over a circular polarization basis in a cylindrical coordinate rotated frame. In this basis, the two polarization channels still both carry the OAM $\ell = +2$. However, since in the global lab frame, circular polarizations are shifted in angular momentum compared to the rotated frame, the circular right and left decomposition of our vector beam carry an OAM of $\ell_R = \ell - 1 = +3$ resp. $\ell_L = \ell - 1 = +1$.



## 5.4. Examples of radiation patterns

The purpose of the previous section was to provide qualitative insight in the radiation patterns expected for $N$ equally spaced antennas on a ring, driven with an orbital angular momentum $\ell$, where we concluded that:

- In a scalar treatment $N$ evenly spaced antennas on a ring, driven with phase dependence $e^{i\ell\phi}$ will result in a radiation pattern that contains all orbital angular momentum of orders $\ell' = \ell + qN$, with $q \in \mathbb{Z}$.

- Each OAM contribution has a donut-shaped intensity distribution, described by a Bessel function $J_{\ell'}(kR\sin\theta)$, where the order increases with $\ell'$. Thus the beam opening angle ($\theta$) of the first fringe is directly related to the diameter of the ring of antennas, and to the OAM order.

- Adding polarization to the analysis, if all antennas are radially oriented, each of the terms with OAM order equal to $\ell'$ will actually appear as contributions at $\ell' \pm 1$ when analysed in a lab-frame circular polarization basis (R resp. L). For tangentially oriented antennas a similar argument holds.

In this section we will supplement this analysis with calculated radiation profiles for various scenarios in which $N$ antennas on a ring are driven by an assumed whispering gallery mode with azimuthal quantum number $m$. The

calculations consist in numerically evaluating the full vectorial radiation diagrams of $N$ point dipoles of fixed (complex-valued) dipole moment taking due account of the phase factor $e^{i\mathbf{k}\cdot\mathbf{r}_p}$ related to the placement of the dipole and the viewing direction specified by $\mathbf{k}$. This means we did not *impose* the results of the analysis in the previous section. Also it should be noted that the calculation does not evaluate near-field / multiple scattering interactions. This is not a limitation per se, since section 5.2 reports that, even if one rigorously includes these interactions, while they will renormalize mode eigenfrequencies, nonetheless the induced antenna moments will simply trace out $e^{i\ell\phi}$, i.e., pure single-valued OAM. As radiation pattern of the single antenna we consider far-field radiation of dipoles in free space, ignoring that (our) experiment will involve dielectric interfaces due to substrate and cavity. The diagrams report intensity and phase as a function of viewing direction, specified by parallel momentum ($k_x$ and $k_y$) normalized to the wave number. Equivalently, these are the amplitude and phase distributions as expected in the back focal plane (BFP) of a Fourier microscope. Polarization analysis has been performed in the BFP coordinate system. The BFP image of an objective contains the spherical wave radiated by the object transformed into a cylindrical coordinate system. Going back to spherical coordinates, BFP lattitudinal polarization actually corresponds to $p$-polarized light, while azimuthal polarization equals $s$-polarization.



### **5.4.1.** Superposition of OAM terms

As a first example, Figure 5.6 shows the radiation profile of a ring of radius 1 µm, with $N = 5$ radially oriented antennas, driven by a radially polarized field with phase distribution $e^{im\phi}$ and azimuthal mode number $m = 7$. Here, the radiation pattern has been separated in what would be latitudinal (a) and azimuthal (b) polarization channels in the back focal plane. We obverse that for both channels the pattern is not simply rotation invariant as one would expect for a single OAM contribution (e.g., the simple *donut* shape of Laguerre-Guaussian beams). Instead, the far-field radiation diagram has 5-fold rotation symmetry in both polarization channels. Additionally, the azimuthally and latitudinally polarized intensity distributions are markedly different. In particular, for grazing angles ($|\mathbf{k}_\parallel/k_0| \approx 1$ ) light is only scattered into azimuthal polarization. This is easy to understand since $|\mathbf{k}_\parallel/k_0| \approx 1$ corresponds to wave vectors in the $k_x, k_y$-plane (no z-component) and $p$-polarization corresponds to polarization along the $z$-axis. Since the dipole distribution is radial, i.e. fully contained in the $xy$-plane, the electric field can have no $z$-component in the $k_x, k_y$ plane.

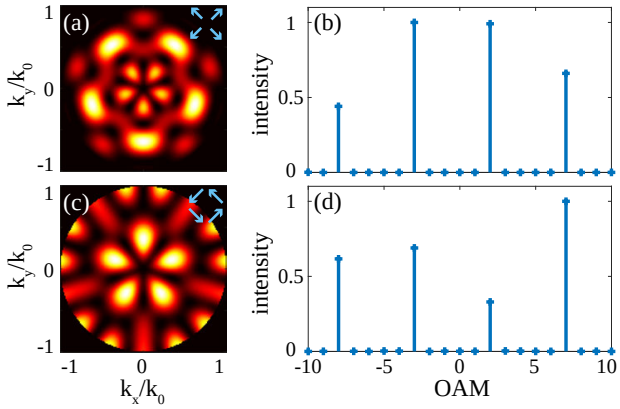


**Figure 5.6:** Harmonics of orbital angular momentum for an array of $N = 5$ radially oriented antennas, placed on a disk of radius 1 μm and mode number $m = 7$. (a,c) Radiation pattern for respectively latitudinal and azimuthal polarization. (b,d) Orbital angular momentum content for respectively latitudinal and azimuthal polarization. We observe that light is scattered with a multitude of orbital angular momentum harmonics OAM $= m - N + qN = +2 + qN$, with $q \in \mathbb{Z}$.

5

Decomposing the *field* in OAM contributions[2], we find that the fundamental OAM is $\ell = m - N = +2$, and harmonics are separated by integer multiples of $N = 5$. This exactly follows the reasoning that a discretized current distribution carries a comb of OAM orders. Each of the OAM contributions taken separately *is* rotationally invariant in intensity. However, the interference of the many OAM itself does not respect the rotation invariance of the intensity of each OAM contribution, and this causes the $N = 5$-fold rotation symmetry. Indeed, according to Section 5.3.2, OAM harmonics $\ell_a$ and $\ell_b$ must obey $m - l_a = aN$ and $m - l_b = bN$. The interference pattern between these two harmonics will therefore exhibit a $\cos(a-b)N\psi$ dependence. The slowest spatial variation possible in the interference between two harmonics is obtained for $|a - b| = 1$ and has $N = 5$-fold symmetry. Since all higher order interference terms also possess this symmetry (and higher multiples), the total radiation pattern is $N = 5$-fold symmetric.

As a second example Figure 5.7 considers a case with a far larger set of $N = 23$ antennas, driven by a $m = 25$ whispering gallery mode (ring radius now assumed 2 μm), so that the *difference* $m - N$ is identical to that in the previous example. Since the higher the OAM, the further from the paraxial direction ($\mathbf{k}_\parallel / k_0 \approx 0$) light is emitted, when $N$ is large enough, the higher

[2]We perform the OAM decomposition of a complex far-field distribution, projected onto an arbitrary polarization $F_S(\theta_\psi)$ similarly as it was described in reference [260]. We first calculate the angular Fourier coefficients $c_m(\nu) = \frac{1}{2\pi}\int_0^{2\pi} F_s(\nu,\psi)e^{-im\psi}d\psi$, where $\nu \equiv \|\mathbf{k}_\parallel\|/k_0$. Then the intensity of the beam into the $m$-order OAM state is obtained from the coefficients $c_m$ by integrating their square modulus along the *radial* coordinate $\nu$, $P(m) = \int_0^1 |c_m(\nu)|^2 d\nu$.

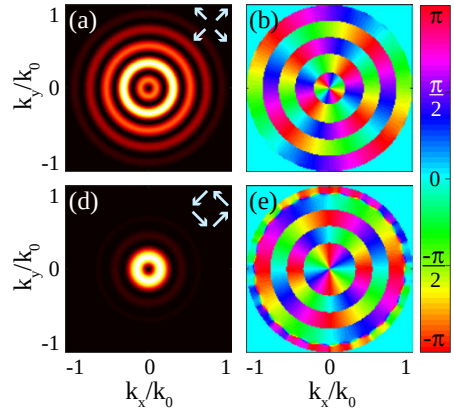


**Figure 5.7:** Radiation diagram for latitudinal and azimuthal polarization radiated by an array of $N = 23$ radially oriented antennas, placed on a disk of radius 2 µm and mode number $m = 25$. (a,d) Intensity profiles for resp. latitudinal and azimuthal polarization. (b,e) Phase profiles for resp. latitudinal and azimuthal polarization: both polarizations carry an OAM $= m - N = +2$.



harmonics in OAM now do not interfere significantly with the fundamental term. Consequently, now the radiation pattern is essentially rotation invariant, while the phase of the field varies by $2\pi l$ with $\ell = 2$ when encircling the paraxial direction. At very high angles, $|\mathbf{k}_\parallel / k_0| \approx 1$ higher harmonics do still play some role as it can be observed in the phase profile in Fig. 5.7(e). In terms of distribution of intensity, one should note that a ring of antennas will not provide a Laguerre-Gaussian beam after collection by an objective lens, but instead a superposition of Bessel functions. There is also a marked difference between the latitudinal and azimuthal polarization channel, due to different symmetries of the two polarizations. Figure 5.8 shows an analysis of the same physical system, but in circular polarization channels. We note that for this polarization channels, the amplitude profile follows a pure Bessel function (in the paraxial approximation), and demonstrates the appearance of spin in the OAM selection rule, as expected.

### 5.4.2. Generating pure OAM in a single circular polarization state

We have seen that regular arrays of radially polarized antennas will simultaneously scatter light in both left and right circular polarization, with different OAM. The notion that one can modulate the antenna orientation to further engineer the superposition of OAM makes it in principle possible to selectively generate a single OAM in a single circular polarization channel. We envision that a waveguide-driven generator of *pure* OAM in a single polarization channel without the need for *a posteriori* circular polarization selection could be of use in applications. Recently such a source has been realized in form

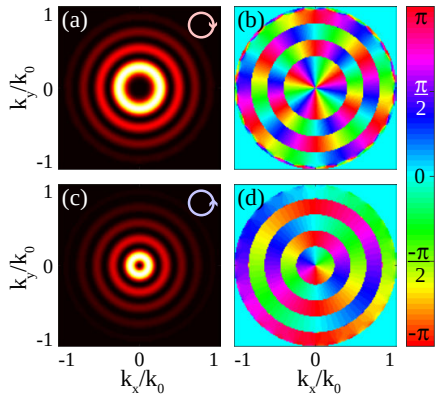


**Figure 5.8:** Radiation diagram for circular polarizations, for the configuration as in Fig. 5.7. (a,c) Intensity profiles for resp. circular right and circular left polarization. (b,d) Phase profiles for resp. circular right and circular left polarization: right handed light carries $\ell_R = m - N + 1 = +3$ while left handed light carries $\ell_L = m - N - 1 = +1$.



of an OAM microlaser, not using geometry, but using a rather peculiar spin-selective gain memory in a quantum well system, whereby chiral pump light can select a pure circular polarization output and hence OAM [252]. In a lasing system, a slight intrinsic chiral preference suffices for high OAM/helicity purity, but this is not the case in scattering based implementations of WGM sources. Our idea is that for a target OAM of value of $l+1$ that is of pure circular polarization, and using a whispering gallery mode of azimuthal quantum number $m$, one should still use a total of $N$ scattering unit cells, but instead of having a single antenna per unit cell, one needs a more complex unit cell response for polarization control. This is realizable by having two antennas per unit cell.

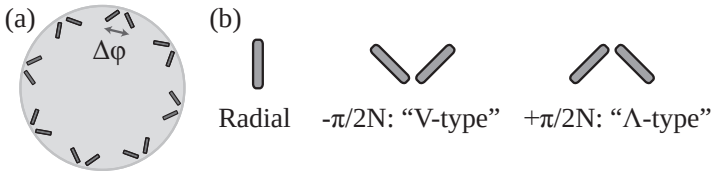


**Figure 5.9:** (a) Sketch of a disk dressed with N pairs of antennas. In each pair, antennas are rotated by $+45°$ and $-45°$ from the radial direction, and separated by an angle $\Delta\phi$ (center to center). (b) We propose three geometries for our experiment; radial orientation, V-type and $\Lambda$-type.

We propose the design sketched in Figure 5.9, where essentially two interspersed arrays of $N$ antennas are placed on a ring, one array with antennas rotated by $+45°$ from the radial direction (and hence from the driving cavity field for a TE mode, if we envision driving by a WGM), and the second rotated

by −45°. The two arrays are placed at the same radial distance from the center of the cavity, but are azimuthally shifted by an angle Δ. Once antennas are polarized by a cavity WGM of mode number $m$ (radial field varying as $e^{im\phi}$), the distribution of dipole moments is described via

$$\begin{cases} p_r(\phi) \propto & \sum_{n=1}^{N} e^{+im\phi}\left[\delta(\phi - \frac{2\pi}{N}n + \frac{\Delta}{2}) + \delta(\phi - \frac{2\pi}{N}n - \frac{\Delta}{2})\right] \\ p_\phi(\phi) \propto & \sum_{n=1}^{N} e^{+im\phi}\left[\delta(\phi - \frac{2\pi}{N}n + \frac{\Delta}{2}) - \delta(\phi - \frac{2\pi}{N}n - \frac{\Delta}{2})\right], \end{cases} \tag{5.26}$$

which can be simplified by considering only the first relevant harmonics $\ell$, i.e. responsible for scattering the fundamental OAM $\ell = m - N$ as

$$\begin{cases} p_r(\phi) \propto & e^{+i\ell\phi}\cos\frac{N\Delta}{2} \\ p_\phi(\phi) \propto & -ie^{+i\ell\phi}\sin\frac{N\Delta}{2}, \end{cases} \tag{5.27}$$

This (vectorial) distribution can be expressed in the *lab frame* circular polarization basis $p_{L/R} = \frac{1}{\sqrt{2}}\left(p_r \pm ip_\phi\right)$as

$$\begin{cases} p_L(\phi) \propto & e^{i(l+1)\phi}\cos\left(\frac{N\Delta}{2} - \frac{\pi}{4}\right) \\ p_R(\phi) \propto & e^{i(l-1)\phi}\cos\left(\frac{N\Delta}{2} + \frac{\pi}{4}\right). \end{cases} \tag{5.28}$$

In order to only have right (left) handed light radiated into the far field it suffices to remove the left (right) handed source component by proper adjustment of the antenna spacing Δ, setting $\Delta = (-)\frac{\pi}{2N}$. We call structures with $\Delta = +\frac{\pi}{2N}$ $V$-type, and $\Delta = +\frac{\pi}{2N}$ $\Lambda$-type (Fig. 5.9). Intuitively, this choice of Δ can be understood as a requirement for the two orthogonal dipoles in one unit cell to radiate with a $\pm\pi/2$ phase difference, i.e., as a purely circular dipole. In more microscopic detail, the second dipole is $\pm m\frac{\pi}{2N}$ delayed/advanced compared to the first inside the cavity mode profile, because the driving is delayed. Because it is also rotated by $\pm\frac{\pi}{2N}$, it emits the OAM of $\ell = m - N$ with a phase advance of $\pm l\frac{\pi}{2N}$, and therefore the accumulated phase delay of the contribution of the second antenna compared to the first one is $\pm(m - l)\frac{\pi}{2N} = \pm\frac{\pi}{2}$. The parasitic higher harmonic OAM contributions due to the discretization (at $\ell' = m - kN$) are not strictly circularly polarized.

## 5.5. Design of an experimental realization

Putting together the results of Sections 5.2 and 5.3, we envision that the platform of $Si_3N_4$ microdisk cavities decorated with antennas that was developed in Chapter 4 may be used for a proof of principle for generating pure OAM in polarization-pure radiation patterns. Here the envisioned scenario is that

microdisks are driven with a narrow band laser via a fibre taper, and that their radiation patterns into the far field may show pure OAM in distinct lab-frame circular polarization, depending on whether the disks are decorated with radially oriented antennas, or unit cells containing dimers of antennas in orthogonal V or Λ configuration. In this section we discuss the requirements for actual experimental realizations according to full wave simulations, going beyond the simplifications of our model.

### 5.5.1. Antennas

The predictions discussed in previous sections all consider antennas to be point dipole scatterers that are polarizable along just a single axis. Nanorod antennas will provide an anisotropic polarizability dominantly along their long axis when used at the long-axis resonance frequency, but with a weak residual short axis polarizability. We preferably reach a design for a nanorod antenna where resonances are sufficiently separated such that an appreciable anisotropy between the short and long axis polarizability arises (contrast of order $|\alpha_{long}/\alpha_{short}|^2 > 100$). Furthermore, these objects need to remain small compared to the wavelength of the drive field in the microdisk[3]. This criterion excludes high-index dielectric particles. We therefore turn to metallic antennas, where the surface plasmon confinement allows for small resonant objects, with however the downside of optical absorption. Due to the high plasma frequency of aluminium, aluminium nanorods can be made resonant along their long axis in our laser range for aspect ratio as large as 3-4, as compared to an aspect ratio of just two for gold rods with the same long-axis resonance frequency. Thus, aluminium allows for a 10× higher anisotropy $|\alpha_{long}/\alpha_{short}|^2$ of the polarizability compared to gold antennas. The disadvantages of aluminium are the inter-band absorption at 780 nm, and the grain size of evaporated metal for nanolithographic fabrication, detrimental for the optical quality of our nanostructures.

To optimize the shape of our antennas we perform FEM simulations (COMSOL Multiphysics®) of aluminium antennas (tabulated permittivity taken from [267]) placed on an air-glass interface[4] ($n_{glass} = 1.5$). For a fixed thickness of antennas of 30 nm, a width of 30 or 40 nm (to account for fabrication imprecision) and a wavelength of operation of 773 nm, we calculate the polarizability of antennas along their long and short axis (both parallel to the glass interface). Figure 5.10 summarizes our simulations. We see in Fig. 5.10(a) that wider antennas have a stronger polarizability, even though they resonate for longer dimensions (change of sign of real part of $\alpha_{xx}$). However, Fig. 5.10(b) suggests that the anisotropy between short and long axis polarizability is most favourable for narrower antennas. To

[3]The effective wavelength inside the cavity is 550 nm, for spectral range of interest set by our laser (765 – 781 nm)

[4]The reason to take glass, not silicon nitride, becomes apparent in the next subsection.

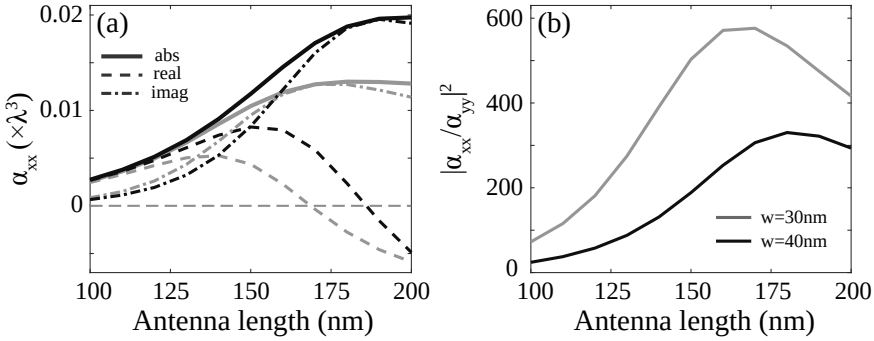


**Figure 5.10:** Polarizability of a 30 nm thick aluminium nanorod antenna on glass at $\lambda = 770$ nm for varied length and width. Red lines are for antenna width of 30 nm, blue are for width of 40 nm (a) Element of diagonal element $\alpha_{x,x}$ along the antenna long axis, solid lines are $|\alpha_{x,x}|$, dashed lines are real$(\alpha_{x,x})$ and dash-dotted are imag$(\alpha_{x,x})$. (b) Shows the anisotropy between the long and short axis polarizabilities (parallel to the glass plane).

5

have an appreciable anisotropy (> 100) we need to be close to the resonance of the nanorod. To obtain an anisotropy > 100, with antennas as small as possible, we chose to design our samples with 140 nm long, 30 nm thick and between 30 and 40 nm wide antennas (precise width is difficult to control in fabrication). Such antennas will be somewhat blue-detuned from our cavities operating at $765 - 781$ nm, which mitigates the broadening of cavity resonances ($\alpha_{xx}$ is mostly real according to Fig. 5.10(a)).

### 5.5.2. Cavity

The cavities we envision for this study are silicon nitride ($Si_3N_4$) microdisks. Our fabrication is limited to a fixed 200 nm thickness, and the disks must be wider than 3 µm in diameter to allow for the fabrication of a pillar holding the structure such that the whispering gallery mode decouples from the underlying silicon substrate. In addition to these fabrication constraints, we also add the constraint of our experiment. As explicit in Eq.(5.20), the beam radiated by a ring of antennas will have a Bessel profile with an opening angle (maximum of first fringe) which is directly related to the radius of the ring of antennas, and therefore to the radius of the supporting microdisk. This means that the bigger the disk, the narrower the features in the far-field. A 10 µm wide disk would have an opening angle for the first fringe of only 2.6° for OAM of $\ell = \pm 1$, whereas the resolution of our Fourier microscope is only 0.6° per pixel. Therefore we choose to use disks of around 4 µm diameter, which give a fringe diameter of 6.6° for OAM of $\ell = \pm 1$. Such disks would support TE WGM where the fundamental radial mode has an azimuthal mode number in the range of $m = 20 - 25$. This means that we need almost as many antennas on the disk to create an OAM of $\ell = 0$ to $+3$.

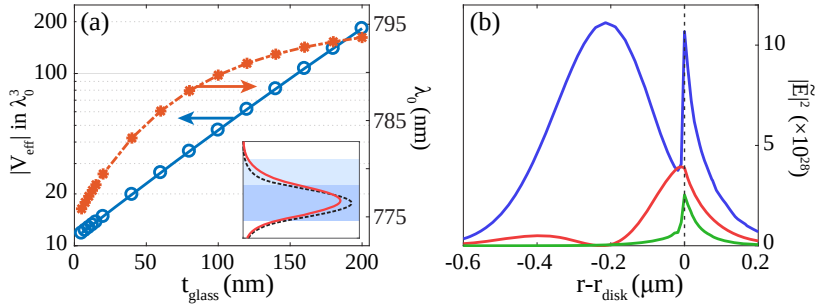


**Figure 5.11:** Mode volume and normalized electric field at the glass-air interface of a microdisk cavity (radius 2 μm, $t_{Si_3N_4} = 200$ nm, mode $m = 22$). (a) Effective mode volume (in unit of wavelength) at the maximum of the field at glass-air interface (solid blue), and resonance wavelength (dashed orange) as a function of top glass layer thickness. The mode volume exponentially increases as we increase the glass layer thickness ($n = 1.5$) as the glass-air interface is moving away from the $Si_3N_4$ where the field remains confined. The inset shows in dashed black the normalized field intensity of the mode for the symmetric $Si_3N_4$ cavity ($t_{glass} = 0$) and in red for $t_{glass} = 150$ nm. Since away for the core the mode field is decreasing exponentially, the mode is feeling less and less the perturbation by additional glass thickness and therefore the resonance wavelength converges towards ≈ 795 nm. (b) Normalized intensity of the 3 components of the cavity electric field $m = 22$ at the glass-air interface for $t_{glass} = 150$ nm: blue is $|\tilde{E}_r|^2$, red $|\tilde{E}_{phi}|^2$ and green is $|\tilde{E}_z|^2$. We note that 230 nm from the edge of the disk, the field is maximal on its radial component and minimal on the other two.

5

### 5.5.3. Antenna-cavity coupling strength

An important design criterion is the linewidth of the cavity resonance once antennas are placed on top on it. We estimate using Eq.(5.13) from the imaginary part of the polarizability of our antennas (Fig. 5.10(a)) and an effective mode volume of $V_{\text{eff}} \approx 10\lambda^3$ that 20 antennas placed directly on the disk would broaden the linewidth of the cavity by 4 THz, and therefore limit the quality factor of the system to $Q < 100$. An antenna-dominated low-Q is not a problem *per se* in the sense that for the envisioned experiment it is required that the losses of our system are dominated by antenna radiation. However, we do need a clear separation between resonances of different $m$. This means a linewidth broadened by the antennas to a level where it becomes on the order of the free-spectral range of the cavity is undesirable. Inserting a low refractive index spacer in between the disk and the antennas would allow to raise the antennas out of the mode profile, and thereby provides control over the cavity $Q$. A solution, compatible with our established fabrication used in Chapter 4, is to evaporate a layer of glass ($n_{glass} \approx 1.5$, when $n_{Si_3N_4} \approx 2.0$) on the disks prior to fabricating the antennas. To reach a Q of at least 1000 for the system at hand, we need to increase $V_{\text{eff}}$ by a factor of at least $\sim 10$. Figure 5.11(a)

shows that for the fundamental TE mode for $m = 22$ of disk of 4 µm diameter, 200 nm of $Si_3N_4$, this is possible for a glass layer thickness of > 120 nm. In this scenario one does need to compensate for a shift in the resonance wavelength of the cavity due to the glass layer (using different disk radius and/or higher mode number $m$). Finally, one needs to place the antennas in terms of their *radial* position well within the mode profile of the cavity since, to benefit optimally from the polarizability anisotropy, a purely radial polarization of the mode at the antenna ring must be ensured. In Figure 5.11(b), for a disk of 4 µm, with 150 nm of glass we see that if we want the cavity field (at the air-glass interface) to be only radial at the position of the antennas, the antennas must be placed 230 nm from the edge of the disk.

## 5.6. Experiment

### 5.6.1. Fabrication



We use two-step lithography to realize $Si_3N_4$ disks, hybridized with aluminium antennas. First, we fabricate $Si_3N_4$ microdisks on silicon pedestals. In the following step, we evaporate the glass spacer and finally antennas are deposited using thermal evaporation. We start from a silicon wafer with a 200 nm LPCVD layer of $Si_3N_4$ (Lionix BV), cleaned using a base piranha etch. We deposit a 430 nm layer of CSAR 62 resist (All Resist GmbH) and perform e-beam lithography at 50 keV (Raith Voyager), using a 1 nA current and 160 µC/cm$^2$ dose. Samples are then developed in pentyl-acetate (120 s) followed by an o-xylene dip (7 s). We etch the $Si_3N_4$ using inductively coupled plasma (ICP) reactive ion etching (RIE) with a mix of $SF_6$ and $CHF_3$ gasses at flow rates of 16 and 80 standard cubic centimeters per minute (sccm), respectively, with 50 W RIE forward power and 500 W ICP power at a gas pressure of 9 mTorr, a temperature of 0 °C and an etch time of 100 s. Afterwards, we remove the resist using acetone and a base piranha clean, immediately followed by a Si underetch (40 wt% potassium hydroxide (KOH) at 70 °C, 120 seconds) to create free-standing disk edges. Before moving on to place the antennas, we first deposit a $SiO_2$ layer using e-beam evaporation (Polyteknik Flextura M508 E) at a rate of 0.1 nm/s. Using a movable shutter, we deposit 112(5) nm on one half of the sample, and 156(5) nm on the other half.

To fabricate the antennas, we then spincoat a MMA/PMMA bilayer resist stack. Measured far away from the structures on a flat substrate, MMA and PMMA thicknesses were 620 and 80 nm, respectively. This should roughly correspond to layer thicknesses of 120 and 30 nm, respectively, at the edge of the disk cavities, as verified through FIB-crosscuts of disks with resist on top. We then perform a second e-beam step (0.5 nA, 400 µC/cm$^2$ dose), aligned to the first using alignment markers, and develop the sample (75 seconds) in a 1:3 methylisobutyl ketone and isopropanol mixture. This is followed by

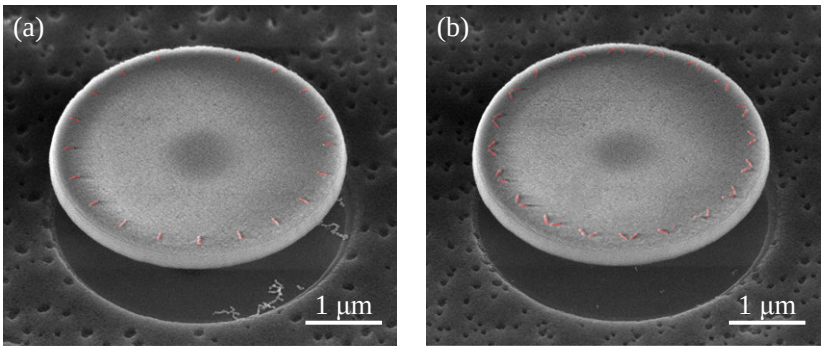


**Figure 5.12:** Electron micrograph of structures fabricated by H. M. Doeleman and I. Palstra, following a technique developed by Hugo Doeleman. (a) Radial type structure with 20 antennas. (b) Λ-type structure with 2×20 antennas. We highlight the antennas in red for better readability. A glass *shadow* is visible under the disks as we used directional evaporation for the glass layer.



aluminium evaporation (thermal evaporator at 0.1 nm/s evaporation rate, targeting 30 nm thickness) and lift-off in acetone at 45 °C. Finally, we make sure that the samples are accessible to optical fibre taper coupling by using a diamond saw to remove a 150 μm thick layer from the entire sample, except for a 150 μm wide ridge on which the structures stand. During this process the sample is covered by a 3 μm protective polymer resist that is stripped after sawing (Microposit S1800). This results in a series of disks with targeted diameters 3.88, 3.92, 3.96, 4.00 and 4.04 μm and 200 nm thickness $Si_3N_4$ microdisks, with ≈140 nm long ≈40 nm wide and ≈30 nm thick, radially oriented Al antennas, placed 230 nm from the disk edge.

We fabricated devices with radial, V-type and Λ-type structures, consisting $N = 19 - 23$ units cells (and kept some cavities without any antennas for calibration purpose). Indeed, for the fabricated samples, assuming a glass refractive index of 1.5, we expect to observe at least one mode $m = 22$ or $m = 23$ in the experiment (COMSOL simulations for all five disk sizes, Fig. 5.13), and therefore to generate OAM in the range of $-2$ to $+5$. The calculated mode volumes are always within 10% of $52\lambda_{res}^3$ for all considered $m$, and simulated Qs of bare cavities are within 10% of $1.4{\cdot}10^5$ (m=22), $2.8{\cdot}10^5$ (m=23) and $6{\cdot}10^5$ (m=24).

Figure 5.12 shows scanning electron micrographs of two fabricated dressed cavities. Because of the directional nature of our glass evaporation, in the shadow of the microdisks we have a silicon/air interface at the substrate, but outside the shadow, we have a silicon/glass/air interface. While the reflectivity of a silicon/glass/air stack is about 10% for near-normal incidence, it will be about 30% for the silicon/air interface right under the disk. This is of relevance because our structure by itself (i.e., antenna-disk system with no silicon substrate) is expected to radiate almost 3 times more downward than

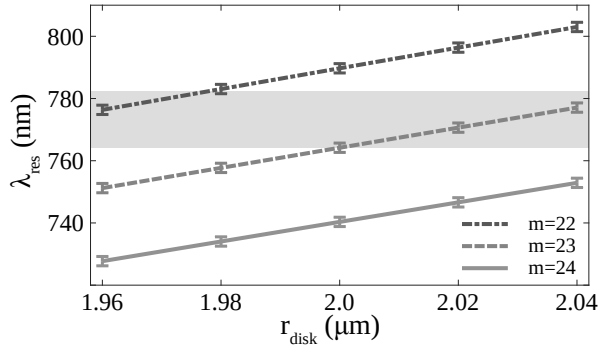


**Figure 5.13:** Resonance for the fundamental WGM for a disk cavity with $t_{Si_3N_4} = 200$ nm and $t_{glass} = 150$ nm as a function of disk radius, for $m = 22$ (dash-dotted) $m = 23$ (dashed) and $m = 24$ (solid). Gray shaded area indicates the range of our scannable laser (765 – 781 nm). Error bars attempt to account for some fabrication uncertainty for $t_{glass} = 150 \pm 10$ nm, $n_{glass} = 1.5 \pm 0.05$ and up to 10 nm of glass evaporated on the edge of the disk (ideally, it should be 0).

5

upward according to FEM simulations. This means that the direct scattering into our objective will have a similar order of magnitude as the reflection by the substrate, and therefore the Bessel-like mode profile we estimated for a microdisk freestanding in vacuum will be modulated by the interference of two contributions. Figure 5.12 shows that the evaporated glass has non-negligible roughness, especially on the substrate (which reflects part of the collected signal). For this reason, we have only been able to perform satisfactory measurements on the cavities with a 110 nm glass thickness instead of 150 nm as originally envisioned. A somewhat higher cavity-antenna coupling is required to raise the antenna scattering over the speckle due to scattering by the glass roughness. Finally, we quantified thanks to scanning electron micrographs (SEM) an excellent yield of antennas present on the sample after fabrication above 97.5%.

### 5.6.2. Experimental setup

To test for the generation of OAM we modified the setup used in Chapter 4. The principle is to use tapered fibre excitation (Corning HI 780C), and perform phase-resolved Fourier imaging of the radiation pattern, using interferometry as shown in Figure 5.14. The light collected through our NA 0.95 IR objective is recombined with a reference beam onto a circular polarization analyser consisting of a quarter wave plate, followed by a linear polarizer. The interferogram is then recorded by a CCD camera. The reference beam has a relatively homogeneous intensity over the camera, but a parabolic phase-front. We align the center of this parabola to the center of the NA of the objective, which corresponds also to the center of the emitted helical beam.

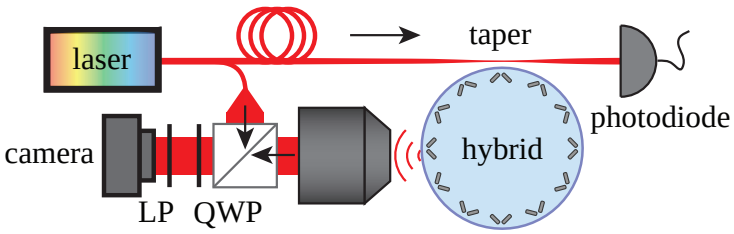


**Figure 5.14:** Sketch of our experimental setup. The light from a fibre coupled tunable diode laser ($\lambda = 765 - 781$ nm) is coupled into the antenna-dressed microdisk via evanescent coupling from a tapered fibre. The transmission signal through the taper is used to measure the linewidth of resonant modes of the cavity. The light scattered by the sample is collected from the top by a 0.95 NA objective and the far-field (Fourier plane) electric field is recombine with a reference beam (parabolic phase) on the camera after projection onto circular polarization with quarter wave plate (QWP) and linear polarizer (LP). These interferometric measurements allow us to analyse the phase and therefore the orbital angular momentum of the produced helical wavefront.



For phasefronts with pure OAM, the interferogram should therefore exhibits spirals with number of arms equal to the OAM of the investigated beam (as the example shown in Fig. 5.1(i)). While one could extract phase from a single interferogram by digital off-axis holography [243, 260, 261], we instead use on-axis interferometry, which allows for higher resolution in phase retrieval. We measure a set of interferograms with varying phase differences between reference and analysed beams. In our setup, the easiest way to controllably change this phase delay is to slightly vary the excitation wavelength (< 1 pm, much less than the dressed cavity linewidth). Indeed, with an optical path difference in the order of $50 - 60$ nm in our setup, for a wavelength of $\lambda = 780$ nm, a change of $\delta\lambda = 0.5$ pm leads to a phase shift of $6\pi$.

### 5.6.3. Results

We interrogate cavities with $N = 19 - 23$ unit cells (unit cells of three types: single radial I-antenna, V-antenna and $\Lambda$ antenna ($I, \vee, \wedge$), and 110 nm of glass coverage. With the fabricated sample, the only measurable fundamental radial TE mode in the range of our tunable laser ($\lambda = 765 - 781$ nm) is $m = 22$. This mode is always measurable for two different disk sizes in each set of 5 different sizes we fabricated. We measured for a disk without any antenna a quality factor $Q \approx 2 \times 10^4$. This Q drops to around $500 - 1000$ with antennas, leading to a linewidth of the order of 1 nm. For each measurement sequence, our protocol is to first find the peak of the resonance of the dressed cavities in the scattering spectrum. Then we set the circular polarization analyser to left handed polarization, measure the intensity of the emitted beam and the reference separately, then recombine the two beams and record 200 interferograms with a phase delay varied from 0 to $6\pi$ (3 fringes). We then repeat the procedure for right handed polarization.

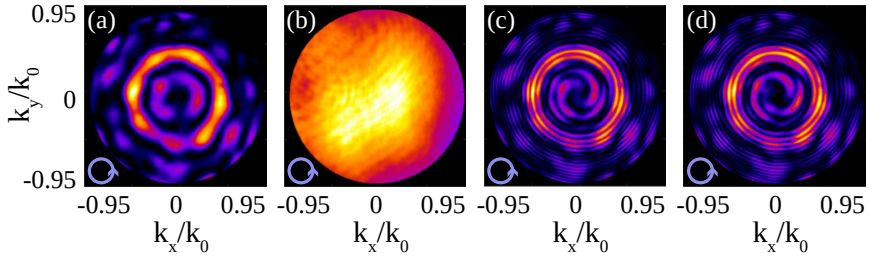


**Figure 5.15:** Raw experimental data. (a) Fourier image of the far field intensity radiated in left handed circular polarization (LHCP) by a cavity of radius 2 µm, dressed by $N = 19$ pairs of antennas for the V-type structure, at resonance for a WGM $m = 22$ at $\lambda = 772.5$ nm. (b) Fourier image of the intensity (in LHCP) of the reference beam used for interferometric phase retrieval. (c-d) Interferograms obtained when combining reference and analysed beam (for two different phase delays). We see a spiral with two arms which confirms the generation of a beam of OAM $\ell = m - N - 1$ for LHCP.

5

Figure 5.15 documents this protocol for an example data set. As a first step, we record the intensity profile of the analysed beam (panel (a)), and the reference beam (panel (b)). Then we record our set of interferograms (panels (c-d)), always making sure to not saturate the camera. The interferograms show a distinct two-arms spiral structure that is characteristic for beams carrying OAM of $\ell = \pm 2$. As we change the phase difference between the signal and the reference beam, the spiral rotates around there center ($\mathbf{k}_\parallel / k_0 = 0$), as can be seen by comparing panel (c) and (d), and the direction of rotation tells us about the sign of the OAM.

We analyse the sets of interferograms using principal component analysis (PCA) [268] to extract the reconstructed phase and intensity of the analysed beam, disentangling it from the reference beam. The reconstructed and measured intensities should match exactly (Fig. 5.15(a)), and we compensate in post-process for the parabolic phase of the reference beam. The advantage of this PCA based technique is that it does not require any calibration of the phase delay, and it, in principle, only requires 5 interferograms (we used 200 interferograms to be conservative and to be able to process the data with other algorithms if necessary). We present in Figure 5.16 the complete analysis of a dataset, i.e. phase and intensity profiles of the scattered field in both circular polarization channels, obtained for $m = 22$ and $N = 20$, for the radial-type (a,b,g,h), V-type (c,d,i,j) and Λ-type structures. We first observe that, the radial structure scatters as much light in left handed circular polarization (LHCP) as in right handed circular polarization (RHCP) (panels (a) and (g)). On the other hand, the V-type structure clearly favours LHCP over RHCP, and we only observe weak speckle noise in the RHCP channel. The Λ-type structure dominantly outputs into RHCP over LHCP (panels (e,k)), however not cancelling out LHCP completely down to a speckle noise level. Additionally, we note that the opening angle of the radiation pattern in the

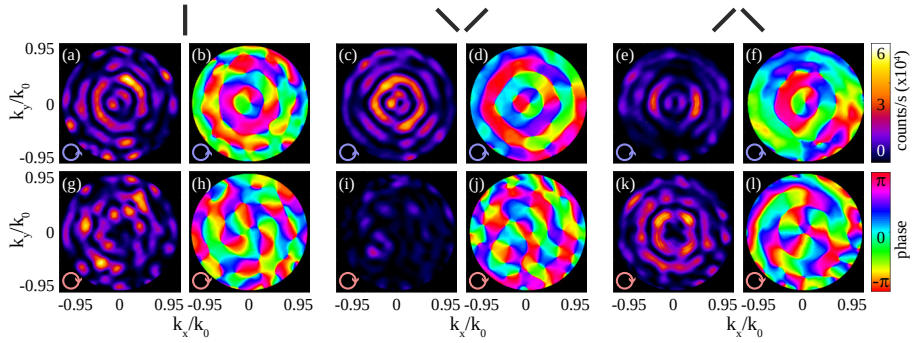


**Figure 5.16:** Reconstructed phase and intensity of radiated OAM beams for $m = 22$ and $N = 20$. Panels (a,b,g,h) (2 leftmost columns) correspond to a radial I-type structure, (c,d,i,j) (middle columns) to a V-type structure and (e,f,k,l) (rightmost columns) to a Λ-type structure. Figures (a-d) (top row) are obtained for left handed circular polarization (LHCP), (e-h) (bottom row) for right handed circular polarization (RHCP). For each structure and polarization channels, we plot the intensity (left image) and phase profile (right image) retrieved from our interferometric measurements. We observe that for the radial structure (a,g), both polarizations have similar intensity, whereas for the V and Λ-type structures, resp. left (c,i) or right (e,k) polarization is favoured. For all structure types, we observe in (a,c,e) that the left polarized channel exhibits a central phase singularity corresponding to an OAM of $\ell_L = m - N - 1 = +1$. For the right hand circular polarized channel, the expected charge of $\ell_R = m - N + 1 = +3$ is actually split into 3 charges $+1$ due to imperfections of our sample and measurements for (g) and (l). Due to the excellent cancellation of the right hand circular polarization by the V-type structure, we only observe in (i-j) a speckle noise pattern.

LHCP channel (a,c,e) is smaller than for the RHCP channel (g,i,k). This is commensurate with the notion that for the considered geometry, the RHCP channel is expected to carry an OAM of $\ell_R = m - N + 1 = +3$, higher than for LHCP with $\ell_L = m - N - 1 = +1$. By analysing the phase profiles, we indeed confirm that LCHP (b,d,f) exhibits a central phase singularity of charge equal to the expected OAM of $\ell_L = +1$. Less evidently, for RCHP, panels (h) and (l) suggest an OAM of $+3$. However, closer inspection shows not a single singularity of charge 3, but rather 3 singularities of charge $+1$ which stem from the splitting of the single expected charge $\ell_R = +3$. This splitting is due to sample and measurement imperfections, which reduce the OAM purity by mixing in background fields.

We analyse more quantitatively the content of each of the reconstructed radiation diagrams according to the projection method used in subsection 5.4.1, taken from [260], and summarize our findings in Figure 5.17 for a range of devices that (are expected to) produce OAM from $-2$ to $+4$. We observe that for an array composed of radially polarized antennas (Fig. 5.17(a,d)), our system radiates a similar amount of intensity in both circular polarization channels ($I_L/I_R = 47/53$ on average). As expected, left handed circularly polarized light is scattered with an OAM of $\ell_L = m - N - 1$ and right handed

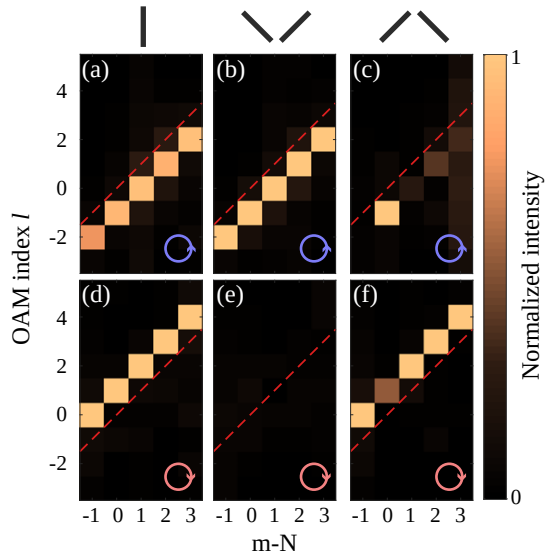


**Figure 5.17:** Selection rules for orbital angular momentum and polarization of beam scattered by the WGM $m = 22$ of microdisks dressed by regular arrays of nanoantennas with number of (pairs of) antennas varied from $N = 19$ to 23. Panels (a,d) regroup results for radial I-type structure, (b,e) for a V-type structure, and (c,f) for a Λ-type structure. Panels (a-c) correspond to LHCP, (d-f) to RHCP. The intensity is normalized to the maximum of each column of each vertical pair of panels so that we can quantitatively compare RHCP and LHCP contents. The dashed red-lines indicate $\ell = m-N$. We confirm the OAM selection rule for LHCP and RHCP, where the produced OAM is systematically $\ell_L = m - N - 1$ and $\ell_R = m - N + 1$, as well as the polarization cancellation operated by V and Λ-type structures respectively on RHCP and LHCP.

circular light, with $\ell = m-N+1$. We confirm that our $V$ and Λ designs enable polarization selectivity: (I) V-type antennas always favour left-handed polarization ($I_L/I_R = 94/6$ on average, see Fig. 5.17(b-e)), and (II) Λ-type antennas favour right-handed polarization, however systematically less efficiently than V-type structures ($I_L/I_R = 20/80$ on average, see Fig. 5.17(c-f)).

Finally, we had expected for the case $m = N$, that there would be no strong polarization selectivity. In this case the degeneracy of the cavity mode is lifted, and the WGM modes split into standing waves, only one of which couples strongly to the antennas. The standing wave character means that the phase delay between the two antennas in a unit cell is no longer pinned at the value required for circular polarization. While Figure 5.17(c-f) shows this feature, it is surprising that the V-antenna case in Fig. 5.17(b-e) does not. We attribute this to fabrication imperfections in the particular device, which according to scanning electron microscope inspection happened to miss a few antennas due to fabrication errors. For the interrogated cavity in (c-f), we verified with spectroscopic measurements that we indeed have a lifted degeneracy, with

one high-Q mode ($Q \approx 10^4$) and a lower-Q one ($Q \approx 800$), while the case in (b,e) did not.

## 5.7. Conclusion and outlook

In conclusion, we have analysed the mode structure of a ring cavity supporting whispering gallery modes interacting with an azimuthal array of $N$ nanoantennas and have identified two distinct scenarios. Either $N$ is commensurate with the mode number $m$, in which case the antennas lift the degeneracy between the two standing-wave modes, or when $N$ and $m$ are not commensurate and the hybrid modes remain degenerate, but become associated with radiating orbital angular momentum (OAM) content into the far field. Due to the discrete nature of the current distribution of a set of antennas, usually the system will scatter light at a comb of OAM values, i.e., a fundamental OAM $\ell_0$ set by $N - m$, and its harmonics. However, if the number of antennas is high enough, these higher harmonics carry phase singularities of charges which are too high to be observed in the paraxial direction, and therefore the far-field beam can be assumed to carry a single OAM $\ell_0$. In this scenario, if one considers the light scattered by a regular array of radially oriented antennas, but analysed in lab-frame circular polarization contributions, this light will not carry identical OAM $\ell_0$, but instead $\ell_0 \pm 1$ where the sign is set by the spin (polarization). It is therefore straightforward to understand that a radial array of antennas cannot produce a pure OAM beam in a single desired circular polarization. We proposed that more complex scattering units, such as V and $\Lambda$-type structures give a route to engineer polarization selectivity, and thereby also OAM purity. Finally, we designed samples based on $Si_3N_4$ microdisks platforms dressed by aluminium antennas, and confirmed the expected behaviour qualitatively in experiment.



As an outlook, we consider the possibility of pushing our work to the generation of exotic beams. There is an increasing interest in literature in higher order beams that exhibit spatially inhomogenous states of polarization. In particular, several groups have suggested *vortex vector beams*, also known as spirally polarized beams, usually encountered in fibre optics [115, 269, 270]. The additional degrees of freedoms in such beams open up many opportunities for application such as spectroscopy, microscopy and optical trapping and even communication [227, 271].

Vector vortex beams can be described in the framework of higher-order Poincaré spheres. Indeed, as for the polarization state of a homogenous beam, which can be mapped onto a unit sphere through the Stokes parameters of its Jones vector, vector vortex beams can be projected onto higher-order Poincaré spheres (HOPS) [262]. In essence, vector vortex beams are constructed as linear combinations of orthogonal, circularly polarized beams of different topological charges (OAM). We focus only on the case when the topological charges of the eigenstate are opposite in sign, since the general case requires

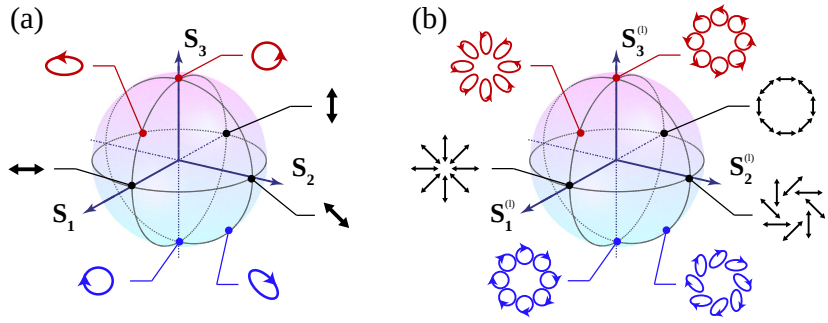


**Figure 5.18:** (a) Representation of the state of polarization of a transverse electromagnetic field on Poincaré sphere. (b) Representation of vectorial vortex beams on the higher order Poincaré sphere of order $\ell = +1$, $\sigma = +1$.

to use hybrid-order Poincaré sphere [272]. Suppose that one has their paraxial OAM beams in left and right handed polarization (circular basis), and suppose that we limit the discussion to a pair of beams with opposite OAM *and* opposite handedness

$$\begin{cases} |\mathbf{R}_\ell(\psi)\rangle &= e^{-i\ell\psi}|\mathbf{R}\rangle \\ |\mathbf{L}_\ell(\psi)\rangle &= e^{+i\ell\psi}|\mathbf{L}\rangle. \end{cases} \tag{5.29}$$

In the following we do not specify any radial intensity dependence, but note that it should be equal for the two polarization states, as it would be using our OAM generation method. Using these two beams as basis vectors, one can define a vector vortex light beam as

$$|\mathbf{v}_\ell\rangle = c_R^{(\ell)}|\mathbf{R}_\ell\rangle + c_L^{(\ell)}|\mathbf{L}_\ell\rangle. \tag{5.30}$$

Generally, for any $\ell$, one could define higher-order Stokes parameters by

$$\begin{cases} S_0^{(\ell)} &= |\langle\mathbf{R}_\ell|\mathbf{v}_\ell\rangle|^2 + |\langle\mathbf{L}_\ell|\mathbf{v}_\ell\rangle|^2 \\ S_1^{(\ell)} &= 2\,\mathrm{Re}\{\langle\mathbf{R}_\ell|\mathbf{v}_\ell\rangle^* \cdot \langle\mathbf{L}_\ell|\mathbf{v}_\ell\rangle\} \\ S_2^{(\ell)} &= 2\,\mathrm{Im}\{\langle\mathbf{R}_\ell|\mathbf{v}_\ell\rangle^* \cdot \langle\mathbf{L}_\ell|\mathbf{v}_\ell\rangle\} \\ S_3^{(\ell)} &= |\langle\mathbf{R}_\ell|\mathbf{v}_\ell\rangle|^2 - |\langle\mathbf{L}_\ell|\mathbf{v}_\ell\rangle|^2. \end{cases} \tag{5.31}$$

For $\ell = 0$, and taking spatially homogeneous beams as basis vectors, the space of beams spanned by Eq.(5.30) reduces to standard plane wave states of arbitrary, but uniform, polarization, with conventional Stokes parameters given by Eq.(5.31). Generalized to nonzero $\ell$, $S_0^{(\ell)}$ relates to the total intensity of the beam, $S_1^{(\ell)}$ and $S_2^{(\ell)}$ give information about the orientation the polarization relative to the cylindrical local frame, and $S_3^{(\ell)}$ is the overall degree

of ellipticity. In this representation, the poles of the HOPS sphere represent beams of uniform circular polarization of opposite handedness and opposite OAM, as pictured in Fig. 5.18. As for the classical Poincaré sphere, the equator regroups all linearly polarized beams with different orientation of polarization. To describe an arbitrary vector beam one would need more than a single HOPS, and, the beam would therefore be *partially polarized* on each sphere, i.e. $(S_0^{(\ell)})^2 \leqslant (S_1^{(\ell)})^2 + (S_2^{(\ell)})^2 + (S_3^{(\ell)})^2$. Note that for a fixed value of $l \neq 0$, two different higher-order Poincaré spheres can be defined, for $\text{sign}(\ell) = \text{sign}(\sigma)$ and $\text{sign}(\ell) = -\text{sign}(\sigma)$.

In our work we demonstrated a dimer array design that enables circular polarization selectivity, meaning that for a certain direction of light circulation we can generate a pure OAM which furthermore sits at the pole of a higher-order Poincaré sphere. By linear superposition of two such beams, one could construct any state of the corresponding HOPS. A first option to realize such a superposition would be to place two arrays of antenna-dimers, one with $N_R = m + \ell + 1$ and V-type structures to produce the circular right state, and another with $N_R = m - \ell - 1$ and $\Lambda$-type structures for circular left polarization. Tuning the coupling strength to the cavity and the relative angle between the two arrays could then enables the control over the higher-order Stokes parameters. A second and much simpler option to realize a superposition is to use simultaneously the two degenerate whispering gallery mode of a cavity, at $+m$ and $-m$ that can be individually adressed by exciting from opposing ends of the tapered fibre. Reversing the direction of propagation of light in our design changes the handedness and sign of the OAM of the scattered light, meaning that coupling to $+m$ generates one pole of the HOPS, while $-m$ generates the other. In our current experimental setup addressing both the $+m$ and $-m$ mode simultaneously is tantamount to injecting excitation light into both ends of the taper. The two excitation beams should be coherent with each other, and the relative phase and amplitude would allow to sweep the full corresponding HOPS. Additionally, as mentioned earlier, for a fixed $\ell$, two HOPS can be defined. One can be addressed by using a V-type, and the other using a $\Lambda$-type structure. We envision that such a schemes could be used to dynamically tuned vectors beams in sorting applications for tiny particles or enantiomers.

# 6

# MOLECULAR OPTOMECHANICS WITH HYBRIDS

## 6.1. Introduction

As first theoretically described by Smekal in 1923 [273] and experimentally demonstrated by Raman in 1928 [274], upon illumination by a monochromatic beam (laser), many molecules (or crystals) scatter a distinct set of spectral lines that are shifted in frequency from the incident light, and that provide a unique fingerprint to identify chemical species and crystalline order on the basis of their vibrational energy structure. The underlying physics is a weak interaction between photons and molecular mechanical degrees of freedom. A completely classical viewpoint [275] is that a molecule, when it is illuminated by light that is not resonant with any quantum mechanical transition, presents an induced electric dipole moment in response to the optical driving at frequency $\omega_L$, quantified through a frequency-dependent polarizability. This polarizability leads to Rayleigh scattering. If this polarizability varies in magnitude over time, for instance by a mechanical oscillation within the molecule at frequency $\Omega_m$, scattered light will appear not just as Rayleigh scattering at frequency $\omega_L$ but also in sidebands shifted from $\omega_L$ by $\pm\Omega_m$. The common quantum mechanical viewpoint [275] is that the incident photon is first absorbed by an intermediate virtual state (which can be thought of as an off-resonant superposition of real states), and is re-emitted as a scattered photon that is either red-shifted from the original photon of energy $\hbar\omega_L$ due to transferring a vibrational quantum of energy $\hbar\Omega_m$ to a molecular bond, or is instead blue-shifted upon taking a vibrational quantum from the ther-

mal occupation of vibrations in the matter. These processes are sketched in Figure 6.1, and are respectively known as Stokes and anti-Stokes Raman scattering. Raman spectroscopy and Raman microscopy are nowadays common spectroscopic techniques to identify molecular bonds, molecular species, and crystalline solids. As a technique, it should be distinguished from, and is complementary to, for instance infrared absorption that corresponds to direct excitation of vibrations by absorption of light at the vibrational resonance frequency $\Omega_m$, and that is generally subject to different quantum mechanical selection rules [275].

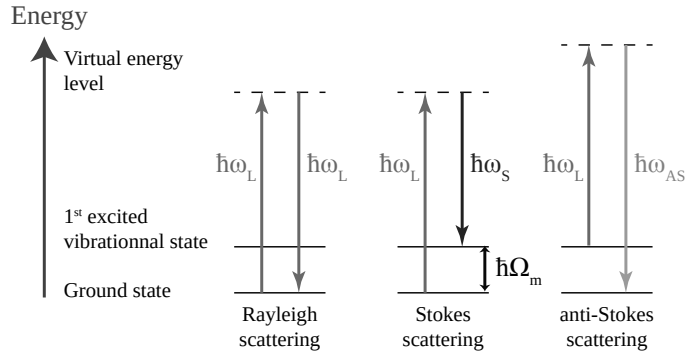


**Figure 6.1:** Three different type of scattering of light. In Rayleigh scattering, no net energy is exchanged between matter and light field, incident and scattered photons have the same energy $\hbar\omega_L$. In Raman scattering, an energy corresponding to the difference between the 1st excited vibrational state and the ground state can be exchanged; for the Stokes process, the incident photon gives energy and the scattered photon is therefore red-shifted ($\omega_S = \omega_L - \Omega_m$), whereas for the anti-Stokes process, the incident photon takes energy leading to a blue-shifted scattering ($\omega_{AS} = \omega_L + \Omega_m$).

While the assignment of Raman transitions to chemical structure is primarily a discipline that is concerned with electronic and vibrational wave functions and selection rules [275], it also has a rich, though controversial, history in plasmonics and nano-optics which started in 1973 with the observation of enhanced Raman scattering of pyridine adsorbed on electrochemically roughened silver [276, 277]. The cross-section of Raman scattering is extremely small (around $10^{-30} - 10^{-25}\,\mathrm{cm}^2$, as compared to $10^{-15}\,\mathrm{cm}^2$ for the fluorescence cross-section of typical organic fluorophores), but, according to literature reports, can be enhanced by factors up to $10^{14}$ by exploiting localized plasmonic resonances in the near field of metallic nanoparticles or rough surfaces (SERS) [24, 25, 168, 169, 278, 279], or tips (TERS) [280–283]. The magnitude of the enhancement has been strongly debated for decades in literature owing to the fact that there are also chemical enhancement mechanisms [284, 285] which can contribute to the enhancement by factors of the order of $10^3$. Nonetheless there is consensus that the electromagnetic enhancement follows an '$|E/E_0|^4$ law' [286–288]. This means that the enhancement of the Raman

cross-section is proportional to the fourth power of the field enhancement by a plasmonic hotspot. According to classical electrodynamic simulations, field enhancements in nanometric gaps of plasmonic dimer can reach factors up to $|E/E_0| \leq 10^3$ [287]. The Raman enhancement is often viewed as decomposable in the product of two contributions [286–288]. The first contribution scales as $\left|\frac{E(\omega_L)}{E_0(\omega_L)}\right|^2$ and relates to the enhancement of the incident field intensity. The second factor $\left|\frac{E(\omega_{S/AS})}{E_0(\omega_{S/AS})}\right|^2$ corresponds to an enhancement of the local density of states available for the photon to be emitted into (LDOS). Figure 6.2 sketches the enhancement of Raman scattering by a plasmonic resonance; the main contribution to the enhancement in this situation is the LDOS boost as the laser frequency is chosen such that the Stokes emission is resonant with the plasmonic cavity, when in practice, the laser pump should be slightly detuned from the plasmon resonance to optimize the enhanced Raman signal by balancing enhancement of the pump and the emission [289]. Surface enhanced Raman spectroscopy (SERS) has enabled in the end of the 1990's the detection of vibrational fingerprints of single molecules [168, 169]. The current state of the art is that tip-enhanced Raman spectroscopy allows spatial resolution such that individual chemical bonds of molecules can be probed [290–292]. Recently self-assembled nano- and picocavities, formed in the gaps in between a metal film and metal nanospheres, have been investigated as a more compact way of studying vibrations at the sub-nanometric level, without the requirement for cumbersome scanning probe apparatus [14, 293]. It has been suggested that the main fundamental limitation on the enhancement factor for Raman spectroscopy by plasmonic effects is fundamental in nature, and is due to electron tunneling [74], which becomes relevant in sub-nanometer gaps and reduces the field strength. At this length scale, selection rules for Raman scattering may also break down, and one may not longer be able to separate the quantum mechanical treatment of the molecular structure from a classical treatment of the light field. A practical limitation on plasmon enhanced Raman scattering is that efficient collection of signal is challenging. By their localized nature, plasmon antennas are not well matched to collection optics or to integrated optics [294–297]. A few works have studied dielectric cavities for Raman scattering, which can give high field enhancement and at the same time offer a monomode output channel to efficiently collect emitted light [298, 299]. However, such resonators rely on high quality factors Q to compensate for drastically smaller field confinement than plasmonics [300–302]. The consequence is that one typically enhances only the pump intensity, or only the LDOS term at the Stokes-shifted frequency, but not both.

This work is motivated by recent theoretical developments that recognize interesting and powerful analogies between plasmon-enhanced Raman scattering and the field of cavity optomechanics [201, 303–305]. In cavity optomechanics, the basic system under study is a high-Q optical cavity that

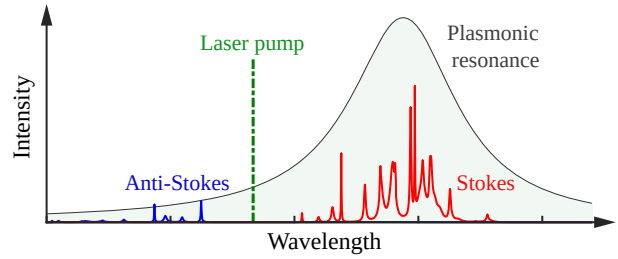


**Figure 6.2:** Plasmon enhanced Raman scattering spectrum. When the pump (green) is blue-detuned by approximately the vibrational frequency, the Stokes process (red) is selectively enhanced over the anti-Stokes process (blue) from the plasmonic resonance (grey line).

couples to a resonant macroscopic motional degree of freedom, such as the resonant movement of one cavity mirror. The coupling of light to motion is through a shift of the resonance frequency of the optical cavity upon motion, while conversely radiation pressure exerted by light stored in the mode pushes against the mirror. The field of cavity optomechanics has promises that go very far beyond the optical read out of mechanical motion via frequency-shifted sidebands [306]. These promises include displacement measurements at and beyond the standard quantum limit [307, 308], parametric amplification as well as cooling of macroscopic mechanical degrees of freedom [50, 309, 310], and coherent quantum state transfer and entanglement between photons and phonons [311–313].

The analogy between plasmon-enhanced Raman scattering and cavity optomechanics that sparks this chapter identifies the optical cavity with the plasmon resonator, and the mechanical motion with the molecular vibration [201, 303–305]. This new viewpoint suggests that one may push the analogy beyond the optical read out of motion, i.e., beyond Raman scattering. It projects that there may be interesting optomechanical regimes beyond plasmon-enhanced Raman scattering if one reaches a higher degree of control over the optomechanical coupling strength between plasmon and mechanical resonator. This emerging field has been coined *molecular optomechanics*. In this chapter we explore if hybrid structures composed of both a metallic and a dielectric resonator [92, 101–103] could be advantageous for molecular optomechanics. On paper, they combine advantages of both dielectric and plasmonic resonators [94], namely tight confinement of field, and at the same time control over the resonance Q-factor. It has even already been suggested that such structures could reach new interesting quantum regimes for the interaction of molecular vibrations and light [208]. From the viewpoint of molecular optomechanics a unique advantage over the usual plasmonic resonators is that the resonance linewidth of hybrids could be tuned such that it is narrower than mechanical resonance frequency. In optomechanical terms, standard SERS

is not resolved-sideband as the plasmon resonance is so broad that it spans both the pump and Raman-shifted frequencies. Hybrids could instead give access to resolved-sideband molecular optomechanics. Sideband resolution is crucial for many achievements in cavity optomechanics. A physics aspect of molecular optomechanics that is different from cavity optomechanics is that the molecular potential for vibration can easily be strongly anharmonic. This might allow to unravel new phenomena [208, 314].

The approach in this chapter is different from that in previous chapters, where we strived to use the quasinormal mode (QNM) approach to rigorously deal with cavities interacting with antennas. Instead, this chapter should be read as the first steps in a feasibility study for possible experiments. It uses the approximations typical of coupled mode theory. These include fundamentally problematic, but practically effective, approximations, such as the assignment of (real-valued) mode volumes to cavities and antennas. It is certainly an important challenge, but not the purpose of this chapter, to develop a more rigorous description of molecular optomechanics in QNM terms. This chapter is structured as follows. Section 6.2 summarizes the formalism for molecular optomechanics put forward by Roelli et al. [201], in particular focusing on how to predict SERS spectra in the simplest, i.e., classical approximation with no backaction. Next, in Section 6.3, we put forward an extension of the work of Roelli [201], adapted to include the main physics of hybrids of whispering gallery mode resonators and plasmonic antennas, and to account for the addressing of such a system through both waveguide and far field channels. We discuss the relation of this formalism to the coupled mode formalism presented for hybrids in Ref. [94]. Section 6.4 presents an evaluation of the expected Raman spectroscopy accessible in practically realizable hybrids, and of the design trade offs that are relevant for resolved-sideband molecular optomechanics.



## 6.2. Review of molecular optomechanics

The recent theoretical developments in the context of plasmon-enhanced Raman scattering recognizes a formal analogy between the Hamiltonian for Raman scattering by a Raman active molecule coupled to a single mode photonic resonator, and cavity optomechanics, where the resonant movement of a mirror (or any geometrical feature) couples to a cavity field, cf. Figure 6.3(a). This analogy was put forward by Roelli et al [201], and further extended by [303–305]. This section serves to summarize the main aspects of this analogy, i.e., the Hamiltonian that is used as starting point, the equations of motion in the classical limit, and the reported procedures to extract predictions for spectroscopic observables.

### 6.2.1. Hamiltonian and classical equation of motion

We refer to [306] for an in-depth tutorial into cavity optomechanics. Here we review the basic ingredients as adapted to molecular optomechanics by Roelli et al. [201]. The Hamiltonian describing the amplitudes of the cavity field and the mechanical motion is

$$\hat{H} = \hbar\omega_p \hat{a}^\dagger \hat{a} + \hbar\Omega_m \hat{b}^\dagger \hat{b} + \hat{H}_{dr}, \tag{6.1}$$

where one assumes that the photonic cavity and the mechanical mode can both be approximated by harmonic oscillators of respective energies $\omega_p$ and $\Omega_m$, and field operators $\hat{a}$ and $\hat{b}$. Here the zero-point energy has been dropped (constant offset) and $\hat{H}_{dr}$ accounts for the driving of the system (by a laser).

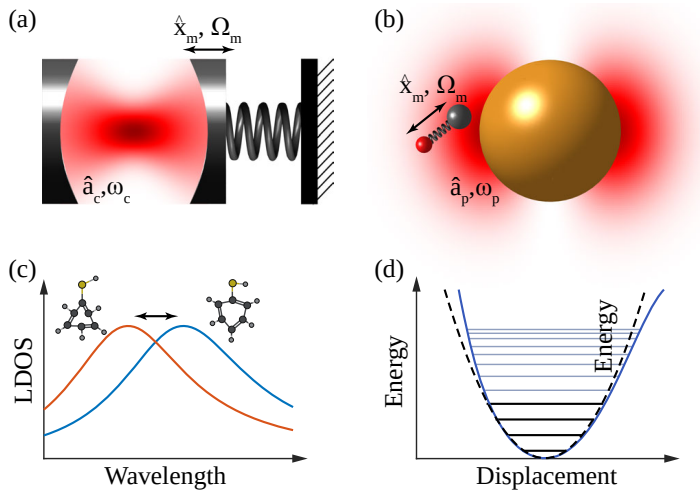


**Figure 6.3:** Cavity optomechanics model of the interaction between a photonic resonator and molecular vibration. (a) Optical Fabry-Perot cavity coupled to the vibration of one of its mirrors. (b) Hotspot of a plasmonic resonator hosting a molecule with a Raman-active vibrational mode. (c) During vibrational motion, the change of the polarizability of the molecule (thiophenol in the figure) induces a shift of the resonance frequency of the plasmonic resonator at the origin of the parametric opto-mechanical coupling. d) Sketch of the molecular energy potential as a function of the vibrational coordinate. The oscillator can be described as harmonic for small vibration amplitudes (i.e. low excitation numbers, indicated as dark lines) but anharmonicity must be taken into account under high amplification (high levels, indicated as blue lines).

In optomechanics, the coupling between cavity and motion is purely parametric in the sense that the resonance frequency of the cavity can be expressed, to first order (considering motion much slower than the optical frequency $\Omega_m \ll \omega_p$) as

$$\hat{\omega}_p(x_m) = \omega_a - G_m \hat{x}_m, \tag{6.2}$$

where $\hat{x}_m = x_{zpf}(\hat{b}^\dagger + \hat{b})$ is the position operator in the normal coordinate frame, with $x_{zpf} \equiv \sqrt{\frac{\hbar}{2m\Omega_m}}$ the zero-point motion of an oscillator of mass $m$, and where we defined the optomechanical coupling rate $G_m \equiv -\frac{\partial \omega_p}{\partial x_m}$. The Hamiltonian of the system in the presence of optomechanical coupling is therefore written

$$\hat{H} = \hbar\omega_a \hat{a}^\dagger \hat{a} + \hbar\Omega_m \hat{b}^\dagger \hat{b} - \hbar G_m x_{zpf} \hat{a}^\dagger \hat{a}(\hat{b}^\dagger + \hat{b}) + \hat{H}_{dr}. \tag{6.3}$$

In the field now known as *molecular optomechanics*, it is not the movement of a mirror that shifts the cavity frequency, but instead the *change* in electrodynamic polarizability $\alpha_m$ of the molecule induced by molecular vibration. One can picture this effect as a change of the effective index, and therefore a change of the optical path of light in the cavity (Fig. 6.3(a-b)). Conventional first order perturbation theory (ignoring the important corrections to it that the QNM formalism provides [139, 140]) therefore gives us the optomechanical coupling rate

$$G_m = \omega_a \left(\frac{\partial \alpha_m}{\partial x_m}\right) \frac{1}{2\epsilon_0 \epsilon V_a} = \frac{\omega_a}{2\epsilon_0 \epsilon V_a} \frac{1}{x_{zpf}} \sqrt{\frac{\hbar R_m}{2\Omega_m}}, \tag{6.4}$$

where $V_a$ is the mode volume of the cavity at the position of the molecule [1], and $R_m \equiv \frac{1}{m}\left(\frac{\partial \alpha_m}{\partial x_m}\right)^2$ is the so-called *Raman activity* of the molecular vibration. The Raman activity is a molecular property that can be quantified from experimental data and DFT calculations. Thereby Eq.(6.4) is a mapping from the optomechanical coupling rate onto tabulated molecular Raman activities. It should be noted that since in the remainder of this chapter, $G_m$ always appears in products with the position $x_m$, quantitative knowledge of $x_{zpf}$ (or equivalently the mass $m$) is not required. We note that the analogy of cavity optomechanics to Raman scattering assumes that the laser driving is not exciting any electronic transition of the molecule, and that the molecular vibration can be described by a harmonic oscillator, which is usually a safe assumption for small vibration amplitudes (Fig. 6.3(c)). As single molecule Raman scattering experiments are extremely challenging [14], the authors of Ref. [201] also studied the case where one instead assumes an ensemble of $N$ identical molecules coupled to light solely via the optical mode with the same coupling rate $G_m$. They concluded that the optomechanical interaction between this ensemble and the cavity mode boils down to the interaction between a single collective "superradiant" mechanical mode and the cavity, with an optomechanical coupling $G_m$ scaled by a factor $\sqrt{N}$.

From the Hamiltonian Eq.(6.3), in the rotating frame at the frequency of the driving laser $\omega_L$, one can derive two coupled quantum-Langevin equation for

[1] Compared to Roelli et al. [201] there is a factor $1/2$ difference in mode volume definition, for consistency with Ref. [94].

the evolution of $\hat{a}$ and $\hat{b}$ [201, 306] on basis of which they can set up a master-equation formalism to capture all coupling to photonic and phononic baths [208, 303, 304]. In this chapter we focus solely on effects that do not require a quantum treatment, and therefore we focus on the classical equation of motion obtained by taking the expectation value of cavity field and molecular position operators $a \equiv \langle \hat{a} \rangle$ and $x_m \equiv \langle \hat{x}_m \rangle$ (we used $\hat{x}_m = x_{zpf}\left(\hat{b}^\dagger + \hat{b}\right)$ and the momentum operator $\hat{p}_m = i x_{zpf} m \Omega_m \left(\hat{b}^\dagger - \hat{b}\right)$ for an effective mass of $m$). Fluctuations, i.e. laser noise and molecular fluctuations (thermal), and driving, can be reintroduced in this equation in a manner that respects the fluctuation-dissipation theorem [315, 316]. Thus one obtains a set of coupled equations of motion[2] with an external optical driving and associated fluctuations $s_{in,a}$, vacuum noise $\delta s_{0,a}$ and a mechanical driving force $F_{ext}$

$$\begin{cases} \dot{a} + (-i(\omega_L - \omega_a) + \gamma_a/2)a - iG_m x_m a & = \sqrt{\eta_{a,in}\gamma_a}\, s_{in,a} + \sqrt{(1-\eta_{a,in})\gamma_a}\,\delta s_{0,a} \\ \ddot{x}_m + \Omega_m^2 x_m + \Gamma_m \dot{x}_m - \frac{\hbar}{m} G_m |a|^2 & = F_{ext}/m, \end{cases} \tag{6.5}$$

with $\gamma_a$ the decay rate of the cavity. We assumed here for simplicity that the antenna only possesses a single input/output channel $s_{in,a}$, namely far-field radiation, and we denote with $\eta_{a,in} < 1$ the coupling rate to this channel normalized by the total decay rate. $\Gamma_m$ is the decay rate of the molecular vibration. The equation of motion (EOM) for $x$ is second order in time and does not contain any complex term as $x_m$ must be real valued. The equation for the cavity field is first order as it only describes the evolution of the envelope of the fast electric field oscillations (300 – 600 THz in the visible against 10 – 50 THz for molecular vibration). These two equations are coupled through terms proportional to the optomechanical coupling rate $G_m$. In the EOM for the cavity, this optomechanical coupling term can be read as a position dependent shift of the cavity resonance frequency. In the EOM for $x_m$, the coupling term represents a radiation pressure proportional to the intensity of the light field. Note that re-injecting the EOM for $x_m$ into the equation for $a$ gives rise to a third order Kerr-like non-linear term when the driving of the vibration by the optics dominates thermal fluctuations $F_{ext}$.

### 6.2.2. Raman scattering in a homogeneous medium

The formalism introduced by Roelli et al. [201], and most subsequent works [208, 304] with notable exception of Dezfouli et al. [303] always approximate the photonic environment of the molecule to be a single cavity mode. One of the consequences is that this framework cannot quantify the enhancement of

[2] The time convention in this chapter differs from all other chapters in this thesis, in order to be consistent with the molecular optomechanics literature. Indeed, the cavity and molecular optomechanics community uses $e^{-i\omega t}$, where the rest of this thesis uses $e^{+i\omega t}$. In practice, this means that this chapter considers negative imaginary part for complex frequency, i.e. loss terms in $-i\gamma/2$ instead of $+i\gamma/2$.

Raman scattering by the cavity by comparing it to emission in a homogeneous medium (i.e. without the cavity). To do so, we therefore resort to a classical description of Raman scattering [275]: in a homogeneous medium of refractive index $n$, the power radiated by a dipole $p_m$ at a frequency $\omega_D$ is given by Larmor's formula

$$W_0 = \frac{\omega_D^4 n |p_m|^2}{12\pi\epsilon_0 c^3}. \tag{6.6}$$

The Raman scattering by a molecule of polarizability $\alpha_m$ (taken at the frequency $\omega_L$ of the pump laser) can be thought as being the radiation by an equivalent Raman dipole

$$p_m(\omega_D = \omega_L + \Omega) = \frac{\partial \alpha_m}{\partial x_m} x_m(\Omega) E_{inc}(\omega_L) \tag{6.7}$$

due the the molecular motion $x_m$ at the frequency $\Omega$. In the considered regime, the molecular motion is stochastic and driven by thermal fluctuation as opposed to the regime where it is driven by radiation pressure. Therefore, the spectrum of radiation of a Raman dipole in an homogeneous medium of index $n$, $W_0 \to S_{00}(\omega_D)$ can be calculated by Larmor's formula by substituting

$$|p_m|^2 \to \left|\frac{\partial \alpha_m}{\partial x_m}\right|^2 S_{xx}(\Omega) \left|E_{inc}(\omega_L)\right|^2, \tag{6.8}$$



where $S_{xx}(\Omega)$ is the spectral density of the position fluctuations of the oscillator. For weak damping, and assuming that the Raman "transition" dipole moment does not depend on the laser frequency (i.e. we do not consider selection rules [275]), $S_{xx}(\Omega)$ is given by [316]

$$S_{xx}(\Omega) = x_{zpf}^2 \left[ \frac{\bar{n}_m \Gamma_m}{(\Omega - \Omega_m)^2 + (\Gamma_m/2)^2} + \frac{(\bar{n}_m + 1)\Gamma_m}{(\Omega + \Omega_m)^2 + (\Gamma_m/2)^2} \right] \tag{6.9}$$

with $\bar{n}_m \equiv \left\langle \hat{b}^\dagger \hat{b} \right\rangle = \left( e^{\frac{\hbar\Omega_m}{k_B T}} - 1 \right)^{-1}$ the thermal occupancy at temperature $T$ of the first excited vibrational state of the molecule of energy $\hbar\Omega_m$ ($k_B$ is the Boltzmann constant). The Raman spectrum of radiation in a homogeneous medium of refractive index $n$ results as

$$S_{00}(\omega_D) = \frac{\omega_D^4 n}{12\pi\epsilon_0 c^3} \left|\frac{\partial \alpha_m}{\partial x_m}\right|^2 S_{xx}(\Omega) \left|E_{inc}(\omega_L)\right|^2. \tag{6.10}$$

Figure 6.4 illustrates the Raman spectrum emitted in vacuum ($n = 1$) as a function of the laser frequency $\omega_L$ and the detected frequency $\omega_D = \omega_L + \Omega$ for an ensemble of $N = 10^3$ Raman active molecules with vibration of frequency $\Omega_m/(2\pi) = 30$ THz, ($\Delta\nu = 1000$ cm$^{-1}$, $\hbar\Omega_m = 125$ meV) and a

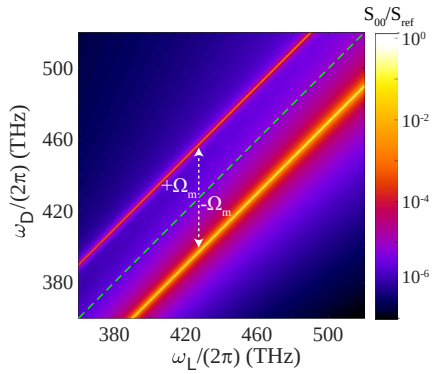


**Figure 6.4:** Normalized Raman spectrum $S_{00}$ in vacuum for a Raman vibration energy of $\Omega_m/(2\pi) = 30$ THz, for a quality factor of $Q_m = 200$ at room temperature, as function of incident laser frequency ($\omega_L$) and detected frequency ($\omega_D$). The green dashed line indicate the laser frequency, and we observe a red-shifted Stokes line and blue-shifted anti-Stokes line, indicated by the white arrows.

decay rate $\Gamma_m = 150$ GHz ($Q_m = 200$) at room temperature of $T = 300$ K ($k_B T = 26$ meV). We normalize the spectrum to $S_{\text{ref}}$, the Stokes emission at a frequency $\omega_D/(2\pi) = \omega_a/(2\pi) = 460$ THz (defined later as the resonance of a plasmonic antenna), i.e. for a laser frequency $\omega_L = \omega_a + \Omega_m$. This normalization at a somewhat arbitrary fixed frequency serves to quantify the enhancement of Raman scattering by resonators, yet still allows to observe the frequency dependence of Raman scattering (scaling as $\omega^4$ in free space, as for Rayleigh scattering). The incident electric field strength is assumed to be the equivalent field one would obtain by focusing a power $P_{inc} = \pi(d_L/2)^2 \frac{\epsilon_0 \epsilon c}{2} |E_{inc}|^2$ over a diffraction limited spot (diameter $d_L = 1.22\lambda_0$, where $\lambda_0$ is taken to be the resonant wavelength $\frac{2\pi c}{\omega_a}$ of the photonic resonator). The incident power in this example, and all other examples in this chapter, is 500 µW. For fair comparison with our SERS model later on, which assumes that the mode volume of the plasmonic hotspot does not depend on wavelength, we choose a fixed value for $\lambda_0 = \frac{2\pi c}{\omega_a}$. We observe a Stokes line systematically red-shifted by $-\Omega_m$ for the laser frequency, and the corresponding blue-shifted anti-Stokes line, $I_S/I_{AS} = 120$ times weaker than Stokes at room temperature for the considered Raman shift.

### 6.2.3. Plasmon enhanced Raman scattering spectrum

The classical equations of motion Eq.(6.5) are nonlinear, and hence contain rich physics well beyond linear Raman spectroscopy. Indeed, in [201], Roelli et al. describe the effects of dynamical backaction evidenced by a superlinear enhancement of the Raman scattering signal with enough pump intensity. This backaction appears in Eq.(6.5) via the non-linear term radiation pressure

term $\frac{\hbar}{m} G_m |a|^2$ in the equation for $x_m$. While this physics is interesting, here our main focus is first to understand the origin of linear Raman spectra from the equations of motion. To this end, one must assume that if the cavity has an average strength $\bar{a}$ but only small fluctuations around it. The dynamical back-action term reduces to a constant $\frac{\hbar}{m} G_m |\bar{a}|^2$ so that the molecular coordinate only experiences a shift in equilibrium position from radiation pressure, but decouples entirely from the cavity dynamics. The equation of motion for the cavity then still stipulates that the molecular vibration (motion now defined to be around the shifted equilibrium position, with concomitant small shift in cavity resonance absorbed in $\omega_a$) imprints on the cavity field

$$\dot{a} + (-i(\omega_L - \omega_a) + \gamma_a/2)a - iG_m x_m a = \sqrt{\eta_{a,in}\gamma_a}\, s_{in,a}. \tag{6.11}$$

We can express Eq.(6.11) in a rotated frame frequency domain, where $a(t) \to a(\Omega)$, $x_m(t) \to x_m(\Omega)$ and $s_{in,a}(t) \to s_{in,a}(\Omega)$

$$-i\Omega a + (-i(\omega_L - \omega_a) + \gamma_a/2)a - iG_m[x_m \star a] = \sqrt{\eta_{a,in}\gamma_a}\, s_{in,a}, \tag{6.12}$$

where $[x_m \star a](\Omega) \equiv \int_{-\infty}^{+\infty} x_m(\Omega - \Omega')a(\Omega')d\Omega'$ is the convolution of $a(\Omega)$ and $x_m(\Omega)$. Note that since $\Omega$ is in the frame rotating at the laser frequency $\omega_L$, corresponding optical signals in the laboratory frame actually have frequencies $\omega \equiv \Omega + \omega_L$. Furthermore, the quantity $a(\Omega = 0)$ is simply the average cavity occupation $\bar{a}$, while $a(\Omega \neq 0)$ is the fluctuation in cavity occupation due to the molecular vibration.

The convolution term means that in principle inserting molecular motion at one frequency $\Omega_m$ into Eq.(6.12) will drive the cavity field to fluctuate not only at the Raman sideband $\Omega_m$ but also at an infinite sequence of weaker higher order sidebands. These can be neglected if the cavity field has only small fluctuations $a(\Omega \neq 0)$ around the average amplitude $\bar{a} = a(\Omega = 0)$. In this limit, one finds the average field in the cavity as

$$\bar{a} = \frac{i\sqrt{\eta_{a,in}\gamma_a}\bar{s}_{in,a}}{\omega_L - \omega_a + i\gamma_a/2}, \tag{6.13}$$

while for the fluctuations one applies Eq.(6.12) replaced by $x_m(\Omega)\bar{a}$. This results in a fluctuation of the cavity field at frequency $\Omega$, i.e., detection at physical frequency $\omega_D = \omega_L + \Omega$

$$a(\Omega = \omega_D - \omega_L) = i\chi_a(\omega_D)G_m\bar{a}x_m(\Omega)$$
$$\text{with} \quad \chi_a(\omega) \equiv \frac{i}{\omega - \omega_a + i\gamma_a/2}. \tag{6.14}$$

Here we have introduced $\chi_a$ as a cavity susceptibility describing the amplitude of the cavity field at frequencies other than the laser driving, due to $x_m$. The susceptibility of the cavity is resonant for $\omega_D = \omega_L - \Omega_m$ (i.e. Stokes

emission), when the laser is blue-detuned from the cavity such that $\omega_L = \omega_a + \Omega_m$, and for $\omega_D = \omega_L + \Omega_m$ (i.e. anti-Stokes emission), when the laser is red detuned from the cavity such that $\omega_L = \omega_a - \Omega_m$. As for the case of vacuum, one can now express the spectral density of the cavity amplitude (when neglecting noise in the drive laser field) in terms of the spectral density of the thermal noise $S_{xx}(\Omega)$ in $x_m$ as a linear transduction

$$S_{aa}(\omega_D) = |\chi_a(\omega_D)|^2 |G_m \bar{a}|^2 S_{xx}(\Omega). \tag{6.15}$$

The signal intensity spectrum at the far field output channel through which one reads out the Raman scattering is simply the intensity of the cavity field multiplied by the loss rate of this channel

$$S_{out,a}(\omega_D) = \eta_{a,out}\gamma_a S_{aa}(\omega_D) = \eta_{a,out}\gamma_a |\chi_a(\omega_D)|^2 |G_m \bar{a}|^2 S_{xx}(\Omega). \tag{6.16}$$

### 6.2.4. Factorization into pump field and LDOS contributions

The Raman spectrum collectible in the far field that we derived can be factorized into three terms as

$$S_{out,a}(\omega_D) = \underbrace{\eta_{a,out} F_a}_{\text{LDOSC}} \underbrace{\left|\frac{\bar{a}\tilde{E}_a}{E_{inc}}\right|^2}_{\text{pump}} \underbrace{S_{00}(\omega_D)}_{\text{free space}}, \tag{6.17}$$

i.e., as the product of the free space Raman spectrum, a pump field enhancement term, and a term related to the (collected part) of the LDOS at the (anti)-Stokes shifted frequency. As evidence for this assertion, note that the LDOS enhancement factor for a dipole emitter of unit dipole moment, and emitting at frequency $\omega$ generally reads

$$F = 1 + \frac{6\pi\epsilon_0 c^3}{\omega^3 n} \mathrm{Im}\{p_m^* E\}$$

where $E$ is the field emitted by the dipole, evaluated at the dipole. Within the confines of our model that treats the optics as a phenomenological single mode cavity of real mode volume $V_a$, this expression is equivalent to

$$F = 1 + \frac{3\pi c^3}{\omega^2 n^3 V_a} \mathrm{Re}\,\chi_a(\omega) \equiv 1 + F_a$$

where $F_a$ is the Purcell factor set by $V_a$ and the cavity damping $\gamma_a$. Since within this model $\mathrm{Re}\,\chi_a(\omega_D) = \frac{\gamma_a}{2}|\chi_a(\omega_D)|^2$, indeed the leading term $\eta_{a,out}\gamma_a|\chi_a(\omega_D)|^2$ in the Raman spectrum is the product of light extraction efficiency ($\eta_{a,out}$) and LDOS enhancement at the (anti)-Stokes frequency. The pump enhancement evidently appears in the Raman spectrum through $\bar{a}$, while the remaining factors regroup into the Raman spectrum of the molecular species in free space. We therefore find that the molecular optomechanics framework of Roelli [201], taken to the limit of linear SERS enhancement, is consistent with the "$E^4$" law factorized in pump and LDOS terms.

### 6.2.5. SERS example calculation

As an example, Figure 6.5 shows predicted Raman spectra for an ensemble of $N = 10^3$ molecules with the same vibrational resonance as used in Fig. 6.4, coupled to a plasmonic cavity, or antenna. We assumed a Raman activity $R_m = 500\,\text{Å}^4 \cdot \text{amu}^{-1}$. The parameters of the plasmonic antenna are the same as used in Section 2 of Ref. [94], i.e. we consider an antenna with a polarizability resonant at $\omega_a/(2\pi) = 460$ THz with an intrinsic Ohmic linewidth of $\gamma_{a,0}/(2\pi) = 19.9$ THz and an oscillator strength of $\beta_a = 0.12$ C/kg. It should be noted that here and in the following, the total damping rate that appears in the polarizability is

$$\gamma_a(\omega) = \gamma_{a,0} + \gamma_{a,rad}(\omega) \qquad \text{with} \qquad \gamma_{a,rad}(\omega) = \beta_a \frac{n\omega^2}{6\pi\epsilon_0 c^3}.$$

The total damping rate is the sum of intrinsic Ohmic damping, and radiative damping that increases in proportion to the particle oscillator strength (stronger scatterers have more radiative loss), and in proportion to the free space LDOS. This is required so that , in absence of absorption, the resulting polarizability satisfies the optical theorem (exctinction equals scattering). Equivalently this can be seen as including non-electrostatic corrections to the dipolar Mie expansion coefficient for a small scatterer (cf. Chapter 2). For our

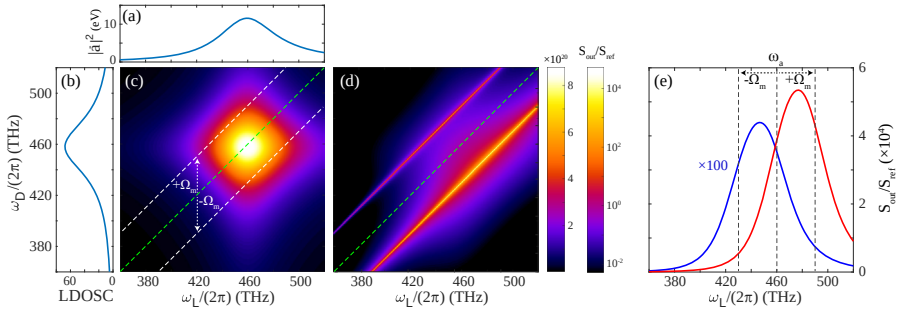


**Figure 6.5:** Molecular optomechanics with a single plasmonic cavity. (a) Average intensity of the cavity field, i.e. at the driving laser frequency. (b) Local density of states for photons collected in the far-field. (c) Transfer function between $x_m$ and $a$ of the antenna $S_{a,out}/S_{xx}$. (d) Raman spectrum $S_{a,out}$, normalized by $S_{ref}$ (Stokes emission in homogeneous medium at $\omega_a$) for $10^3$ molecules coupled to a single plasmonic cavity as a function of driving and detected frequencies. We assume the same Raman parameters for molecules as for Fig. 6.4. We observe an enhancement of the Raman scattering due to the plasmonic resonance of almost 5 orders of magnitude. The green dashed lines in (c) and (d) indicate the laser frequency, while the white dashed lines indicate Stokes and anti-Stokes emission. (e) Raman spectrum as a function of laser frequency taken at the Stokes (red) or anti-Stokes peak (blue). These plots are therefore diagonal slices of (d) for $\omega_D = \omega_L \pm \Omega_m$. We note that the Stokes and anti-Stokes scattering are optimum for a laser respectively blue and red detuned from the cavity by $\sim \Omega_m/2$.

example, we obtain a radiative loss rate of $\gamma_{a,rad}(\omega_a)/(2\pi) = 35.5$ THz and

a resulting albedo of $A(\omega_a) = 0.64$, typical of a gold antenna on resonance. We assume that the molecules are positioned at a small distance from the antenna edge such that the apparent mode volume that they are subject to is $V_a = 0.003\lambda^3$. The calculation further assumes perfect matching of excitation (power again assumed at 500 µW) and collection over a half space (NA = 1 in vacuum , or $\sim \eta_{a,\text{in/out}}\gamma_a \approx \gamma_{a,rad}/2$).

Figures. 6.5(a-c) graphically illustrates the factorization of the transfer function from vibrational to optical fluctuations into a pump term, the intensity of the laser field inside the cavity $|\bar{a}|^2$ which depends on the laser frequency $\omega_L$, and a term quantifying the collected local density of states (LDOSC) in the antenna radiation channel which depends on the frequency of the photon observed $\omega_D$, as shown in Eq.(6.17). Figure 6.5(d) shows the expected Raman spectrum $S_{out,a}$ as a function of laser frequency and detected frequency normalized by the Stokes signal emitted in a homogeneous medium at $\omega_D = \omega_a$ (i.e. $\omega_L = \omega_a + \Omega_m$), $S_{ref} = S_{00}$. We observe an enhancement of the Stokes emission of almost five orders of magnitude. Also, we can clearly identify that one requires different laser frequencies to optimize either the Stokes or anti-Stokes emission. For the considered molecules and plasmonic cavity, the Raman shift is smaller than the cavity linewidth $\Omega_m/(2\pi) = 30$ THz$< \bar{\gamma}_a/(2\pi) = 55.4$ THz, i.e. we are in the non-resolved-sideband regime. In this situation, the enhancement of the pump (at $\omega_L - \omega_a = 0$) and LDOS (at $\omega_L - \omega_a = \pm\Omega_m$) give rise to a single "average" optimum at $\omega_L - \omega_a = +\Omega_m/2$ for Stokes emission and $\omega_L - \omega_a = -\Omega_m/2$ for anti-Stokes emission, as shown in Fig. 6.5(e).

## 6.3. Molecular optomechanics with antenna-cavity hybrid resonators

In this section we discuss how to extend the framework of Roelli et al. [201] to the coupled mode description of antenna-cavity hybrid resonators of the type studied by Doeleman et al. [94], and studied in this thesis in Chapters 4 and 5. The aim is to account for the structured LDOS that they offer as well as for the input-output efficiencies for waveguide-based and far-field addressing that will determine pump field enhancement and extraction efficiency. Hybrid resonators composed of plasmonic antenna and dielectric cavity have shown the potential to exceed their individual components in term of emission enhancement (LDOS), and can provide sub-diffraction limit mode volumes at high quality factors. Furthermore, they have recently been proposed to give access to new interesting physics in the context of nonlinear molecular optomechanics by Dezfouli et al. [208].

### 6.3.1. Coupled mode equations for antenna-cavity system

We study the scenario of a hybrid composed of a single plasmonic antenna resonator and a whispering gallery mode (WGM) dielectric resonator, such as a microdisk, that is coupled to a waveguide that is placed alongside it. The dielectric cavity is described by a pair of intrinsically degenerate whispering gallery modes of resonance frequency $\omega_c$, and quality factor $Q_c$ (cf. Fig. 6.6(a)). We assume that the coupling of the antenna to all modes other than the cavity mode, i.e., to free space, can be lumped into a single loss rate, i.e., a single input/output far-field channel. The cavity possesses two relevant input/output channels, as appropriate for side coupling in a typical tapered fibre set up to address microdisks (cf. Fig. 6.6(a)). For simplicity, we assume that losses of the cavity other than radiation inside these two channels, i.e. absorption and other far-field radiation can be formally treated as absorption. This implies that their radiation patterns in the far-field have negligible overlap so that interference in the far field can be ignored (opposite to the scenario probed in Chapter 2).

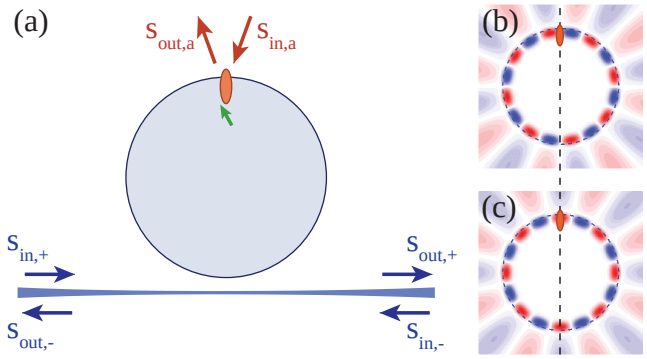


**Figure 6.6:** Considered system for molecular optomechanics with antenna-cavity hybrid. (a) Sketch of the hybrid; a plasmonic cavity, or antenna, (orange) is coupled to Raman active molecules (green), and to a microdisk dielectric cavity supporting whispering gallery modes (blue). The antenna has only a far-field radiation input/output channel, whereas the cavity is assumed to have two input/output channels, accessible for instance via evanescent coupling to a nearby waveguide. (b) and (c) sketch the degenerate modes of the cavity, in the standing wave basis, respectively the anti-symmetric and symmetric modes (with respect to a plane define by antenna position). In this basis, the antenna is at a node of the field of the anti-symmetric mode and therefore does not couple to this mode.

For a cavity supporting whispering gallery modes with two input/output channels (Fig. 6.6(a)), but fed from just one side, the coupled-mode equations are usually written as

$$\begin{cases} -i\left(\omega_L - \omega_c + i\gamma_c/2\right) c_+ = \sqrt{\eta_{c,in}\gamma_c}\, s_{+,in} \\ -i\left(\omega_L - \omega_c + i\gamma_c/2\right) c_- = 0 \end{cases} \tag{6.18}$$

for the clockwise and counterclockwise mode $c_{\pm}$. Here the input waveguide only feeds the counterclockwise mode $c_+$. We define $\omega_L$ as the laser frequency, $\omega_c, \gamma_c$ as the cavity frequency and loss rate, and $\eta_c$ as the fraction of the cavity loss rate that is due to the adjacent input/output waveguide. The perturbation of the cavity by a plasmon antenna will lift the mode degeneracy and lead to split symmetric and antisymmetric modes (symmetry relative to the antenna) $c_{S,A} = \frac{1}{\sqrt{2}}(c_+ \pm c_-)$. In this basis, the equations of motion (at zero perturbation strength) are identical and read

$$\chi_c^{-1}(\omega) c_{S,A} = \sqrt{\eta_{c,in}\gamma_c/2}\, s_{+,in} \qquad \text{with} \qquad \chi_c(\omega) \equiv \frac{i}{\omega - \omega_c + i\gamma_c/2}. \quad (6.19)$$

Both the symmetric and anti-symmetric modes are now driven at a coupling rate that is divided by a factor $1/\sqrt{2}$. Since the antenna will be at a node of the anti-symmetric cavity mode, only the symmetric cavity mode will play a role in the formation of hybrid modes relevant for our Raman scattering problem (Fig. 6.6(b-c)).

Generically, in optomechanics with whispering gallery mode cavities, both cavity modes may couple with the same mechanical degree of freedom. Such multimode coupling has been the key to recent experiments on optomechanically induced transparency, non-reciprocity and optical circulation [71, 72, 317, 318] experiments where one deploys a WGM resonator in two or four port configurations (one or two tapered fibres), and uses a control beam at frequency $\omega_L$ to control probe signals at side band frequencies $\omega_L + \Omega_m$. However, in this work we explore Raman scattering as the optomechanical interaction, where we assume that the molecular matter is only coupled to the system via the antenna plasmonic mode. This assumption is reasonable as long as the mode volume of the dielectric cavity modes is more than 2 orders of magnitude bigger than the antenna, and the matter is placed in the near-field of the antenna. Further we focus on Raman scattering (molecular motion weak and only driven by thermal fluctuations), and exclude the possibility of coherent control and probe beams to address the vibration, as in optomechanically induced transparency [317, 318]. Focusing on this scenario avoids issues in the definition of optomechanical coupling rates, since in this scenario the motion does not couple the symmetric mode to the antisymmetric mode. This means that (anti)-Stokes shifted light will only appear in the symmetric mode, and will distribute equally over both output ports. Only for reflection and transmission spectra of the pump light one still needs to consider the anti-symmetric mode to account for the interference in the forward direction with the direct drive beam [94]. In this Chapter, we only report Raman spectrum, and hence will not consider the anti-symmetric WGM mode.

Next, we follow the approach of Doeleman et al. [94] to include a plasmonic antenna coupled to the symmetric cavity mode. An idealized model of a plasmonic antenna ascribes to it a Lorentzian polarizability $\alpha(\omega)$ (resonance

$\omega_a$ and damping $\gamma_a$ that includes Ohmic and radiation loss), so that the dipole moment $p$ in the antenna couples to the cavity mode of amplitude $c$ (dropping the subscript) according to

$$\begin{cases} \left(\omega_a^2 - \omega^2 - i\omega\gamma_a\right)p - \beta_a \tilde{E}_c c = \beta_a E_{ext} \\ \left(\omega_c^2 - \omega^2 - i\omega\gamma_c\right)c - \frac{\omega^2}{2}\tilde{E}_c p = -2i\omega\sqrt{\eta_{c,in}\gamma_c}\, s_{c,in} \end{cases} \tag{6.20}$$

with $\tilde{E}_c \equiv \tilde{\mathbf{E}}_c \cdot \mathbf{e_p}$ the projection of the mode profile of the cavity mode on the antenna direction. Since here we evaluate a coupled mode formalism, and not QNM theory, this presupposes that the mode is normalized such that $|c|^2$ represents the energy stored in the mode. The driving channels in this model are the waveguide ports into the cavity ($|s_{c,in}|$), and $E_{ext}$ driving the antenna. While Doeleman et al. [94] considered a spontaneous emitter to provide $E_{ext}$, in this work this term will provide the route through which molecular motion is introduced in the equation system. Ref [94] verifies that this equation set accurately predicts waveguide input-output spectra, far field scattering and LDOS for a spontaneous emitter if one inserts as parameters resonance frequencies, quality factors, oscillator strengths and mode volumes that are obtained from full wave simulations of the bare antenna (no cavity, calculating scattering and extinction cross-section spectra) and bare cavity (calculating LDOS spectra from which Q and also the effective mode volume, through Purcell's formula, are extracted).

Evidently, the formalism proposed by Doeleman et al. to describe hybrid plasmonic-photonic systems is second order in time, while the formalism proposed by Roelli et al. [201] for molecular optomechanics (Section 6.2) is first order in time. As long as the frequency *differences* between all optical frequencies in the problem are small compared to the frequencies themselves, we can assume $\omega_{a,c}^2 - \omega^2 \approx 2\omega(\omega_{a,c} - \omega)$ to convert the hybrid plasmonic-photonic system equations to first order. Furthermore, the equation system can be cast in a symmetric notation

$$\begin{cases} -i\left(\omega - \omega_a + i\gamma_a/2\right)a - iKc = \sqrt{\eta_{a,in}\gamma_a}\, s_{a,in} \\ -i\left(\omega - \omega_c + i\gamma_c/2\right)c - iKa = \sqrt{\eta_{c,in}\gamma_c}\, s_{c,in} \end{cases} \tag{6.21}$$

by rescaling of quantities to

$$a \equiv \frac{\omega}{\sqrt{2\beta}}p, \quad K \equiv \sqrt{\frac{\beta_a}{2}}\frac{\tilde{E}_c}{2} = \frac{1}{2}\sqrt{\frac{\beta_a}{\epsilon_0 \epsilon V_c}} \quad \text{and} \quad \sqrt{\eta_{a,in}\gamma_a}\, s_{a,in} \equiv \frac{i}{2}\sqrt{\frac{\beta_a}{2}}E_{ext}, \tag{6.22}$$

where $V_c(\mathbf{r}_0) = \frac{\int \epsilon(\mathbf{r})\|\tilde{\mathbf{E}}_c(\mathbf{r})\|^2 d\mathbf{r}}{\epsilon(\mathbf{r}_0)|\tilde{E}_c(\mathbf{r}_0)|^2} = \frac{2}{\epsilon_0 \epsilon |\tilde{E}_c(\mathbf{r}_0)|^2}$ is the mode volume of the cavity mode at the position of the antenna, projected along the direction of the antenna. We will refer to $a$ as *cavity amplitude* for the plasmon antenna, and to $K$ as antenna-cavity coupling strength. Viewing these symmetric equations as

a linear system, one can diagonalize to obtain the response in both resonators to external driving as

$$\begin{cases} \chi_a'^{-1} a = \sqrt{\eta_{a,in}\gamma_a}\, s_{a,in} + iK\chi_c \sqrt{\eta_{c,in}\gamma_c}\, s_{c,in} \\ \chi_c'^{-1} c = \sqrt{\eta_{c,in}\gamma_c}\, s_{c,in} + iK\chi_a \sqrt{\eta_{a,in}\gamma_a}\, s_{a,in} \end{cases} \tag{6.23}$$

where we introduced the hybridized antenna and cavity susceptibilities

$$\begin{cases} \chi_a'^{-1} \equiv \chi_a^{-1} + K^2\chi_c \\ \chi_c'^{-1} \equiv \chi_c^{-1} + K^2\chi_a \end{cases} . \tag{6.24}$$

These hybridized susceptibilities can be seen as the original susceptibilities of the antenna and cavity dressed by an infinite series of cavity-antenna scattering events.

### 6.3.2. Molecular optomechanics

Next we include molecular motion in vein of Section 6.2, under the assumption that dynamical backaction mechanisms can be neglected. Thus, we assume a laser frequency $\omega_L$ driving the system, and determine the average field $\bar{a}$ and $\bar{c}$ inside the antenna and cavity at the laser frequency. At $\omega_L$ the system is driven either via the far-field through the antenna dipole moment, or via the cavity input channel, thus setting the average amplitudes

$$\begin{cases} -i\left(\omega_L - \omega_a + i\gamma_a/2\right)\bar{a} - iK\bar{c} = \sqrt{\eta_{a,in}\gamma_a}\,\bar{s}_{a,in} \\ -i\left(\omega_L - \omega_c + i\gamma_c/2\right)\bar{c} - iK\bar{a} = \sqrt{\eta_{c,in}\gamma_c}\,\bar{s}_{c,in} \end{cases} \tag{6.25}$$

Next we find the spectrum of fluctuations in $a$ and $c$ (detection frequency $\omega_D = \omega_L + \Omega$). At $\omega_D \neq 0$, the Raman equivalent dipole $p_m$ enters as a driving of the antenna dipole moment

$$\begin{cases} -i\left(\omega_D - \omega_a + i\gamma_a/2\right)a - iKc = f_R \\ -i\left(\omega_D - \omega_c + i\gamma_c/2\right)c - iKa = 0. \end{cases} \tag{6.26}$$

We will now argue why the driving term $f_R$ has the form $iG_m\bar{a}x_m$, i.e., the molecular optomechanics driving term that appears also in the work of Roelli et al. [201]. We assume that the Raman active vibration only directly couples to the antenna, and not the cavity mode. As in the earlier derivation of the effective Raman dipole appearing in plasmon enhanced SERS (Eq.(6.4)), the coupling between a molecular dipole and the antenna reads

$$f_R = i\frac{\omega_D}{4}\tilde{E}_a p_m, \tag{6.27}$$

with $\tilde{E}_a$ the normalized antenna mode field at the position of the molecule. In turn, the molecular dipole moment is induced by the antenna field, so that

the fluctuating part due to the molecular vibration, i.e., the effective Raman dipole reads

$$p_m(\omega_D = \omega_L + \Omega) \equiv \delta\alpha_m E_{a\to m}. \tag{6.28}$$

Here $\delta\alpha_m = \left(\frac{\partial\alpha_m}{\partial x_m}\right)x_m$ is the variation of the molecule polarizability due to the vibration, and $E_{a\to m} = \tilde{E}_a\bar{a}$ is the electric field polarizing this Raman dipole, approximated as the average field stored by the antenna. If one defines as a short hand an antenna mode volume in terms of the antenna normalized mode field as $V_a(\mathbf{r}_m) = \frac{2}{\epsilon_0\epsilon|\tilde{E}_a(\mathbf{r}_0)|^2}$, we can express $f_R$ in Eq.(6.27) as

$$f_R = i\frac{\omega_D}{4}\tilde{E}_a p_m = i\frac{\omega_D}{4}\tilde{E}_a\left[\left(\frac{\partial\alpha_m}{\partial x}\right)x_m\right]\left[\tilde{E}_a\bar{a}\right] = i\omega_D\left(\frac{\partial\alpha_m}{\partial x}\right)\frac{1}{2\epsilon_0\epsilon V_a}\bar{a}x_m \approx iG_m\bar{a}x_m.$$

To summarize, we can now predict SERS spectra in plasmonic hybrids under assumptions similar to the molecular optomechanics approach of Roelli et al. [201]. To this end one first determines from Eq.(6.25) the average plasmonic and antenna excitation at the laser frequency $\omega_L$, and subsequently uses that as input for Eq.(6.26) that returns the resulting response at shifted frequencies $\omega_D$ generated by the molecular vibration. We verified that in the limit $K \to 0$, i.e. no antenna-cavity coupling, the equations for $\bar{a}$ and $a$ reduce to the case of a single antenna.

The remaining task is to convert antenna and cavity amplitudes to observable spectra in the output ports, taking into account that the molecular motion spectral density is due to thermal fluctuations. As a helpful step, we abbreviate Eq.(6.26) for the fluctuating amplitudes with the help of the hybridized cavity and antenna susceptibilities

$$\begin{cases}\chi_a'^{-1}(\omega_D)a = iG_m\bar{a}x_m \\ \chi_c'^{-1}(\omega_D)c = iK\chi_a(\omega_D)G_m\bar{a}x_m.\end{cases} \tag{6.29}$$

We immediately identify the transfer function between $a$ and $x_m$, and between $c$ and $x_m$, and can calculate the spectra at the antenna and cavity output from the spectral density of the molecular motion as

$$\begin{cases}S_{out,a}(\omega_D) = \eta_{a,out}\gamma_a|\chi_a'(\omega_D)|^2|G_m\bar{a}|^2 S_{xx}(\Omega) \\ S_{out,c}(\omega_D) = \eta_{c,out}\gamma_c|\chi_c'(\omega_D)|^2K^2|\chi_a(\omega_D)|^2|G_m\bar{a}|^2 S_{xx}(\Omega).\end{cases} \tag{6.30}$$

We have verified by direct comparison to a calculation for LDOS, i.e., for spontaneous emission enhancement experienced by a drive dipole calculated in Ref. [94], within the same coupled-mode assumptions, that also in hybrids the Raman enhancement factorizes as the product of the free space Raman spectrum, the enhancement of pump field, and an LDOS term at the (anti)-Stokes shifted frequency. The LDOS term in fact corresponds to the collected part of the LDOS in a given output channel. This corresponds to the fraction of the LDOS that feeds into the waveguide output via the cavity mode, resp. the fraction of LDOS that corresponds to antenna free-space loss.

## 6.4. Results

### 6.4.1. Enhancement spectra

We study the enhancement of Raman scattering for a ensemble of $N = 10^3$ molecules with the same vibrational parameters as used in Figs. 6.4 and 6.5, by a hybrid resonator composed of the same antenna as in Fig. 6.4, and a cavity resonant at $\omega_c/(2\pi) = 400$ THz, with a quality factor $Q_c = 10^4$, and a mode volume at the position of the antenna of $V_c = 10\lambda^3$. We assume critical coupling to the taper. Figure 6.7 reports the spectrum obtained in the (antenna) far-field channel, for 500 μW input coupled in from the same channel.

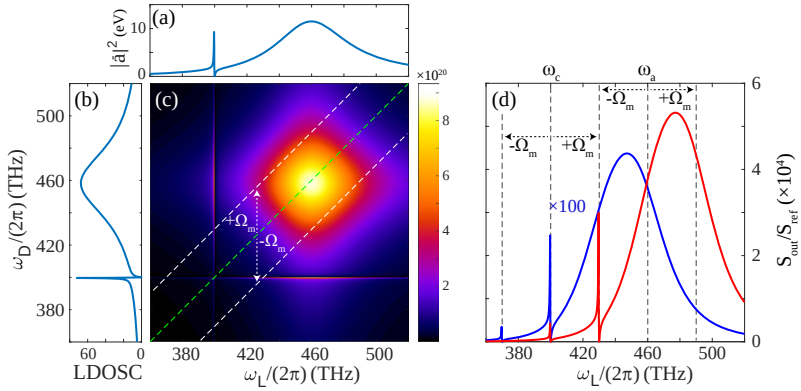


**Figure 6.7:** Molecular optomechanics with a cavity-antenna hybrid observed through antenna radiation channel (same parameters as 6.5, with a cavity resonant at $\omega_c/(2\pi) = 400$ THz, $Q_c = 10^4$, and $V_c = 10\lambda^3$). (a) Average intensity of the cavity field, i.e. at the driving laser frequency. (b) Local density of states for photons collected in the far-field. (c) Transfer function between $x_m$ and $a$ of the antenna $S_{a,out}/S_{xx}$. The green dashed line indicates the laser frequency, and the white dashed lines indicate Stokes and anti-Stokes emission. (d) Raman spectrum as a function of laser frequency taken at the Stokes (red) or anti-Stokes peak (blue). We observe the same broad features as in 6.5(e), due to the "hybrid antenna" mode. Additionally, both Stokes and anti-Stokes spectra exhibit 2 new peaks, due to the "hybrid cavity" mode. Stokes and anti-Stokes exhibit one peak at the same laser frequency; this peak is due to enhancement of the number of pump photon inside the cavity. The other peak, red shifted for Stokes and blue shifted for anti-Stokes by $\pm\Omega$, is due to an hybrid increase in LDOS favouring the emission of Raman photons.

As in Fig. 6.5(a-c), we observe in Fig. 6.7 the joint effect of a pump enhancement and LDOS enhancement in the plasmonic cavity susceptibility, and therefore the Raman signal scattered in the far-field. However, both these contributions now exhibit, additionally to the antenna (hybrid) peak, a cavity-like hybrid peak. Since this new hybrid feature is a high-Q resonance, it falls in the resolved-sideband regime for the considered Raman shift. As a result, Fig. 6.7(e) reveals two high-Q Fano peaks separated by $\Omega_m$, for both

Stokes and anti-Stokes spectra. The first peak, common for Stokes and anti-Stokes, corresponds to tuning of the pump laser to the cavity-like hybrid mode, leading to pump field enhancement. At this frequency, free space light can couple into the cavity mode via the antenna, subsequently boosting antenna excitation. At the same time, the LDOS at the Raman-shifted frequency is only moderately enhanced by the broader hybrid mode, i.e. by the antenna-like mode. Conversely, for the second peak, Stokes (or anti-Stokes) emission is enhanced due to the hybrid boost of the LDOS at the Raman shifted frequency due to the cavity-like hybrid mode (when $\omega_L \approx \omega_c' + \Omega_m$ ($\omega_L \approx \omega_c' - \Omega_m$)). In this case the pump is not enhanced by the presence of the cavity mode, but only by the broad antenna hybrid mode. In both scenarios, the enhancement of Raman scattering does not exceed the enhancement that can be obtained near the antenna resonance, i.e. far detuned from the cavity mode. This might appear surprising since the cavity hybrid mode actually provides a higher LDOS than the antenna alone, and the maximum pump enhancement at the hybrid cavity mode is comparable to that provided by the bare antenna on its resonance. However, maximum Raman enhancement requires the *product* of pump enhancement and LDOS enhancement to be optimum. A bare antenna exploits simultaneously an enhancement of the pump and the LDOS, whereas a non-optimized hybrid only enhances either the pump or the emission process, but not both simultaneously.



### **6.4.2.** Combinations of input and output channels

Since Raman enhancement needs to exploit *both* pump field enhancement *and* enhancement of the (extracted) LDOS, it is not sufficient to choose an optimum set of drive and resonator frequencies, but one also needs to exploit the appropriate channels for injecting and extracting light. To illustate this. we present in Figure 6.8 the Raman spectrum $S_{out,+}$ extracted at one of the cavity output channels for the exact same parameters as in Fig. 6.7, while again assuming that the pump light addresses the antenna from free space. Since we still consider pumping from the far field, the pump field enhancement factor is the same as in Fig. 6.7(a). However, the extracted LDOS contribution is now different (panel (b)) compared to Fig. 6.7(b). Since only photons resonant with the cavity hybrid mode can efficiently make their way to the cavity output channels, the enhancement contribution at the Raman-shifted frequency is now highly peaked (Fig. 6.8(b)) and the Raman transfer function is now markedly asymmetric in the 2D representation (Fig. 6.8(c)) as function of laser and detection frequency. This spectral selectivity of the cavity output channel implies in Fig. 6.8(d) that the only relevant peaks in Raman spectra are the ones where the Stokes (or anti-Stokes) emission is resonant with the cavity hybrid mode ($\omega_L = \omega_c' \pm \Omega_m$). Such a spectral filtering property may be useful for compact and highly selective chip-integrated Raman devices to detect specific chemical traces, without the use of a bulky spectrometer. In this

example, the signal that would be extracted through the waveguide is still one order of magnitude weaker than the signal that is radiated into the far-field. However, it should be noted that the far field channel optimistically assumes that all photons can be collected in a full half space of $2\pi$ sr, whereas usual microscope objective even at high NA capture only 10 to 50% of that.

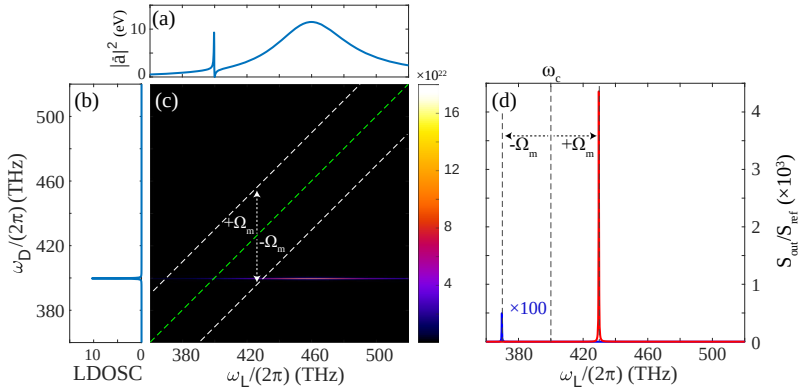


**Figure 6.8:** Molecular optomechanics with a cavity-antenna hybrid (same parameters as Fig. 6.7), observed through cavity output channel. (a) Average intensity of the cavity field (b) Local density of states for photons collected in cavity output channel. (c) Transfer function between $x_m$ and $c$ of the cavity $S_{c,out}/S_{xx}$. The green dashed line indicates the laser frequency, and the white dashed lines indicate Stokes and anti-Stokes emission. (d) Raman spectrum as a function of laser frequency taken at the Stokes (red) or anti-Stokes peak (blue). Since photons need to be resonant with the cavity hybrid mode to be scattered efficiently through the cavity output channel, Stokes and anti-Stokes emission is only significant when the laser is respectively blue or red shifted of $\pm\Omega_m$ from the cavity.

A systematic comparison of all combinations of input and output channels for Raman spectroscopy schemes is shown in Fig. 6.9, focusing on Stokes scattering only. We find that generally, pumping via the waveguide is disadvantageous, since it only allows pump light to actually reach the antenna and molecular matter when it is resonant with the cavity hybrid mode ($\omega_L = \omega_c'$). At this condition, there is no strong LDOS enhancement at the shifted frequency. Conversely, if the cavity resonance is overlapped with the Stokes-shifted line, the pump field is actually suppressed at the antenna compared to free space excitation. Therefore the collected signal in any channel is always at least two orders of magnitude lower than for far-field driving. This is particularly true for the cavity output channel (panel (a)) as both the pump and the Raman signal need to go through the cavity for one to detect any signal in the cavity output channel. The optimum usage scenario is hence to use free space at a laser frequency that is shifted by exactly the Raman shift from the hybrid resonance, combined with waveguide collection. In [94], the authors suggested that it is even possible to extract from the cavity loss chan-

nels almost all the light emitted by a dipole source at the antenna. However, this would require very strong antenna-cavity detuning, detrimental in our Raman scheme for field enhancement.

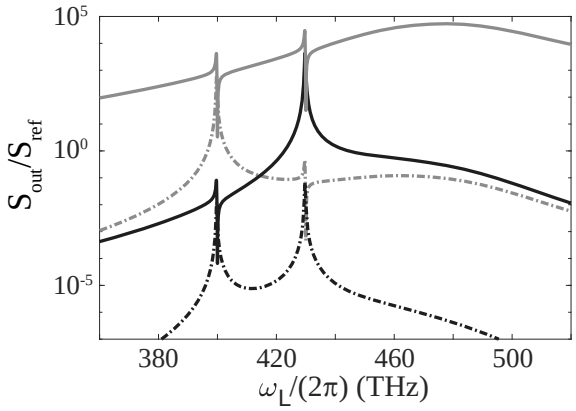


**Figure 6.9:** Stokes emission spectrum as a function of laser frequency for different input-output configurations. Solid lines indicate antenna far-field input, while dashed lines indicate input through the waveguide into the cavity. All considered cases assume an input power of 500 µW. Gray lines represent the scattering into the antenna radiation (far-field) output channel, and black lines, the cavity output channel. We note that pumping the system from the cavity input channel leads to weaker scattering in either channel by at least 2 orders of magnitude than via the antenna because the pump needs to be resonant with the narrow cavity hybrid mode.



### 6.4.3. Optimal cavity-antenna detuning

In [94], a main result is that there exists an optimum cavity-antenna detuning to obtain the highest emission enhancement of an emitter, and even beat the limit on LDOS enhancement by any dipolar antenna that is imposed by radiation damping. However, by definition, this LDOS enhancement is only relevant for the emission process, and not for pump field enhancement which in Raman scattering is equally important as LDOS control. Additionally, we understand from previous sections that exploiting both the antenna and cavity hybrid modes simultaneously could be beneficial in molecular optomechanics, whereas for the LDOS boost only the cavity hybrid mode is relevant. Therefore, it is important to assess also for Raman scattering what the optimal tuning choice is for cavity and antenna relative to each other and to the laser wavelength.

We study qualitatively in Figure 6.10 the optimum cavity antenna detuning, where we keep all parameters of our calculation the same as in Figs. 6.7 and 6.8, except for the resonance frequency of the cavity, for which we step from red detuned to blue detuned relative to the antenna. We report the Stokes (panels (a,b)) and anti-Stokes (d,e) intensity as function of laser wavelength,

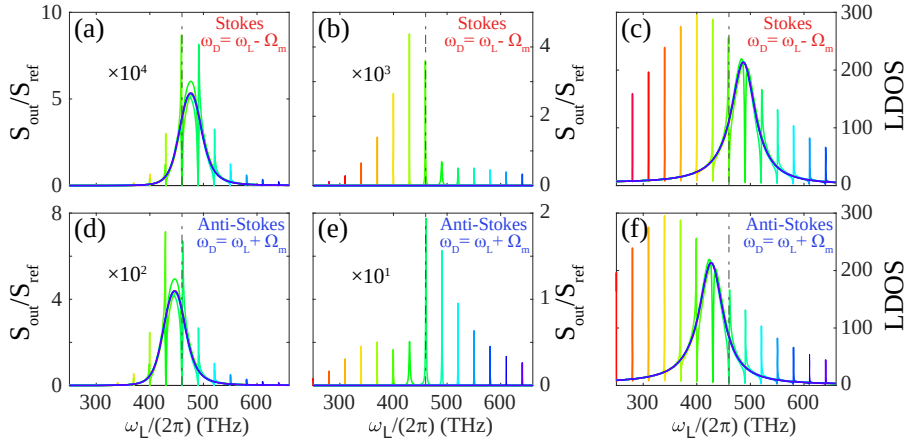


**Figure 6.10:** Cavity-antenna detuning dependence. Stokes (panel (a,b)) and anti-Stokes (panel (d,e)) intensity as function of laser frequency for different choices of hybrid. Each colour curve corresponds to a different hybrid, where all hybrids assume the same antenna (fixed antenna resonance $\omega_a$), but a different cavity mode frequency. To obtain a representative sampling of cavity-antenna detunings, we sample a ladder of 14 different resonance frequencies. The cavities all have identical Q, and identical mode volume (in units of cubic wavelength). For all panels we assumed pumping from free space driving of the antenna, while we consider collection through free space (panels (a,d)) and waveguide (panels (b,e)). For reference, (c) and (f) represent the total LDOS at the detected frequency $\omega_D$, which is $\omega_D = \omega_L - \Omega_m$ for Stokes and $\omega_D = \omega_L + \Omega_m$ for anti-Stokes. Note that (c) and (f) are the same plot shifted by $2\Omega_m$. In all panels, we indicate with a vertical dashed line the resonance frequency of the antenna $\omega_a$.

where the antenna is kept constant for all curves, and each curve represents a distinct resonator frequency choice. Results are shown for both free space detection (panels (a,d)) and extraction through the waveguide ports (panels (b,e)). Our first observation is that for Stokes and anti-Stokes emission (Figs. 6.10(a,d)), a hybrid offers a modest benefit compared to a bare antenna in terms of signal scattered into the far-field. If one wants to benefit from the maximum hybrid LDOS boost mentioned by Doeleman et al. in [94], the cavity must be detuned from the antenna by more than the antenna linewidth $\gamma_a$. For most Raman scenarios, typically $\Omega_m < \gamma_a$ so that a compromise must be sought between a good benefit from LDOS and a good pump field enhancement.

Panels (b,e) consider the scenario where one extracts the Raman signal from a waveguide via the cavity output channel, which is not possible for standard SERS with a simple antenna. We observe in panel (b) that Stokes emission is favoured when the cavity is red-detuned from the antenna by $\sim -\Omega_m$, corresponding to the previously identified regime where the pump is enhanced by the antenna mode, while the Raman emission is boosted by the high hybrid LDOS. For anti-Stokes detection, the argument for an optimal

cavity-antenna detuning is less clear. With a cavity-blue detuned from the antenna one can simultaneously benefit from the antenna resonance for pump field enhancement, and from the cavity hybrid LDOS. However, due to the intrinsic frequency dependence of the antenna radiation loss, the LDOS boost is not as good for blue, as for red-detuned cavities (cf. Ref. [94]).

## 6.5. Conclusion and outlook

In conclusion, we have adapted the molecular optomechanics model proposed by Roelli et al. [201] in the classical and linear regime to account for the main physics of hybrid resonators composed of whispering gallery mode cavity and a plasmonic antenna. With this theory, we have shown that the hybrid enhanced Raman scattering collected at an output channel is determined by a resonant enhancement of the pump intensity, and the fraction of the LDOS collected at this particular output channel. While in conventional plasmonics system this factorization is usually close to a $|E/E_0|^4$ law for scaling of Raman signal with field enhancement, in hybrids it is a crucial realization that the pump and the LDOS enhancement contributions are distinct. We have identified a regime of particular interest, where the pump is enhanced by the plasmonic confinement of the antenna-like hybrid mode and the Raman signal benefit from the LDOS boost enabled by high-Q cavity like hybrid mode. In this scenario, the signal collected in the cavity output channel exhibits a strong spectral selectivity related to the narrow bandwidth of the cavity hybrid mode.



### 6.5.1. Outlook on experiments

We foresee that experimental realization of hybrid resonators in the context of SERS is possible using purely top-down, bottom-up, and mixed fabrication approaches. A promising route is to coat colloidal plasmonic particles on dielectric cavities [101, 102]. Also, one can envision lithographically prepared antennas on cavities, as we realized for Chapters 4 and 5. Finally, one could envision using a plasmonic near-field tip coupled to a cavity as in Ref. [171]. In any of these strategies, a main challenge is selective adsorption of molecules in the proximity of the hotspots of the antenna. Another challenge will be to go beyond large but linear SERS enhancement effects, pushing towards the regime of dynamical backaction. This dynamical backaction (DBA) regime, also called vibrational pumping, is attained when the optomechanically induced damping rate $\Gamma_{dba}$, which scales as $Q^2/V^2$ (but also involves $R_m/\Omega_m$ and the laser intensity as parameters), is of the same order of magnitude as the intrinsic damping rate of the molecular vibration $\Gamma_m$ [201]. First reports [14, 297] are appearing that claim observed signatures of dynamical backaction for ensembles of molecules ($N = 750$) and single molecules in nanoscale and picoscale gap antenna systems, with claimed $Q$'s around $Q =$

10 and mode volume $V = 2\times10^{-6}\lambda^3$ (gold dimers, molecular ensemble), resp. $V = 3\times10^{-7}\lambda^3$ and quality factor $Q = 15$ which corresponds to $Q^2/V^2 \approx 10^{15}\lambda^{-6}$ (picocavity [14]). Hybrids trade $Q$ for $V$, while having the abilitry to preserve the $Q/V$ value of the antenna one starts with. Even though the design studied in this chapter ($V_{hyb} = 10^{-1}$, $Q_{hyb} = 10^4$) is far from adequate with only $Q^2/V^2 \approx 10^8\lambda^{-6}$, the best realistic hybrid design discussed in [95] ($V_{hyb} < 10^{-4}$, $Q_{hyb} > 10^3$) could potentially reach the required conditions for DBA with $Q^2/V^2 \approx 10^{14}\lambda^{-6}$. This assumes a photonic crystal nanobeam cavity (with $V = \lambda^3/8$, effectively $2\lambda^3$ at the surface where an antenna could be placed) and a dimer gap antenna with a 1 nm gap. Raising that to a 5 nm gap, reduces the performance in terms of $Q/V$ by one order of magnitude. It is unknown if better hybrid resonators exist outside the design space of dipolar gap antennas coupled perturbatively to a cavity. Evidently, hybrids do give access to a different SERS regime then plasmon antennas, through sideband resolution, but do not intrinsically relax the constraints on antenna gap dimension. The requirements would be relaxed for the study of dynamical backaction or vibrational pumping in the case of collective molecular oscillation. In this situation, one could imagine exploiting the waveguide channel of the hybrid to send a probe beam shifted by $\Omega_m$ from the laser and observe optomechanically induced transparency [317, 318] induced by coherent vibrational response of the molecular ensemble by a pump beam. Also, hybrid resonators could help fill the gap existing in the availability of solutions for efficient detection of IR and THz electromagnetic waves. Since incident IR/THz absorption in a molecular species can cause vibrational excitation above the thermal equilibrium occupation, once can envision read out of IR/THz light by monitoring anti-Stokes shifted scattering, on the proviso that the molecular species is both IR and Raman active. Using a hybrid resonator to selectively enhance Stokes and anti-Stokes lines of the vibration of interest and to collect the signal through waveguides towards detectors, with the potential of using a distinct channel for Stokes an anti-Stokes, would eliminate the need to use spectrometers to analyse the Raman scattered light and could allow for integrated devices.



### 6.5.2. Challenges for theory

If hybrid plasmonic-dielectric resonators do become a major device in molecular optomechanics and applications, one would need to significantly expand the work presented in this chapter. Indeed, the first and most obvious limitation of our work is the fact that we assumed a regime where dynamical backaction does not play a role, and therefore that the vibration of the molecule is purely driven by thermal fluctuation as expressed in Eqs.(6.16 and 6.30). However, this can easily be fixed by including the equation of motion for $x_m$ as it is originally present in Eq.(6.5), but neglected in subsequent part of the chapter. A second limitation comes from the fact that our theory precludes

quantum phenomena, such as the anharmonic cavity-QED regime described in [208] or phonon-stimulated Raman scattering treated in [304]. An option to solve this issue would be to integrate the second photonic mode (cavity) in the Hamiltonian of the system in Eq.(6.3), and from there choose either a classical, semi-classical or quantum treatment depending on the phenomenon of interest [305]. Finally, in this work, we assumed that the molecules only couple to the hybrid through the plasmonic field, and do not directly scatter into the cavity. This does not hold generally for a hybrid, as it requires that the effective mode volumes of both resonators have a more than $\sim 2$ orders of magnitude difference. For spontaneous emission, Doeleman et al. [94] already noted important corrections to the Purcell factor due to direct coupling of the assumed emitter to *both* modes. For optomechanics this leads to a fundamental challenge. Not only does one need to define an optomechanical coupling rate $G_{m,a}$ and $G_{m,c}$ for both antenna and cavity mode separately (Eq.(6.4)), but also one can imagine that the mechanical motion of the molecular matter causes optomechanical cross-terms $G_{m,ac}$ and $G_{m,ca}$ [306]. Such cross-terms should be expected not just in molecular optomechanics, but are a challenge for any multimode perturbation theory. We anticipate that these terms would scale as $1/\sqrt{V_a V_c}$, and would contribute to the Hamiltonian as an additional interaction $H_{cross} = -\hbar\left[G_{m,ac}\hat{a}^\dagger\hat{c} + G_{m,ca}\hat{c}^\dagger\hat{a}\right]x_{zpf}(\hat{b}^\dagger + \hat{b})$, which implies that the antenna and cavity hybridize not only via direct interaction, but also through the molecular vibrations. In this case, the hybrid properties, such as LDOS, should dynamically depend on the molecular motion $x_m$, leading to new unexplored properties. Ref. [303] suggests that a quantum mechanical approach based on a quasinormal mode formalism is a fruitful approach to tackling these challenges.

# References


1. F. Zernike, *Phase contrast, a new method for the microscopic observation of transparent objects*, Physica **9**, 686 (1942).
2. D. Huang, E. Swanson, C. Lin, J. Schuman, W. Stinson, W. Chang, M. Hee, T. Flotte, K. Gregory, C. Puliafito, and A. Et, *Optical coherence tomography*, Science **254**, 1178 (1991).
3. S. W. Hell and J. Wichmann, *Breaking the diffraction resolution limit by stimulated emission: stimulated-emission-depletion fluorescence microscopy*, Opt. Lett. **19**, 780 (1994).
4. T. H. Maiman, *Stimulated optical radiation in ruby*, Nature **187**, 493 (1960).
5. W. D. Phillips, *Nobel lecture: Laser cooling and trapping of neutral atoms*, Rev. Mod. Phys. **70**, 721 (1998).
6. A. Aspect, J. Dalibard, and G. Roger, *Experimental test of Bell's inequalities using time-varying analyzers*, Phys. Rev. Lett. **49**, 1804 (1982).
7. B. P. Abbott *et al.*, *Observation of gravitational waves from a binary black hole merger*, Phys. Rev. Lett. **116**, 061102 (2016).
8. J. Hecht, *City of Light: The Story of Fiber Optics* (Oxford Unviersity Press, 2004).
9. N. Gisin and R. Thew, *Quantum communication*, Nat. Photonics **1**, 165 (2007).
10. B. J. Shastri, A. N. Tait, T. Ferreira de Lima, M. A. Nahmias, H.-T. Peng, and P. R. Prucnal, *Neuromorphic Photonics, Principles of* (Springer Berlin Heidelberg, 2018).
11. R. Hamerly *et al.*, *Experimental investigation of performance differences between coherent Ising machines and a quantum annealer*, Sci. Adv. **5**, eaau0823 (2019).
12. A. F. Koenderink, A. Alu, and A. Polman, *Nanophotonics: Shrinking light-based technology*, Science **348**, 516 (2015).
13. T. Asano, Y. Ochi, Y. Takahashi, K. Kishimoto, and S. Noda, *Photonic crystal nanocavity with a Q factor exceeding eleven million*, Opt. Express **25**, 1769 (2017).
14. F. Benz *et al.*, *Single-molecule optomechanics in "picocavities"*, Science **354**, 726 (2016).

15. G. Grynberg, A. Aspect, and C. Fabre, *Introduction to Quantum Optics: From the Semi-classical Approach to Quantized Light* (Cambridge University Press, 2010).
16. L. Novotny and B. Hecht, *Principles of Nano-Optics* (Cambridge University Press, 2006).
17. E. M. Purcell, *Spontaneous emission probabilities at radio frequencies*, Phys. Rev. **69**, 681 (1946).
18. K. Drexhage, *Influence of a dielectric interface on fluorescence decay time*, J. Lumin. **1-2**, 693 (1970).
19. P. Lodahl, A. Floris van Driel, I. S. Nikolaev, A. Irman, K. Overgaag, D. Vanmaekelbergh, and W. L. Vos, *Controlling the dynamics of spontaneous emission from quantum dots by photonic crystals*, Nature **430**, 654 (2004).
20. L. Langguth, R. Fleury, A. Alù, and A. F. Koenderink, *Drexhage's experiment for sound*, Phys. Rev. Lett. **116**, 224301 (2016).
21. A. F. Koenderink, *Single-photon nanoantennas*, ACS Photonics **4**, 710 (2017).
22. J. R. Lakowicz, *Plasmonics in biology and plasmon-controlled fluorescence*, Plasmonics **1**, 5 (2006).
23. S. A. Mann, R. R. Grote, R. M. Osgood, A. Alù, and E. C. Garnett, *Opportunities and limitations for nanophotonic structures to exceed the shockley–queisser limit*, ACS Nano **10**, 8620 (2016).
24. E. C. Le Ru and P. G. Etchegoin, *Principles of Surface-Enhanced Raman Spectroscopy* (Elsevier, 2009).
25. J. Langer *et al.*, *Present and future of surface enhanced Raman scattering*, ACS Nano , 9b04224 (2019).
26. R. Waldron, *Perturbation theory of resonant cavities*, Proc. IEE Part C **107**, 272 (1960).
27. H. A. Bethe and J. Schwinger, *Perturbation theory for cavities* (Massachusetts Institute of Technology, Radiation Laboratory, 1943).
28. P. Lunnemann, F. T. Rabouw, R. J. A. van Dijk-Moes, F. Pietra, D. Vanmaekelbergh, and A. F. Koenderink, *Calibrating and controlling the quantum efficiency distribution of inhomogeneously broadened quantum rods by using a mirror ball*, ACS Nano **7**, 5984 (2013).
29. Y. C. Jun, R. D. Kekatpure, J. S. White, and M. L. Brongersma, *Nonresonant enhancement of spontaneous emission in metal-dielectric-metal plasmon waveguide structures*, Phys. Rev. B **78**, 153111 (2008).
30. B. Corcoran, C. Monat, C. Grillet, D. J. Moss, B. J. Eggleton, T. P. White, L. O'Faolain, and T. F. Krauss, *Green light emission in silicon through slow-light enhanced third-harmonic generation in photonic-crystal waveguides*, Nat. Photonics **3**, 206 (2009).
31. S. J. Dewhurst, D. Granados, D. J. P. Ellis, A. J. Bennett, R. B. Patel, I. Farrer, D. Anderson, G. A. C. Jones, D. A. Ritchie, and A. J. Shields,

*Slow-light-enhanced single quantum dot emission in a unidirectional photonic crystal waveguide*, Appl. Phys. Lett. **96**, 031109 (2010).

32. L. Langguth, D. Punj, J. Wenger, and A. F. Koenderink, *Plasmonic band structure controls single-molecule fluorescence*, ACS Nano **7**, 8840 (2013).
33. K. Vynck, M. Burresi, F. Riboli, and D. S. Wiersma, *Photon management in two-dimensional disordered media*, Nat. Mater. **11**, 1017 (2012).
34. L. Sapienza, H. Thyrrestrup, S. Stobbe, P. D. Garcia, S. Smolka, and P. Lodahl, *Cavity quantum electrodynamics with Anderson-localized modes*, Science **327**, 1352 (2010).
35. F. D. Martini, G. Innocenti, G. R. Jacobovitz, and P. Mataloni, *Anomalous spontaneous emission time in a microscopic optical cavity*, Phys. Rev. Lett. **59**, 2955 (1987).
36. R. J. Thompson, G. Rempe, and H. J. Kimble, *Observation of normal-mode splitting for an atom in an optical cavity*, Phys. Rev. Lett. **68**, 1132 (1992).
37. J. Kasprzak *et al.*, *Bose–Einstein condensation of exciton polaritons*, Nature **443**, 409 (2006).
38. J. B. Khurgin, *How to deal with the loss in plasmonics and metamaterials*, Nat. Nanotechnol. **10**, 2 (2015).
39. S. Strauf, N. G. Stoltz, M. T. Rakher, L. A. Coldren, P. M. Petroff, and D. Bouwmeester, *High-frequency single-photon source with polarization control*, Nat. Photonics **1**, 704 (2007).
40. N. Somaschi *et al.*, *Near-optimal single-photon sources in the solid state*, Nat. Photonics **10**, 340 (2016).
41. J. P. Reithmaier, G. Sęk, A. Löffler, C. Hofmann, S. Kuhn, S. Reitzenstein, L. V. Keldysh, V. D. Kulakovskii, T. L. Reinecke, and A. Forchel, *Strong coupling in a single quantum dot–semiconductor microcavity system*, Nature **432**, 197 (2004).
42. Y. Akahane, T. Asano, B.-S. Song, and S. Noda, *High-q photonic nanocavity in a two-dimensional photonic crystal*, Nature **425**, 944 (2003).
43. J. D. Joannopoulos, S. G. Johnson, J. N. Winn, and R. D. Meade, *Photonic Crystals* (Princeton University Press, 2008).
44. E. Yablonovitch, *Inhibited spontaneous emission in solid-state physics and electronics*, Phys. Rev. Lett. **58**, 2059 (1987).
45. S. John, *Strong localization of photons in certain disordered dielectric superlattices*, Phys. Rev. Lett. **58**, 2486 (1987).
46. T. Yoshie, A. Scherer, J. Hendrickson, G. Khitrova, H. M. Gibbs, G. Rupper, C. Ell, O. B. Shchekin, and D. G. Deppe, *Vacuum Rabi splitting with a single quantum dot in a photonic crystal nanocavity*, Nature **432**, 200 (2004).
47. A. Faraon, I. Fushman, D. Englund, N. Stoltz, P. Petroff, and J. Vučković, *Coherent generation of non-classical light on a chip via photon-induced tunnelling and blockade*, Nat. Phys. **4**, 859 (2008).

48. H. Altug, D. Englund, and J. Vučković, *Ultrafast photonic crystal nanocavity laser*, Nat. Phys. **2**, 484 (2006).
49. A. Reinhard, T. Volz, M. Winger, A. Badolato, K. J. Hennessy, E. L. Hu, and A. Imamoğlu, *Strongly correlated photons on a chip*, Nat. Photonics **6**, 93 (2012).
50. J. Chan, T. P. M. Alegre, A. H. Safavi-Naeini, J. T. Hill, A. Krause, S. Gröblacher, M. Aspelmeyer, and O. Painter, *Laser cooling of a nanomechanical oscillator into its quantum ground state*, Nature **478**, 89 (2011).
51. R. Leijssen, G. R. La Gala, L. Freisem, J. T. Muhonen, and E. Verhagen, *Nonlinear cavity optomechanics with nanomechanical thermal fluctuations*, Nat. Commun. **8**, ncomms16024 (2017).
52. D. W. Vernooy, V. S. Ilchenko, H. Mabuchi, E. W. Streed, and H. J. Kimble, *High-Q measurements of fused-silica microspheres in the near infrared*, Opt. Lett. **23**, 247 (1998).
53. D. K. Armani, T. J. Kippenberg, S. M. Spillane, and K. J. Vahala, *Ultra-high-Q toroid microcavity on a chip*, Nature **421**, 925 (2003).
54. T. J. Kippenberg, S. M. Spillane, and K. J. Vahala, *Demonstration of ultra-high-Q small mode volume toroid microcavities on a chip*, Appl. Phys. Lett. **85**, 6113 (2004).
55. F. Vollmer and S. Arnold, *Whispering-gallery-mode biosensing: Label-free detection down to single molecules*, Nat. Methods **5**, 591 (2008).
56. A. M. Armani and K. J. Vahala, *Heavy water detection using ultra-high-Q microcavities*, Opt. Lett. **31**, 1896 (2006).
57. M. de Goede, M. Dijkstra, R. Obregón, J. Ramón-Azcón, E. Martínez, L. Padilla, F. Mitjans, and S. M. Garcia-Blanco, *$Al_2O_3$ microring resonators for the detection of a cancer biomarker in undiluted urine*, Opt. Express **27**, 18508 (2019).
58. T. J. Kippenberg, S. M. Spillane, D. K. Armani, and K. J. Vahala, *Ultralow-threshold microcavity Raman laser on a microelectronic chip*, Opt. Lett. **29**, 1224 (2004).
59. P. Del'Haye, A. Schliesser, O. Arcizet, T. Wilken, R. Holzwarth, and T. J. Kippenberg, *Optical frequency comb generation from a monolithic microresonator*, Nature **450**, 1214 (2007).
60. T. J. Kippenberg, R. Holzwarth, and S. A. Diddams, *Microresonator-based optical frequency combs*, Science **332**, 555 (2011).
61. T. W. Hänsch, *Nobel lecture: Passion for precision*, Rev. Mod. Phys. **78**, 1297 (2006).
62. E. Temprana, E. Myslivets, B. P.-P. Kuo, L. Liu, V. Ataie, N. Alic, and S. Radic, *Overcoming Kerr-induced capacity limit in optical fiber transmission*, Science **348**, 1445 (2015).
63. I. Coddington, N. Newbury, and W. Swann, *Dual-comb spectroscopy*, Optica **3**, 414 (2016).

64. E. Peter, P. Senellart, D. Martrou, A. Lemaître, J. Hours, J. M. Gérard, and J. Bloch, *Exciton-photon strong-coupling regime for a single quantum dot embedded in a microcavity*, Phys. Rev. Lett. **95**, 067401 (2005).
65. K. Srinivasan and O. Painter, *Linear and nonlinear optical spectroscopy of a strongly coupled microdisk–quantum dot system*, Nature **450**, 862 (2007).
66. B. Peng, S. K. Özdemir, F. Lei, F. Monifi, M. Gianfreda, G. L. Long, S. Fan, F. Nori, C. M. Bender, and L. Yang, *Parity-time-symmetric whispering-gallery microcavities*, Nat. Phys. **10**, 394 (2014).
67. H. Hodaei, M.-A. Miri, M. Heinrich, D. N. Christodoulides, and M. Khajavikhan, *Parity-time-symmetric microring lasers*, Science **346**, 975 (2014).
68. P. Miao, Z. Zhang, J. Sun, W. Walasik, S. Longhi, N. M. Litchinitser, and L. Feng, *Orbital angular momentum microlaser*, Science **353**, 464 (2016).
69. B. Peng, a. K. Özdemir, M. Liertzer, W. Chen, J. Kramer, H. Yilmaz, J. Wiersig, S. Rotter, and L. Yang, *Chiral modes and directional lasing at exceptional points*, Proc. Natl. Acad. Sci. **113**, 6845 (2016).
70. Z. Shen, Y.-L. Zhang, Y. Chen, C.-L. Zou, Y.-F. Xiao, X.-B. Zou, F.-W. Sun, G.-C. Guo, and C.-H. Dong, *Experimental realization of optomechanically induced non-reciprocity*, Nat. Photonics **10**, 657 (2016).
71. F. Ruesink, M.-A. Miri, A. Alù, and E. Verhagen, *Nonreciprocity and magnetic-free isolation based on optomechanical interactions*, Nat. Commun. **7**, 13662 (2016).
72. F. Ruesink, J. P. Mathew, M.-A. Miri, A. Alù, and E. Verhagen, *Optical circulation in a multimode optomechanical resonator*, Nat. Commun. **9**, 1798 (2018).
73. D. Kosters, A. de Hoogh, H. Zeijlemaker, H. Acar, N. Rotenberg, and L. Kuipers, *Core–shell plasmonic nanohelices*, ACS Photonics **4**, 1858 (2017).
74. W. Zhu and K. B. Crozier, *Quantum mechanical limit to plasmonic enhancement as observed by surface-enhanced Raman scattering*, Nat. Commun. **5**, 5228 (2014).
75. M. Agio and A. Alù, *Optical antennas* (Cambridge University Press, 2011).
76. S. Khatua, P. M. R. Paulo, H. Yuan, A. Gupta, P. Zijlstra, and M. Orrit, *Resonant plasmonic enhancement of single-molecule fluorescence by individual gold nanorods*, ACS Nano **8**, 4440 (2014).
77. A. Kinkhabwala, Z. Yu, S. Fan, Y. Avlasevich, K. Müllen, and W. E. Moerner, *Large single-molecule fluorescence enhancements produced by a bowtie nanoantenna*, Nat. Photonics **3**, 654 (2009).
78. S. Bidault, A. Devilez, V. Maillard, L. Lermusiaux, J.-M. Guigner, N. Bonod, and J. Wenger, *Picosecond lifetimes with high quantum yields from single-photon-emitting colloidal nanostructures at room temperature*, ACS Nano **10**, 4806 (2016).
79. G. M. Akselrod, C. Argyropoulos, T. B. Hoang, C. Ciracì, C. Fang, J. Huang, D. R. Smith, and M. H. Mikkelsen, *Probing the mechanisms of*

*large Purcell enhancement in plasmonic nanoantennas*, Nat. Photonics **8**, 835 (2014).

80. J. Khurgin, W. Y. Tsai, D. P. Tsai, and G. Sun, *Landau damping and limit to field confinement and enhancement in plasmonic dimers*, ACS Photonics **4**, 2871 (2017).
81. K. J. Savage, M. M. Hawkeye, R. Esteban, A. G. Borisov, J. Aizpurua, and J. J. Baumberg, *Revealing the quantum regime in tunnelling plasmonics*, Nature **491**, 574 (2012).
82. A. G. Curto, G. Volpe, T. H. Taminiau, M. P. Kreuzer, R. Quidant, and N. F. Van Hulst, *Unidirectional emission of a quantum dot coupled to a nanoantenna*, Science **329**, 930 (2010).
83. A. F. Koenderink, *Plasmon nanoparticle array waveguides for single photon and single plasmon sources*, Nano Lett. **9**, 4228 (2009).
84. T. Coenen, E. J. R. Vesseur, A. Polman, and A. F. Koenderink, *Directional emission from plasmonic Yagi-Uda antennas probed by angle-resolved cathodoluminescence spectroscopy*, Nano Lett. **11**, 3779 (2011).
85. A. Apuzzo, M. Février, R. Salas-Montiel, A. Bruyant, A. Chelnokov, G. Lérondel, B. Dagens, and S. Blaize, *Observation of near-field dipolar interactions involved in a metal nanoparticle chain waveguide*, Nano Letters **13**, 1000 (2013).
86. B. Luk'Yanchuk, N. I. Zheludev, S. A. Maier, N. J. Halas, P. Nordlander, H. Giessen, and C. T. Chong, *The Fano resonance in plasmonic nanostructures and metamaterials*, Nat. Mater. **9**, 707 (2010).
87. A. Lovera, B. Gallinet, P. Nordlander, and O. J. Martin, *Mechanisms of Fano resonances in coupled plasmonic systems*, ACS Nano **7**, 4527 (2013).
88. M. Hentschel, M. Schäferling, X. Duan, H. Giessen, and N. Liu, *Chiral plasmonics*, Sci. Adv. **3**, e1602735 (2017).
89. E. Hendry, T. Carpy, J. Johnston, M. Popland, R. V. Mikhaylovskiy, A. J. Lapthorn, S. M. Kelly, L. D. Barron, N. Gadegaard, and M. Kadodwala, *Ultrasensitive detection and characterization of biomolecules using superchiral fields*, Nat. Nanotechnol. **5**, 783 (2010).
90. M. Hentschel, M. Schäferling, T. Weiss, N. Liu, and H. Giessen, *Three-dimensional chiral plasmonic oligomers*, Nano Lett. **12**, 2542 (2012).
91. B. Lounis and M. Orrit, *Single-photon sources*, Rep. Prog. Phys. **68**, 1129 (2005).
92. W. Kim, V. P. Safonov, V. M. Shalaev, and R. L. Armstrong, *Fractals in microcavities: Giant coupled, multiplicative enhancement of optical responses*, Phys. Rev. Lett. **82**, 4811 (1999).
93. M. Barth, S. Schietinger, S. Fischer, J. Becker, N. Nüsse, T. Aichele, B. Löchel, C. Sönnichsen, and O. Benson, *Nanoassembled plasmonic-photonic hybrid cavity for tailored light-matter coupling*, Nano Lett. **10**, 891 (2010).

94. H. M. Doeleman, E. Verhagen, and A. F. Koenderink, *Antenna-cavity hybrids: Matching polar opposites for Purcell enhancements at any linewidth*, ACS Photonics **3**, 1943 (2016).
95. I. M. Palstra, H. M. Doeleman, and A. F. Koenderink, *Hybrid cavity-antenna systems for quantum optics outside the cryostat?* Nanophotonics **8**, 1513 (2019).
96. F. De Angelis, M. Patrini, G. Das, I. Maksymov, M. Galli, L. Businaro, L. C. Andreani, and E. Di Fabrizio, *A hybrid plasmonic-photonic nanodevice for label-free detection of a few molecules*, Nano Lett. **8**, 2321 (2008).
97. M. A. Santiago-Cordoba, M. Cetinkaya, S. V. Boriskina, F. Vollmer, and M. C. Demirel, *Ultrasensitive detection of a protein by optical trapping in a photonic-plasmonic microcavity*, J. Biophotonics **5**, 629 (2012).
98. V. R. Dantham, S. Holler, C. Barbre, D. Keng, V. Kolchenko, and S. Arnold, *Label-free detection of single protein using a nanoplasmonic-photonic hybrid microcavity*, Nano Lett. **13**, 3347 (2013).
99. D. Conteduca, F. Dell'Olio, F. Innone, C. Ciminelli, and M. N. Armenise, *Rigorous design of an ultra-high Q/V photonic/plasmonic cavity to be used in biosensing applications*, Opt. Laser Technol. **77**, 151 (2016).
100. A. Bozzola, S. Perotto, and F. De Angelis, *Hybrid plasmonic-photonic whispering gallery mode resonators for sensing: A critical review*, Analyst **142**, 883 (2017).
101. J. N. Liu, Q. Huang, K. K. Liu, S. Singamaneni, and B. T. Cunningham, *Nanoantenna-microcavity hybrid resonators with highly cooperative plasmonic-photonic coupling*, IEEE IPC Part II , 1 (2018).
102. J. Zhang, J. Li, S. Tang, Y. Fang, J. Wang, G. Huang, R. Liu, L. Zheng, X. Cui, and Y. Mei, *Whispering-gallery nanocavity plasmon-enhanced Raman spectroscopy*, Sci. Rep. **5**, 15012 (2015).
103. S. Soltani, V. M. Diep, R. Zeto, and A. M. Armani, *Stimulated anti-Stokes Raman emission generated by gold nanorod coated optical resonators*, ACS Photonics **5**, 3550 (2018).
104. Y. W. Hu, B. B. Li, Y. X. Liu, Y. F. Xiao, and Q. Gong, *Hybrid photonic-plasmonic mode for refractometer and nanoparticle trapping*, Opt. Commun. **291**, 380 (2013).
105. P.-T. Lin, H.-Y. Chu, T.-W. Lu, and P.-T. Lee, *Trapping particles using waveguide-coupled gold bowtie plasmonic tweezers*, Lab. Chip **14**, 4647 (2014).
106. D. Conteduca, C. Reardon, M. G. Scullion, F. Dell'Olio, M. N. Armenise, T. F. Krauss, and C. Ciminelli, *Ultra-high q/v hybrid cavity for strong light-matter interaction*, APL Photonics **2**, 086101 (2017).
107. S. V. Boriskina and B. M. Reinhard, *Spectrally and spatially configurable superlenses for optoplasmonic nanocircuits*, Proc. Natl. Acad. Sci. **108**, 3147 (2011).
108. Y.-F. Xiao, Y.-C. Liu, B.-B. Li, Y.-L. Chen, Y. Li, and Q. Gong, *Strongly*

*enhanced light-matter interaction in a hybrid photonic-plasmonic resonator*, Phys. Rev. A **85**, 031805 (2012).

109. M. K. Dezfouli, R. Gordon, and S. Hughes, *Modal theory of modified spontaneous emission of a quantum emitter in a hybrid plasmonic photonic-crystal cavity system*, Phys. Rev. A **95**, 013846 (2017).
110. S. Cui, X. Zhang, T.-l. Liu, J. Lee, D. Bracher, K. Ohno, D. Awschalom, and E. L. Hu, *Hybrid plasmonic photonic crystal cavity for enhancing emission from near-surface nitrogen vacancy centers in diamond*, ACS Photonics **2**, 465 (2015).
111. H. M. Doeleman, *Hybrid resonators for light trapping and emission control*, Ph.D. thesis, Univerty of Amsterdam (2019).
112. R. P. Feynman, R. B. Leighton, M. Sands, and R. B. Lindsay, *The Feynman Lectures on Physics, Vol. 3: Quantum Mechanics* (Addison–Wesley, 1966).
113. J. S. Toll, *Causality and the dispersion relation: Logical foundations*, Phys. Rev. **104**, 1760 (1956).
114. D. Marcuse, *Theory of Dielectric Optical Waveguides* (Elsevier, 1991).
115. A. W. Snyder and J. D. Love, *Optical Waveguide Theory* (Springer US, 1984).
116. G. Mie, *Beiträge zur Optik trüber Medien, speziell kolloidaler Metallösungen*, Ann. Phys. **330**, 377 (1908).
117. M. B. Doost, W. Langbein, and E. A. Muljarov, *Resonant state expansion applied to two-dimensional open optical systems*, Phys. Rev. A **87**, 043827 (2013).
118. P. T. Kristensen and S. Hughes, *Modes and mode volumes of leaky optical cavities and plasmonic nanoresonators*, ACS Photonics **1**, 2 (2014).
119. D. A. Powell, *Resonant dynamics of arbitrarily shaped meta-atoms*, Phys. Rev. B **90**, 075108 (2014).
120. X. Zheng *et al.*, *Implementation of the natural mode analysis for nanotopologies using a volumetric method of moments (V-MoM) algorithm*, IEEE Photon. J. **6**, 1 (2014).
121. B. Vial, F. Zolla, A. Nicolet, and M. Commandré, *Quasimodal expansion of electromagnetic fields in open two-dimensional structures*, Phys. Rev. A **89**, 023829 (2014).
122. T. Weiss, M. Mesch, M. Schäferling, H. Giessen, W. Langbein, and E. A. Muljarov, *From dark to bright: First-order perturbation theory with analytical mode normalization for plasmonic nanoantenna arrays applied to refractive index sensing*, Phys. Rev. Lett. **116**, 237401 (2016).
123. F. Alpeggiani, N. Parappurath, E. Verhagen, and L. Kuipers, *Quasinormal-mode expansion of the scattering matrix*, Phys. Rev. X **7**, 021035 (2017).
124. C. Sauvan, J. P. Hugonin, I. S. Maksymov, and P. Lalanne, *Theory of*

*the spontaneous optical emission of nanosize photonic and plasmon resonators*, Phys. Rev. Lett. **110**, 237401 (2013).

125. P. Lalanne, W. Yan, K. Vynck, C. Sauvan, and J. P. J.-P. Hugonin, *Light interaction with photonic and plasmonic resonances*, Laser Photonics Rev. **12**, 1700113 (2018).
126. P. T. Leung, S. Y. Liu, and K. Young, *Completeness and time-independent perturbation of the quasinormal modes of an absorptive and leaky cavity*, Phys. Rev. A **49**, 3982 (1994).
127. P. T. Leung, S. Y. Liu, and K. Young, *Completeness and orthogonality of quasinormal modes in leaky optical cavities*, Phys. Rev. A **49**, 3057 (1994).
128. M. I. Abdelrahman and B. Gralak, *Completeness and divergence-free behavior of the quasi-normal modes using causality principle*, OSA Continuum **1**, 340 (2018).
129. P. T. Kristensen, C. Van Vlack, and S. Hughes, *Effective mode volumes for leaky optical cavities*, AIP Conf. Proc. **1398**, 100 (2011).
130. E. A. Muljarov and W. Langbein, *Exact mode volume and Purcell factor of open optical systems*, Phys. Rev. B **94**, 235438 (2016).
131. P. T. Kristensen, C. Van Vlack, and S. Hughes, *Generalized effective mode volume for leaky optical cavities*, Opt. Lett. **37**, 1649 (2012).
132. Q. Bai, M. Perrin, C. Sauvan, J.-P. Hugonin, and P. Lalanne, *Efficient and intuitive method for the analysis of light scattering by a resonant nanostructure*, Opt. Express **21**, 27371 (2013).
133. P. Lalanne *et al.*, *Quasinormal mode solvers for resonators with dispersive materials*, J. Opt. Soc. Am. A **36**, 686 (2019).
134. W. Yan, R. Faggiani, and P. Lalanne, *Rigorous modal analysis of plasmonic nanoresonators*, Phys. Rev. B **97**, 205422 (2018).
135. R. Faggiani, A. Losquin, J. Yang, E. Mårsell, A. Mikkelsen, and P. Lalanne, *Modal analysis of the ultrafast dynamics of optical nanoresonators*, ACS Photonics **4**, 897 (2017).
136. M. B. Doost, W. Langbein, and E. A. Muljarov, *Resonant-state expansion applied to three-dimensional open optical systems*, Phys. Rev. A **90**, 013834 (2014).
137. P. Fauché, S. G. Kosionis, and P. Lalanne, *Collective scattering in hybrid nanostructures with many atomic oscillators coupled to an electromagnetic resonance*, Phys. Rev. B **95**, 195418 (2017).
138. B. Vial and Y. Hao, *A coupling model for quasi-normal modes of photonic resonators*, J. Opt. **18**, 115004 (2016).
139. J. Yang, H. Giessen, and P. Lalanne, *Simple analytical expression for the peak-frequency shifts of plasmonic resonances for sensing*, Nano Lett. **15**, 3439 (2015).
140. K. G. Cognée, W. Yan, F. La China, D. Balestri, F. Intonti, M. Gurioli, A. F.

Koenderink, and P. Lalanne, *Mapping complex mode volumes with cavity perturbation theory*, Optica **6**, 269 (2019).

141. O. Klein, S. Donovan, M. Dressel, and G. Grüner, *Microwave cavity perturbation technique: Part I: Principles*, Int. J. Infrared Millimeter Waves **14**, 2423 (1993).
142. W. Yan, P. Lalanne, and M. Qiu, *Perturbation theory of quasinormal modes for geometrically deformed nanoresonators*, arxiv 1909.03386 (2019).
143. L. Lalouat, B. Cluzel, P. Velha, E. Picard, D. Peyrade, J. P. Hugonin, P. Lalanne, E. Hadji, and F. De Fornel, *Near-field interactions between a subwavelength tip and a small-volume photonic-crystal nanocavity*, Phys. Rev. B **76**, 041102 (2007).
144. L. Ramunno and S. Hughes, *Disorder-induced resonance shifts in high-index-contrast photonic crystal nanocavities*, Phys. Rev. B **79**, 161303 (2009).
145. M. Burresi, T. Kampfrath, D. Van Oosten, J. C. Prangsma, B. S. Song, S. Noda, and L. Kuipers, *Magnetic light-matter interactions in a photonic crystal nanocavity*, Phys. Rev. Lett. **105**, 123901 (2010).
146. L. Neumeier, R. Quidant, and D. E. Chang, *Self-induced back-action optical trapping in nanophotonic systems*, New J. Phys. **17**, 123008 (2015).
147. K. D. Heylman, K. A. Knapper, E. H. Horak, M. T. Rea, S. K. Vanga, and R. H. Goldsmith, *Optical microresonators for sensing and transduction: A materials perspective*, Adv. Mater. **29**, 1700037 (2017).
148. A. Badolato, K. Hennessy, M. Atatüre, J. Dreiser, E. Hu, P. M. Petroff, and A. Imamoğlu, *Deterministic coupling of single quantum dots to single nanocavity modes*, Science **308**, 1158 (2005).
149. A. F. Koenderink, M. Kafesaki, B. C. Buchler, and V. Sandoghdar, *Controlling the resonance of a photonic crystal microcavity by a near-field probe*, Phys. Rev. Lett. **95**, 153904 (2005).
150. S. Mujumdar, A. F. Koenderink, T. Sünner, B. C. Buchler, M. Kamp, A. Forchel, and V. Sandoghdar, *Near-field imaging and frequency tuning of a high-q photonic crystal membrane microcavity*, Opt. Express **15**, 17214 (2007).
151. F. Intonti *et al.*, *Spectral tuning and near-field imaging of photonic crystal microcavities*, Phys. Rev. B **78**, 041401 (2008).
152. N. Le Thomas and R. Houdré, *Inhibited emission of electromagnetic modes confined in subwavelength cavities*, Phys. Rev. B **84**, 035320 (2011).
153. F. Ruesink, H. M. Doeleman, R. Hendrikx, A. F. Koenderink, and E. Verhagen, *Perturbing open cavities: Anomalous resonance frequency shifts in a hybrid cavity-nanoantenna system*, Phys. Rev. Lett. **115**, 203904 (2015).
154. S. Vignolini, F. Intonti, F. Riboli, L. Balet, L. H. Li, M. Francardi, A. Gerardino, A. Fiore, D. S. Wiersma, and M. Gurioli, *Magnetic imaging in photonic crystal microcavities*, Phys. Rev. Lett. **105**, 123902 (2010).
155. J.-M. Gérard, *Solid-state cavity-quantum electrodynamics with self-assembled quantum dots*, Top. Appl. Phys. **90**, 269 (2003).

156. E. A. Muljarov and W. Langbein, *Resonant-state expansion of dispersive open optical systems: Creating gold from sand*, Phys. Rev. B **93**, 075417 (2016).
157. A. Gras, W. Yan, and P. Lalanne, *Quasinormal-mode analysis of grating spectra at fixed incidence angles*, Opt. Lett. **44**, 3494 (2019).
158. A. Taflove, S. G. Johnson, and A. Oskooi, *Advances in FDTD Computational Electrodynamics: Photonics and Nanotechnology* (Artech House, 2013).
159. H. M. Lai, P. T. Leung, K. Young, P. W. Barber, and S. C. Hill, *Time-independent perturbation for leaking electromagnetic modes in open systems with application to resonances in microdroplets*, Phys. Rev. A **41**, 5187 (1990).
160. M. Langlais, J.-P. Hugonin, M. Besbes, and P. Ben-Abdallah, *Cooperative electromagnetic interactions between nanoparticles for solar energy harvesting*, Opt. Express **22**, 577 (2014).
161. C. Sauvan, P. Lalanne, and J. P. Hugonin, *Slow-wave effect and mode-profile matching in photonic crystal microcavities*, Phys. Rev. B **71**, 165118 (2005).
162. N. Caselli, F. Intonti, F. La China, F. Riboli, A. Gerardino, W. Bao, A. W. Bargioni, L. Li, E. H. Linfield, F. Pagliano, A. Fiore, and M. Gurioli, *Ultra-subwavelength phase-sensitive Fano-imaging of localized photonic modes*, Light: Sci. Appl. **4**, e326 (2015).
163. P. de Vries, D. V. van Coevorden, and A. Lagendijk, *Point scatterers for classical waves*, Rev. Mod. Phys. **70**, 447 (1998).
164. A. F. Koenderink, M. Kafesaki, C. M. Soukoulis, and V. Sandoghdar, *Spontaneous emission rates of dipoles in photonic crystal membranes*, J. Opt. Soc. Am. B **23**, 1196 (2006).
165. H. Altug and J. Vučković, *Photonic crystal nanocavity array laser*, Opt. Express **13**, 8819 (2005).
166. P. Lodahl, S. Mahmoodian, and S. Stobbe, *Interfacing single photons and single quantum dots with photonic nanostructures*, Rev. Mod. Phys. **87**, 347 (2015).
167. E. Lassalle, N. Bonod, T. Durt, and B. Stout, *Interplay between spontaneous decay rates and Lamb shifts in open photonic systems*, Opt. Lett. **43**, 1950 (2018).
168. K. Kneipp, Y. Wang, H. Kneipp, L. T. Perelman, I. Itzkan, R. R. Dasari, and M. S. Feld, *Single molecule detection using surface-enhanced Raman scattering (SERS)*, Phys. Rev. Lett. **78**, 1667 (1997).
169. S. Nie and S. R. Emory, *Probing single molecules and single nanoparticles by surface-enhanced Raman scattering*, Science **275**, 1102 (1997).
170. J. A. Fan, C. Wu, K. Bao, J. Bao, R. Bardhan, N. J. Halas, V. N. Manoharan, P. Nordlander, G. Shvets, and F. Capasso, *Self-assembled plasmonic nanoparticle clusters*, Science **328**, 1135 (2010).
171. F. De Angelis *et al.*, *Nanoscale chemical mapping using three-dimensional adiabatic compression of surface plasmon polaritons*, Nat. Nanotechnol. **5**, 67 (2010).

172. M. Notomi, E. Kuramochi, and T. Tanabe, *Large-scale arrays of ultrahigh-Q coupled nanocavities*, Nat. Photonics **2**, 741 (2008).

173. J. D. Thompson, B. M. Zwickl, A. M. Jayich, F. Marquardt, S. M. Girvin, and J. G. E. Harris, *Strong dispersive coupling of a high-finesse cavity to a micromechanical membrane*, Nature **452**, 72 (2008).

174. J. C. Sankey, C. Yang, B. M. Zwickl, A. M. Jayich, and J. G. E. Harris, *Strong and tunable nonlinear optomechanical coupling in a low-loss system*, Nat. Phys. **6**, 707 (2010).

175. A. Kuzyk, R. Schreiber, Z. Fan, G. Pardatscher, E.-M. Roller, A. Högele, F. C. Simmel, A. O. Govorov, and T. Liedl, *DNA-based self-assembly of chiral plasmonic nanostructures with tailored optical response*, Nature **483**, 311 (2012).

176. V. K. Valev, J. J. Baumberg, C. Sibilia, and T. Verbiest, *Chirality and chiroptical effects in plasmonic nanostructures: Fundamentals, recent progress, and outlook*, Adv. Mater. **25**, 2517 (2013).

177. W. Suh, Z. Wang, and S. Fan, *Temporal coupled-mode theory and the presence of non-orthogonal modes in lossless multimode cavities*, IEEE J. Quantum Electron. **40**, 1511 (2004).

178. J. M. Gérardy and M. Ausloos, *Absorption spectrum of clusters of spheres from the general solution of maxwell's equations. ii. optical properties of aggregated metal spheres*, Phys. Rev. B **25**, 4204 (1982).

179. B. Willingham and S. Link, *A kirchhoff solution to plasmon hybridization*, Appl. Phys. B **113**, 519 (2013).

180. J. B. Pendry, A. I. Fernández-Domínguez, Y. Luo, and R. Zhao, *Capturing photons with transformation optics*, Nat. Phys. **9**, 518 (2013).

181. M. Frimmer and A. F. Koenderink, *Superemitters in hybrid photonic systems: A simple lumping rule for the local density of optical states and its breakdown at the unitary limit*, Phys. Rev. B **86**, 235428 (2012).

182. E. Prodan, C. Radloff, N. J. Halas, and P. Nordlander, *A hybridization model for the plasmon response of complex nanostructures*, Science **302**, 419 (2003).

183. S. Franke, S. Hughes, M. K. Dezfouli, P. T. Kristensen, K. Busch, A. Knorr, and M. Richter, *Quantization of quasinormal modes for open cavities and plasmonic cavity quantum electrodynamics*, Phys. Rev. Lett. **122**, 213901 (2019).

184. J. R. de Lasson, P. T. Kristensen, J. Mørk, and N. Gregersen, *Semi-analytical quasi-normal mode theory for the local density of states in coupled photonic crystal cavity-waveguide structures*, Opt. Lett. **40**, 5790 (2015).

185. J. Yang, M. Perrin, and P. Lalanne, *Analytical formalism for the interaction of two-level quantum systems with metal nanoresonators*, Phys. Rev. X **5**, 021008 (2015).

186. B. Gurlek, V. Sandoghdar, and D. Martín-Cano, *Manipulation of quenching*

*in nanoantenna-emitter systems enabled by external detuned cavities: A path to enhance strong-coupling*, ACS Photonics **5**, 456 (2018).

187. P. Zijlstra, M. Orrit, and A. Femius Koenderink, *Metal Nanoparticles for Microscopy and Spectroscopy. In: de Mello Donegá C. (eds) Nanoparticles.* (Springer Berlin Heidelberg, 2014).
188. R. H. Dicke, *Coherence in spontaneous radiation processes*, Phys. Rev. **93**, 99 (1954).
189. A. Raman and S. Fan, *Photonic band structure of dispersive metamaterials formulated as a hermitian eigenvalue problem*, Phys. Rev. Lett. **104**, 087401 (2010).
190. N. W. Ashcroft and D. N. Mermin, *Solid state physics* (Brooks Cole, 1976).
191. M. Mansuripur, M. Kolesik, and P. Jakobsen, *Leaky modes of solid dielectric spheres*, Phys. Rev. A **96**, 013846 (2017).
192. F. J. García de Abajo, *Nonlocal effects in the plasmons of strongly interacting nanoparticles, dimers, and waveguides*, J. Phys. Chem. C **112**, 17983 (2008).
193. M. K. Dezfouli, C. Tserkezis, N. A. Mortensen, and S. Hughes, *Nonlocal quasinormal modes for arbitrarily shaped three-dimensional plasmonic resonators*, Optica **4**, 1503 (2017).
194. R. Esteban, A. G. Borisov, P. Nordlander, and J. Aizpurua, *Bridging quantum and classical plasmonics with a quantum-corrected model*, Nat. Commun. **3**, 825 (2012).
195. J. A. Scholl, A. Garcia-Etxarri, G. Aguirregabiria, R. Esteban, T. C. Narayan, A. L. Koh, J. Aizpurua, and J. A. Dionne, *Evolution of plasmonic metamolecule modes in the quantum tunneling regime*, ACS Nano **10**, 1346 (2016).
196. D. Knebl, A. Hörl, A. Trügler, J. Kern, J. R. Krenn, P. Puschnig, and U. Hohenester, *Gap plasmonics of silver nanocube dimers*, Phys. Rev. B **93**, 081405 (2016).
197. K. J. Vahala, *Optical microcavities*, Nature **424**, 839 (2003).
198. C. Santori, D. Fattal, and Y. Yamamoto, *Single-photon Devices and Applications* (Wiley-VCH, 2010).
199. P. Törmä and W. L. Barnes, *Strong coupling between surface plasmon polaritons and emitters: a review*, Rep. Prog. Phys. **78**, 013901 (2015).
200. D. G. Baranov, M. Wersäll, J. Cuadra, T. J. Antosiewicz, and T. Shegai, *Novel nanostructures and materials for strong light–matter interactions*, ACS Photonics **5**, 24 (2018).
201. P. Roelli, C. Galland, N. Piro, and T. J. Kippenberg, *Molecular cavity optomechanics as a theory of plasmon-enhanced Raman scattering*, Nat. Nanotechnol. **11**, 164 (2016).
202. T. B. Hoang, G. M. Akselrod, and M. H. Mikkelsen, *Ultrafast room-temperature single photon emission from quantum dots coupled to plasmonic nanocavities*, Nano Lett. **16**, 270 (2016).

203. R. Chikkaraddy, B. de Nijs, F. Benz, S. J. Barrow, O. A. Scherman, E. Rosta, A. Demetriadou, P. Fox, O. Hess, and J. J. Baumberg, *Single-molecule strong coupling at room temperature in plasmonic nanocavities,* Nature **535**, 127 (2016).
204. A. I. Fernández-Domínguez, S. I. Bozhevolnyi, and N. A. Mortensen, *Plasmon-enhanced generation of nonclassical light,* ACS Photonics **5**, 3447 (2018).
205. R. Ameling and H. Giessen, *Microcavity plasmonics: strong coupling of photonic cavities and plasmons,* Laser Photonics Rev. **7**, 141 (2013).
206. W. Ahn, S. V. Boriskina, Y. Hong, and B. M. Reinhard, *Photonic-plasmonic mode coupling in on-chip integrated optoplasmonic molecules.* ACS Nano **6**, 951 (2012).
207. F. Ruesink, H. M. Doeleman, E. Verhagen, and A. F. Koenderink, *Controlling nanoantenna polarizability through backaction via a single cavity mode,* Phys. Rev. Lett. **120**, 206101 (2018).
208. M. K. Dezfouli, R. Gordon, and S. Hughes, *Molecular optomechanics in the anharmonic Cavity-QED regime using hybrid metal-dielectric cavity modes,* ACS Photonics **6**, 1400 (2019).
209. M. Gross and S. Haroche, *Superradiance: An essay on the theory of collective spontaneous emission,* Phys. Rep. **93**, 301 (1982).
210. L. Novotny and N. F. van Hulst, *Antennas for light,* Nat. Photonics **5**, 83 (2011).
211. N. Engheta, *Circuits with light at nanoscales: Optical nanocircuits inspired by metamaterials,* Science **317**, 1698 (2007).
212. J. Wiersig, *Structure of whispering-gallery modes in optical microdisks perturbed by nanoparticles,* Phys. Rev. A **84**, 063828 (2011).
213. F. J. García de Abajo, *Colloquium : Light scattering by particle and hole arrays,* Rev. Mod. Phys. **79**, 1267 (2007).
214. M.-A. Miri and A. Alù, *Exceptional points in optics and photonics,* Science **363**, eaar7709 (2019).
215. Y. Shen, X. Wang, Z. Xie, C. Min, X. Fu, Q. Liu, M. Gong, and X. Yuan, *Optical vortices 30 years on: OAM manipulation from topological charge to multiple singularities,* Light: Sci. Appl. **8**, 90 (2019).
216. L. Allen, M. W. Beijersbergen, R. J. C. Spreeuw, and J. P. Woerdman, *Orbital angular momentum of light and the transformation of Laguerre-Gaussian laser modes,* Phys. Rev. A **45**, 8185 (1992).
217. E. Brasselet, M. Malinauskas, A. Žukauskas, and S. Juodkazis, *Photopolymerized microscopic vortex beam generators: Precise delivery of optical orbital angular momentum,* Appl. Phys. Lett. **97**, 211108 (2010).
218. X. X.-L. Cai, J.-W. U. o. B. J. Wang, M. J. Strain, B. Johnson-Morris, J.-B. J. Zhu, M. Sorel, J. L. O'Brien, M. G. Thompson, and S. S.-Y. Yu, *Integrated compact optical vortex beam emitters,* Science **338**, 363 (2012).

219. R. C. Devlin, A. Ambrosio, D. Wintz, S. L. Oscurato, A. Y. Zhu, M. Khorasaninejad, J. Oh, P. Maddalena, and F. Capasso, *Spin-to-orbital angular momentum conversion in dielectric metasurfaces*, Opt. Express **25**, 377 (2017).

220. J. Wang, J. Y. Yang, I. M. Fazal, N. Ahmed, Y. Yan, H. Huang, Y. Ren, Y. Yue, S. Dolinar, M. Tur, and A. E. Willner, *Terabit free-space data transmission employing orbital angular momentum multiplexing*, Nat. Photonics **6**, 488 (2012).

221. A. E. Willner *et al.*, *Optical communications using orbital angular momentum beams*, Adv. Opt. Photonics **7**, 66 (2015).

222. M. Erhard, R. Fickler, M. Krenn, and A. Zeilinger, *Twisted photons: New quantum perspectives in high dimensions*, Light: Sci. Appl. **7**, 17146 (2018).

223. M. Ghadimi Nassiri and E. Brasselet, *Multispectral management of the photon orbital angular momentum*, Phys. Rev. Lett. **121**, 213901 (2018).

224. D. G. Grier, *A revolution in optical manipulation*, *Nature*, Nature **424**, 810 (2003).

225. M. Padgett and R. Bowman, *Tweezers with a twist*, Nat. Photonics **5**, 343 (2011).

226. K. Dholakia and T. Čižmár, *Shaping the future of manipulation*, Nat. Photonics **5**, 335 (2011).

227. M. Woerdemann, C. Alpmann, M. Esseling, and C. Denz, *Advanced optical trapping by complex beam shaping*, Laser Photonics Rev. **7**, 839 (2013).

228. L. Marrucci, C. Manzo, and D. Paparo, *Optical spin-to-orbital angular momentum conversion in inhomogeneous anisotropic media*, Phys. Rev. Lett. **96**, 163905 (2006).

229. K. Y. Bliokh, F. J. Rodríguez-Fortuño, F. Nori, and A. V. Zayats, *Spin-orbit interactions of light*, Nat. Photonics **9**, 796 (2015).

230. L. T. Vuong, A. J. Adam, J. M. Brok, P. C. Planken, and H. P. Urbach, *Electromagnetic spin-orbit interactions via scattering of subwavelength apertures*, Phys. Rev. Lett. **104**, 083903 (2010).

231. O. G. Rodríguez-Herrera, D. Lara, K. Y. Bliokh, E. A. Ostrovskaya, and C. Dainty, *Optical nanoprobing via spin-orbit interaction of light*, Phys. Rev. Lett. **104**, 253601 (2010).

232. Y. Gorodetski, A. Drezet, C. Genet, and T. W. Ebbesen, *Generating far-field orbital angular momenta from near-field optical chirality*, Phys. Rev. Lett. **110**, 203906 (2013).

233. P. Lodahl, S. Mahmoodian, S. Stobbe, A. Rauschenbeutel, P. Schneeweiss, J. Volz, H. Pichler, and P. Zoller, *Chiral quantum optics*, Nature **541**, 473 (2017).

234. F. Alpeggiani, K. Y. Bliokh, F. Nori, and L. Kuipers, *Electromagnetic helicity in complex media*, Phys. Rev. Lett. **120**, 243605 (2018).

235. W. C. Cheong, W. M. Lee, X.-C. Yuan, L.-S. Zhang, K. Dholakia, and H. Wang, *Direct electron-beam writing of continuous spiral phase plates in negative resist with high power efficiency for optical manipulation*, Appl. Phys. Lett. **85**, 5784 (2004).

236. S. S. R. Oemrawsingh, J. A. W. van Houwelingen, E. R. Eliel, J. P. Woerdman, E. J. K. Verstegen, J. G. Kloosterboer, and G. W. 't Hooft, *Production and characterization of spiral phase plates for optical wavelengths*, Appl. Opt. **43**, 688 (2004).

237. J. E. Curtis, B. A. Koss, and D. G. Grier, *Dynamic holographic optical tweezers*, Opt. Commun. **207**, 169 (2002).

238. E. Brasselet and C. Loussert, *Electrically controlled topological defects in liquid crystals as tunable spin-orbit encoders for photons*, Opt. Lett. **36**, 719 (2011).

239. M. Caño-García, X. Quintana, J. M. Otón, and M. A. Geday, *Dynamic multilevel spiral phase plate generator*, Sci. Rep. **8**, 15804 (2018).

240. A. Aleksanyan and E. Brasselet, *Self-eclipsing: alignment-free vortex coronagraphy*, Opt. Lett. **42**, 1237 (2017).

241. A. Aleksanyan, N. Kravets, and E. Brasselet, *Multiple-star system adaptive vortex coronagraphy using a liquid crystal light valve*, Phys. Rev. Lett. **118**, 203902 (2017).

242. H. Kim, J. Park, S.-W. Cho, S.-Y. Lee, M. Kang, and B. Lee, *Synthesis and dynamic switching of surface plasmon vortices with plasmonic vortex lens*, Nano Lett. **10**, 49 (2010).

243. R. Röhrich, C. Hoekmeijer, C. I. Osorio, and A. F. Koenderink, *Quantifying single plasmonic nanostructure far-fields with interferometric and polarimetric k-space microscopy*, Light: Sci. Appl. **7**, 65 (2018).

244. R. M. Kerber, J. M. Fitzgerald, D. E. Reiter, S. S. Oh, and O. Hess, *Reading the orbital angular momentum of light using plasmonic nanoantennas*, ACS Photonics **4**, 891 (2017).

245. D. K. Sharma, V. Kumar, A. B. Vasista, D. Paul, S. K. Chaubey, and G. V. Pavan Kumar, *Optical orbital angular momentum read-out using a self-assembled plasmonic nanowire*, ACS Photonics **6**, 148 (2018).

246. R. M. Kerber, J. M. Fitzgerald, S. S. Oh, D. E. Reiter, and O. Hess, *Orbital angular momentum dichroism in nanoantennas*, Commun. Phys. **1**, 87 (2018).

247. Y. Yang, W. Wang, P. Moitra, I. I. Kravchenko, D. P. Briggs, and J. Valentine, *Dielectric meta-reflectarray for broadband linear polarization conversion and optical vortex generation*, Nano Lett. **14**, 1394 (2014).

248. K. E. Chong *et al.*, *Polarization-independent silicon metadevices for efficient optical wavefront control*, Nano Lett. **15**, 5369 (2015).

249. J. Sun, X. Wang, T. Xu, Z. A. Kudyshev, A. N. Cartwright, and N. M. Litchinitser, *Spinning light on the nanoscale*, Nano Lett. **14**, 2726 (2014).

250. D. Hakobyan, H. Magallanes, G. Seniutinas, S. Juodkazis, and

E. Brasselet, *Tailoring orbital angular momentum of light in the visible domain with metallic metasurfaces*, Adv. Opt. Mater. **4**, 306 (2016).

251. V. G. Sala *et al.*, *Spin-orbit coupling for photons and polaritons in microstructures*, Phys. Rev. X **5**, 011034 (2015).
252. N. Carlon Zambon *et al.*, *Optically controlling the emission chirality of microlasers*, Nat. Photonics **13**, 283 (2019).
253. Y. Wang, X. Feng, D. Zhang, P. Zhao, X. Li, K. Cui, F. Liu, and Y. Huang, *Generating optical superimposed vortex beam with tunable orbital angular momentum using integrated devices*, Sci. Rep. **5**, 10958 (2015).
254. Q. Xiao, C. Klitis, S. Li, Y. Chen, X. Cai, M. Sorel, and S. Yu, *Generation of photonic orbital angular momentum superposition states using vortex beam emitters with superimposed gratings*, CLEO 2016 **24**, 3168 (2016).
255. S. Li, Z. Nong, X. Wu, W. Yu, M. He, C. Klitis, Y. Zhu, S. Gao, J. Liu, Z. Li, L. Liu, M. Sorel, S. Yu, and X. Cai, *Orbital angular momentum vector modes (de)multiplexer based on multimode micro-ring*, Opt. Express **26**, 29895 (2018).
256. G. C. Berkhout, M. P. Lavery, J. Courtial, M. W. Beijersbergen, and M. J. Padgett, *Efficient sorting of orbital angular momentum states of light*, Phys. Rev. Lett. **105**, 153601 (2010).
257. I. A. Litvin, A. Dudley, F. S. Roux, and A. Forbes, *Azimuthal decomposition with digital holograms*, Opt. Express **20**, 10996 (2012).
258. W. H. Peeters, E. J. Verstegen, and M. P. Van Exter, *Orbital angular momentum analysis of high-dimensional entanglement*, Phys. Rev. A **76**, 042302 (2007).
259. H. Di Lorenzo Pires, H. C. B. Florijn, and M. P. van Exter, *Measurement of the spiral spectrum of entangled two-photon states*, Phys. Rev. Lett. **104**, 020505 (2010).
260. A. D'Errico, R. D'Amelio, B. Piccirillo, F. Cardano, and L. Marrucci, *Measuring the complex orbital angular momentum spectrum and spatial mode decomposition of structured light beams*, Optica **4**, 1350 (2017).
261. G. Kulkarni, R. Sahu, O. S. Magaña-Loaiza, R. W. Boyd, and A. K. Jha, *Single-shot measurement of the orbital-angular-momentum spectrum of light*, Nat. Commun. **8**, 1054 (2017).
262. G. Milione, H. I. Sztul, D. A. Nolan, and R. R. Alfano, *Higher-order Poincaré sphere, Stokes parameters, and the angular momentum of light*, Phys. Rev. Lett. **107**, 053601 (2011).
263. J. E. Rosenthal and G. M. Murphy, *Group theory and the vibrations of polyatomic molecules*, Rev. Mod. Phys. **8**, 317 (1936).
264. N. A. Mirin, K. Bao, and P. Nordlander, *Fano resonances in plasmonic nanoparticle aggregates*, J. Phys. Chem. A **113**, 4028 (2009).
265. H. H. Jen, M.-S. Chang, and Y.-C. Chen, *Cooperative light scattering from helical-phase-imprinted atomic rings*, Sci. Rep. **8**, 9570 (2018).

266. J. Zhu, X. Cai, Y. Chen, and S. Yu, *Theoretical model for angular grating-based integrated optical vortex beam emitters*, Opt. Lett. **38**, 1343 (2013).
267. A. D. Rakić, A. B. Djurišić, J. M. Elazar, and M. L. Majewski, *Optical properties of metallic films for vertical-cavity optoelectronic devices*, Appl. Opt. **37**, 5271 (1998).
268. J. Vargas, J. A. Quiroga, and T. Belenguer, *Phase-shifting interferometry based on principal component analysis*, Opt. Lett. **36**, 1326 (2011).
269. F. Gori, *Polarization basis for vortex beams*, J. Opt. Soc. Am. A **18**, 1612 (2001).
270. Q. Zhan, *Cylindrical vector beams: from mathematical concepts to applications*, Adv. Opt. Photonics **1**, 1 (2009).
271. A. Trichili, C. Rosales-Guzmán, A. Dudley, B. Ndagano, A. Ben Salem, M. Zghal, and A. Forbes, *Optical communication beyond orbital angular momentum*, Sci. Rep. **6**, 27674 (2016).
272. X. Yi, Y. Liu, X. Ling, X. Zhou, Y. Ke, H. Luo, S. Wen, and D. Fan, *Hybrid-order Poincaré sphere*, Phys. Rev. A **91**, 023801 (2015).
273. A. Smekal, *Zur Quantentheorie der Dispersion*, Die Naturwissenschaften **11**, 873 (1923).
274. C. V. Raman, *A new radiation,* Indian J. Phys. **2**, 387 (1928).
275. D. A. Long, *The Raman effect* (John Wiley & Sons, Ltd, 2002).
276. M. Fleischmann, P. Hendra, and A. McQuillan, *Raman spectra of pyridine adsorbed at a silver electrode*, Chem. Phys. Lett. **26**, 163 (1974).
277. M. G. Albrecht and J. A. Creighton, *Anomalously intense Raman spectra of pyridine at a silver electrode*, J. Am. Chem. Soc. **99**, 5215 (1977).
278. A. M. Michaels, Jiang, and L. Brus, *Ag nanocrystal junctions as the site for surface-enhanced Raman scattering of single rhodamine 6G molecules*, J. Phys. Chem. B **104**, 11965 (2000).
279. J. P. Camden, J. A. Dieringer, Y. Wang, D. J. Masiello, L. D. Marks, G. C. Schatz, and R. P. Van Duyne, *Probing the structure of single-molecule surface-enhanced Raman scattering hot spots*, J. Am. Chem. Soc. **130**, 12616 (2008).
280. M. S. Anderson, *Locally enhanced Raman spectroscopy with an atomic force microscope*, Appl. Phys. Lett. **76**, 3130 (2000).
281. B. Pettinger, B. Ren, G. Picardi, R. Schuster, and G. Ertl, *Nanoscale probing of adsorbed species by tip-enhanced Raman spectroscopy*, Phys. Rev. Lett. **92**, 096101 (2004).
282. C. C. Neacsu, J. Dreyer, N. Behr, and M. B. Raschke, *Scanning-probe Raman spectroscopy with single-molecule sensitivity*, Phys. Rev. B **73**, 193406 (2006).
283. A. Hartschuh, E. J. Sánchez, X. S. Xie, and L. Novotny, *High-resolution near-field Raman microscopy of single-walled carbon nanotubes*, Phys. Rev. Lett. **90**, 095503 (2003).

284. D. L. Jeanmaire and R. P. Van Duyne, *Surface Raman spectroelectrochemistry*, J. Electroanal. Chem. Interfacial Electrochem. **84**, 1 (1977).
285. J. R. Lombardi, R. L. Birke, T. Lu, and J. Xu, *Charge-transfer theory of surface enhanced Raman spectroscopy: Herzberg–Teller contributions*, J. Chem. Phys. **84**, 4174 (1986).
286. F. J. García-Vidal and J. B. Pendry, *Collective theory for surface enhanced Raman scattering*, Phys. Rev. Lett. **77**, 1163 (1996).
287. H. Xu, J. Aizpurua, M. Käll, and P. Apell, *Electromagnetic contributions to single-molecule sensitivity in surface-enhanced Raman scattering*, Phys. Rev. E **62**, 4318 (2000).
288. E. C. Le Ru, E. Blackie, M. Meyer, and P. G. Etchegoin, *Surface enhanced Raman scattering enhancement factors: A comprehensive study*, J. Phys. Chem. C **111**, 13794 (2007).
289. F. J. Colas *et al.*, *Red-shift effects in surface enhanced Raman spectroscopy: Spectral or intensity dependence of the near-field?* J. Phys. Chem. C **120**, 13675 (2016).
290. R. Zhang, Y. Zhang, Z. C. Dong, S. Jiang, C. Zhang, L. G. Chen, L. Zhang, Y. Liao, J. Aizpurua, Y. Luo, J. L. Yang, and J. G. Hou, *Chemical mapping of a single molecule by plasmon-enhanced Raman scattering*, Nature **498**, 82 (2013).
291. M. D. Sonntag, E. A. Pozzi, N. Jiang, M. C. Hersam, and R. P. Van Duyne, *Recent advances in tip-enhanced Raman spectroscopy*, J. Phys. Chem. Lett. **5**, 3125 (2014).
292. J. Lee, K. T. Crampton, N. Tallarida, and V. A. Apkarian, *Visualizing vibrational normal modes of a single molecule with atomically confined light*, Nature **568**, 78 (2019).
293. C. Carnegie, J. Griffiths, B. De Nijs, C. Readman, R. Chikkaraddy, W. M. Deacon, Y. Zhang, I. Szabó, E. Rosta, J. Aizpurua, and J. J. Baumberg, *Room-temperature optical picocavities below 1 nm 3 accessing single-atom geometries*, J. Phys. Chem. Lett. **9**, 7146 (2018).
294. F. Peyskens, A. Dhakal, P. Van Dorpe, N. Le Thomas, and R. Baets, *Surface enhanced Raman spectroscopy using a single mode nanophotonic-plasmonic platform*, ACS Photonics **3**, 102 (2016).
295. F. Peyskens, P. Wuytens, A. Raza, P. Van Dorpe, and R. Baets, *Waveguide excitation and collection of surface-enhanced Raman scattering from a single plasmonic antenna*, Nanophotonics **7**, 1299 (2018).
296. J. Losada, A. Raza, S. Clemmen, A. Serrano, A. Griol, R. Baets, and A. Martínez, *SERS detection via individual bowtie nanoantennas integrated in $Si_3N_4$ waveguides*, IEEE J. Sel. Topics Quantum Electron. **25**, 1 (2019).
297. W. Zhu, D. Wang, and K. B. Crozier, *Direct observation of beamed Raman scattering*, Nano Lett. **12**, 6235 (2012).
298. T. Hummer, J. Noe, M. S. Hofmann, T. W. Hänsch, A. Hogele,

and D. Hunger, *Cavity-enhanced Raman microscopy of individual carbon nanotubes*, Nat. Commun. **7**, 12155 (2016).

299. S. H. Huang, X. Jiang, B. Peng, C. Janisch, A. Cocking, a. K. Özdemir, Z. Liu, and L. Yang, *Surface-enhanced Raman scattering on dielectric microspheres with whispering gallery mode resonance*, Photonics Res. **6**, 346 (2018).
300. J. E. Bjorkholm, *Efficient optical parametric oscillation using doubly and singly resonant cavities*, Appl. Phys. Lett. **13**, 53 (1968).
301. A. Rodriguez, M. Soljacic, J. D. Joannopoulos, and S. G. Johnson, $\chi$ *(2) and* $\chi$ *(3) harmonic generation at a critical power in inhomogeneous doubly resonant cavities*, Opt. Express **15**, 7303 (2007).
302. M. Minkov, D. Gerace, and S. Fan, *Doubly resonant* $\chi$ *(2) nonlinear photonic crystal cavity based on a bound state in the continuum*, Optica **6**, 1039 (2019).
303. M. K. Dezfouli and S. Hughes, *Quantum optics model of surface-enhanced Raman spectroscopy for arbitrarily shaped plasmonic resonators*, ACS Photonics **4**, 1045 (2017).
304. M. K. Schmidt, R. Esteban, A. González-Tudela, G. Giedke, and J. Aizpurua, *Quantum mechanical description of Raman scattering from molecules in plasmonic cavities*, ACS Nano **10**, 6291 (2016).
305. M. K. Schmidt, R. Esteban, F. Benz, J. J. Baumberg, and J. Aizpurua, *Linking classical and molecular optomechanics descriptions of SERS*, Faraday Discuss. **205**, 31 (2017).
306. M. Aspelmeyer, T. J. Kippenberg, and F. Marquardt, *Cavity optomechanics*, Rev. Mod. Phys. **86**, 1391 (2014).
307. J. D. Teufel, T. Donner, M. A. Castellanos-Beltran, J. W. Harlow, and K. W. Lehnert, *Nanomechanical motion measured with an imprecision below that at the standard quantum limit*, Nat. Nanotechnol. **4**, 820 (2009).
308. G. Anetsberger, E. Gavartin, O. Arcizet, Q. P. Unterreithmeier, E. M. Weig, M. L. Gorodetsky, J. P. Kotthaus, and T. J. Kippenberg, *Measuring nanomechanical motion with an imprecision below the standard quantum limit*, Phys. Rev. A **82**, 061804 (2010).
309. E. Verhagen, S. Deléglise, S. Weis, A. Schliesser, and T. J. Kippenberg, *Quantum-coherent coupling of a mechanical oscillator to an optical cavity mode*, Nature **482**, 63 (2012).
310. J. D. Teufel, T. Donner, D. Li, J. W. Harlow, M. S. Allman, K. Cicak, A. J. Sirois, J. D. Whittaker, K. W. Lehnert, and R. W. Simmonds, *Sideband cooling of micromechanical motion to the quantum ground state*, Nature **475**, 359 (2011).
311. T. A. Palomaki, J. D. Teufel, R. W. Simmonds, and K. W. Lehnert, *Entangling mechanical motion with microwave fields*, Science **342**, 710 (2013).
312. T. A. Palomaki, J. W. Harlow, J. D. Teufel, R. W. Simmonds, and K. W. Lehnert, *Coherent state transfer between itinerant microwave fields and a mechanical oscillator*, Nature **495**, 210 (2013).

313. A. P. Reed, K. H. Mayer, J. D. Teufel, L. D. Burkhart, W. Pfaff, M. Reagor, L. Sletten, X. Ma, R. J. Schoelkopf, E. Knill, and K. W. Lehnert, *Faithful conversion of propagating quantum information to mechanical motion*, Nat. Phys. **13**, 1163 (2017).
314. A. Lombardi, M. K. Schmidt, L. Weller, W. M. Deacon, F. Benz, B. De Nijs, J. Aizpurua, and J. J. Baumberg, *Pulsed molecular optomechanics in plasmonic nanocavities: From nonlinear vibrational instabilities to bond-breaking*, Phys. Rev. X **8**, 011016 (2018).
315. H. B. Callen and T. A. Welton, *Irreversibility and generalized noise*, Phys. Rev. **83**, 34 (1951).
316. A. A. Clerk, M. H. Devoret, S. M. Girvin, F. Marquardt, and R. J. Schoelkopf, *Introduction to quantum noise, measurement, and amplification*, Rev. Mod. Phys. **82**, 1155 (2010).
317. S. Weis, R. Rivière, S. Deléglise, E. Gavartin, O. Arcizet, A. Schliesser, and T. J. Kippenberg, *Optomechanically induced transparency*, Science **330**, 1520 (2010).
318. A. H. Safavi-Naeini, T. P. M. Alegre, J. Chan, M. Eichenfield, M. Winger, Q. Lin, J. T. Hill, D. E. Chang, and O. Painter, *Electromagnetically induced transparency and slow light with optomechanics*, Nature **472**, 69 (2011).

# SUMMARY

Light is essential in our lives. Not only is it a crucial element of our ecosystem and our interactions with it, but also it is involved in more and more aspects of our modern civilization. Indeed, the study of light, also known as photonics, is said by many to be for the 21st century what electronics has been for the 20th as it might lead to a paradigm shift in the way we treat and secure information. This revolution is already happening through the massive usage of fibre optics for telecommunication over long distances, the implementation of fast optical interconnects between nodes in data centers, and a lot of research aiming to directly exploit light for digital, analog or quantum computation and information processing. Furthermore, photovoltaics and solar light are one of the leading options to solve the current global energy crisis. All the promises made by light are entangled with our ability to make it interact with physical objects through refraction, reflection, diffraction, emission, and absorption. The interaction between a grain of light called a *photon*, and matter is relatively low. Even though this low interaction is essential for propagation of light via fibre optics (negligible absorption in glass at 1550 nm), it is problematic for the processing of the data carried by this light. In Chapter 1 of this thesis, after briefly introducing the figure of merit relevant in the context of light-matter interaction, we present the two strategies which have been employed historically to enhance light-matter interaction. On the one hand, light can be forced to interact multiple times with matter by trapping it inside a dielectric cavity with a high quality factor Q, i.e., for many optical cycles. On the other hand, light is squeezed in tiny volumes smaller than what is allowed by the fundamental diffraction limit for dielectric materials, to enhance the electric field strength of the photon right at the location of the matter. This can be done by coupling light to the collective oscillations of free electrons, also called *plasmons*, at the interface of a metal with a dielectric (usually air). Both cavity-based and plasmonic approaches have been successfully used in the last few decades to enable strong non-linear interaction between a light-field and matter, but also to observe and exploit quantum phenomena on the single photon level. In this thesis, we focus on an emerging alternative route; hybrid resonators composed of both a dielectric cavity and a plasmonic resonator, where the benefits of these bare constituents are largely preserved. No matter what type of photonic resonator one uses, the performances are always limited by losses, either optical absorption or radiation into the far-field. This poses important fundamental challenges for the description of resonators, their hybridization, and light-matter interac-

tion. This thesis is motivated by the question of how to understand light-matter interaction in hybrid photonic resonator systems, fully accounting for the open and lossy nature of photonics. To this end, we make use of the so-called *quasinormal mode* (QNM) theory. Chapter 1 provides a review of QNM formalism that was developed over the last 6 years as an efficient way to describe lossy dielectric and plasmonic cavity. Indeed, this framework is particularly well suited to account for the radiation properties of photonic resonators. This is demonstrated in Chapter 2 for the case of perturbation of a high Q cavity by a non-resonant scatterer. We show that QNM perturbation theory proposes a very elegant way to quantify the increase, but also the decrease of the radiative losses of a high-Q cavity due to the interference with the field scattered by a tiny object perturbing the cavity. The prediction relies on the concept of complex-valued mode volumes of resonators, where the real part accounts for the strength of the confinement of the light-field, and the imaginary part contains a phase information necessary to account for radiation and interference effects. With the help of experimental results on the perturbation of a photonic crystal cavity by a near-field probe, we show that this complex mode volume can even be measured. In Chapter 3, we develop an eigenproblem formulation of a QNM theory which can be used to predict the hybridized properties emerging when coupling two or more photonic resonators. Once the obtained QNMs are normalized, observables such as extinction cross-section or Purcell enhancement can be obtained semi-analytically for any source at any frequency. To discuss the similarity with the hybridization rules between two resonant point dipoles, we simplify our model and describe each resonator in an assembly by a single QNM. We show that our model can not only predict the bonding and antibonding nature of hybridized modes and the corresponding energies (resonance frequencies), but also the sub- or superradiant characteristics of these modes. By extension, we demonstrate that the theory is suited to predict Fano lineshapes related to the interference between a sub- and superradiant mode, in the extinction spectrum of oligomers upon plane wave illumination. We briefly discuss the convergence of this theory when more QNMs are included in the description of each resonator. In Chapter 4, we study a hybrid structure composed of a microdisk cavity supporting a pair of degenerate whispering gallery modes, dressed by two plasmonic antennas placed at the edge of the microdisk. In the context of enhancement of the emission by a quantum emitter placed in the vicinity of one of the antennas, this structure presents interesting properties. Indeed, we show that not only it allows for Purcell enhancements comparable to what is achievable with a single antenna hybrid, but with the added benefit of providing control over the direction into which light is emitted inside the cavity, depending on the relative position of the antennas within the cavity mode profile. This directionality property stems from the interference between the light emission in the two perturbed cavity whispering gallery mode (WGM). The phase difference relevant in this interference depends completely

on the spectral properties of these two modes as a function of the position of the antennas in the cavity mode profile. We present spectroscopic evidence for the predicted mode structure collected on an experimental realization of the system in a platform composed of silicon nitride microdisks and two aluminium antennas. The measurements demonstrate the tunability of the spectral properties of the cavity modes as a function of the relative distance between the antennas. While the work of Chapter 4 sets the first stone towards the study of phased array of antennas, Chapter 5 builds on it by investigating azimuthally distributed arrays of antennas which scatter beams with *orbital angular momentum* (OAM) from the cavity whispering gallery mode it is coupled to. In particular, after carefully studying the scattering and resonant properties of such structures, we propose a design which enables the emission of pure OAM associated with a single state of polarization. The principle of operation relies on the superposition of two concentric arrays of antennas, one with antennas oriented $+45°$ from the radial direction, the other with antennas at $-45°$. These two arrays scatter light with a different OAM for the left and right-handed circular polarization channels. The interference of the two arrays can lead to a suppression of one of these two polarization channels. We confirm this property with an experimental realization and speculate on the relevance of such a structure for the generation of arbitrary vector vortex beams. Finally, Chapter 6 investigates the relevance of hybrid resonators composed of a single antenna and a single cavity in the context of *molecular optomechanics*, where Raman active molecules are coupled to the antenna part of the hybrid resonators. Preliminary theoretical results, which do not yet involve a QNM treatment, show that the enhancement of Raman scattering respects the commonly accepted factorization into a pump and an emission enhancement effect, for both Stokes and anti-Stokes scattering. This factorization involves the cavity hybrid resonance but also the antenna one. Consequently, this ensures a strong enhancement of Raman scattering, comparable with SERS on single antennas, while enabling spectral selectivity of the collected Raman signal in the output channels of the cavity.

# SAMENVATTING

Licht is essentieel in ons leven. Het vormt een cruciaal onderdeel van ons ecosysteem, en van onze interactie met onze omgeving. Bovendien is licht in toenemende mate onmisbaar in de technologie van onze moderne samenleving. Het vakgebied dat licht bestudeert wordt ook wel fotonica genoemd. Er wordt wel gezegd dat waar de 20e eeuw de eeuw was van het elektron, op basis van de kennis van elektriciteit en micro-elektronica, de 21e eeuw het tijdperk zal worden waarin licht en fotonica een vergelijkbare revolutie teweeg zal brengen in hoe wij digitale informatie verwerken en beveiligen. Voor een deel is deze revolutie al gaande door massaal gebruik van glasvezel optiek voor telecommunicatie en breedband internet, de implementatie van snelle, optische verbindingen tussen en binnen datacentra, en het intensieve wetenschappelijke en toegepaste onderzoek naar het direct gebruiken van licht voor digitale, analoge, of kwantum berekeningen en informatieverwerking. Daarnaast is kennis over licht-materie interactie essentieel voor het ontwikkelen van hoogstaande zonne-energie technologie, en voor het ontwikkelen van energiezuinige technologieën zoals LED-verlichting. Daarmee is fotonica een belangrijk vakgebied voor het oplossen van de energiecrisis. De belangrijkste fysische mechanismen om licht te beheersen zijn refractie, diffractie, verstrooiing, emissie en absorptie, allen fenomenen die de interactie van materie met licht gebruiken. De interactie tussen een lichtdeeltje (een *foton*) en een enkel microscopisch bouwblok van materie, zoals een atoom of molecuul, is desondanks in de meeste gevallen vrij laag. Deze lage interactie is in sommige toepassingen van groot nut, bijvoorbeeld voor het versturen van lichtsignalen over lange afstanden in glasvezelkabels, waarbij het feit dat er nagenoeg geen absorptie in glas is bij 1550 nm cruciaal is. Anderzijds is de lage interactie tussen licht en materie problematisch voor het verwerken van de data die door dit licht gedragen wordt. Na kort de relevante context van licht-materie interactie toe te lichten, presenteren wij in Hoofdstuk 1 van dit werk de twee strategieën die typisch gebruikt worden om licht-materie interactie te vergroten. De eerste strategie is om de interactie-tijd tussen licht en materie zo lang mogelijk te maken, door licht op te sluiten in een trilholte met hoge kwaliteitsfactor Q, waarin het licht lang rond zingt, en er dus vele malen gelegenheid tot interactie is tussen het licht en de materie. De tweede aanpak richt zich niet op tijd, maar op ruimte als vrijheidsgraad, door licht op te sluiten in extreem kleine volumes, kleiner dan de fundamentele diffractie limiet. Dit verhoogt de elektrische veldsterkte op de plek waar de interactie gewenst is. De benodigde veldversterking wordt verkregen door

licht te koppelen aan collectieve oscillaties van vrije elektronen aan de oppervlakte van een metaal. Deze oscillaties worden ook wel *plasmonen* genoemd. Zowel de aanpak met trilholtes met hoge Q en met plasmonen voor extreme opsluiting zijn over de laatste tientallen jaren succesvol toegepast om sterke, niet-lineaire interactie tussen licht en materie mogelijk te maken, maar ook om kwantum fenomenen op het niveau van enkele fotonen aan te sturen en te benutten. In dit proefschrift richten wij ons op een alternatieve strategie: hybride resonatoren die gemaakt zijn uit zowel een trilholte als een plasmonische resonator, waar de voordelen van deze beide componenten behouden blijven. Ongeacht welk type fotonische resonator men gebruikt, de prestaties ervan zullen altijd worden beperkt door verliezen in de vorm van optische absorptie en afstraling naar het verre veld. Deze verliezen maken het beschrijven van resonatoren, hun hybridisatie, en de interactie tussen licht en materie een belangrijke fundamentele uitdaging. Deze uitdaging vormt de basis van dit proefschrift: hoe kunnen we de interactie tussen licht en materie begrijpen in systemen opgebouwd uit hybride fotonische resonatoren, waarbij volledig rekening wordt gehouden met de onvermijdelijk open en verliesgevende aard? Om deze vraag te beantwoorden maken wij gebruik van de *quasi-eigentoestand* (QNM – quasinormal mode) theorie. Hoofdstuk 1 geeft een overzicht van het QNM formalisme dat over de afgelopen zes jaar is ontwikkeld tot een efficiënt beschrijving van verliesgevende diëlektrische en plasmonische trilholtes. Dit formalisme is bijzonder geschikt om de stralingseigenschappen van fotonische resonatoren mee te nemen. Dit wordt aangetoond in Hoofdstuk 2 voor het specifieke geval van een niet-resonante verstrooier die een trilholte met een hoge kwaliteitsfactor verstoort. We laten zien dat QNM storingsrekening een heel elegante manier is om de toename, maar ook de afname van stralingsverliezen te kwantificeren voor trilholtes met een hoge kwaliteitsfactor die worden verstoord door een klein object. Uit de QNM storingsrekening volgt dat de verandering van stralingsverliezen kan worden verklaard door de interferentie van het elektrisch veld van de quasi-eigentoestand van de trilholte met het verstrooide veld van het kleine object. Deze voorspelling is gebaseerd op het concept van complexe waarden voor het mode volume van resonatoren, waarbij het reële deel informatie geeft over de mate waarop het lichtveld wordt opgesloten en het imaginaire deel fase informatie bevat die relevant is voor stralings- en interferentie-effecten. Aan de hand van experimenten waarin de verstoring van fotonische kristal trilholtes door een nabije veld sonde gemeten is laten we zien dat dit complexe eigentoestandsvolume zelfs gemeten kan worden.

In Hoofdstuk 3 ontwikkelen we een uitbreiding van QNM theorie die gebruikt kan worden om de eigenschappen te verklaren die ontstaan wanneer twee of meer fotonische resonatoren aan elkaar koppelen, op basis van de eigenschappen van de enkele resonatoren. Wanneer de QNMs eenmaal zijn genormeerd kunnen uit de eigentoestanden en eigenfrequenties ook meetbare grootheden zoals de werkzame doosneden voor verstrooiing

en uitdoving op semi-analytische wijze worden bepaald, en de Purcell versterkingsfactor voor elk type lichtbron, voor elke frequentie, plaatsing en polarisatie. We laten zien dat de hybridisatieregels voor dimeren van plasmon antennes gelijkenis hebben met bekende hybridisatieregels voor resonante puntdipolen, als we ons model beperken tot het beschrijven van elke resonator met een enkele QNM. Ons model voorspelt niet alleen de symmetrische en antisymmetrische gehybridiseerde eigentoestanden met de daarbij behorende energieën (resonantiefrequenties), maar ook de sub- of superstralende eigenschappen van deze eigentoestanden. Als uitbreiding op dit model laten we zien dat de theorie ook geschikt is voor het voorspellen van Fano lijnvormen die ontstaan door de interferentie tussen een sub- en superstralende eigentoestand. Tot slot bespreken we kort de convergentie van deze theorie als functie van het aantal QNMs dat wordt meegenomen in de beschrijving. In Hoofdstuk 4 bestuderen we een hybride structuur die bestaat uit een trilholte in de vorm van een microschijf gebaseerd op het fluistergalerijprincipe, met twee plasmonische antennes op de rand. Dit type structuur biedt interessante mogelijkheden voor het verhogen van de emissie van een kwantumemitter in de buurt van de antennes. We tonen aan dat met deze structuur een Purcellversterking mogelijk is die vergelijkbaar is met die van een hybride met slechts een enkele antenne, ondank de verstrooiing en absorptie verliezen die de tweede antenne in principe met zich mee brengt. Het voordeel van de structuur is dat deze controle biedt over de richting waarin het licht uitgezonden wordt in de trilholte, door middel van de relatieve positie van de antennes ten opzichte van elkaar in het mode profiel van de trilholte. Deze directionaliteit komt voort uit interferentie van licht dat uitgezonden wordt via twee verschillende paden in de trilholte. Het faseverschil dat van belang is in deze interferentie wordt bepaald door de spectrale eigenschappen van de twee paden en hangt af van de positie van de antennes in de trilholte. Voor dit voorspelde gedrag laten we experimenteel spectroscopisch bewijs zien. Hiervoor hebben we een hybride system geconstrueerd dat bestaat uit een microschijf van siliciumnitride met twee aluminium antennes. De metingen tonen aan dat de spectrale eigenschappen van het systeem te beïnvloeden zijn door de relatieve afstand tussen de antennes te veranderen. Voortbordurend op Hoofdstuk 4 waarin de eerste stappen naar het bestuderen van antenne-kettingen zijn gezet onderzoeken we in Hoofdstuk 5 azimuthaal regelmatig verdeelde kettingen van antennes die lichtbundels met baanimpulsmoment verstrooien vanuit de trilholte. Na een nauwkeurige studie van de verstrooiings- en resonantie-eigenschappen van zulke structuren presenteren we een ontwerp dat emissie van licht met een puur baanimpulsmoment in een enkele polarisatietoestand mogelijk maakt. De werking is gebaseerd op de superpositie van twee concentrische kettingen van antennes: één met antennes onder een hoek van $+45°$ met de radiale richting en de ander met antennes onder een hoek van $-45°$. Deze twee arrays verstrooien links- en rechtshandig circulair

gepolariseerd licht met een ander baanimpulsmoment. Interferentie tussen de twee arrays maakt het mogelijk een van deze twee polarisaties te onderdrukken. We hebben deze eigenschap experimenteel bevestigd en we bediscussiëren de mogelijke toepassing van zulke structuren voor het genereren van willekeurige vectoriële vortexbundels van licht. Ten slotte onderzoeken we in Hoofdstuk 6 het belang voor *moleculaire optomechanica* van hybride resonatoren bestaand uit een enkele antenne en trilholte. Hiervoor ontwikkelen we een eenvoudige klassieke beschrijving voor inelastische lichtverstrooiing die plaats vindt omdat moleculen die het Ramaneffect vertonen worden gekoppeld aan de antenne van de hybride resonator. Dit hoofdstuk is een haalbaarheidsstudie met eerste theoretische resultaten die nog niet gebruik maken van QNM storingsrekening. De studie laat zien dat de versterking van Ramanstrooiing de algemeen aanvaarde ontbinding in effecten van pompversterking en emissieverhoging volgt voor zowel Stokes- als anti-Stokesverstrooiing. Aangezien deze ontbinding betrekking heeft op de resonanties van zowel de trilholte als de antenne zorgt dit voor een hoge versterking van Ramanverstrooiing, vergelijkbaar met SERS op enkele antennes, en biedt het daarnaast spectrale selectiviteit van het Ramansignaal in de uitgaande kanalen van de trilholte.

# RÉSUMÉ

La lumière est essentielle dans nos vies. Elle est non seulement un élément crucial de notre écosystème et de nos interactions avec lui, mais elle est également impliquée dans de plus en plus d'aspects revêtant un caractère important dans notre civilisation moderne. En effet, il est dit que l'étude de la lumière, également connue sous le nom de photonique, est au XXIe siècle ce que l'électronique a été pour le XXe car elle pourrait conduire à des bouleversements majeurs dans la manière dont nous traitons et sécurisons l'information. Cette révolution est déjà en cours, de par l'utilisation massive de fibres optiques pour les télécommunications sur de longues distances, la mise en place d'interconnexions optiques rapides entre les nœuds dans les centres de données, et de nombreuses études visant à exploiter directement la lumière pour le calcul numérique, analogique ou quantique et le traitement de l'information. De plus, le photovoltaïque, exploitant la lumière solaire, est l'une des options privilégiées pour résoudre la crise énergétique actuelle à l'échelle mondiale. Toutes les promesses faites par la lumière sont intimement liées à notre capacité à la faire interagir avec des objets physiques par réfraction, réflexion, diffraction, émission et absorption. L'interaction entre un grain de lumière, appelé *photon*, et la matière est relativement faible. Même si cette faible interaction est essentielle pour la propagation de la lumière via des fibres optiques (absorption négligeable dans le verre à 1550 nm), c'est un inconvénient majeur pour le traitement de données encodées par cette lumière. Dans le Chapitre 1 de cette thèse, après avoir brièvement introduit la figure de mérite pertinente dans le contexte de l'interaction lumière-matière, nous présentons les deux stratégies qui ont été utilisées historiquement pour augmenter/accroître cette interaction. D'une part, la lumière peut être contrainte à interagir plusieurs fois avec la matière en la piégeant dans une cavité diélectrique avec un facteur de qualité élevé pendant de nombreux cycles optiques, augmentant ainsi le champs électrique du photon par un effet temporel. D'autre part, la lumière peut être comprimée dans des volumes minuscules très inférieurs à ceux autorisés par la limite de diffraction, augmentant ainsi le champs électrique du photon par un effet d'espace. Cela peut être réalisé en couplant la lumière aux oscillations collectives d'électrons libres, également appelés *plasmons*, à l'interface d'un métal et d'un diélectrique. Les approches basées sur l'utilisation de cavités et d'éléments plasmoniques ont été utilisées avec succès au cours des dernières décennies pour permettre une forte interaction non-linéaire entre un champ lumineux et la matière, mais également pour observer et exploiter des

phénomènes quantiques à l'échelle de photons uniques. Dans cette thèse, nous portons notre attention sur une voie alternative qui émerge actuellement; les résonateurs hybrides composés à la fois d'une cavité diélectrique et d'un résonateur plasmonique, où les avantages de ces constituants pris individuellement seraient largement préservés. Quel que soit le type de résonateur photonique utilisé, les performances sont toujours limitées par les pertes, soit par absorption optique, soit par couplage au champ lointain rayonné. Cela pose d'importants défis fondamentaux pour la description des résonateurs, leur hybridation ainsi que l'interaction lumière-matière. Une seconde motivation de ce travail est de comprendre l'interaction lumière-matière dans les systèmes photoniques hybrides, tout en tenant compte de la nature ouverte et à pertes des résonateurs photoniques. Pour ce faire, nous utilisons la théorie dite des *modes quasinormaux* (QNM - quasinormal modes). Le Chapitre 1 passe en revue les progrès récents importants enregistrés ces dix dernières années pour faciliter la modélisation des cavités diélectriques et plasmoniques à pertes. Le Chapitre 2 revisite la théorie de perturbation des cavités à facteur de qualité élevé par un petit objet diffusant. Nous montrons, pour la première fois, que la théorie de perturbation QNM propose un moyen très puissant pour quantifier l'augmentation et la diminution du facteur de qualité engendrées par la présence de la perturbation. Les prédictions du modèle reposent sur le concept de volume modal à valeurs complexes des QNMs, où la partie réelle détermine l'intensité du confinement du champ lumineux, et la partie imaginaire contient l'information de phase primordiale pour rendre compte des effets de rayonnement et d'interférence. Grâce à des mesures faites sur une cavité à cristaux photoniques par une sonde de champ proche, nous montrons que ce volume modal complexe peut même être mesuré. Dans le Chapitre 4, nous développons une théorie QNM pour prédire les propriétés hybrides émergeants lors du couplage de plusieurs résonateurs photoniques à partir de la seule connaissance des QNMs individuels des résonateurs non couplés. Une fois les QNMs obtenus normalisés, les observables tels que la section efficace d'extinction ou le facteur de Purcell peuvent être obtenus de manière analytique pour n'importe quelle source, à n'importe quelle fréquence. Dans le cas ou chaque résonateur peut être modélisé par un seul QNM, nous montrons que notre théorie peut non seulement expliquer la nature liante et antiliante des modes hybrides et les énergies correspondantes (fréquences de résonance), mais également les caractéristiques sous- ou super-radiantes de ces modes. Par extension, la théorie est adaptée pour prédire les résonances Fano liées à l'interférence entre un mode sous-radiant et un mode super-radiant dans le spectre d'extinction d'oligomères. Nous présentons également une étude de convergence de cette théorie avec le nombre de QNMs considérés dans la description de chaque résonateur. Au Chapitre 4, nous étudions une structure hybride composée d'une cavité microdisque supportant une paire de modes dégénérés de galerie, habillée de deux antennes plasmoniques

placées en périphérie du microdisque. Dans le contexte de l'augmentation du rayonnement d'un émetteur quantique placé au voisinage de l'une des antennes, cette structure présente des propriétés intéressantes. Nous montrons qu'elle permet d'obtenir une augmentation du facteur de Purcell, de contrôler la direction dans laquelle la lumière est émise à l'intérieur de la cavité en fonction de la position relative des antennes dans le profil modal des modes de galerie. Cette propriété de directivité découle de l'interférence entre l'émission de lumière dans les deux modes galeries de la cavité (WGM) perturbées par les antennes. La différence de phase pertinente dans cette interférence dépend entièrement des propriétés spectrales de ces deux modes et de la position des antennes dans le profil modal de la cavité. Par le biais d'une réalisation expérimentale du système, basée sur l'utilisation de microdisques en nitrure de silicium et de deux antennes en aluminium, nous présentons des résultats expérimentaux qui mettent en lumière les propriétés modales prédites par notre analyse. Alors que les travaux du Chapitre 4 jettent les bases de l'étude d'un réseau d'antennes à commande de phase, le Chapitre 5 s'appuie sur un réseau d'antennes à répartition azimutale qui diffuse un champ lumineux présentant un *moment angulaire orbital* en découplant les modes de galerie de la cavité. En particulier, après avoir étudié les propriétés de diffusion résonante de telles structures, nous proposons un prototype qui permet l'émission d'un moment angulaire orbital pur associé à un seul état de polarisation. Le principe de fonctionnement repose sur la superposition de deux réseaux d'antennes concentriques, l'un avec des antennes orientées à $+45°$, de la direction radiale, l'autre avec les antennes à $-45°$. Ces deux réseaux diffusent la lumière avec un moment angulaire orbital différent selon le mode de polarisation circulaire, gauche ou droit, et l'interférence qui en résulte peut alors entraîner la suppression de l'un des deux modes de polarisation. Nous confirmons cette propriété avec une réalisation expérimentale et analysons la pertinence d'une telle structure pour la génération à la demande de faisceaux de vortex vectoriels. Enfin, le Chapitre 6 étudie la pertinence des résonateurs hybrides composés d'une seule antenne et d'une seule cavité pour *l'optomécanique moléculaire*, où des molécules présentant une activité Raman sont couplées à la composante antenne de résonateurs hybrides. Les résultats théoriques préliminaires, qui n'impliquent pas encore de traitement QNM, montrent que l'augmentation de la diffusion Raman respecte la factorisation communément admise en un effet d'amplification du faisceau pompe, et un effet d'exaltation (amplification va) du rayonnement, et ce à la fois pour les diffusions Stokes et anti-Stokes. Cette factorisation fait intervenir les résonances du système hybride, dont l'une est de type 'cavité' et l'autre de type 'antenne'. Nous montrons alors que le système garantit, à la fois, une forte amplification de la diffusion Raman, comparable au signal SERS obtenu avec/sur une antenne unique, et une sélectivité spectrale du signal Raman collecté dans les canaux de sortie de la cavité.

# Acknowledgments

I never enjoyed going to school, and it took my younger sister joining me when she was old enough to finally stop crying about it. After a while, my passion for physics took over and carried me to the PhD level. However, since I seem to enjoy making my life more complicated than it needs to be, I decided to do a joint PhD in France and the Netherlands. A PhD is stressful and demanding, but add having to change life twice a year and then it also becomes painful. We almost developed a split personality! Thankfully, both Bordeaux and Amsterdam are amazing places to live, and I was always surrounded by the best people I could have asked for, and they were all crucial for me to go through this chapter of my life.

First, there were my supervisors, Philippe and Femius. I hope I managed to "hybridize", not only photonic resonators but also the best both of you could teach me. Even though the collaboration did not always go smoothly, I consider myself privileged of having benefited from the supervision of two excellent teachers. You have a completely different approach to almost everything, even sometimes on physics itself, and this gave me a unique perspective on nanophotonics, but more importantly on how to be a good and efficient scientist.

Femius, you seem to have your eyes on everything, from managing your group to your vast knowledge of physics and maths. I do not know how you manage that. There is absolutely no doubt about the fact that you are looking out for all your people, and I knew I could rely on you having my back for everything, even though you are not the cheering type of supervisor. I was always delighted to see you behave as a kid having a new toy whenever a new math or physics problem was brought to your attention. You also seem to appreciate good humor, especially when it comes at the expense of French people; you make a lot of jokes, some of them even good!

Philippe, ce qui me marquera le plus c'est ta passion pour la bonne physique et ta manière de penser non-conventionnelle, que ce soit par tes idées farfelues pour faire faire à COMSOL ce qu'il n'est pas programmé pour, ou bien le fait que tu sembles comprendre un nouveau concept en profondeur avant d'en avoir accepté toutes les bases simples. Tu es très exigeant, mais aussi très compréhensif et attentif, et je pense que ce fût une excellente combinaison pour me faire progresser. Cependant, il a aussi fallu que j'accepte d'avoir des "discussions" très animées avec toi, et de nombreux détours.

Then there were my group members and visitors in Bordeaux; Kevin V.,

Rémi, Jianji, Shelvon, Lamis, Spyros, Pierre, Sofia, Alexis, Louis, Wei, Alex, Maxime, Mélanie and Tong, and in Amsterdam; Marko, Hugo, Clara, Cocoa, Wouter, Annemarie, Christiaan, Ruslan, Isabelle, Chris, Rémi, Noor, Sachin, Sylvianne, Ilse, Tomas, Ben, Radek, Tom, Ilan and Stefanos. I am grateful to all of you for a great synergic working environment, but also a lot of fun and laughter. Hugo, you are the second person I met when I was visiting AMOLF (after Juliette at reception of course), and by such, you might have played a role in me coming to work in the resonant nanophotonics group. However, you definitely played one in me staying, and I would not have achieved what I did in my PhD without your immense contribution (teaching me Victorinox, how to pull tapered fibres, making samples for me, singing lullabies to sooth me, ...). Kevin V., j'ai toujours eu l'impression que tu étais la voix de la raison du groupe au LP2N, calme et patient (mais tu as quand même des limites que j'ai quelquefois testées), toujours très interessé et interessant dans toutes les discussions scientifiques qui peuvent avoir lieu autour de toi, en particulier pendant le trajet quotidien vers le restaurant CNRS. Désolé pour tous les emails de Philippe m'étant destinés qui te sont parvenus par erreur. Wei, thank you for all your precious help and very interesting discussions. I am disappointed by the fact that I never heard you rap properly though. Clara, I am sad that we only overlapped 4 months before you finished your contract. We had such nice discussions about physics, and well, virtually anything. I thank you both with Cocoa for making me feel home in the group. Alex, on est devenu de très bons amis en un temps record. Cela est probablement lié à ta personnalité très ouverte et, il faut l'avouer, assez étrange parfois. Je considère nos longs et inutiles (parceque j'ai raison) débats sur Star Wars, et les vidéos que tu m'as montrées (toutes plus chelous les unes que les autres), comme partie integrante de ma formation de doctorant. Merci. Isabelle, I tried to get rid of you by changing office, but you still managed to disturb my peace =P. I was asked stay politically correct here, but you know have much I enjoyed all the bantering we did, thank you. Louis, je n'imaginais pas vraiment devenir ami avec un punk monégasque (le seul à priori), mais ça toujours été un plaisir de discuter avec toi, de physique, mais aussi, évidement, de concerts et de bagarres. Tomas, at first I found it odd to supervise a Master student way taller than me, and a bit older, in particular when I was trying to be intimidating. Hopefully, you also became an excellent friend, and I must come back to the Netherlands as much as I can so we can hang out on your boat again. Rémi F., le seul thésard que j'ai cottoyé qui jure plus que moi. Un peu un exemple à suivre en quelque sorte. Marko, thank you for being the mama hen of the group, taking care of your baby PhD and Masters students. Please, never shave your beard again, I was confused for weeks. Christiaan, we should definitely go back to Tibidabo one day, preferably when it is open! Alexis, les soirées au Swing étaient toutes mémorables, en particulier celle où, aprés que je t'ai racompagné chez toi, tu es retourné dans les rues de Bordeaux à 3-4h du matin à traîner avec les punks à chiens. Annemarie, please keep on

being overexcited and cheerful about almost everything, it brings happiness around you. Maxime, si tu as besoin d'aide pour récuperer les clés de ton appartement, fais moi signe. Ruslan, I am going to miss your anecdotes and other fun facts. I learned a lot, and if I ever win some money at a TV show, you get a share. Ben, I was very happy when you joined: finally an Italian in the group, someone who understands that lunch is sacred. Please keep your passion for good physics. Radek, thank you for very interesting scientific discussions, but also for sharing you own experience of joint-PhD. Ilan, je mesure souvent le niveau d'amitié avec les français en comptant à quel point ils me chambrent; en à peine 4 mois j'an ai pris pour mon (nouveau) grade, donc il y a du potentiel. Merci de continuer le projet Raman, je suis sûr que tu fera du bon boulot. Tom, thank you for your amazing sense of humor (and you are not even trying that hard!).

I had the chance to work in two very good labs and benefit from the experience of many excellent researchers. At AMOLF, I want to thank you Ewold, Said, Kobus, Albert, Esther, Erik, Bruno and Alejandro for very instructive discussions, and the very well oiled machine that are the Thursday nanophotonics colloquia, poster sessions, and tutorials. At LP2N, thank you Simon, Jean-Baptiste, Philippe T., Brahim, Laurent C., Pierre N., Pierre B., Xavier, Romain, and Gaelle for the same thing, but also, for teaching me during my Masters a lot of what I now know and use on daily basis.

It would, however, be foolish to assume that we only learn from professors. Indeed, I probably learned the most during the discussions I had at colloquia, poster sessions, coffee breaks or even around a beer with my group members, but also Moritz, Sophie, Magda, Nassim, Verena, Benjamin B., Nick, Freek, Roel, Rick, Eitan, Robin, Jente, Juha, Dolphine, Lorenzo, Giada , David, Andrea, Sander, Benjamin D., Dominique, Lucie, Javier, Cyrian, Jesse, Filipo, Joe, Kevin, Hessel, Jan Bonne, John, Nikhil and Marco V. at AMOLF, and Caroline, William, Maxime B., Noémie, Antoine at LP2N. I am grateful for all the nice interactions we had, however, some of you also had a strong role in my life on a more personal level. Moritz, you always look so calm and peaceful. Such a reassuring presence that it almost makes it difficult to realize that you are actually a war machine when it comes to PhD work, or that you are like a kid whenever an opportunity to do something foolish presents itself. Somehow, at parties, you always seem to have a drink for you in one hand, and for me in the other. Very generous of you, hangover me is always grateful. Laura, thank you for your kindness, the very good food, and the confused expression on your face when Moritz was cycling with me in a trailer inside the Gamma. Sophie, tu as été un peu comme une grande sœur dès que je suis arrivé à AMOLF; très certainement un exemple à suivre (pas quand il s'agit de nager dans les canaux), mais aussi quelqu'un de très attentionnée. Magda, thank you for being one of the kindest persons I know, even-though you are starting to develop a serious rebellious attitude and make fun of me. Thank you, and also Nassim and Verena for the dinner evenings. It was difficult to schedule,

but always a lot of fun. Beste Nick, ik vergeet soms dat je niet Frans bent. Je spreekt perfect Frans, hebt in Frankrijk gewoond, en bovenal begrijp je echt de Franse mindset. Je bent volledig geïntegreerd, als een Tarzan tussen Franse apen. Op professioneel gebied waren mijn wetenschappelijke discussies met jou de beste en meest plezierige van mijn gehele PhD. Dominique, thank you for your kindness; our tea breaks were the sunshine of my days in the last intensive month of writing. Benjamin B., it is always nice to catch up with you. We definitely need to drink that bottle of wine one of these days. Jenny, thank you for the emotional support during the writing. Nikhil, thank for your help setting up my thesis, and sorry if my bad luck did rub on your setup as you jokingly claimed. Hessel, Jan Bonne, and John, thank for your help with the pulling setup, not just the technical, but also the emotional one. Luuk and Danai, my final officemates of the PhD, thank you for being patient with my swearing in French. I hope it is not the only thing you will remember of my language. I also want to thank my collaborators, in particular, Massimo, for your curiosity on QNMs, and Eitan for the samples we used for Tomas' project, and for the very interesting scientific discussions we had.

A healthy PhD includes many good parties and fun. And for that, I thank you, Nicola, Giorgio, Andrea G., Federica, Vanessa, Cesare, Cristina, Agata, Mario, Olga, Hans, Carolyn, Arno, Agustin, Gede, Parisa, Thijs, Olesia, Jeffrey, Teresa, Masha, and so many more. However, I must extend a special thanks to a few people. First, a collective thank you to the whole Italian crew of AMOLF-ARCNL, kind of my foster culture. It is a shame that I still don't know the lyrics to "Con Te Partirò"! Thank you Giulia and Judith for saving me from living under a bridge for almost two years. Ale, I always had a lot of fun hanging out with you, even when you emptied my water boiler. Marco S., thank you for the nice Marvel discussions, but I must say that I have doubts about your level of geekness; come on, 3 months to watch Endgame? You cannot be serious! Lukas, thank you for your sharp and funny attitude, and for throwing the best house parties in Amsterdam.

There were also a few friends that I knew before I started my PhD, but with whom I really bonded going through this intense period of my existence. David, je te suis extrêmement reconnaissant pour le soutient que tu m'as fourni quand j'en avais vraiment besoin. Aussi, merci de m'avoir mis en contact avec une bonne partie des amis que tu t'es fait à Bordeaux. En particulier, je pense à l'adorable Sébastien, qui a toujours été bon public pour mes blagues foireuses (il est trop gentil !). Maelig, merci pour ta patience, surtout pendant les traditionnelles 9 minutes de l'épisode "Mass effect" de Papy Grenier que l'on regarde avec David à chaque fois que je viens chez vous. Arnaud, merci pour les corrections que tu m'as infligées à Mario Kart presque tous les Dimanches, et tous les fous rires en regardant Suits (la grand-mère...).

Finally, I want to thank all the people who made my life easier in Bordeaux and Amsterdam. Tata Pastis, qu'est-ce qu'on ferait sans toi ? Non seulement tu es partout au LP2N, tu m'as évité de finir à la rue dès la première semaine de

ma thèse, mais tu as aussi un peu fait office de psy à de nombreuses occasions, et je t'en remercie. I am also grateful to the H.R. department of AMOLF, in particular Wouter and Reshma, for making my arrival in the Netherlands so smooth regarding housing, contract, taxes, ... Fabien, merci d'être le clown de l'administration du LP2N; toujours une blague un peu (voire beaucoup) déplacée, mais excellente, sous le coude. Floortje, thank you for being the gardian angel of the Resonant Nanophotonics group. Bob, Dimitry, Igor, Hans, Brahim and Niels, and more generally all AMOLF technical support, thank you for your help, direct and indirect in particular through Hugo. Thank you to the whole facilities crew of AMOLF, especially for keeping the coffee flowing. Yussuf and James, I was always delighted to listen to your stories about Nigeria and Brazil. And a final thank you to all AMOLF PV members, past and present, for organizing all these amazing borels and parties.

# List of Publications

a). K. G. Cognée, W. Yan, F. La China, D. Balestri, F. Intonti, M. Gurioli, A. F. Koenderink, and P. Lalanne, *Mapping complex mode volumes with cavity perturbation theory*, Optica **6**, 269 (2017) (**Chapter 2**).

b). K. G. Cognée, W. Yan, A. F. Koenderink, and P. Lalanne, *A coupled mode formalism for quasi-normal modes of photonic resonators*, in preparation (**Chapter 3)**.

c). K. G. Cognée, H. M. Doeleman, P. Lalanne, and A. F. Koenderink, *Cooperative interactions between nanoantennas in a high Q cavity for unidirectional light sources*, in press Light Science and Application (**Chapter 4**).

d). K. G. Cognée, H. M. Doeleman, P. Lalanne, and A. F. Koenderink, *Generation of pure OAM beams with a single state of polarization*, in preparation (**Chapter 5**).

e). K. G. Cognée, I. Shlesinger, P. Lalanne, and A. F. Koenderink, *Molecular optomechanics in the context of multiple photonic resonances*, in preparation (**Chapter 6**).

# About the author

Kévin Georges Guy Cognée was born in 1992 in Confolens, France. After two years of preparatory classes (math-physics) at the Lycée du Parc in Lyon (France) (2010-2012), he was admitted at the Institut d'Optique Graduate School (Palaiseau and Talence, France) where he obtained in 2015 an engineering (Master) degree in Optics and Photonics. In parallel, he obtained a Bachelor degree in Fundamental Physics at the University of Paris XI in 2013 (with honors), and a Master in Physics from the University of Bordeaux in 2015 (with high honors). He concluded his Master studies with a short research project supervised by Prof. Philippe Lalanne at LP2N-Institut d'Optique in France (Talence) and wrote a thesis on light extraction from thin films using metallic nanoparticles. He then started in 2015 a joint-PhD as part of a collaboration between the research groups of Prof. Philippe Lalanne and Prof. Femius Koenderink at AMOLF (Amsterdam, the Netherlands). The results are presented in this thesis. Kévin has been given the opportunity to present his work at several national and international conferences, and was awarded the prize for the best poster presentation at the European Optical Society Annual Meeting (EOSAM) in 2018.